


For Reference

NOT TO BE TAKEN FROM THIS ROOM

Ex LIBRIS
UNIVERSITATIS
ALBERTAENSIS





Digitized by the Internet Archive
in 2023 with funding from
University of Alberta Library

<https://archive.org/details/Nam1978>

The University of Alberta

A Kilowatt, Photo-initiated, Impulse-enhanced,
Electrically-excited (P.I.E.) CO₂ C.W. Laser

by



Kyong Ho Nam

A Thesis

Submitted to the Faculty of Graduate Studies and Research in
Partial Fulfilment of the Requirements for the Degree
of Doctor of Philosophy

Department of Electrical Engineering

Edmonton, Alberta

Fall 1978

DEDICATION

To my wife, daughter and sons
for providing purpose for this work;
To my Father and Mother for
their early inspiration of education.

ABSTRACT

An alternate excitation technique for high power, continuous wave carbon dioxide lasers is described. In this Photo-initiated Impulse-enhanced, Electrically-excited (P.I.E.) approach, the laser plasma is generated and maintained through sequential photo and impulse ionization processes in a controlled repetitive manner. Primary vibrational excitation is subsequently provided by a continuous non-avalanching dc discharge.

The design and construction of an experimental 1 kW pulse sustained CO₂ laser employing this excitation technique is presented. The results of a detailed parametric study and companion computer modeling of this machine are also given. The experimental data and operational characteristics strongly indicate that the P.I.E. excitation approach is a viable and less expensive, alternative to high energy electron beams in high power CO₂ laser design.

Hard U.V. from spark plugs and ionizing pulse were generated by discharging capacitors by means of a thyratron (Hyl802). Reliable pulse operation was achieved with the help of a set of saturable inductors that efficiently isolated the power supply and pulse circuit. A resonant charging scheme transferred more than 90% of the source energy to the U.V. and ionizing pulses, at a rate of more than 20kHz and at a voltage in excess of 20 kV.

The most durable and efficiently cooled U.V. transmitting anode was found to be a grate-type electrode constructed with 6.3 mm diameter copper tube. An electrolytic solution ballasted and cooled pin cathode exhibited the most satisfactory performance. Extensive

experimentation documented that both electrodes are suitable for a high power TE laser.

Most of the cathode pin materials tested, such as tungsten, nickel, steel, aluminum, copper and brass showed poor performance due to excessive corrosion and/or unnecessary passivation of the surface. Stainless steel, on the other hand proved to be an excellent material, exhibiting the lowest corrosion rate in a potassium carbonate aqueous solution ($K_2CO_3 + H_2O$) and the lowest sputtering rate in the gas discharge. A potassium carbonate aqueous solution has shown excellent performance as the ballasting agent. Assuming that each pin carries 50 mA dc current the lifetime of the pins in the distributed cathode has been calculated to exceed 1000 hours. Economical industrial applications thus appear fully feasible.

Approximately 33 kW of dc sustainer power was pumped into a 3.7 litre discharge volume. This value, corresponding to a power density of 8.8 W/cm^3 , is near the thermal limit for the laser gas having a 2 ms residence time. Approximately 1.2 kW of optical output power, (0.3 W/cm^3) was extracted using a 5-pass optical system.

With a focused power density of $\sim 1.3 \times 10^5 \text{ W/cm}^2$, the laser beam easily cut through 2 cm thick carbon steel. Excellent penetration butt-joint welding was also achieved on 3 mm wall pipe.

ACKNOWLEDGEMENTS

The author wishes to acknowledge his supervisor, Dr. H.J.J. Seguin, for unfailing encouragement and continuous financial support arranged through the National Research Council of Canada.

Many helpful discussions with Dr. J. Tulip, Dr. V. Merchant and Dr. D. McKen are greatly appreciated. The expert programming assistance received from Dr. R. Torgson is gratefully acknowledged. A special gratitude is extended to Mr. K. Doerrbecker and his staff for the prompt and excellent service provided in the machine and optic shops.

The author also expresses a deep appreciation to his wife, Sung Nim, for her unfailing patience during the research.

A special acknowledgement is extended to Ms. Barbara J. Gallaiford for the excellent typing of this thesis.

TABLE OF CONTENTS

	Page
Chapter 1	1
1-1	2
1-2	3
CO ₂ C.W. Laser	
1-3	8
1-3-1	9
1-3-2	12
1-4	15
Gas Mixture	
1-5	20
Conventional Electric Discharge	
for High Power CO ₂ Lasers	
1-6	22
P.I.E. (Photo Initiated, Impulse	
Enhanced, Electrically Excited)	
Technique	
1-6-1	23
1-6-2	26
Chapter 2	33
Experimental System Design and	
Operation	
2-1	37
Gas Transport System	
2-1-1	37
Laser Box	
2-1-2	39
Blower	
2-1-3	39
Heat Exchanger and Duct Assemblies	
2-1-4	40
Anode Electrode	

	Page
2-1-5 Cathode Electrode	43
2-1-6 Graphite Cathode	44
2-1-7 Copper Cathode	46
2-1-8 General Comments on the Continuous Surface Cathode	47
2-1-9 Multipin, Electrolyte Ballasted Cathode	48
2-1-10 Comparison With Conventional Multi- element Electrodes	50
2-2 Electrical System	52
2-2-1 Trigger Unit	52
2-2-2 High Voltage and High Repetition Rate (HVHRR) Switch	54
2-2-3 Preionizer Unit	57
2-2-4 Preionizer Component Design Consideration	60
2-2-5 Operational Characteristics	66
2-2-6 The Pulser Performance	72
2-2-7 Sustainer Power Supply	74
2-3 Optical System	75
2-3-1 Optical Power Extraction	76
2-3-2 Laser Resonator Employed	79
2-3-3 Equivalent Sequence of Lenses	82
2-3-4 Simple Technique to Change the Trans- mittivity of the Output Mirror	84
2-3-5 Window	85

		Page
Chapter 3	Experimental Results and Discussion	87
3-1	Laser Operation with Solid Cathode; First Electrode Configuration	89
3-1-1	Performance of Solid Electrodes in Low Pressures	89
3-1-2	Comparison of the Preionization Efficiency Under Different Conditions	92
3-1-3	V-I Characteristics in Low Pressure P.I.E. Laser	99
3-1-4	The Gas Impedance of the Low Pressure P.I.E. Laser	103
3-1-5	Gain Measurements	105
3-1-6	Absorption of the Laser Energy by a Pulse Excited CO ₂ Plasma	108
3-1-7	Output Power at Low Pressure	110
3-2	General Characteristics of Electro- lytic Solution Ballasting	114
3-2-1	Tap Water as a Ballasting Fluid	114
3-2-2	Temperature Dependence of Water Resistance	117
3-2-3	Discharge Characteristics of Various Pin Materials in Gas	118
3-2-4	The Performance of Various Pin Materials in Tap Water	122
3-2-5	The Use of Electrolytic Aqueous Solutions for Ballasting	124

		Page
3-2-6	Stainless Steel Pin Corrosion in Potassium Carbonate Solution ($K_2CO_3 \cdot \frac{1}{2} H_2O$)	125
3-2-7	Estimation of Pin Lifetime	131
3-2-8	Concentration of Potassium Carbonate and Resistances of the Solution	132
3-3	Laser Operation with 276-pin, Tap Water Ballasted Cathode; 2nd Electrode Configuration	141
3-3-1	Relationship Between Pulser and D.C. Input Powers	142
3-3-2	General Discharge Characteristic of 2nd Electrode Configuration	146
3-3-3	Small Signal Gain Measurements	148
3-3-4	Optical Output Power Characteristic	162
3-3-5	Translational Temperature Measurements	171
3-4	Laser Operation with 512-pin Cathode; 3rd Electrode Configuration	176
3-4-1	V-I Characteristics and Operating Impedances	176
3-4-2	Spatial Gain Profile and Discharge Characteristics	181
3-4-3	Output Power Characteristics	185
3-4-4	Material Processing Experiments	190

		Page
Chapter 4	P.I.E. Laser Theoretical Modeling	198
4-1	Approximations Made for the Theoretical Modeling	198
4-2	Energy Balance Equations	200
4-3	Description of Symbols	207
4-4	Computer Simulation of P.I.E. Laser Model	216
4-5	Comparison of the Results with the Experimental Measurements	219
Chapter 5	Conclusion	230
References		239
Vita		250
Appendix A	Computer Program	252

LIST OF TABLES

Table	Description	Page
1-1	Basic Vibrational Energy of CO ₂ Modes	11
2-1	Pulse and U.V. Capacitances	65
2-2	I.R. Window Materials	85
3-1	Ionization and Recombination Coefficients	97
3-2	The City of Edmonton Analysis of Treated Tap Water	115
3-3	Work Functions	120
3-4	Relative Sputtering Rate in H ₂	122
3-5	Composition of 304 Stainless Steel	123
3-6	Comparison of the Corrosion Rate Exhibited by Different Metals	127
3-7	Electrode Pin Arrangement	141
4-1	Temperature Dependant Rate Constants	215

LIST OF FIGURES

Figure	Description	Page
1-1	Energy Level Diagram of the CO ₂ Laser Gas Mixture	4
1-2	Fractional Electron Power Transfer in a CO ₂ Laser Gas Mixture	10
2-1	Schematic Diagram of Experimental P.I.E. Laser System	34
2-2	Nomenclature of the System	35
2-3	Schematic Diagram of the Copper Tube Anode	41
2-4	Rogowski Profiled Graphite Cathode Electrode	45
2-5	Schematic Diagram of Copper Pipe Cathode Electrode	45
2-6	Schematic Diagram of Multipin Cathode	49
2-7	Schematic Diagram of Trigger Unit	53
2-8	Schematic Diagram of Preionizer Unit	58
2-9	Saturation Curve for 3c8 Ferrite Core	63
2-10	Sectional View of Pulse Energy Storage Capacitor	64
2-11	Sectional View of U.V. Source Capacitor Bank	64
2-12	Waveform of Alternate Saturation of Saturable Inductor	67
2-13	Waveform of a Typical Anode Voltage of HY 1802	69

Figure	Description	Page
2-14	HY 1802 Thyratron Anode Voltage vs. Current Characteristic	73
2-15	Output Power Extraction Efficiency vs. Gain- Length Product	77
2-16	Optimum Mirror Transmission vs. Gain-Length Product	78
2-17	5 Pass Folded Path Optical Resonator	80
2-18	Equivalent Sequence of Lenses	82
3-1	Photos of Low Pressure Discharge	91
3-2	Relative Plasma Generation at 5 torr	93
3-3	Relative Plasma Generation at 10 torr	94
3-4	Relative Plasma Generation at 20 torr	95
3-5	Discharge Characteristic in He and CO ₂ :He Mixture	96
3-6R	Plasma Decay in CO ₂ , N ₂ and He	98
3-7R	Typical Characteristics for Self Sustained Low Pressure Discharge	100
3-8	V-I Characteristics of Low Pressure P.I.E. Laser	102
3-9	Total Gas Impedance vs. Total Current	104
3-10	Equipment Layout for the Gain Measurements	106
3-11	Gain Coefficient vs. Input Power Density	107
3-12	Total Laser Absorption vs. Pulse Power	109
3-13	Variation of V-I Characteristic with Pre- ionizer Frequency	111

Figure	Description	Page
3-14	Voltage vs. Laser Output Power	113
3-15	Water Discharge Test Device	118
3-16	Resistance Change with Water Temperature	119
3-17	Corrosion Rates of Different Metals in Potassium Carbonate Solution	128
3-18	Brass Pin Passivation Rate	129
3-19	V-I Characteristic in Potassium Carbonate Solution	130
3-20	Edge Round-off	131
3-21	Corrosion Rate of 304 Stainless Steel Pin	133
3-22	Pin Length Loss vs. Operating Time	134
3-23	Electrolytic Solution Resistance vs. Operating Voltage at Low Concentration	136
3-24	Electrolytic Solution Resistance vs. Operating Voltage at High Concentration	137
3-25	Subelectrode Resistance vs. Gap Spacing in the Solution	138
3-26	Total Electrode Resistance vs. Total Current	140
3-27	Input Power vs. Preionizer Frequency at 10 kV	143
3-28	Input Power vs. Preionizer Frequency at 15 kV	144
3-29	Pulser Output Voltage and Current Waveforms	145
3-30	Photo of Glow Discharge at 45 torr	147
3-31	Spatial Small Signal Gain Profile Between the Rows	150
3-32	Variation in Small Signal Gain from Cathode to Anode	151

Figure	Description	Page
3-33	Spatial Gain Variations at Different Current Densities	152
3-34	Spatial Gain Profile in the Direction of Flow	154
3-35	Small Signal Gain Coefficient vs. Total Current	155
3-36	Total Small Signal Gain vs. Gas Flow Velocity	157
3-37	Specific Gain Coefficient vs. CO_2 and N_2 Partial Pressures	159
3-38	Specific Gain Coefficient vs. He Partial Pressure	160
3-39	Specific Gain Coefficient vs. Air Partial Pressure	161
3-40	Dependence of Laser Power Output with CO_2 Partial Pressure	163
3-41a	Dependence of Laser Power Output with N_2 , He	165
b	Partial Pressure	166
3-42	Dependence of Laser Power Output with Partial Air Pressure	168
3-43	Dependence of Laser Power Output on Gas Flow Velocity	169
3-44	Dependence of Laser Power Output on Pulser Repetition Rate	170
3-45	Optical Power Output vs. Discharge Input Power With and Without Preionization	172
3-46	Translational Temperature Change With Input Power	175

Figure	Description	Page
3-47	V-I Characteristics of P.I.E. Discharge in High Pressure	177
3-48	Log-Log Plot of V-I Characteristics of the P.I.E. Laser	179
3-49	Laser Plasma Impedance vs. Discharge Current	182
3-50	Spatial Gain Profile in the Direction of Flow	183
3-51	Spatial Current Distribution	184
3-52	Subelement Ballasting Resistance and Fluid Gap Spacings	186
3-53	Temporal Behavior of Sustainer Current (short)	187
3-54	Temporal Behavior of Laser Power Output (Long)	188
3-55	Temporal Behavior of Input Power, Output Power and Efficiency	189
3-56	Input-Output Power Characteristic	191
3-57	Photo of Laser Cutting and Cut-edge	193
3-58	Photo of Vertical Seam Welding	197
3-59	Photo of Laser Drilled Holes	196
3-60	Hole Depth vs. Drilling Time	197
4-1	CSMP Program Structure	217
4-2	Comparison of the Measured Total Signal with the Computed Value	221
4-3	Comparison of the Measured Translational Temperature with the Computed Value	221
4-4	Comparison of the Measured Total Signal Gain with Computed Value	222

Figure	Description	Page
4-5	Comparison of the Measured Small Signal Coefficient with the Computed Value	222
4-6	Spatial Dependence of E/N and $J \cdot E$	224
4-7	Schematic Diagram of the Normalized Radiation Intensity	226
4-8	Schematic Diagram of the Normalized Steady State Oscillation Conditions	228

CHAPTER 1

INTRODUCTION

The increasing application of high power lasers in science and industry has intensified research and development on carbon dioxide gas lasers. With a relatively short 13-year history, the CO_2 laser has assumed a leading role in industrial applications. High efficiency and the capacity for convenient electrical excitation have made the Electrical Discharge Laser (E.D.L.) especially popular and widely used. Experience has shown however, that electrically excited lasers cannot be arbitrarily increased in size and power level because of active volume scaling limitations imposed by the onset of electric discharge instabilities.

Over the years a wide variety of discharge systems have been developed in an attempt to produce the large volume uniform glow discharges essential for proper high power laser operation. Among many different forms of these, fast flow devices have been constructed and operated with great success. Further improvement has been made by incorporating preionizing techniques into the flow system.

This thesis addresses itself to the topic by reporting on the development, and characterization of a new type of pulsed maintained laser. In this device both photo and impulse ionization processes are utilized to generate and maintain the required plasma density within the active volume. The term P.I.E. is used in this work as an acronym for "Photo-initiated, Impulse-enhanced, Electrically-excited", and as such describes the methods of operation.

1-1 Scope of the Thesis

The body of this thesis presents the results of an in-depth parametric study on this experimental P.I.E. laser. The extensive amount of data collected serves the dual purpose of device characterization as well as a foundation for a comprehensive computer modeling.

The specific format adopted in this thesis presentation is as follows: Chapter 1 briefly outlines the historical and sequential developments in high power carbon dioxide lasers, from both experimental and theoretical standpoints.

Chapter 2 describes the design and constructional aspects of the P.I.E. laser which forms the basis of this research project.

Experimental data depicting electrical and optical operational parameters of the device are consolidated in Chapter 3.

Device characterization by a computer-modeling forms the subject matter of Chapter 4. The experimentally measured data is compared with theoretical calculations.

A conclusion and discussion has been made in Chapter 5. Also future research work is suggested in this Chapter.

1-2 Historical Review of High Power CO₂ C.W. Laser

Patel's first successful operation of a C.W. carbon dioxide laser in 1964⁽¹⁾ marked the dawn of an era in the development of high power lasers, suitable for industrial application. The subsequent utilization of N₂ and He gases in the laser gas mixture increased the initial milliwatt output power level by many orders of magnitude⁽²⁾.

The relevant energy levels of the CO₂ laser are shown in Figure 1-1. He does not appear in the level diagram because it does not affect the pumping or deactivating of the upper laser level (00°1). The CO appearing in the level diagram is produced by the dissociation of CO₂ under an electric discharge. N₂ in the CO₂ laser mixture acts as an energy storage reservoir for the upper laser level (00°1), while He is an effective coolant that keeps the lower laser levels' (10°0, 02°0) population low by slowing down thermal excitation.

As soon as the benefits of cooling the laser gas mixture were recognized, convective and water cooling⁽³⁾ concepts were adopted as an integral part in high power laser design. The importance of cooling of the laser gas mixture can be readily understood if one considers the fact that laser output energy extraction efficiency is only a few percent. The residual part of the input energy merely serves to increase the gas enthalphy.

The population inversion between the lower laser levels (10°0 and 02°0) and the upper laser level (00°1) decreases with increasing gas temperature. Available information⁽⁵⁾ shows that the population inversion for the 10.6μm transition (00°1 to 10°0) drops to zero when the

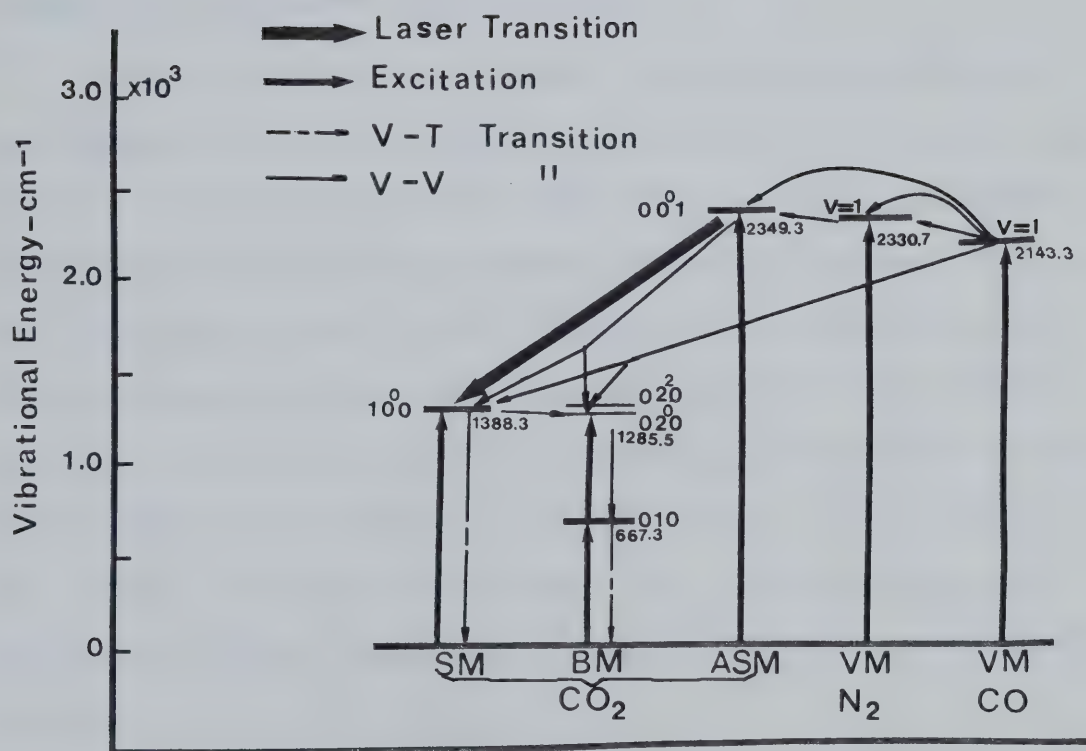


Figure 1-1 Energy Level Diagram of the CO₂ Laser Gas Mixture at 400 °K

V-T Vibrational - Translational
 V-V Vibrational - Vibrational
 SM Symmetric Mode
 BM Bending Mode
 ASM Asymmetric Mode
 VM Vibrational Mode

temperature of the gas rises to 680°K, while the population inversion for the 9.6 μ m transition (00°1 to 02°0) goes to zero when the gas temperature rises to 400°K.

Most present day high power CO₂ lasers employ gas transport systems which circulate the gas mixture through built-in heat exchangers. This technique provides an effective method for removal of residual translational energy from the lasing volume.

In 1969 Tiffany and Targ employed a transverse flow (TF) and longitudinal excitation technique to produce 1.1 kW of C.W. power from an active volume only 1 m long⁽⁴⁾. The advantage of transverse-flow over longitudinal flow can be explained in terms of the gas residence time. The gas residence time, T_r , is defined as d/u where d is the discharge dimension in the flow direction, and u is the gas transport velocity. Consequently, T_r is an effective parameter in determination of gas heating effects within the discharge volume. For a given gas flow velocity a transverse flow geometry will clearly provide a much shorter gas residence time with a concomitant decrease in translational temperature of the active region.

Experiment has demonstrated that the optimum field-pressure ratio (E/P) for efficient CO₂ laser performance is in the region of 10 to 50 V/cm-torr⁽⁵⁾. A one meter longitudinal discharge at 100-torr would thus require an excitation voltage in the many hundred kilovolt range. Consequently, this is not a practical situation for C.W. pumping.

Longitudinal flow and excitation systems have a further disadvantage in that discharge uniformity and stability are difficult to achieve

at high pressure. Consequently, such systems are generally restricted to low pressure operation, usually below 20-torr. For these reasons, longitudinal excitation and flow geometries are not suited to multi-kilowatt laser design.

Modern high power CO₂ lasers employ a transverse excitation (T.E.) and flow (T.F.) technique in which the electric field, gas flow and optical axis are mutually orthogonal^(7,8). As T.F. and T.E. techniques became popular in multikilowatt laser design, the dimension of the discharge was changed in such a way that it became shorter in the optical axis and wider in the gas flow direction. In order to achieve efficient laser power extraction from these wide discharge volumes, multipass optical configuration have been widely used. Most of the large volume multipass systems have been operated with MOPA (master oscillator power amplifier) configurations⁽¹⁰⁾ due to difficulties in mirror alignment and output coupling.

In 1971 Eckbreth⁽⁶⁾ reported on a 1.2 kW C.W. laser amplifier using a 5-pass optical system. A modified version⁽⁷⁾ produced a 1.4 kW C.W. laser output with a 14kW input, at 46 torr, (CO₂ : N₂ : He = 1 : 7 : 12). Hill⁽⁸⁾ built a 20 kW C.W. laser amplifier equipped with a 17-pass optical system. A 100 kW reproducible power input was achieved at 50-torr with a mixture ratio of CO₂ : N₂ : He = 1 : 7 : 25.

One factor that the above lasers have in common is the very low partial pressure of carbon dioxide used in the lasing mixture. This is consistent with the findings from the author's project. With a total operating pressure of about 50-torr, typically less than 2-torr is carbon dioxide.

In 1970 a new concept of laser pumping was reported by Gerry⁽⁹⁾. In this Gas Dynamic Laser (G.D.L.) the laser gas mixture was heated under pressure and expanded through a supersonic nozzle. A multimode, continuous wave power output of 60 kW from a CO_2 - N_2 - He gas dynamic laser was obtained.

Locke⁽¹⁰⁾ was also successful in building a 30 kW C.W. laser by using a gas dynamic pumping concept. The maximum output power obtained from his system was 55 kW.

1-3 Excitation Techniques for CO₂ Lasers

Two pumping methods have been widely used for high power CO₂ lasers. One method is thermal pumping and adiabatic expansion cooling of the laser gas mixture, known as Gas Dynamic Pumping^(9,10). In these systems, the rapid change in the translational temperature of the expanded gases causes the excited vibrational states of the molecules to relax toward thermal equilibrium⁽¹⁰⁾. Since the various V-V and V-T processes involved proceed at different rates, a temporary population inversion (the population of the upper laser level, 00°1, becomes larger than that of the lower laser levels, 10°0 or 02°0) can be produced in the expanding supersonic stream.

The other and even more commonly utilized laser excitation technique is "Electric discharge" pumping. In this process the lasing gas molecules receive energy via two or three body collisions with the abundant discharge electrons. The two predominant pumping mechanisms are (A) direct electron impact and (B) resonance transfer of energy between N₂ (v=1) and CO₂ (00°1).

1-3-1 Pumping by Electron Impact

The basic pumping mechanism in an electric discharge is associated with energy transfer from discharge electrons to the appropriate upper vibrational levels of N_2 and CO_2 . The fractional power transfer data obtained by Wutzke⁽⁴⁸⁾ is reproduced in Figure 1-2 for reference purposes. A large fraction of the electron energy ($\sim 45\%$) is transferred directly to the CO_2 upper laser level (00^01) for an E/N (electric field/neutral particle density) of $\sim 10^{-16}$ V-cm². This is attributed to the very large vibrational excitation cross sections at low electron energies. Hake and Phelps⁽¹²⁾ have measured four cross section peaks for vibrational excitation of CO_2 by electron impact at 0.08, 0.3, 0.6 and 0.9 eV. They are 3, 5, 3.2 and 2.2×10^{-16} cm² respectively. Hake and Phelps associated the 0.3, 0.6 and 0.9 eV with the three levels of the asymmetric mode (ν_3 , $2\nu_3$ and $3\nu_3$) of the CO_2 molecules and 0.08 eV with the lowest bending mode (ν_2). This can be understood by referring to Table 1-1 showing the vibrational energy of the different modes.

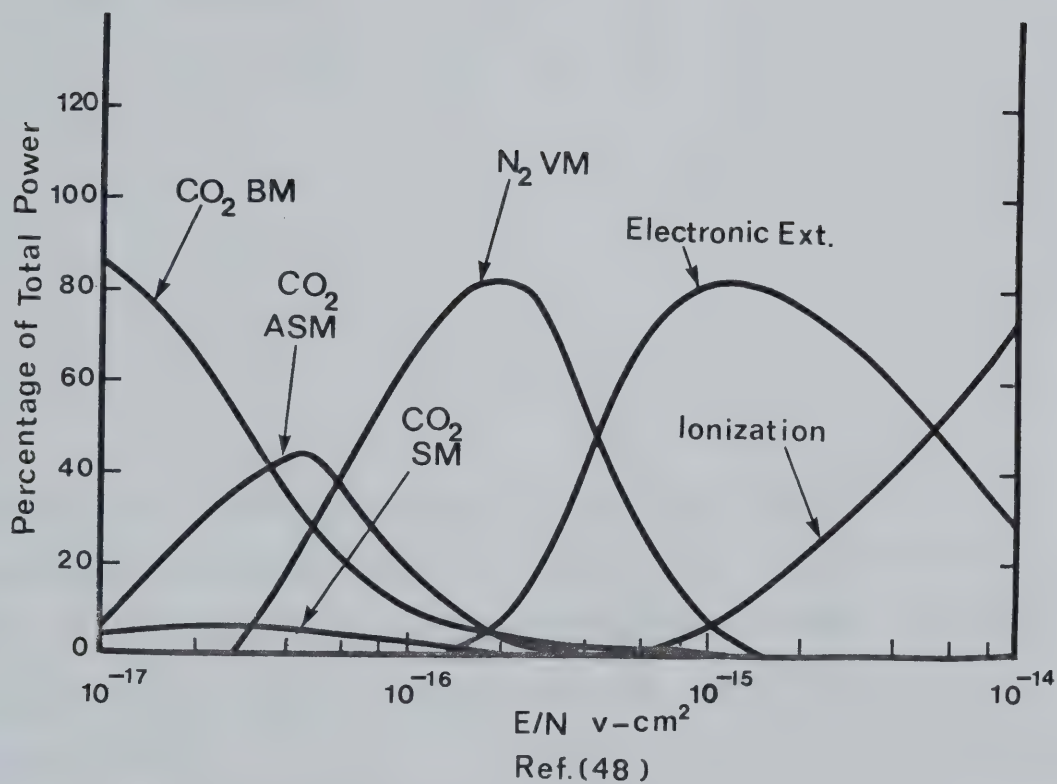


Figure 1-2 Fractional Electric Power Transfer in a CO₂ Laser Gas Mixture
 CO₂:N₂:He = 1:7:20 (Ref. 48)

TABLE 1-1

Basic Vibrational Energy of CO₂ Modes

State of vibration	mode	ν_1	ν_2	ν_3
Energy in wave numbers	cm ⁻¹	1337	667	2349
Energy in electron volts	eV	0.0166	0.083	0.291

* 1eV = 8065.8 cm⁻¹

Figure 1-2 also indicates that N₂ is effectively excited by the electrons in the energy range 0.6 - 3.0 eV. The total excitation cross section, σ_{TN_2} , of N₂ has been investigated by Boness and Schulz⁽²⁰⁾ and shown that it reaches a maximum value of $\sim 3 \times 10^{-16}$ cm² at electron energy ~ 2.3 eV.

1-3-2 Resonant Transfer

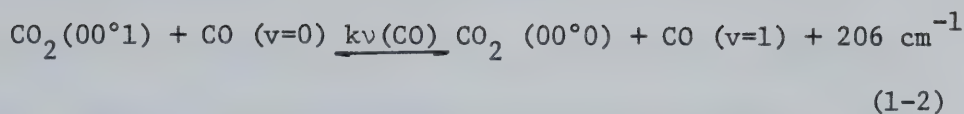
With such a large excitation cross section, N_2 is very readily excited by hot electrons in the discharge. The energy of the first vibrational level of N_2 is extremely close to the CO_2 upper laser level (00^01), and the energy transfer takes place from the N_2 molecules to the CO_2 upper laser level (00^01) by collisions of the second kind i.e. resonant transfer. Because N_2 has a zero permanent dipole moment, N_2 in the $v=1$ vibrational level cannot decay to the ground state. Therefore, it is reasonable to assume that most of the vibrational energy of the N_2 molecules is transferred to the CO_2 upper laser level (00^01).

This process can be expressed by an energy balance equation as follows:

$$N_2(v=1) + CO_2(00^00) \xrightarrow{k_{v'}, k_v} N_2(v=0) + CO_2(00^01) - 18 \text{ cm}^{-1} \quad (1-1)$$

which represents a mixed state of N_2 ($v=1$) and CO_2 (00^01). Thus N_2 acts as an energy reservoir in the CO_2 laser gas mixture, that increases the effective lifetime of the CO_2 (00^01) state.

Furthermore, a substantial amount of CO is present in the laser gas mixture as a result of dissociation of CO_2 during the electric discharge. The pressure of CO can be greater than 50% of the original CO_2 pressure⁽¹²⁾ and contributes to the effective pumping of the laser gas mixture by the following process:



Even though the energy resonance is not as close as that of equation (1-1), this reaction appears to be very significant; particularly for sealed-off CO_2 laser operation. Above the k 's represent the rate constants.

An estimate of laser output may be made if one assumes that the dominant pumping mechanism is resonance transfer from $\text{N}_2(v=1)$ to $\text{CO}_2(00^\circ 1)$. At 1 torr of N_2 partial pressure the rate of excitation of N_2 , X_4 is equal to:

$$X_4 = N_0 N_e \sigma_{\text{TN}_2} v_d \quad (1-3)$$

Where N_0 is the number density of the N_2 , $2.687 \times 10^{19} \times \frac{PN_2}{760}$, N_e is the electron density, σ_{TN_2} is the total excitation cross section of $\text{N}_2(v=1-8)$, v_d is the electron drift velocity and PN_2 is the N_2 pressure. Assigning the laser parameters as follows: $PN_2 = 10$ torr, then

$$N_0 = 3.54 \times 10^{17} / \text{cm}^3$$

$$N_e = 2 \times 10^{10} / \text{cm}^3$$

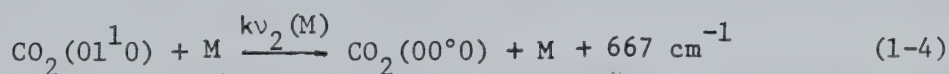
$$v_d = 10^7 \text{ cm/sec}$$

$$\sigma_{\text{TN}_2} = 3 \times 10^{-16} \text{ cm}^2$$

then the N_2 excitation rate is $X_4 = 2 \times 10^{19} \text{ sec}^{-1} \text{ cm}^{-3}$. If a laser tube is 100 cm long and 2.5 cm i.d., this rate could produce a total of $\sim 9.8 \times 10^{21}$ quanta/sec or equivalent to an output power of $\sim 200\text{W}$.

1-4 Relaxation Processes of Laser Gas Mixture

In order to extract laser power from the system a population inversion must first be established. This population inversion may be achieved by pumping the laser gas mixture to the upper laser level (00^01) or alternatively by relaxing the population of the lower laser level (10^00). But both processes are actually utilized simultaneously. It is well established that He plays a very important role in the lower laser levels (10^00 , 02^00) relaxation but it has negligible effects on the excitation and deactivation of the upper CO_2 laser level (00^01). The relaxation processes of the lower laser levels (10^00 , 02^00) are comparable in magnitude to the resonance transfer process for excitation of the upper laser level (00^01). This explains why the use of a CO_2 -He mixture in a CO_2 laser results in an equal or slightly higher power output than that of a CO_2 - N_2 mixture⁽¹¹⁾. One of the levels actively involved in the relaxation rate is the lowest bending mode (01^10). This acts as a "bottle-neck" when the translational gas temperature is high enough ($\sim 300^\circ\text{C}$) for the level to be thermally populated. The relaxation process for the 01^10 level is a vibrational-to-translational (V-T) energy exchange and can be described by:



where M is the collision particle and $k\nu_2(\text{M})$ denotes the relaxation rate constant for the collision with particle M.

Since it is now known that the relaxation rate of the lowest bending

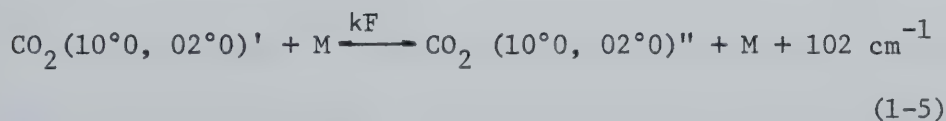
mode, 01^1_0 , is the limiting factor for population inversion, several relaxants are deliberately added. Often, effective relaxants exist naturally as the product of CO_2 dissociation under electric discharge conditions, such as CO. Recently the CO has been recognized as a moderate relaxant of the 01^1_0 level as well as an effective pumping agent of the 00^0_1 level⁽¹¹⁾.

The most effective relaxant for the 01^1_0 level is H_2O . Hydrogen gas is often added to the laser gas mixture since it combines with oxygen to produce H_2O under electric discharge conditions. However, H_2O or H_2 is not extensively used in the high power laser systems because it also relaxes the upper laser level (00^0_1) very effectively. In addition, water vapour appears to readily quench the discharge. Less than 1 torr of water vapour quenched the glow discharge in the 50 torr laser gas mixture tested, and eventually an arc developed. Therefore, when H_2O or H_2 is used as a relaxant, care must be taken to control the concentration for the best operation.

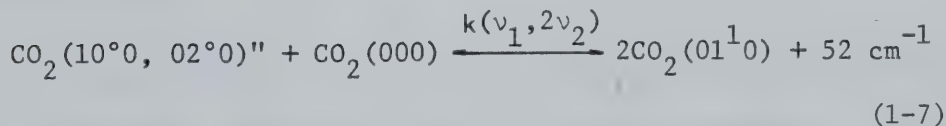
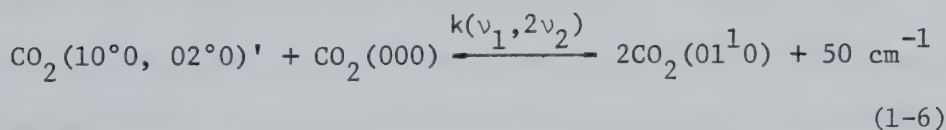
Even though He deactivates the 01^1_0 level less effectively, the best resultant population inversion can still nevertheless be obtained with He because it does not affect the upper laser level (00^0_1). Moreover, He also plays an important role in maintaining the energy distribution of electrons within the discharge in the proper range for more efficient excitation of CO_2 molecules⁽⁵⁾.

It is also necessary to consider the relaxation rates of the lower laser levels, 10^0_0 and 02^0_0 . The relaxation of these two lower laser levels couple through a Fermi resonance. The Raman spectrum

consists of two lines at 1285.5 and 1388.3 cm^{-1} , which are somewhat deviated from the 1334.6 cm^{-1} ($2V_2=667.3 \times 2$) for the $02^\circ 0$ level and 1337 cm^{-1} for the $10^\circ 0$ level respectively. The energy levels of these two lines (1337 and 1334.6 cm^{-1}) are almost in resonance and leads to a perturbation of the energy levels. As a result the $10^\circ 0$ level shifts up by 51.3 cm^{-1} and the $02^\circ 0$ shifts down by 49.1 cm^{-1} . At the same time a mixing of the eigen-functions of the two levels occurs. The two mixed eigen-functions are expressed as $(10^\circ 0, 02^\circ 0)'$ and $(10^\circ 0, 02^\circ 0)''$ and the vibrational-vibrational (V-V) energy exchange between the two levels is described by



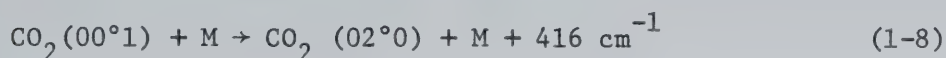
Both of these two levels can decay to the lowest level of the bending mode $(01^1 0)$ through resonant processes:



The rate constant $k(v_1, 2v_2)$ is several orders of magnitude faster than the rate of a second-order transition, such as $10^\circ 0 \rightarrow 01^1 0$, which

would require a Raman-like perturbation ($10^0 0 \rightarrow 00^0 0 \rightarrow 01^1 0$)⁽¹¹⁾. He, CO₂, CO and Xe yield the same order of magnitude of relaxation rates while N₂ yields a three order of magnitude slower rate.

The relaxation rate of the upper laser level ($00^0 1$) is at least one order of magnitude smaller than that of the other levels. In most cases, the relaxation of CO₂ upper laser level ($00^0 1$) takes place through the V-V coupling between upper ($00^0 1$) and lower laser levels ($10^0 0$ or $02^0 0$)⁽¹¹⁾:



Yardley and Moore⁽¹¹⁾ pointed out that in the case of noble gases, the most favorable collisions for the deactivation of the upper laser level ($00^0 1$) occur when only a small amount of energy on the order of kT is exchanged with the translational mode. The highest transition probability for the intermolecular V-V energy transfer, when the difference of energy levels lies within a few hundred cm^{-1} , is due mainly to a mixing of vibrational states through anharmonicity. Therefore, this process cannot be very efficient compared with other collisional relaxation processes.

Although diffusion also plays an important role in the deactivation of the excited CO₂ molecules, it is pressure dependent. For CO₂ pressures greater than 1 torr, overall relaxation is dominated by collisional relaxation. Because the system under consideration is being operated with ~ 2 torr of CO₂, only collisional relaxation need be considered.

Rotational relaxation within a vibrational state occurs extremely fast. Cheo⁽¹¹⁾ showed that the collision time for hard sphere collisions is about 100ns at 1 torr. This corresponds to a rate constant of $10^7 \text{ torr}^{-1} \text{ sec}^{-1}$, if rotational thermalization occurs in one collision. Cheo also showed experimentally that the rotational relaxation is J independent and only one collision is necessary to thermalize all rotational levels. All these tightly coupled rotational levels compete strongly for lasing. As a result oscillation often switches from one line to the next, especially in a high power laser system.

1-5 Conventional Electric Discharge CO₂ Lasers

Because of the various parameters discussed in previous sections, a mixture of CO₂, N₂ and He is generally considered as standard in present day carbon dioxide lasers. The optimum laser gas mixture for the system under consideration has been found to be CO₂ : N₂ : He = 1.7 : 7.3 : 36. Like other high power laser systems such as NASA's 70 kW C.W. laser⁽¹³⁾ and Hill's 20 kW laser⁽⁸⁾, the system does not need a large CO₂ concentration for high power generation. However, even with such a relatively small CO₂ concentration preionization is required to achieve any significant discharge power loading.

Most modern multikilowatt, electric discharge C.W. lasers can be classified into one of two categories, depending on the preionization technique utilized in their discharge volumes. These categories are i) self-sustained and ii) auxiliary sustained.

Self-sustained machines rely on an avalanching dc field to simultaneously provide both volume ionization and vibrational pumping. Such discharges usually operate in a negative resistance "normal glow" regime and hence require external ballast for current stabilization. The system often employs a multi-element cathode geometry in which a matrix array of individually ballasted pins is utilized for current limiting and distribution. In addition, each row of pins, incorporates a "row ballasting resistor" to permit attainment of uniform discharge power loading across the array.

In the second group of high power C.W. systems the active volume plasma is produced independent of the main vibrational pumping energy source.

This type of structure has the advantage that ionization and pumping are performed separately and hence capable of more optimization and control. A typical example is the Electron Beam-sustained E.D.L., in which a C.W. electron gun provides ionization while input energy for vibrational excitation is supplied by an auxiliary, non-self-sustained dc discharge⁽¹⁸⁾. A somewhat similar situation exists in Pulser-sustained lasers⁽¹⁴⁾ except here ionization is derived from controlled Townsend cascade rather than by high energy electron beam impact. This latter difference could conceivably make pulser-sustained devices simpler, less expensive and more efficient to operate. However, apart from a few initial experiments, the literature has provided little information on the C.W. operational characteristics of this type of laser.

A number of auxilliary ionization techniques, other than those discussed above, have been effectively employed. These include, microwave⁽¹⁵⁾, ultra-violet⁽¹⁶⁾, plasma jets⁽¹⁷⁾, and organic gas additives⁽²⁴⁾.

1-6 Employed P.I.E. (Photo-initiated, Impulse-enhanced, Electrically-excited) Technique

The system under consideration here employs a double ionization method which combines ultra-violet (U.V.) preionization followed by impulse cascade enhancement. Uniform, stable and large volume laser plasmas of densities in the range of 10^9 - 10^{10} /cm³ have been produced using this technique.

The feasibility of this technique was reported initially by A.E. Hill⁽²²⁾. In this technique:

1. The laser gas mixture is partially ionized by a fast U.V. burst. A low electron density ($\sim 10^6$ /cm³) is obtained.
2. Immediately following this, a fast rising pulse (~ 30 - 50 ns impulse) with an electric field well above the Townsend breakdown voltage (35 kV/cm-atmos.) is applied between the main electrodes to multiply the electron density to the desired value of 10^9 - 10^{10} /cm³.
3. A continuous electric field of insufficient E/P (3-6 kV/cm-atmos.) to cause further ionization is also maintained across the active volume. This provides electron energy needed to vibrationally excite the laser gas mixture.
4. The U.V. burst and impulse ionization is repeated to maintain the electron density fluctuation within 10-20%.
5. The gas in the discharge volume is rapidly exchanged so as to suppress discharge instabilities due to local heating and contaminants. A typical discharge instability time constant is about 1 millisecond⁽⁷⁵⁾.

1-6-1 Ultra-violet Photo Ionization

In the past, high energy electron beams have been very effectively utilized for auxilliary ionization of CO_2 laser mixtures. This method however, has several disadvantages as follows:

1. A ultra high vacuum system is required.
2. Delicate thin foil electron windows are required to isolate the high pressure laser volume from the high vacuum electron gun.
3. The foil heating imposes additional problems for C.W. operation.
4. It also requires a very high voltage source to accelerate the electrons.

An ultra-violet source, however, can be easily constructed in large arrays giving rise to uniform illumination over extended volumes. The direct-utilization of U.V. photoionization in CO_2 lasers was first reported by Seguin and Tulip⁽¹⁶⁾. Initially two tungsten pins with 2 mm separation were used to generate ultra-violet light. Twenty (20) parallel sparks located behind the mesh screen anode increased the output energy in excess of twice that obtained from other TEA lasers. In order to enhance the photoionization efficiency Levine and Javan⁽²⁴⁾ heavily doped the laser mixture with tri-n-propyl amine. A peak electron density of $10^{13}/\text{cm}^3$ was obtained. The laser output was slightly increased at the expense of efficiency. Judd⁽²⁵⁾ found experimentally that the effective photon mean free path for photoionization, is about 10 cm in the laser gas mixture. The U.V. penetrating depth L_p (calculated in mm) is

expressed by:

$$L_p = \frac{1}{\sigma_i N_0} \quad (1-9)$$

Where σ_i is the photoionization cross-section of i constituent of the laser gas mixture and is in the order of 10^{-18} cm^2 . N_0 is the laser gas mixture number density. Assuming that the operating pressure is ~ 50 torr, then L_p is only ~ 0.6 mm.

Therefore, the long U.V. penetrating depth is attributed to a two-step photoionization process. For one-step photoionization of even the most easily ionized constituent CO_2 at 14.4 eV, ultra-violet light of wavelength less than 900 \AA is required (25, 27, 28). One-step ionization of He and N_2 is almost impossible because CO_2 absorbs the photons of wavelength less than $\sim 1700 \text{ \AA}$ except for a narrow window at $\lambda \sim 1200 \text{ \AA}$, and the ionization wavelengths of both $\text{N}_2 (< 1050 \text{ \AA})$ and He ($< 600 \text{ \AA}$) are considerably below this. Therefore, it is concluded that if one of the laser gases is responsible for the ionization then a two or multi-step process must be the mechanism.

Efficient photoionization at longer wavelengths can be achieved by using additives as proven by McKen's work⁽²⁸⁾. In this the laser mixtures are doped with low ionization potential additives such as tri-n-propyl-amine. It has three absorption bands at $1150\text{--}1230 \text{ \AA}$, $1600\text{--}1715 \text{ \AA}$ and $1715\text{--}2200 \text{ \AA}$. Lind achieved long-pulse ($> 20 \text{ }\mu\text{s}$), high energy-density ($> 50 \text{ J/l atm.}$) laser output which is comparable to the best e-beam systems, by using a U.V. sustained CO_2 laser system (44, 45, 47). He determined that single-step photoionization of the tri-n-propyl-amine by radiation with wavelengths between 1200 and

1700\AA was primarily responsible for the production of plasma density $> 10^{12}/\text{cm}^3$.

However, it is also quite feasible that an impurity in the laser gas mixture with a low ionization threshold is the agent responsible for volume photoionization and that it follows the one-step mechanism. The industrial grade gases are known to have a relatively high concentration of impurities, particularly hydrocarbons⁽²⁸⁾.

1-6-2 Impulse Enhancement

The efficiency of electron production by ultra-violet is limited by the fact that the source generates a wide frequency spectrum most of which is unproductively absorbed by the laser gases. This disadvantage can be largely eliminated by employing impulse enhancement techniques. In this, the electrons generated by photoionization are accelerated toward the anode by a fast rising impulse electric field. These energetic electrons multiply the plasma density by promoting inelastic collisions between the electrons and neutral particles.

In order to obtain a proper mathematical expression for $\langle N_e \rangle$, the average electron density per cm^3 , several electron generation and re-combination equations similar to those used by Hill⁽²²⁾ have been developed. The equations for average electron density $\langle N_e \rangle$, and $N_0/\langle N_e \rangle$, the ratio of initial electron density to average electron density, are erroneous in Reference 22.

Let us assume that S electron-ion pairs/ $\text{cm}^3\text{-sec}$ is generated by a U.V. photon burst. The two body recombination rate equation is expressed by

$$\frac{\partial N_e}{\partial t} = S - \alpha_r N_e^2 \quad (1-10)$$

where N_e is the electron density per cm^3 and α_r is the recombination coefficient. Rearranging terms and taking derivatives:

$$\frac{dN_e}{S - \alpha_r N_e^2} = dt \quad (1-11)$$

Integrating:

$$\int \frac{dN_e}{S - \alpha_r N_e^2} = t + C$$

where C is a constant to be evaluated.

The left hand side is integrated as follows:

$$\begin{aligned} \int \frac{dN_e}{S - \alpha_r N_e^2} &= \frac{1}{\alpha_r} \int \frac{dN_e}{S/\alpha_r - N_e^2} \\ &= \frac{1}{2\sqrt{\alpha_r S}} \ln \frac{\sqrt{S} + \sqrt{\alpha_r} N_e}{\sqrt{S} - \sqrt{\alpha_r} N_e} = t + C \end{aligned} \quad (1-12)$$

when $t = 0$, N_e is 0 and $\ln \frac{\sqrt{S}}{\sqrt{S}} = 0$, therefore $C = 0$.

From Equation (1-12):

$$\ln \frac{\sqrt{S} + \sqrt{\alpha_r} N_e}{\sqrt{S} - \sqrt{\alpha_r} N_e} = 2\sqrt{\alpha_r S} t$$

Taking exponentials and rearranging:

$$N_e \sqrt{\alpha_r} (\text{Exp}(2\sqrt{\alpha_r S} t) + 1) = \sqrt{S} (\text{Exp}(2\sqrt{\alpha_r S} t) - 1)$$

Therefore,

$$N_e = \frac{\sqrt{S}}{\sqrt{\alpha_r}} \frac{\text{Exp}(2\sqrt{\alpha_r S} t) - 1}{\text{Exp}(2\sqrt{\alpha_r S} t) + 1} \quad (1-13)$$

The high voltage pulse following immediately after the U.V. burst will multiply the initial electron density, N_0 , to produce the final

electron density through the following rate process:

$$\frac{\partial N_e}{\partial t} = \alpha_\tau v_d P N_e - \alpha_r N_e^2 \quad (1-14)$$

Where P is the operating pressure, α_τ is the reduced Townsend coefficient, and v_d is the electron drift velocity ($v_d \sim 10^7$ cm/sec and $\alpha_\tau = 0.9$ ion pairs/sec in helium while E/P 215V/cm-torr). Solving Equation (1-14) for N_e :

$$\int \frac{dN_e}{\alpha_\tau v_d P N_e - \alpha_r N_e^2} = \frac{1}{\alpha_\tau v_d P} \ln \frac{N_e}{\alpha_\tau v_d P - \alpha_r N_e} = t + C \quad (1-15)$$

evaluating C by applying the initial conditions, $N_e = N_0$ when $t = 0$

Therefore:

$$C = \frac{1}{\alpha_\tau v_d P} \ln \frac{N_0}{\alpha_\tau v_d P - \alpha_r N_0} \quad (1-16)$$

substituting (1-16) into (1-15) we obtain a general solution:

$$\frac{1}{\alpha_\tau v_d P} \ln \frac{N_e}{\alpha_\tau v_d P - \alpha_r N_e} = t + \frac{1}{\alpha_\tau v_d P} \ln \frac{N_0}{\alpha_\tau v_d P - \alpha_r N_0}$$

And

$$\ln \frac{N_e}{\alpha_\tau v_d P - \alpha_r N_e} = \alpha_\tau v_d P t + \ln \frac{N_0}{\alpha_\tau v_d P - \alpha_r N_0}$$

collecting the log terms:

$$\ln\left(\frac{N_e}{\alpha_{\tau} v_d P - \alpha_r N_e} \times \frac{\alpha_{\tau} v_d P - \alpha_r N_o}{N_o}\right) = \alpha_{\tau} v_d P t \quad (1-17)$$

Taking exponentials

$$\frac{N_e}{N_o} \frac{\alpha_{\tau} v_d P - \alpha_r N_o}{\alpha_{\tau} v_d P - \alpha_r N_e} = \exp(\alpha_{\tau} v_d P t)$$

Collecting N_e for solution

$$\begin{aligned} N_e &= \frac{N_o \exp(\alpha_{\tau} v_d P t)}{\alpha_{\tau} v_d P - \alpha_r N_o} (\alpha_{\tau} v_d P - \alpha_r N_e) \\ &= \frac{N_o \alpha_{\tau} v_d P \exp(\alpha_{\tau} v_d P t) - N_o \alpha_r N_e \exp(\alpha_{\tau} v_d P t)}{\alpha_{\tau} v_d P - \alpha_r N_o} \\ N_e \left(1 + \frac{N_o \alpha_r \exp(\alpha_{\tau} v_d P t)}{\alpha_{\tau} v_d P - \alpha_r N_o}\right) &= \frac{N_o \alpha_{\tau} v_d P \exp(\alpha_{\tau} v_d P t)}{\alpha_{\tau} v_d P - \alpha_r N_o} \quad (1-18) \end{aligned}$$

Therefore:

$$\begin{aligned} N_e &= \frac{N_o \alpha_{\tau} v_d P \exp(\alpha_{\tau} v_d P t)}{\alpha_{\tau} v_d P - \alpha_r N_o + N_o \alpha_r \exp(\alpha_{\tau} v_d P t)} \\ &= \frac{N_o \alpha_{\tau} v_d P}{\alpha_r N_o - (\alpha_r N_o - \alpha_{\tau} v_d P) \exp(-\alpha_{\tau} v_d P t)} \quad (1-19) \end{aligned}$$

During the avalanche, the electron density $N_e(P_1)$ at $t-t(P_1)$ is:

$$N_e(P_1) = \frac{N_o \alpha_r v_d P}{\alpha_r N_o - (\alpha_r N_o - \alpha_r v_d P) \text{Exp}(-\alpha_r v_d P(t-t(P_1)))} \quad (1-20)$$

The electron density falls from the maximum density by recombination as described by the following equation until the next U.V. burst comes.

The electron density after a delay time $\tau(d_1)$ is expressed by:

$$N_e(d_1) = \frac{1}{(1/N_e(P_1) - \alpha_r(t-t_{d_1}))} \quad (1-21)$$

During the second avalanching pulse, the time dependent electron density can be expressed by Equation (1-20) with the initial electron density and time parameter properly changed for the second pulse.

$$N_e(P_2) = \frac{N_e(d_1) \alpha_r v_d P}{\alpha_r N_e(d_1) - (\alpha_r N_e(d_1) - \alpha_r v_d P) \text{Exp}(-\alpha_r v_d P(t-t(P_2)))} \quad (1-22)$$

The electron densities for succeeding recombination and avalanching periods can be adequately expressed by Equations 1-21 and 1-20 with proper initial conditions.

As mentioned earlier, Hill's equations for average electron density $\langle N_e \rangle$, and the ratio of initial electron density to average electron $N_o/\langle N_e \rangle$, are erroneous.

The average electron density over the time interval t_d is obtained by integrating Equation (1-21) and dividing by t_d .

$$\langle N_e \rangle = \frac{1}{t_d} \int_0^{t_d} \frac{1}{1/N_o + \alpha_r t} dt \quad (1-23)$$

where N_0 is the initial (equivalent to the maximum) electron density.

$$\begin{aligned}
 \langle N_e \rangle &= \frac{1}{t_d} \int_0^{t_d} \frac{N_0}{1 + \alpha_r N_0 t} dt \\
 &= \frac{N_0}{t_d} \left\{ \frac{1}{\alpha_r N_0} [\ln(1 + \alpha_r N_0 t)]_0^{t_d} \right\} \\
 \langle N_e \rangle &= \frac{1}{\alpha_r t_d} \ln(1 + \alpha_r N_0 t_d) \quad (1-24)
 \end{aligned}$$

or

$$\alpha_r t_d \langle N_e \rangle = \ln(1 + \alpha_r N_0 t_d)$$

taking exponentials:

$$\text{Exp}(\langle N_e \rangle \alpha_r t_d) = 1 + \alpha_r N_0 t_d$$

solving for N_0 :

$$N_0 = \frac{\text{Exp}(\langle N_e \rangle \alpha_r t_d) - 1}{\alpha_r t_d} \quad (1-25)$$

The ratio $N_0 / \langle N_e \rangle$ which shows the electron density fluctuation about the average electron density is:

$$\frac{N_0}{\langle N_e \rangle} = \frac{\text{Exp}(\langle N_e \rangle \alpha_r t_d) - 1}{\alpha_r t_d \langle N_e \rangle} \quad (1-26)$$

This equation is very important for the P.I.E. laser operation. One can specify the required electron density $\langle N_e \rangle$ and the density fluctuation, then the required repetition rate can be obtained by a graphical or a trial-and-error method.

CHAPTER 2

EXPERIMENTAL SYSTEM - DESIGN AND OPERATION

The schematic diagram the P.I.E. laser developed for this research is shown in Figure 2-1. This experimental system is a modified version of the system reported in References 34 and 35. The blower (centrifugal compressor), step-up driving mechanism and 5-h.p. dc motor are being used without modification. The remaining components have been scaled up for high power operation. A general description of the system operation is given in the following section. Figure 2-2 shows the nomenclature of the system.

P.I.E. C.W. GAS TRANSPORT CO₂ LASER

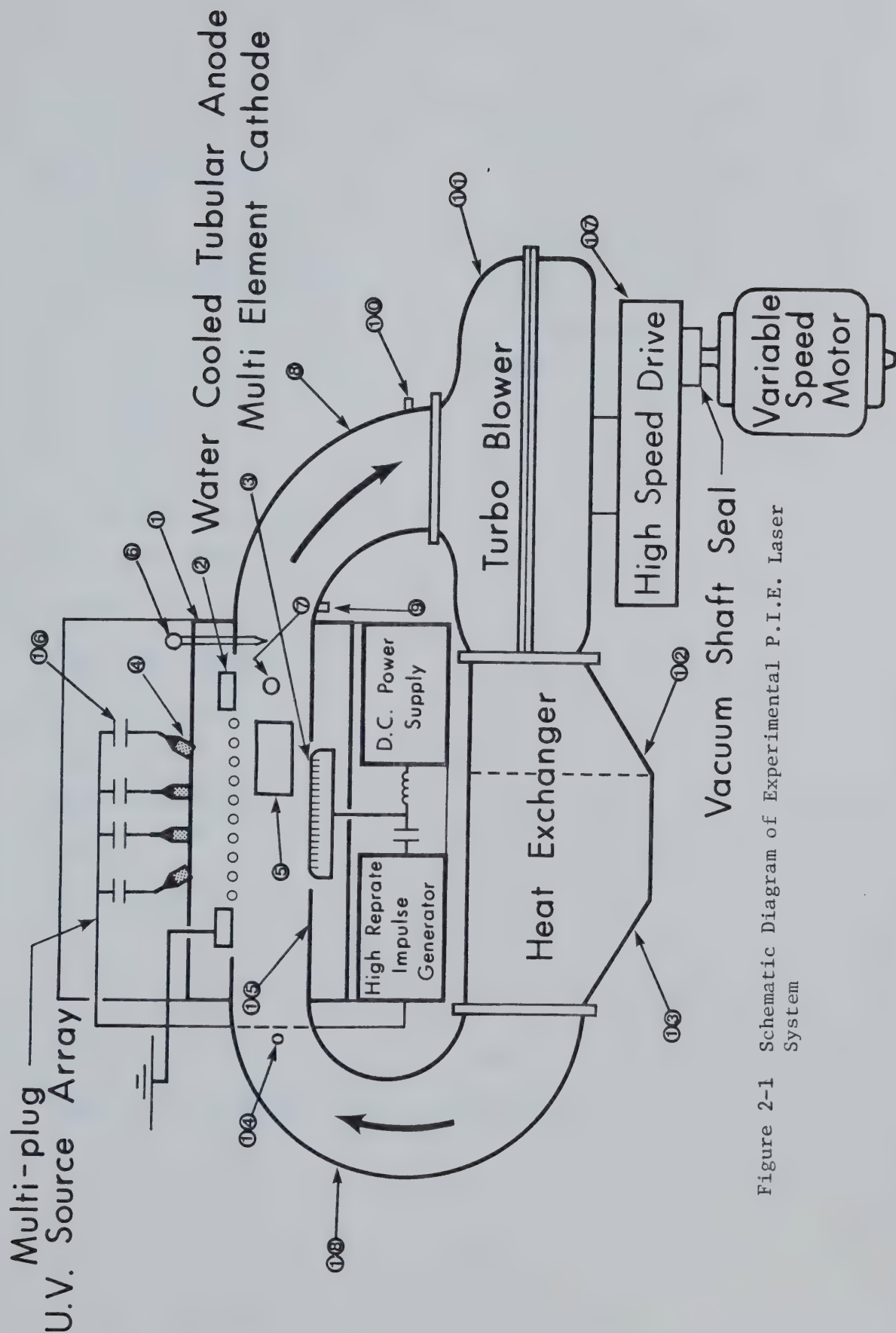


Figure 2-1 Schematic Diagram of Experimental P.I.E. Laser System

- | | |
|---|---------------------------------------|
| 1. Laser Box | 14. Pitot Tube |
| 2. Water Cooled Anode
(0.6 cm dia. copper tube) | 15. Flow Guide Assembly |
| 3. Aqueous Solution Ballasted
Cathode (0.3 cm dia. pins) | 16. Capacitors (U.V.) |
| 4. Spark Plugs (12 each row) | 17. High Speed Drive
(Step-up Box) |
| 5. NaCl Window | 18. Inlet Duct Assembly |
| 6. Thermometer | |
| 7. Viewing Port | |
| 8. Blower Inlet Duct
Assembly | |
| 9. Vacuum Pump Connector | |
| 10. Gas Supply Connector | |
| 11. Blower | |
| 12. Blower Outlet Duct
Assembly | |
| 13. Heat Exchanger | |

Figure 2-2 Nomenclature of the Laser System

The laser system is evacuated to a 50 μm pressure by a 10 cfm Welch pump and is filled with the laser gas mixture to a proper pressure. The high speed blower circulates the laser gas mixture clockwise in the gas transport system. A set of spark plugs initiates U.V. photoionization and the following impulse multiplies the electron density of the discharge volume between the anode and the cathode. In the process of collecting the electrons and ions, the D.C. input energy vibrationally excites the upper laser level ($00^{\circ}1$). Some of this electric energy contributes to heating of the gas mixture. This heat energy is removed by a heat exchanger in the gas transport system.

A 5-pass optical resonator comprising four gold-coated mirrors amplifies the coherent light by stimulated emission of radiation. A part of this light energy is extracted by the partially transmitting output mirror through an NaCl window.

The detailed system's description is provided in the following four sections. The system is divided into four sub-systems for convenience. They are:

1. Gas transport sub-system
2. Electrical sub-system
3. Optical sub-system
4. Water ballasting sub-system

2-1 Gas Transport System

The gas transport system is made of aluminum. It is comprised of a laser box, three duct assemblies, a heat exchanger, a turbo blower, a step-up driving unit and a dc. motor.

2-1-1 Laser Box

The rectangular prism shape laser box is designed to accommodate both cathode and anode electrodes, U.V. spark plugs, a 5-pass optical resonator, two viewing ports, a thermocouple and a flow guide assembly. Four vertical plates are welded together while top and bottom plates are held in place by wing nuts. Two long vertical plates have a rectangular aperture in the center to form part of the flow duct. The short side plates have a rectangular aperture for the optical system.

The cathode is horizontally mounted to the bottom plate in such a manner that it can be moved vertically, and horizontally in the flow direction. This freedom of movement allows optimization of the discharge volume and optical gain medium volume. The top plate carries an anode, 46 spark plugs and capacitors for U.V. production. A shielding box is strategically placed so as to enclose the spark plugs and capacitors and thereby shield the electric noise. The top plate, with its associate components can be lifted up with a hoist and this facilitates the change of electrode configuration. Two viewing ports, one in the back and the other in the front, allow for complete observation of all components inside the box. A thermocouple or the thermometer monitors the final discharge translational gas temperature through a hole provided in the top plate. It is sufficiently remote from the discharge in the downstream

of the gas flow.

Mirror alignment is accomplished in the conventional manner with the use of a low power C.W. He-Ne laser.

2-1-2 Blower

The centrifugal type blower is driven by a 5-hp D.C. motor through a 1 : 10 step-up belt arrangement. The blower speed can be varied from zero to 18000 rpm. At a 50 torr system pressure this becomes translated into a gas flow velocity of zero to 50 m/s respectively. The pulleys are mounted inside a rectangular step-up box which is located under the blower casing. The box is effectively pressure-isolated from the main gas transport system by a series of labyrinth seals around the blower shaft. The high speed drive box is differentially pumped so that the oil vapors in the box are prevented from contaminating the main system. While operating a portion of the laser gas mixture can be replaced by pumping on the pulley box while leaking a fresh gas mixture into the main system.

2-1-3 Heat Exchanger and Duct Assemblies

A conventional automobile radiator has been mounted after the blower in the gas stream. Although it is customary to locate the heat exchanger before the blower to provide better blower efficiency, geometrical difficulties did not allow this. Because the size of the heat exchanger was not optimized the size of the associated duct assemblies became unnecessarily larger. Under normal operating conditions 5-gpm of tap water flowing through the heat exchanger provides adequate cooling.

The blower inlet duct assembly connecting the laser box and the blower is designed to have a straight transition section, adjacent to the blower in order to minimize gas turbulence at the blower inlet. Vacuum connector and gas supply connectors are provided on this duct.

2-1-4 Anode Electrode

Since the U.V. sources are located behind the anode, it was important that it should transmit U.V. as readily as possible. The first material that was considered and subsequently tested was screen. Initially the anode was constructed with #16-mesh stainless steel screen which was rigidly attached to a rectangular water-cooled frame. This anode worked well with a glow discharge until a small arc punctured the screen.

Next a perforated 0.32-cm thick copper plate, with 0.64-cm diameter holes spaced 1.3-cm apart was used. A small arc here did virtually no damage to the surface. Although this anode structure performed well at lower powers, it proved to be unsuccessful under high power operation. The problem here was that at high current densities nonuniform heating of this perforated anode plate caused serious deformation. The resulting twisted electrode surface so formed promoted the onset of discharge instabilities. A satisfactory anode design was finally achieved by using a water cooled tubular structure.

Figure 2-3 is a schematic diagram of the copper tube anode. Fifteen bars are equally spaced to form a 18-cm wide grate. The distance between the tubes and the o.d. of the tubes are both 0.6-cm. Thus 50% U.V. transmittivity is obtained. Each bar is bent 180° at both ends and connected to the 2.0-cm diameter water headers. One of the headers is connected to the 1.0-cm diameter water inlet and outlet tubes. This header is divided in the middle so that each tube will carry the same amount of cooling water.

Anode Electrode Configuration

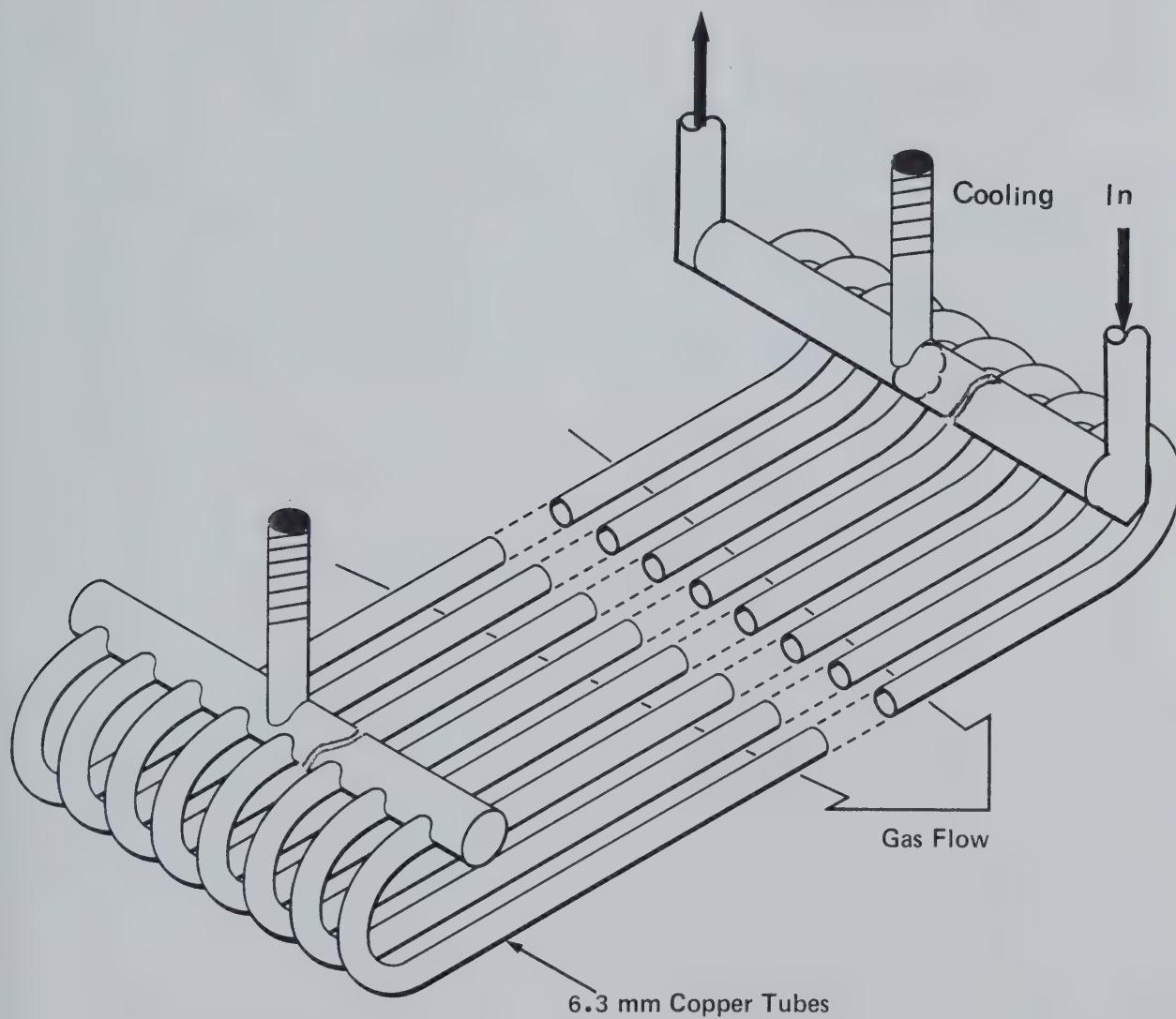


Figure 2-3 Schematic Diagram of the Copper Tube Anode

The advantages of this anode are:

1. Best cooling efficiency tested
2. No severe arc damage
3. Good U.V. transmission

The tubular anode structure outlined above and shown in Figure 2-3 has provided trouble-free performance since initial installation. The present running time of over 400 hours thus far accumulated without failure or deterioration strongly suggests that the design is adequate for high power laser application.

2-1-5 Cathode Electrode

The cathode electrode is by far the most important and difficult single part of the laser system. Experience has shown that cathode geometry as well as material can play a very important role in discharge stability. Uniform field electrode shapes, such as the Rogowski⁽⁴²⁾ and Bruce profiles have been effectively utilized in TEA lasers for several years. These electrode geometries however are best suited for pulsed laser application in which the interelectrode space is initially field and charge free. This is not the case in high power C.W. lasers where the interelectrode volume is dominated by a medium density plasma and gas-flow blows the discharge column downstream. In such instances the uniform field aspects of these profiled electrodes become less significant in comparison to other more important parameters such as, flow uniformity, stagnant boundary layers and gas residence time (the time defined as electrode width divided by flow velocity). Consequently, in most high power C.W. CO₂ lasers the actual cathode shape is relatively unimportant other than some care is taken to eliminate sharp edges, especially on the downstream side. Sharp corners or other prominent surface irregularities on the trailing edge can promote discharge instabilities through field concentration.

During the course of this work several cathode electrodes were tested. The design of these devices, which stressed many different geometries and materials, is outlined chronologically in the following sections.

2-1-6 Graphite Cathode

Figure 2-4 is a schematic diagram of the first cathode electrode constructed. This device was fabricated from a single slab of graphite, machined to an approximate Rogowski profile⁽⁴²⁾. Graphite was initially chosen as the electrode material since it was known to be sputter and arc resistant and as such had proved useful in pulsed TEA laser design.

However, prolonged use of the graphite electrode resulted in the deposition of a thin layer of carbon dust on all surfaces within the gas transport system. This phenomenon was eventually traced to the operation of the high repetition rate ionization system. During pulser operation, the electrode surface was observed to be uniformly covered with countless sparkling particles. These are believed to be a manifestation of the graphite surface porosity in that individual pores acted as minute hollow cathodes. Energetic electrons gradually eroded the sides and edges of these small emitting orifices. Electrode cooling was accomplished by imbedding a metallic water channel into the under side of the graphite structure.

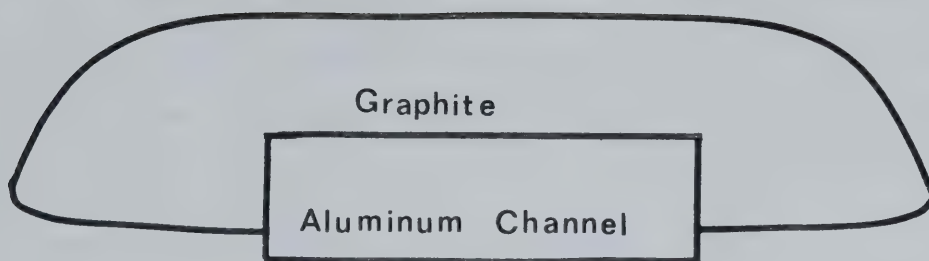


Figure 2-4 Rogowski Profiled Graphite Cathode Electrode

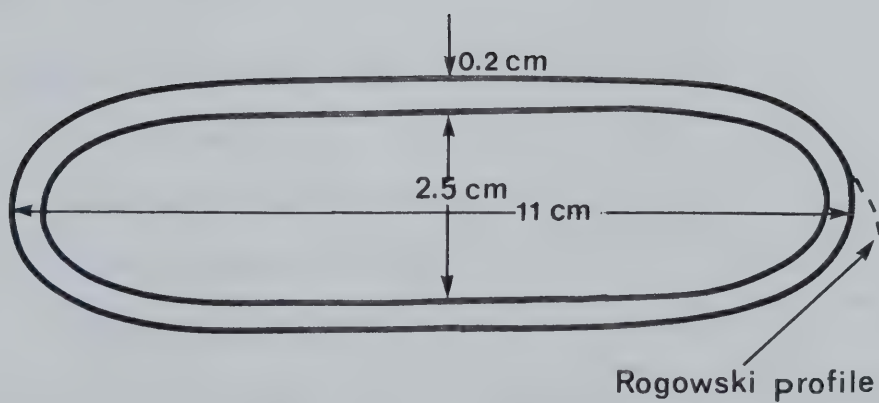


Figure 2-5 Schematic Diagram of Copper Pipe Cathode Electrode

2-1-7 Copper Cathode

The second cathode structure tested is shown in Figure 2-5. Here also an approximate Rogowski shape was utilized. This device was fabricated from a piece of 8 cm o.d. copper pipe annealed at 400°C for over four hours and deformed in a controlled manner. A 2.5 cm thick steel bar was inserted to limit the pressing action.

After both ends were fitted with profiled end plugs, the entire structure was then copper electro-plated to provide a uniform joint-free surface. Cooling water was circulated through the interior and thus gave the electrode a good power handling capability.

Despite the fact that copper has a relatively high sputtering rate the cathode outlined above was found to perform in a satisfactory manner, especially at low pressure. This is in contrast to other previously reported experiences⁽²¹⁾. The copper structure also possessed a remarkable immunity to arc damage.

Summarizing the advantages,

1. Easy to make
2. Good water cooling effect
3. Close to Rogowski profile
4. Durable against arcs

Although 25 kW dc power input was achieved in 100 torr of He with this cathode, high power loading in the laser gas mixture could only be attained at low pressure.

2-1-8 General Comments on the Continuous Surface Cathodes

With the cathode structures discussed earlier it was observed that significant discharge power loading at higher pressures, could only be attained on a short burst basis. More specifically, plasma instabilities became apparent after a few seconds of high powered operation when using the continuous surface cathodes originally developed. These instabilities were manifest in terms of a gradual coalescing, of an initially uniform laser plasma, towards the electrode centers; eventually terminating in a constricted arc. The precise cause of this phenomenon has to date not been determined but may well be the manifestation of non-uniform gas heating in a semi-stagnant boundary layer encompassing the cathode fall region at the electrode surface. Such non-uniformity could give rise to a self generative electro-thermal instability as discussed by Nighan et al.⁽⁷⁵⁾.

Previous work on C.W. discharges has indicated that such gradual collapse of an extended high current dc discharge may be prevented if some means of current density limitation and distribution is incorporated into, or as part of, the cathode electrode surface^(13,34,48). Previous and further experiments with multiple hollow cathode arrays and other current distribution networks have provided some design criteria for the incorporation of such an electrode structure into this P.I.E. laser system.

2-1-9 Multipin, Electrolytic Solution* Ballasted Cathode

The operational concept in this type of electrode system is to provide a uniform current distribution and limitation over the entire electrode area by means of sub-dividing the overall surface into an extended array of independent sub-electrodes, each with its own current ballasting element. Conventional structures of this kind usually employed discrete resistors as the ballasting elements, and consequently experienced difficulties such as flash over, heating etc. The multi-element cathode structure developed for the system under consideration differs considerably from the conventional devices in that it utilizes an internal aqueous electrolytic solution to provide uniform current distribution without the need for external ballast.

The basic electrode geometry is displayed in Figure 2-6. Here it can be seen that the device uses an extended array of sub-electrodes mounted such that their lower ends are submerged in a narrow channel containing a recirculating conducting fluid. The electrolytic solution thus simultaneously provides cooling and current distribution to each element of the cathode. Optimum performance is easily accomplished through adjustment of the electrolyte concentration. In this manner no other external ballasting is required and consequently power loss in the structure can be minimized.

* In this thesis the term "Electrolytic Solution" generally represents tap water and electrolytic aqueous solution.

Pictorial Diagram of Multi-element Cathode

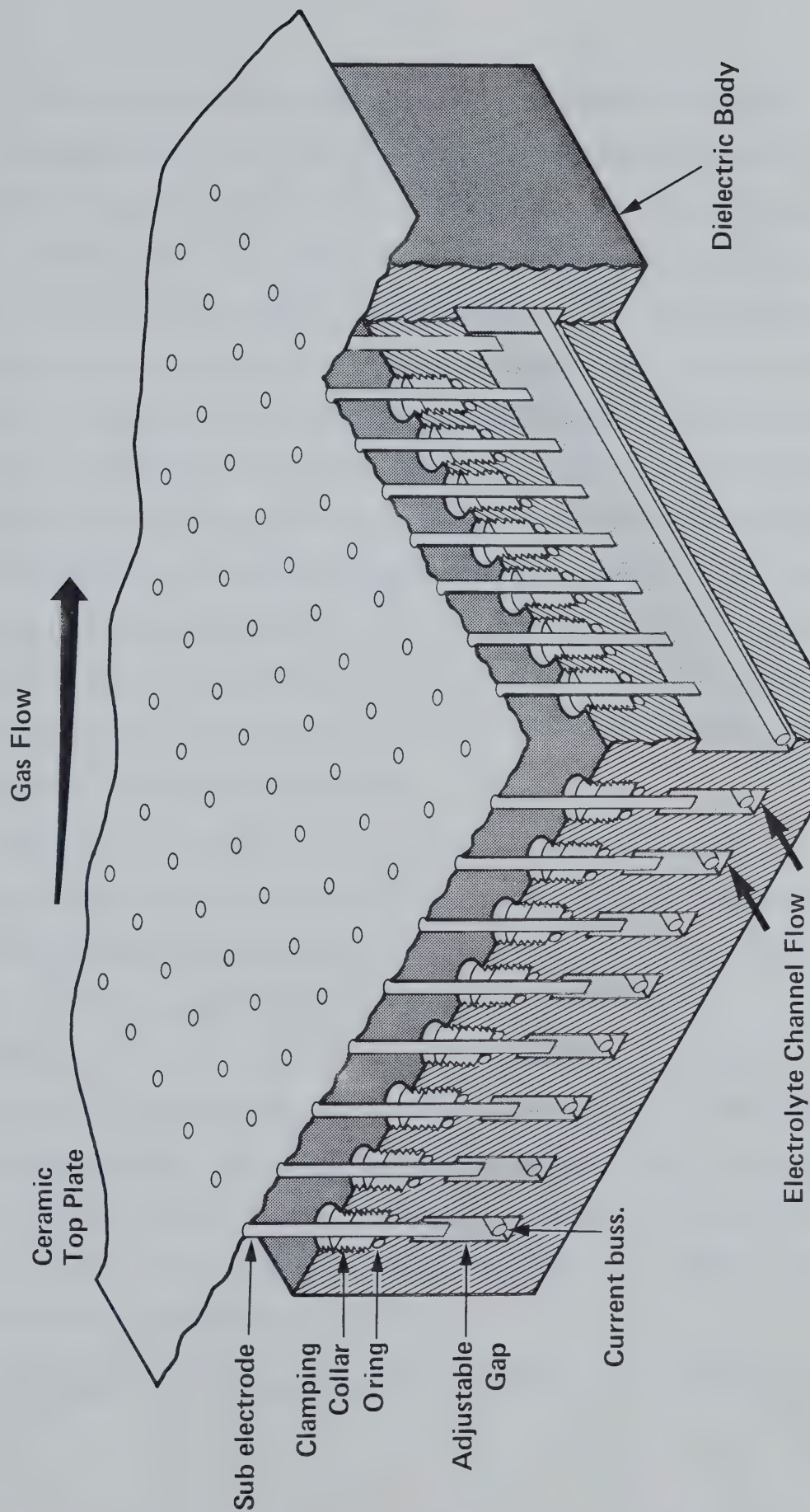


Figure 2-6 Schematic Diagram of Multipin Cathode

2-1-10 Comparison with Conventional Multi-element Electrodes

The operational and constructual aspects of this electrolytic solution ballasted multipin electrode (here the subelectrode is a pin) can be compared with the conventional resistive ballasted multipin electrodes utilized by NASA⁽¹³⁾ and Westinghouse⁽⁴⁸⁾. Both conventional multipin electrodes were constructed on the same basis. Each pin was connected through a separate ballast resistor, 20 k Ω for NASA's electrode and 50 k Ω for Westinghouse's electrode. As the laser gas mixture passes from row to row (row is defined as a row of pins arranged in the optical axis) the discharge impedance decreases due to gas heating. In order to maintain constant power density under such circumstances, a separate row ballasting resistor is connected to each row. This adds more complexity to the electrode construction and introduces higher power loss through the ballasting resistors.

However, the effective row ballasting in the electrolytic solution ballasted multipin electrode for this project is achieved by using differential gap spacing in the electrolytic solution. Typically, each pin in the upstream row is ~ 4 k Ω and linearly increases to approximately 20 k Ω for a pin in the downstream row. A simple calculation, for a typical cathode having 50 subelements per row, reveals that this differential gap row ballasting technique is about an order of magnitude more effective than the series row resistor approach. An additional advantage here is that a resistor cooling system is not required for this solution ballasted multipin structure.

One unique and very important characteristic of the electrolytic

solution ballasted multipin electrode is a tendency for self-optimization.

This aspect has been attributed to initial nonuniform pin corrosion by the electrolyte. Initially each pin experiences different discharge conditions due to nonuniformities in physical construction and assembly etc. Consequently, some pins initially carry more current than others. This increased current selectively accelerates pin corrosion; until such time that the individual gap spacings are adjusted so that each sub-element carries the same current. This inherent tendency for self-optimization has been well documented on a six row multielement cathode constructed with copper and brass pins. After approximately 100 hours of operation the total electrode current input at the instability limit was observed to have increased by a factor of three. The quantitative measurements of pincorrosion rates are presented in Section 3-2-7.

Another unique characteristic of the solution ballasted electrode is the ability of suppressing an arc. Usually the pin involved in an arc actively generates abundant gas bubbles, due to increased current. The bubbles momentarily surround the pin in the solution and decrease the current density sufficiently to extinguish the arc.

2-2 Electrical System

The electrical system is functionally subdivided into two parts. These are the pulser circuit and the sustainer circuit. The pulser circuit is again divided into two different units; (i) trigger unit and (ii) preionizer (thyatron) unit.

2-2-1 Trigger Unit

The purpose of the trigger unit is to repetitively deliver to the grid of the thyatron pulses of sufficient amplitude for switching. The trigger circuit is indicated schematically in Figure 2-7. As shown in the figure, a 6DQ6B vacuum tube is used as the final stage or driver. This tube is activated by pulses from a commercial pulse generator; the HP214.

A common problem encountered in designing thyatron trigger circuits is that the grid potential is brought up to the anode voltage for a brief period of time when the thyatron is turned on. This occurs because the grid to anode capacitance is much greater than the grid to cathode capacitance. The resulting high voltage spike propagates back into the trigger circuits. It is of short duration and carries little energy, but may damage or cause instabilities in the trigger unit components. For this reason a rugged vacuum tube is used as the thyatron driver. In addition the spike is attenuated by a π type LC low pass filter.

2-2-2 High Voltage and High Repetition Rate Switch (HVHRR Switch)

An efficient and reliable HVHRR Switch is needed for preionizer (pulser) circuit design. Usually a HVHRR Switch has an anode-cathode gap space filled with a fast deionizing gas and is triggered by triggering pulses. Then the gas is ionized and the anode-cathode gap space becomes short circuited. Reliable operation of such HVHRR Switches is usually limited by slow drifting positive ions which in many cases force the switch into continuous conduction.

One way of removing the positive ions is blowing high pressure air through the discharge gap. This principle works well in theory but not in practice. Difficulties such as severe time jittering due to the changes in air pressure or velocity, and excessive sputtering due to the charged particle bombardment render the scheme impractical. In addition, the mechanical noise generated by such a switch may be objectionable.

Another way of reducing the switch recovery time is to segment the spark gap by using a series of plates which act as heat sinks. This is called a "Quenching Gap". Because the spark gap is divided into so many short gaps, the charged particles travel a shorter distance, and accordingly the electrons leaving a cathode may not obtain sufficient energy to ionize the gas in its path to the respective anode. This means that in order to support the same switching current, the size of the discharge area must be larger than that of a single gap. This also means that the plasma density in a quenching gap is much lower than the plasma density in a single gap switch under the same operating conditions. The lower plasma density and effective cooling of sparks make the quenching gap recover much faster than the single gap. This feature has been

well demonstrated by Frungel⁽³⁰⁾, and V. Guty and E. Panarella of the National Research Council⁽³¹⁾ of Canada.

However, there are also several drawbacks with quenching gaps.

- Some of them are:
- (1) Construction is difficult, because each plate requires precision machining and each gap requires a vacuum tight seal for proper cooling and gas holding.
 - (2) It is hard to trigger due to the increased capacitance.
 - (3) Since each gap is short (~ 0.1 mm), it can be easily bridged.
 - (4) The overall series resistance of the triggered unit is not negligible.

The author's quenching gap was made of aluminum discs spaced 0.1 mm by a pair of spacer rings and a 1.6 mm thick 'O' ring. The quenching gap was cooled by transformer oil. Due to the triggering problem only 19 gaps were used to hold 7 kV. Unfortunately, after approximately twenty minutes of operation, the hold-off voltage dropped to approximately 4 kV. It was found that several bridged gaps were responsible for the lowering of the hold-off voltage. This may be a serious problem in practical use. The maximum frequency obtained was 34 kHz at 3 kV and 40 A.

The most effective way of removing positive ions from the gap is with a negative bias. This method is extensively employed for hydrogen thyratrons. The thyatron is one of the most efficient HVHRR switches

the author has ever tested. But even the thyatron is not perfect. Its performance is largely dependent upon the driving circuit and load characteristics. To facilitate recovery a negative pulse is superimposed on the negative bias after triggering⁽³²⁾. The preionizer circuit employing a hydrogen thyatron, HY1802, is described in the following section.

2-2-3 Preionizer Unit

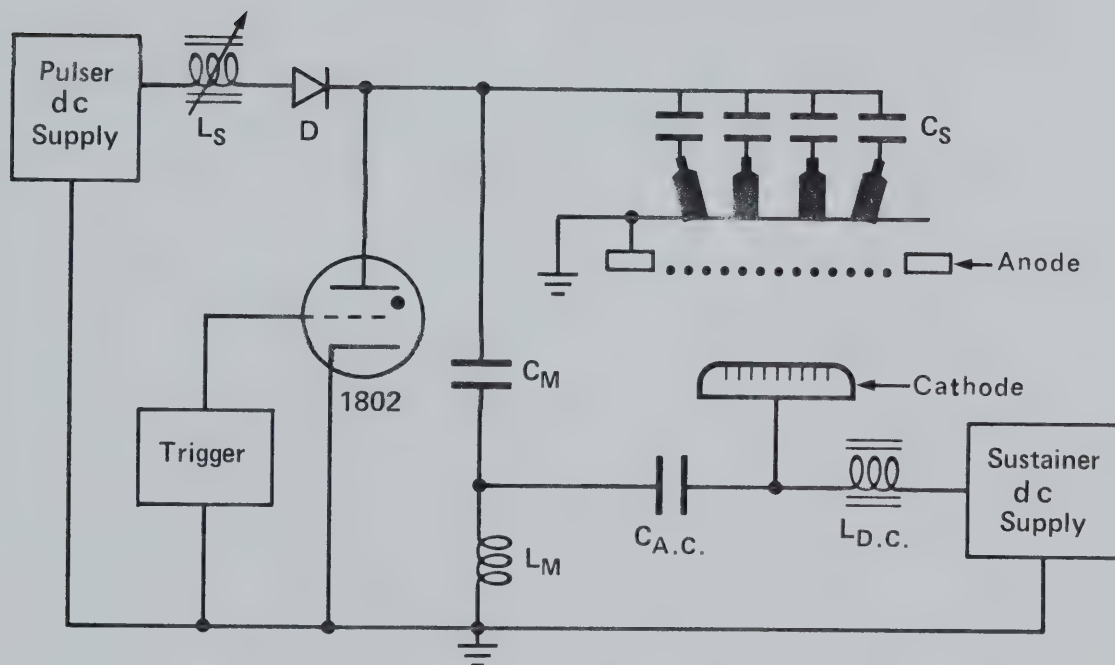
The preionizer unit provides and maintains an electron density of $10^{10}/\text{cm}^3$ for a uniform D.C. discharge. Ultra-violet light from a number of spark plugs creates ion-electron pairs by volume preionization. A high voltage impulse following this U.V. burst then causes an electron avalanche which greatly multiplies the number of ion-electron pairs. These processes have been discussed in more detail in Sections 1-6-1 and 1-6-2.

Figure 2-8 is an electrical schematic diagram of the HVHRR pre-ionizer developed for this project. As can be seen, an 1802 ceramic hydrogen thyatron is used as the main switching element. The main (variable) capacitor, C_M , is the pulse energy storage element, which is resonantly charged through the saturable inductor, L_S , and charging diode, D , via L_M . When the hydrogen thyatron fires the energy stored in capacitor C_M is coupled to the cathode via the coupling capacitor C_{AC} . In addition, the 1802 thyatron functions as the discharge switch for the U.V. capacitor C_S . The auxiliary charging inductor, L_M , exhibits very low impedance, ($< 120 \text{ ohm}$) for the charging cycle and very high impedance ($> 20 \text{ k-ohm}$) for the discharging cycle. The average charging current, \bar{I} , is expressed by⁽²⁹⁾:

$$\bar{I} = V C_t f_r \quad (2-1)$$

where V is the network charging voltage, C_t is the total capacitance for pulse and U.V. source, and f_r is the repetition rate. Twenty kV operation at 20 kHz with $\sim 1200 \text{ pF}$ yields an average current of 0.5

Circuit Diagram of Thyatron Pulser



- L_S = Saturable inductor ≈ 1000 mh unsaturated $\rightarrow \approx 20$ mH saturated
- D = Hold off diode ≈ 30 kV P.I.V.
- 1802 = Ceramic hydrogen thyatron
- C_M = Impulse storage capacitor $\approx 700 \rightarrow 1000$ pF
- C_S = u.v. source capacitors ≈ 20 pf (700 pF total)
- L_M = Bypass recharge inductor $\approx 350 \mu\text{H}$
- $C_{A.C.}$ = Impulse coupling capacitor $\approx .1\mu\text{F}$
- $L_{D.C.}$ = Isolation inductor ≈ 40 H

Figure 2-8 Schematic Diagram of Preionizer Unit

amperes. In this case the power loss through L_M is approximately 30 watts. The U.V. source capacitors are charged to the operating voltage through the plasma around the spark plug gaps.

2-2-4 Preionizer Component Design Consideration

In general, the charging element can be a resistor (resistance-charging), an inductor (inductance charging) or a H.V. switch (triggered charging). Inductance charging however is known to be very efficient in energy transfer (> 90%, compared with 50% for resistance charging), and it provides better isolation between the power supply and the HVHRR switch. For these reasons, inductance charging was adapted for this project.

In addition, inductance charging is especially suitable for high voltage operation because it is possible to make the network voltage, $V(t)$, double the power supply voltage, E . This can be shown as follows: Assume that the network resistance, $R=0$ for simplicity and that $V(0)$, the initial network voltage, is the same for each cycle. Let q be the charge transferred from the power supply to the network. Then:

$$q E = \frac{C_t}{2} \{ [V(t)]^2 - [V(0)]^2 \} \quad (2-2)$$

where C_t is the total network capacitance. The charge q is expressed by:

$$q = C_t [V(t) - V(0)] \quad (2-3)$$

substituting Equation (2-3) into Equation (2-2) and rearranging:

$$V(t) = 2E - V(0) \quad (2-4)$$

Equation (2-4) shows that if $V(0)=0$, $V(t)$ is double the supply voltage E .

Depending whether $V(0)$ is positive or negative, $V(t)$ becomes less than $2E$ or more than $2E$ respectively. $V(0)$ becomes zero when the preionizer is operated at a frequency, f_r , double that of the natural frequency, f_0 ⁽²⁹⁾. The charging system under this condition is called "resonant charging".

The resonant charging state could be extended over a wide frequency range from $0 \sim 2 f_0$ by using a charging diode, D , between the charging inductor L_S and capacitors (C_M and C_S). The use of the charging diode prevents the fully charged capacitors from discharging back into the power supply. Thus the voltage across the capacitor remains at twice the supply voltage until the thyatron fires. This allows the pulser unit to operate at any frequency with an upper limit of twice the natural resonance frequency.

The charging diode must be able to withstand the supply voltage, and handle sufficient current for proper charging. At the present time, no single diode is available that satisfies these requirements. Instead this charging diode is formed by eighty 60A diodes connected in series. A resistor, connected in parallel with each diode, ensures that the voltage is divided evenly amongst the different stages. In addition the diodes are protected from possible damage by transients resulting from the sudden switching of the thyatron. This is achieved by connecting a $0.1 \mu F$ capacitor in parallel with each diode.

A saturable inductor⁽³²⁾ is used to ensure that the charging is initially sufficiently slow to allow the thyatron to recover. The charging inductor L_S is composed of twelve toroid coils connected in series to provide 1.2-henry of unsaturated inductance and ~ 34 milli-

henry of saturated inductance. Each coil consists of 150 turns of Belden 24Ga hook-up wire wound on to a Philip's 3C8 ferrite core. The saturation curve of this core is shown in Figure 2-9. The energy loss in the saturable inductor is so small that natural air circulation provides adequate cooling.

The main pulse capacitor, C_M , is composed of eleven cylindrical capacitor units which can be individually adjusted to obtain a total capacitance of $20 \sim 1100$ pF. Each capacitor unit was made of a glass tube, closed at one end. The capacitor units are enclosed in a double box as shown in Figure 2-10. As illustrated in (b), the outer capacitor element is formed by a coating of "silver preparation", a conductive paint with good mechanical and electrical properties. The metal tube inner element freely slide in and out of the glass tube by means of a controlling rod which connects to the pulser power supply.

Figure 2-11 shows the cross sectional view of a U.V. source capacitor bank driving a row of twelve spark plugs. An inner element common to the outer segments is a copper semi-tube (240° arc and 60 cm long). This fits tightly into a thick wall glass tube. The glass tube is nested in twelve 240° semi-tubular outer segments 3.8 cm in length. Each segment is connected to the respective spark plug. If the glass tube is rotated, the inner semi-tube overlaps the outer segments. The minimum and maximum angular overlaps are 120° and 240° corresponding to 20 pF and 30 pF capacitances respectively. To prevent a corona discharge, all capacitor elements are immersed in transformer oil.

Champion spark plugs, J77, are being used for hard U.V. sources. A typical discharge volume of the system under consideration is ~ 4 liter

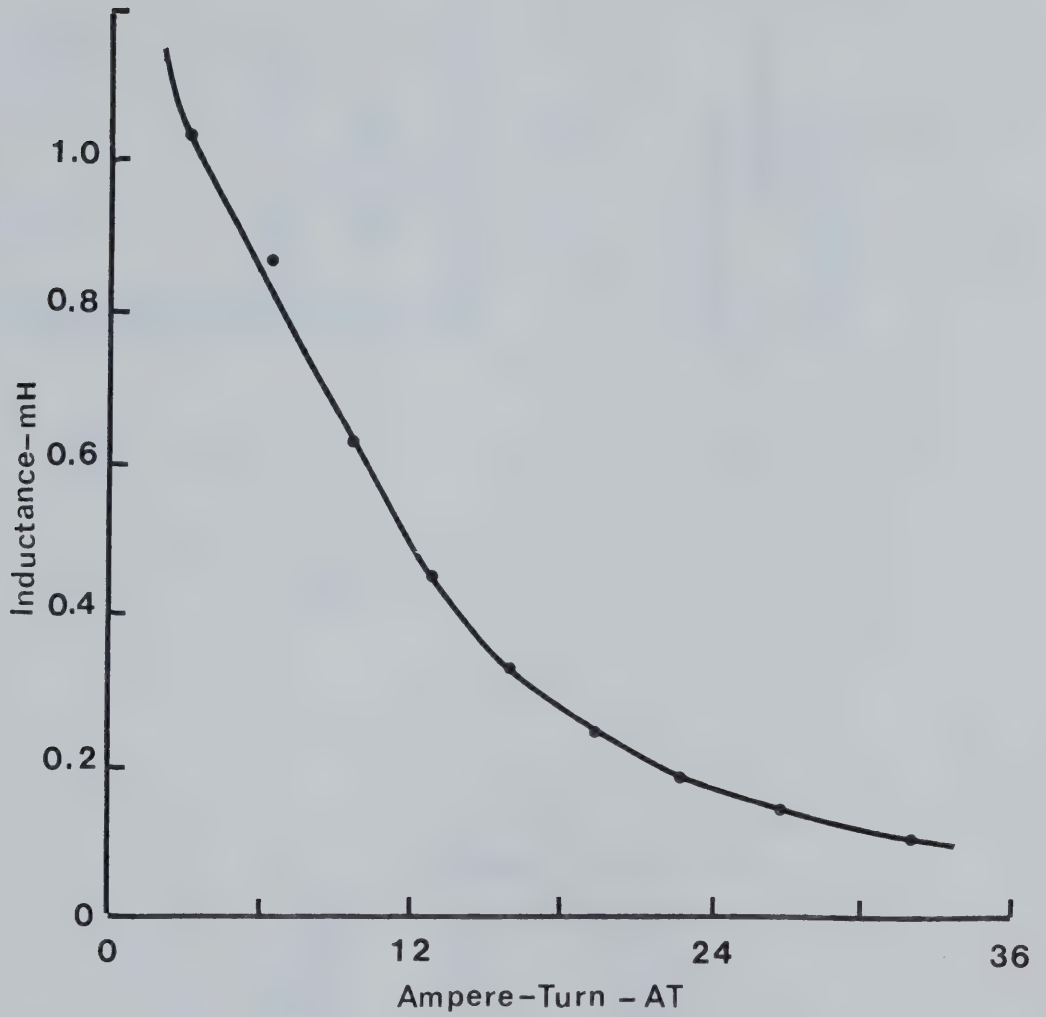


Figure 2-9 Saturation Curve for 3c8 Ferrite Core

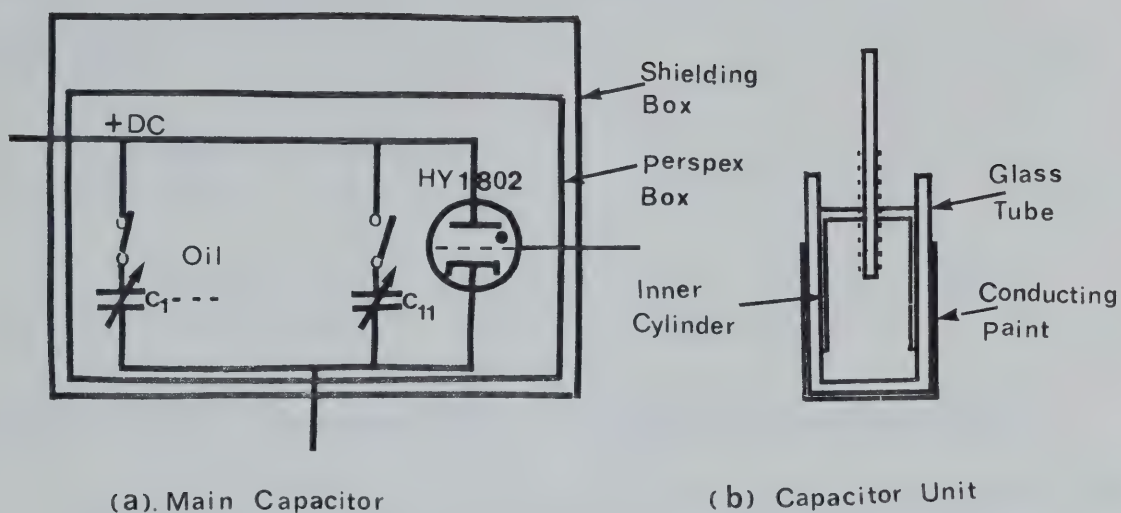


Figure 2-10 Sectional View of Pulse Energy Storage Capacitor

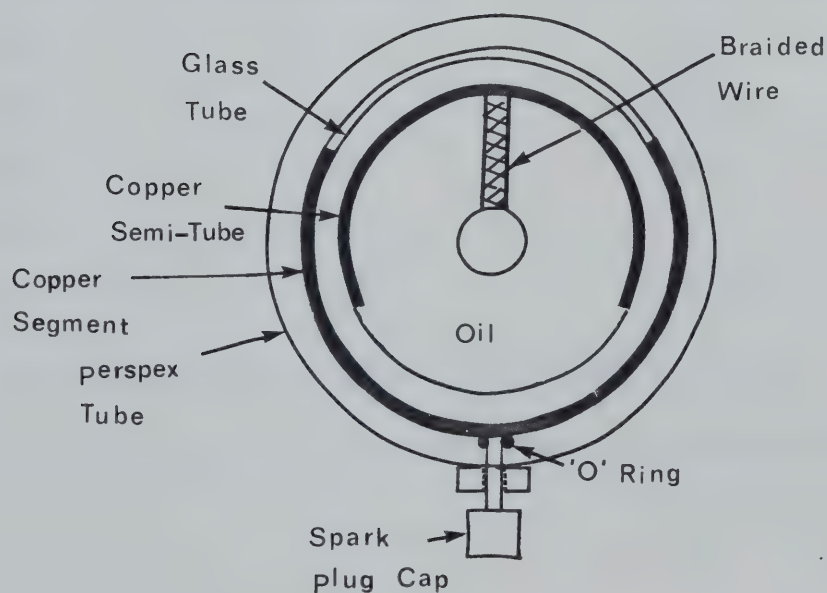


Figure 2-11 Sectional View of U.V. Source Capacitor Bank

which requires $\sim 0.1\text{J}$ of U.V. energy to generate $\sim 10^6$ electrons/cm³ ⁽²²⁾.

Assuming that the pulser is being operated at 15 kV, the required capacitance, C_S , is calculated by

$$C_S = \frac{2Eu}{V^2}$$

$$= 900 \text{ (pF)} \quad (2-5)$$

Where Eu is the U.V. energy and V is the network charging voltage.

To obtain 900 pF at least three capacitor banks are required. The total capacitance of each bank is in Table 2-1.

Table 2-1
Pulse and U.V. Capacitances

<u>Description</u>	<u>Min. Capacitance</u>	<u>Max. Capacitance</u>
1st bank	240 pF	360 pF
2nd bank	220 pF	330 pF
3rd bank	220 pF	330 pF
4th bank	240 pF	360 pF
pulser	20 pF	1120 pF

Note: Row number designated from the gas upstream.

Usually the 1st, 2nd and 3rd capacitor banks are used for U.V. generation.

2-2-5 Operational Characteristics

Although the use of a saturable inductor in high frequency applications is generally avoided because of a potentially nonconsistent mode of operation, good isolation and stable performance can be achieved with proper design. An example of this possible inconsistent recharging type of operation is demonstrated in Figure 2-12. The behaviour here can be explained as follows. When the recharge current is less than the core saturation current the inductor acts linearly. As the average current is raised the core starts to saturate and an unstable state may be reached in which the effective inductance decreases correspondingly. Under these conditions, the charging voltage will overshoot and the charging current will become negative before the switch is fired. Consequently, the next recharge cycle will experience linear charging conditions, with a corresponding increase in period. This longer recharge time thus means that current is still flowing through the inductor in a forward direction when the thyatron next fires. The result of this condition is the generation of a pulse train with alternate high and low amplitudes.

Fortunately however, there is an easy and simple solution to the above problem. The solution merely involves first decreasing slightly the pulse repetition rate, upon encountering the alternate high and low mode described above, and then increasing the operating voltage. In so doing, a stable and constant amplitude operating region can be maintained at any desired repetition rate.

The occurrence of alternate saturation depends largely upon the inductor core material, the values of inductance and capacitance, the load characteristics, the operating voltage and repetition rate.

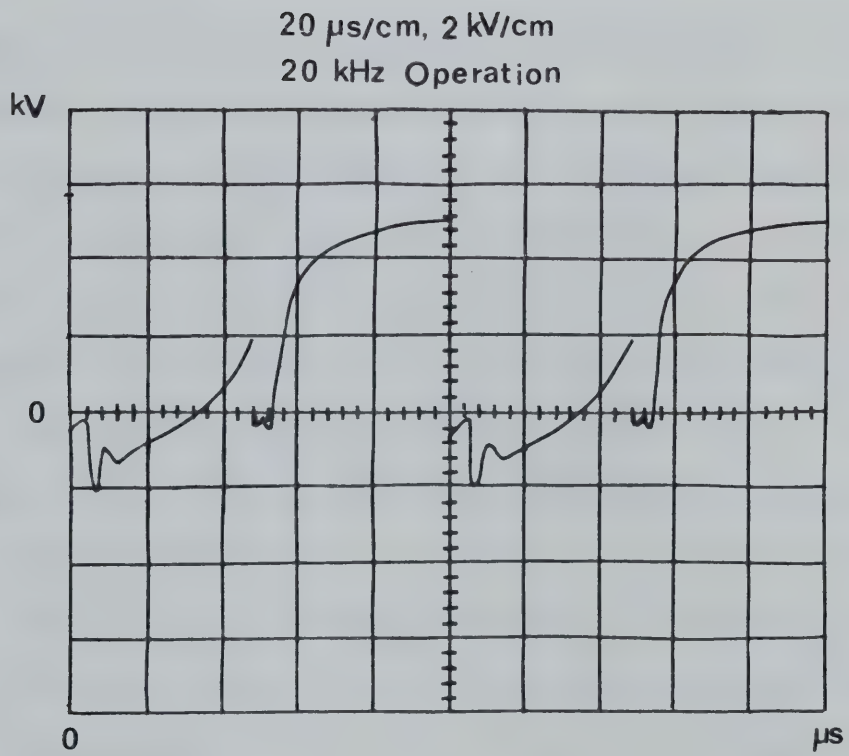


Figure 2-12 Waveform of Alternate Saturation of Saturable Inductor

Saturation was not usually encountered with pulse repetition rates less than 10 kHz and operating voltages above 10 kV.

The thyatron grid is negatively biased to assist in rapid recovery, which is necessary for operation at high voltage and repetition rates. The energy stored in the 160 millihenry isolation inductor in the trigger unit causes a negative swing on the triggering signal. This negative swing is beneficial in that it further promotes the recovery of the thyatron.

A negative anode voltage caused by a voltage reversal or overshoot during operation has been generally found to play an important role in the maximum system operating frequency. Such an anode voltage reversal is a function of the load impedance into which the pulser must operate. For the case considered here, the load impedance is the laser plasma itself. Experiment has shown that the plasma impedance presented by this test laser structure with a typical gas mixture operating at 50 torr is in the range of $50 \sim 100$ ohms. This relatively low value produced a negative impedance mismatch (the load impedance is less than pulser circuit impedance) and resulted in a negative overshoot of the anode potential immediately after the pulse. This anode voltage reversal, which had a duration of approximately 12 μ sec., was found to be particularly beneficial to pulser performance as it effectively permitted a longer inter-pulse recovery time.

Figure 2-13 is a typical anode voltage waveform obtained with the 1802 hydrogen thyatron. A 6 kV anode voltage reversal for a 20 kV operating potential is clearly shown in this photograph.

Resonant Recharge Anode Waveform

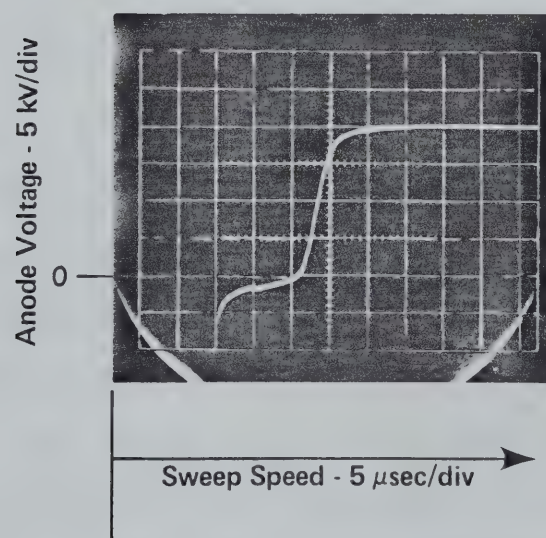


Figure 2-13 Waveform of a Typical Anode Voltage of HY 1802

Because the performance of the preionizer (pulser) largely depends upon the duration of the anode voltage reversal, the factors that affect this duration should be discussed further. Although there are many factors involved only significant ones are considered here. Since the inverse anode voltage is caused by a load mismatch, variations in laser gas mixture and pressure should be reflected in pulser waveform changes. In general, it was observed that low plasma impedances produced the largest anode voltage reversal. Since the recharge cycle starts at the peak of the inverse anode voltage the duration of the anode voltage reversal was directly proportional to the magnitude of the negative overshoot.

The size of energy storing capacitors also (pulse and U.V. source) impose very important effects on duration rather than overshoot amplitude. It is not difficult to understand that the larger the discharged capacitance the longer is the reversal duration. A similar effect is observed with the charging inductor. If the unsaturated inductance is larger, the initial charging current is smaller resulting in a longer period of anode voltage reversal. The above characteristics were well observed by a test made with three charging inductances. Unsaturated charging inductances of 700, 800 and 1200 mH yielded 9, 11 and 18 μsec respectively when the pulser was operated with 8 torr CO_2 and N_2 mixtures. The magnitude of the negative overshoot remained the same at -5 kV for the three cases. This strongly indicates that the magnitude of the negative overshoot is mainly decided by the pulse discharge circuit. The anode voltage reversal period is rather sensitive to variations in the operating frequency. Usually, the negative duration for 20 kHz operation was longer than that for the lower frequency operation. This can be attributed to the anode voltage ripples ($\sim 14\text{kHz}$), which resulted from the reversal

leakage current of the charging diode. Rising and falling of the anode voltage means that the current flowing through the charging diode and inductor is in the forward and reverse directions, respectively. If the thyatron is fired while the current is in the forward direction, saturation of the charging inductor is encouraged and this reduces the negative interval of anode voltage. On the other hand, saturation is delayed if the thyatron is fired when the current is in the reverse direction. Consequently, the negative duration increases. It was found in the experiment that 20kHz operation usually yielded the longest reversal period. This is because the thyatron fires when the reverse current is high.

Summarizing general characteristics:

- 1) The magnitude of the negative overshoot of the anode voltage is independent of the charging inductance, however it is heavily dependent on the load impedance.
- 2) The charging rate is slower with larger inductance.
The charging rate may be increased with higher voltage.
- 3) The positive overshoot (ripple) increases with increasing inductance. The period of ripple becomes also longer with larger inductance.
- 4) Larger storage capacitance extends the duration of anode voltage reversal.

2-2-6 The Pulser Performance

Figure 2-14 shows a typical linear relationship between the network (anode) voltage, V and the maximum pulser current, i_{\max} which can be expressed by⁽²⁸⁾:

$$i_{\max} = V \left(\frac{C_t}{L} \right)^{1/2} \quad (2-6)$$

where C_t is the total pulser energy storage capacitance and L is the pulser discharge circuit inductance. Since the thyatron handles high voltage and current, it is immersed in transformer oil for cooling. By employing the circuit design and construction techniques outlined in the previous sections it was possible to build a very reliable high powered pulser capable of delivering 20 kV , 10 megawatt pulses at a 20 kHz continuous rate. With this device, it was also possible to "trade-off" operating specifications against each other such that stable performance could be obtained at 50 kHz but at a reduced impulse voltage and peak power level of 12 kV and 4 megawatts respectively. Under these operational conditions, the power dissipation factor, P_b (which is a product of anode voltage V , maximum current i_{\max} , and pulse repetition rate f_r) was more than three times larger (191×10^9) than the rating (50×10^9) of the HY 1802 thyatron . To date the pulser has been successfully operated for more than 300 hours continuously producing more than 10^{10} , 5 megawatt pulses.

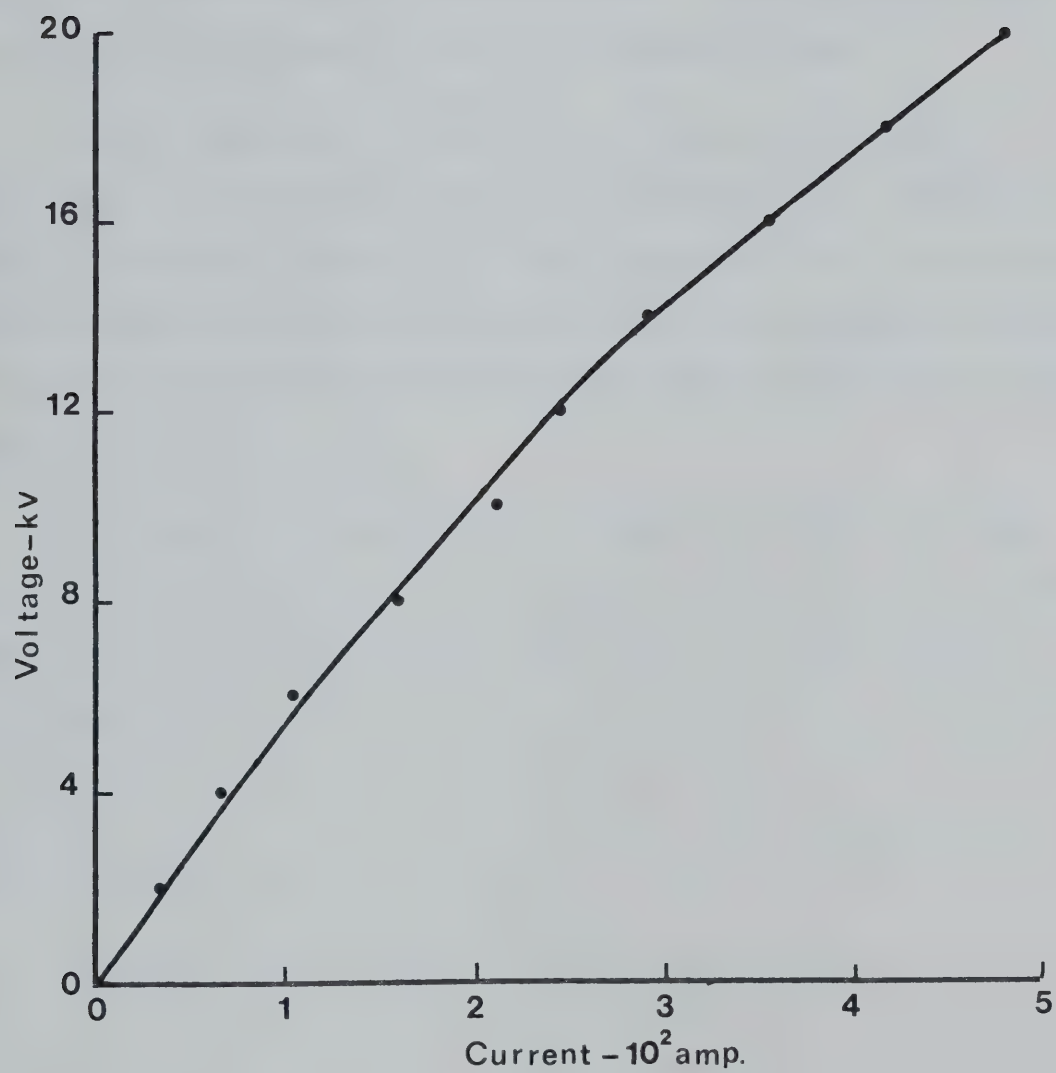


Figure 2-14 HY 1802 Thyatron Anode Voltage vs. Current Characteristic

2-2-7 Sustainer Power Supply

The dc component of the laser excitation was provided by a 50 kVA power supply capable of a maximum current of 50A. A 220V - three phase input was controlled by ganged variacs. The output was filtered by a $375 \mu\text{F} \times 5 \text{ kV}$ capacitor and a 360 Hz resonant filter.

A series inductance of more than ~ 40 henry isolated the dc power supply from the pulser output. This inductance was obtained by using the secondary winding of a 50 kVA transformer. All of the connecting wires were high voltage coaxial cables with outer conductor grounded. This was required to prevent the wires from acting as radiating antennas when the pulser was operated.

Dc current was measured by the voltage drop across a 0.5 ohm resistor connected in series with the positive ground side of the power supply. The discharge voltage and the current were both recorded on an X-Y plotter.

2-3 Optical System

In the early stage of CO₂ laser development, when output power was of the order of a few watts, a simple Fabry-Perot interferometer was used successfully as a laser resonator. Because the power levels were low inside and outside of the resonator, dielectric mirrors with or without coatings were extensively utilized. However, as laser technology has increased the C.W. laser output from a few watts to tens of kilowatts the resonators have been changed accordingly. Multipass stable or unstable resonators are now widely used in high power laser systems.

The stability condition of a laser resonator is expressed by⁽⁵⁶⁾:

$$0 < \left(1 - \frac{\ell}{R_1} \right) \left(1 - \frac{\ell}{R_2} \right) < 1 \quad (2-7)$$

The above equation shows that it is possible to change the stability of a resonator by varying the radii of mirror curvatures, R_1 and R_2 , and the mirror separation, ℓ . Plotting of Equation (2-7) yields a useful stability diagram. For further information on this stability diagram, refer to References 54 and 55.

2-3-1 Optical Power Extraction

The relatively low value of small signal gain coefficient (α_0) exhibited by this P.I.E. device together with a short discharge length of only 50 cm made it impossible to achieve efficient optical energy extraction with a simple resonator system. Some insight into this particular problem can be obtained through utilization of a computer modeling presented by Denes et al.⁽¹⁰⁵⁾. Their results, embodied in Figure 2-15, provide numerical data on the maximum energy extraction possible in a given laser system, as a function of the gain-length product, ($\alpha_0 L$) and mirror losses. The optimum mirror coupling required to achieve this maximum energy extraction is summarized in Figure 2-16.

Energy Extraction Efficiency as defined in these curves, is the amount of optical energy or power that may be coupled out of the active medium, compared to the amount theoretically available for extraction. Thus both excitation efficiency and quantum efficiency must be included in any calculations to obtain meaningful projections on the expected optical power output from a given laser device. By applying these curves to this test laser, having a discharge length of 50 cm and an incremental gain of about 0.3%/cm., $\alpha_0 L$ becomes near 0.15 for a single pass resonator. Thus with a mirror loss of approximately 2%, (1% per surface is a reasonable figure for gold plated BeCu), only about 50% of the available energy may be extracted from the active volume; and this only provided a low loss output coupler having near 6% coupling can be achieved. This aspect is illustrated in the lines labelled A in Figures 2-15 and 2-16.

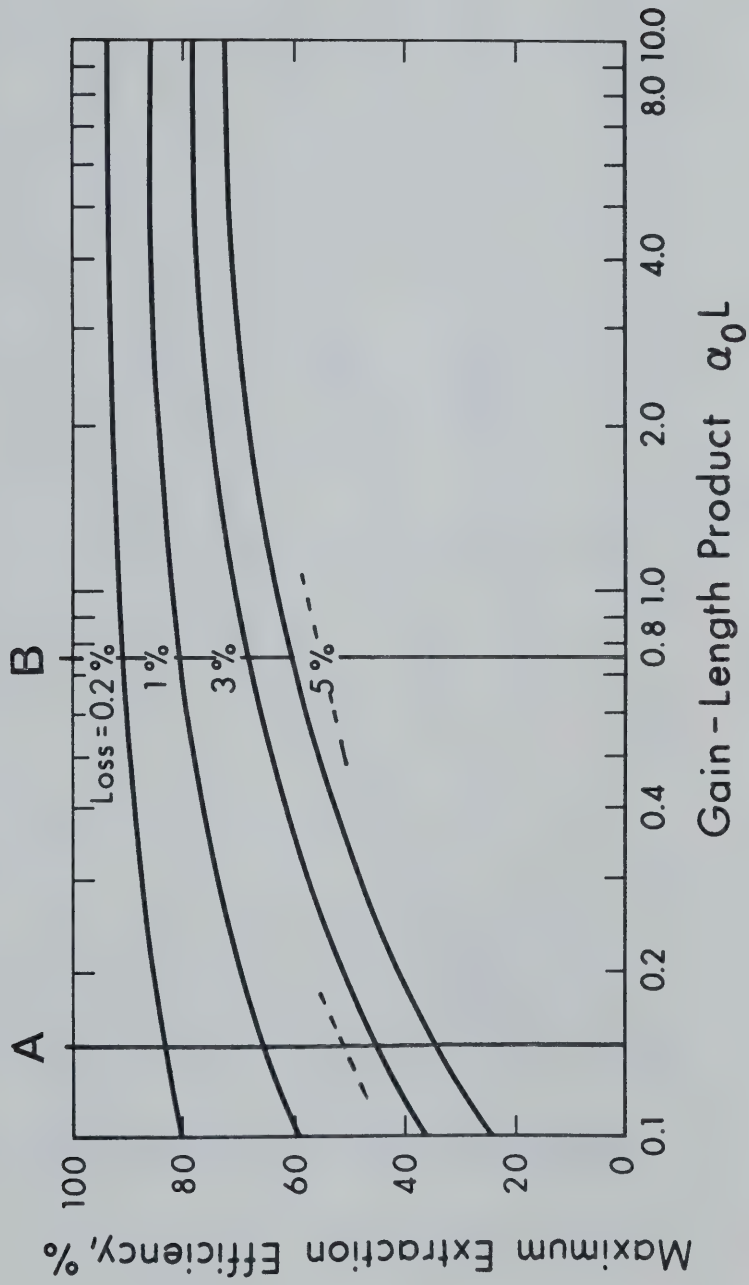


Figure 2-15 Output Power Extraction Efficiency vs. Gain-Length Product

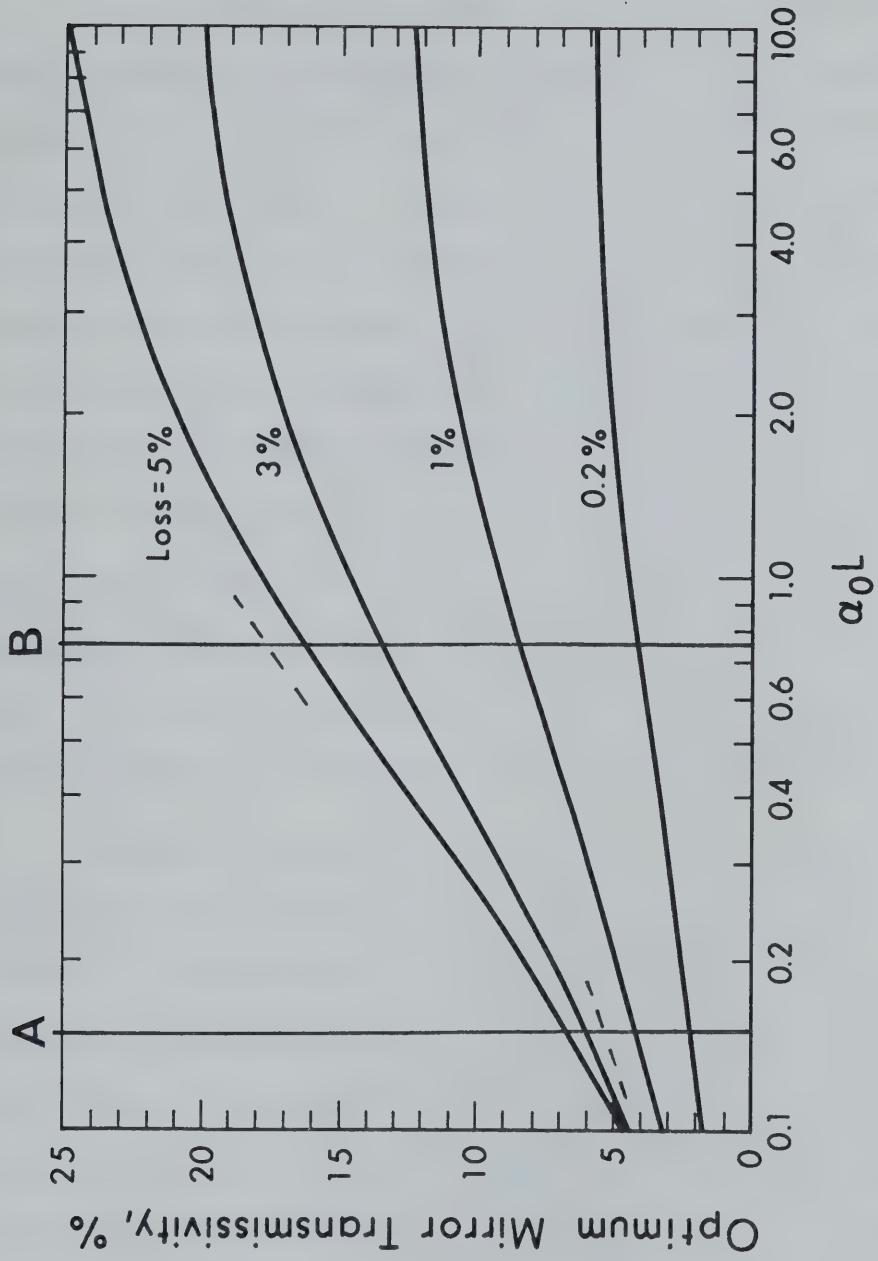


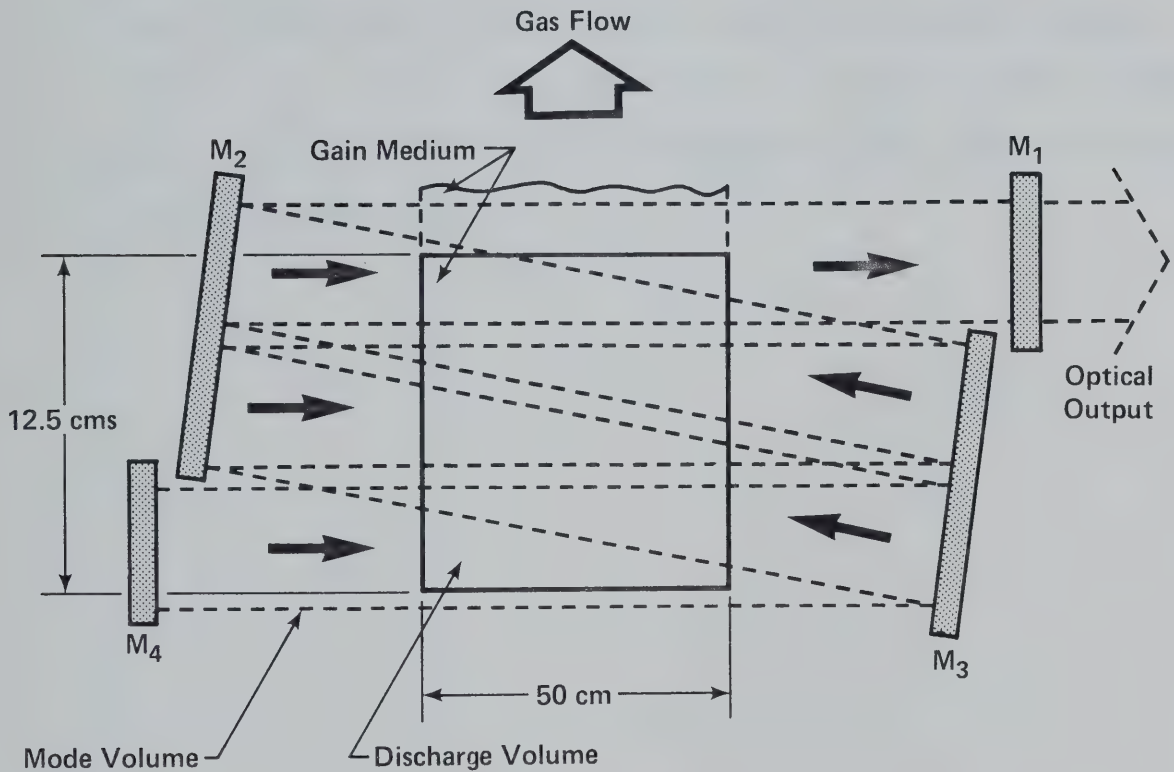
Figure 2-16 Optimum Mirror Transmission vs. Gain-Length Product

2-3-2 Laser Resonator Employed

It is evident from the above curves that devices with small gain-length product are particularly susceptible to poor optics. For this reason a folded path optical system was constructed for optical power extraction experiments. A 5 pass system was selected as the best overall compromise, since with a gain-length product of approximately .75 and an overall mirror loss of about 10%, 50% extraction should still be achievable; but now with a more realistic 18% output coupling. This is shown in lines labelled B of Figures 2-15 and 2-16. Adding more folded paths does not improve the efficiency since mirror losses go up in proportion. Moreover, each additional reflective surface introduces more phase mismatching of the cavity mode, which is manifest as further diffraction loss. Phase matching or compensation can be achieved through special mirror surface profiling but was not considered for the test system described here.

Because of the above considerations, the 5 pass folded optical resonator shown schematically in Figure 2-17, was adapted to the discharge section, to permit optical power output studies. Although the resonator was very lossy and yielded a poor energy extraction efficiency of only a few percent, it nevertheless allowed meaningful studies to be performed. The optical volume covered the entire discharge volume (typically 12.7 cm x 55.9 cm x 6.3 cm) and the extra gain-volume on the downstream side of the discharge. The three mirrors (M_2 , M_3 , and M_4) were beryllium copper (3% Be + 97% Cu) substrates coated with gold. The output mirror, M_4 had the same construction with an array of output power coupling holes. All mirrors were cooled with tap water. Each of the mirrors has a reflecting surface with dimensions 12.7 by 6.4 cm. The intermediate folding

5 Pass Folded Path Laser Resonator



Mirror	Radius	Substrate	Coating
M ₁	30M	Beryllium Copper	Gold
M ₂	∞	Beryllium Copper	Gold
M ₃	∞	Beryllium Copper	Gold
M ₄	20.4 M	Beryllium Copper	Gold

Figure 2-17 5 Pass Folded Path Optical Resonator

mirrors, M_2 , and M_3 , are flat while the output, M_1 , and rear, M_4 mirrors are concave with radii of curvature of 30 m and 20.4 m respectively.

The spacing between these mirrors is 5.5 m with 2.8 m of gain pass. Thus, the cavity constitutes a stable resonator with the multimode dimension of 6.4 by 6.4 cm. The beam is folded twice on each intermediate folding mirror to cover the whole discharge volume and the gain volume stretching 6.4 cm on the downstream side.

2-3-3 Equivalent Sequence of Lenses

In order to provide a better understanding of the optical resonator used for this project, the equivalent sequence of lens system is shown in Figure 2-18.

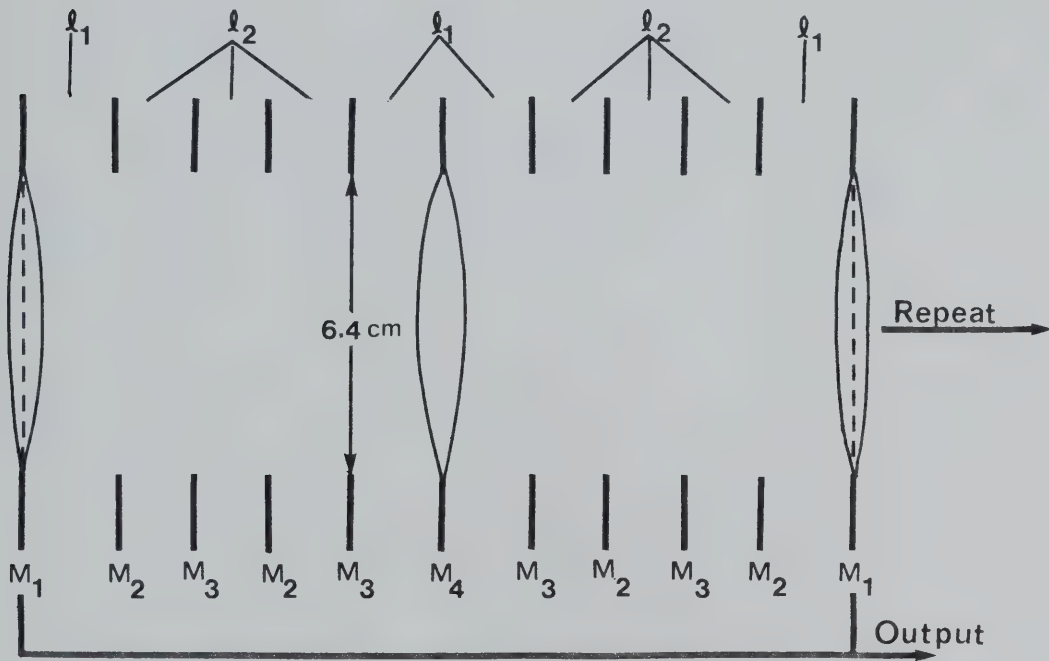


Figure 2-18 Equivalent Sequence of Lenses

In this system the folding mirrors, M_2 and M_3 , are represented by 6.4 cm square apertures. The rear mirror M_4 is represented by a 6.4 cm square converging lens with focal length of 10.2 m while the output mirror M_1 is replaced by a 6.4 cm square converging lens with focal length of 15 m and with a built-in absorbing plate. The absorption of energy is equiva-

lent to the laser energy extracted through the output mirror per pass.

l_1 and l_2 are the mirror spacings of 99 cm and 95 cm respectively.

2-3-4 Simple Technique to Change the Transmittivity of the Output Mirror

It was found possible to change the transmittivity of a multihole output mirror by enlarging the size of holes without noticeable degradation of the mirror surface. The procedure involved first protecting the vulnerable gold coating by a 0.1 mm layer of acrylic spray paint. Then the holes were enlarged by drilling from the polished side. This step was repeated with the drill size increased in small increments up to the desired hole size. Afterwards the acrylic protecting layer was removed by gentle washing in ethyl acetate ($\text{CH}_3\text{COOC}_2\text{H}_5$).

2-3-5 Window

Except for special cases, an output window is required that is capable of isolating the low pressure laser chamber from the atmosphere. The window should have a good transmittance at the laser frequency. Useful IR window materials for the CO₂ laser are listed in Table 2-2 for reference.⁽⁹²⁾

Table 2-2

IR Window Materials

(Longwave Limit-60% trans. 1 cm-thick)

Alkali halides (affected by water)		Other Materials (unaffected by water)	
Material	Microns	Material	Microns
NaF	10.5	Harshaw T-12	10.0
BaF ₂	11.5	Irtran II	10.5
NaCl	16.0	Irtran IV	15.0
KCl	20.0	Silver Chloride	14.5
KBr	25.0		
CsBr	38.0		

The window used for this project consists of a NaCl disc, 14 cm in diameter and 1.3 cm thick. The window is tilted slightly away from the plane perpendicular to the laser axis so as to prevent the beam reflected at the window surface from initiating a laser oscillation.

The limitations of output mirror and window materials are a serious problem in very high power (tens of kilowatts) laser development.

Fortunately, a solution appears to be at hand. Avco's "aerodynamic window" concept has proved very successful⁽⁴⁶⁾. In this technique the laser beam was brought to focus at a chamber wall by a third mirror and then transmitted through a set of small holes in the wall. This aerodynamic window was designed to balance the pressure differential between the low pressure lasing chamber and the outside atmosphere, and thereby prevents any air from entering the chamber.

Another feature of the optical system developed for this project is a beam focusing lens. An 11.4 cm diameter and 0.5 cm thick plano-convex NaCl lens is placed at one end of a perspex beam transport tube to focus the laser beam for metal processing experiments. A terminating funnel was also designed to supply a cover gas to the target. It also helped to keep the beam path free of refuse and vapors liberated by the target.

CHAPTER III

EXPERIMENTAL RESULTS AND DISCUSSION

This chapter presents and discusses a variety of observations of the performance of the developed laser.

In the development of the laser system three different types of electrode configurations have been involved. The same copper tube anode geometry has been used throughout the experiments, consequently only the cathode structure determined these different configurations. These configurations were as follows:

- | | |
|-------------------------|--|
| 1) First configuration | Solid copper cathode |
| 2) Second configuration | Electrolytic solution ballasted
cathode with 276 pins |
| 3) Third configuration | Electrolytic solution ballasted
cathode with 512 pins |

In this thesis the terminology "Electrolytic Solution" is used to denote tap water as well as electrolytic aqueous solutions. However, differentiation will be made when the necessity arises.

The first few sections of this chapter present data on the discharge parameters obtained with the first configuration at low (< 20 torr) pressures. The second configuration was used to determine the discharge characteristics over a wider pressure range and for optimizing the optical output power. The results appear in the middle part of this chapter. The third configuration was used for parametric studies to determine stability conditions and operational lifetimes.

In the P.I.E. laser operation, three different modes of operation

are realized.

1) Preionizer sustained mode; this mode occurs at low sustainer (dc) voltage and high preionization electron density. The dc discharge is sustained with the aid of preionization, such that the discharge terminates when preionization is removed.

2) The self-sustained mode; here the dc discharge is sustained by a glow discharge process so that the system can be operated without preionization.

3) The preionizer maintained mode; in this mode the preionizing electrons control the uniformity of the discharge so that the initiation of instability is suppressed. The open circuit dc voltage is higher than the self-sustained glow discharge voltage so that the removal of preionization initiates an arc. This phenomenon is attributed to the very poor regulation of the sustainer dc power supply.

These three modes of operation will be discussed in more detail in Section 3-4-1.

3-1 Laser Operation with Solid Cathode; 1st Electrode Configuration

3-1-1 Performance of Solid Electrodes in Low Pressures

The influence of a cathode in a gas discharge prompted an investigation on the cathode materials suitable for P.I.E. lasers. Three different cathode materials have been tested. A graphite cathode was tested and quickly rejected at an early stage of the experiments due to surface disintegration and resulting system contamination. This aspect was described in Section 2-1-6.

The use of an aluminum cathode resulted in a glow discharge distributed uniformly across the electrode surface. However, prolonged operation developed a dark oxide film with localized spots. The non-uniformity of this oxide film created a corresponding discharge non-uniformity, eventually developing into an arc. These localized arc points, of high current density, were observed to puncture the resistive aluminum oxide film and cause pitting of the aluminum cathode surface. These pits or damage points then became initiation centers for subsequent discharge instabilities and thereby greatly deteriorated cathode performance. For these reasons it was considered undesirable to utilize aluminum as the cathode material in a high power CW laser system. No useful data were taken using either the graphite or aluminum cathode.

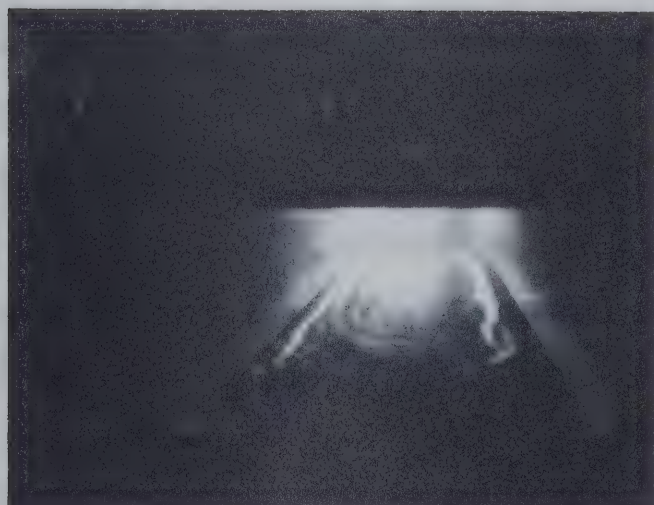
Most of the low pressure data was obtained using the copper pressed cathode. The copper surface was hardly discolored even with prolonged operation. This may be because the high cooling efficiency prevented the surface from getting sufficiently hot for an oxidation reaction. Alternately, the high sputtering rate of copper (ten times higher than that of aluminum) may have resulted in cleaning of the surface. The

former explanation appears more likely since a trace of dark oxide film appeared when the water flow rate was decreased.

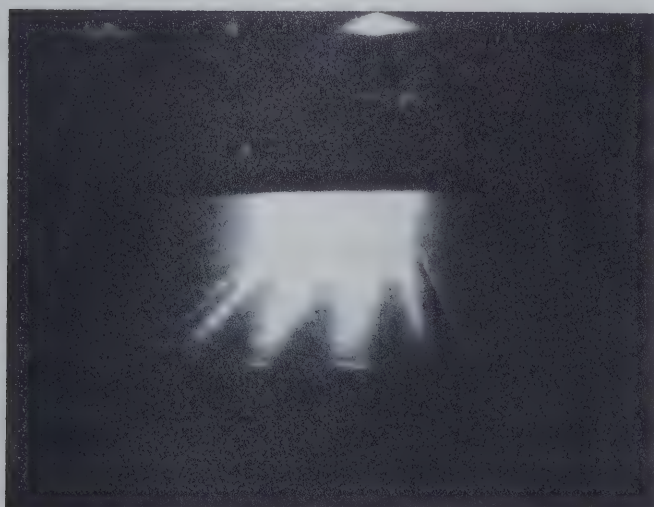
The following visual observations were made with a glow discharge at low pressure (< 20 torr). Without U.V. initiation, the glow on the cathode became irregular as illustrated in Figure 3-1(a). As U.V. was turned on, intense glow stripes matching the U.V. source pattern appeared on the cathode surface as shown by Figure 3-1(b). This effect was most pronounced with a small ($< 1A$) sustainer current. As the sustainer current was increased the stripes became less distinct and were indistinguishable under a higher sustainer current of a few amperes.

Only four parts of the glow discharge could be observed; negative glow, Fraday dark space, positive column and anode glow. With U.V. and/or pulse preionization the dark space becomes less distinct. This occurs because the pulse generates energetic electrons which reduce the extent of the electron decelerating region in the dark space. With a separate test arrangement, it was found that as the voltage was increased the dark space was gradually replaced by the positive column. It was also observed that the negative glow extended to the anode in low pressure (< 1 torr) discharges. This observation is consistent with the findings of References (35, 92).

Another peculiar phenomenon often observed in the discharge was development of anode spots. A trace of foreign contaminants produced numerous anode spots of various sizes. When the sustainer current was increased, several spots expanded while the rest of them gradually disappeared. In a manner similar to the cathode spots, some of the expanding anode spots grew until they initiated an instability. The



(a)



(b)

Figure 3-1 Photos of Low Pressure Discharges. $C_M \sim 360$ pf, pulser 7KV at 10KC

D.C. Current 1A, $CO_2:He=10:10$ (torr)

a) Pulse Preionization Only

b) U.V. Initiated, Pulse Ionized

contaminants which produced this phenomenon were: water vapor, silicon sealant vapor and tri-n-propyl-amine.

3-1-2 Comparison of the Preionization Efficiency Under Different Conditions

In this section the system was operated in the preionizer sustained mode where the dc discharge was completely controlled by the preionizer. The dc discharge voltage was set at a value lower than that of a self-sustained glow discharge. The preionizing input power was varied by changing the pulser frequency from 1 kHz to 10 kHz while the pulser voltage was kept constant at 13 kV. The resulting dc current was plotted on an X-Y plotter for various preionization conditions. These measurements were repeated for different gas mixtures at different pressures.

The results for three pressures, 5, 10 and 20 torr, were summarized in Figures 3-2, 3-3 and 3-4 respectively. These figures commonly show that under the same E/N the discharges in He produced the largest dc current. The slope of each curve represents the relative effectiveness of the preionization by different sources. The most effective pre-ionization is achieved by the pulse.

It is interesting to see that CO₂ which has the lowest ionization potential among the laser gas constituents produced the smallest dc current under the same preionization condition. This fact is realistically illustrated in Figure 3-5 which shows the results of input-power-test for two extreme laser gas constituents, CO₂ and He. It seems that CO₂ controls the discharge behavior of the laser gas mixture. Thus, as shown in this figure, a 25 kW input at 100 torr in He dropped to 8 kW when

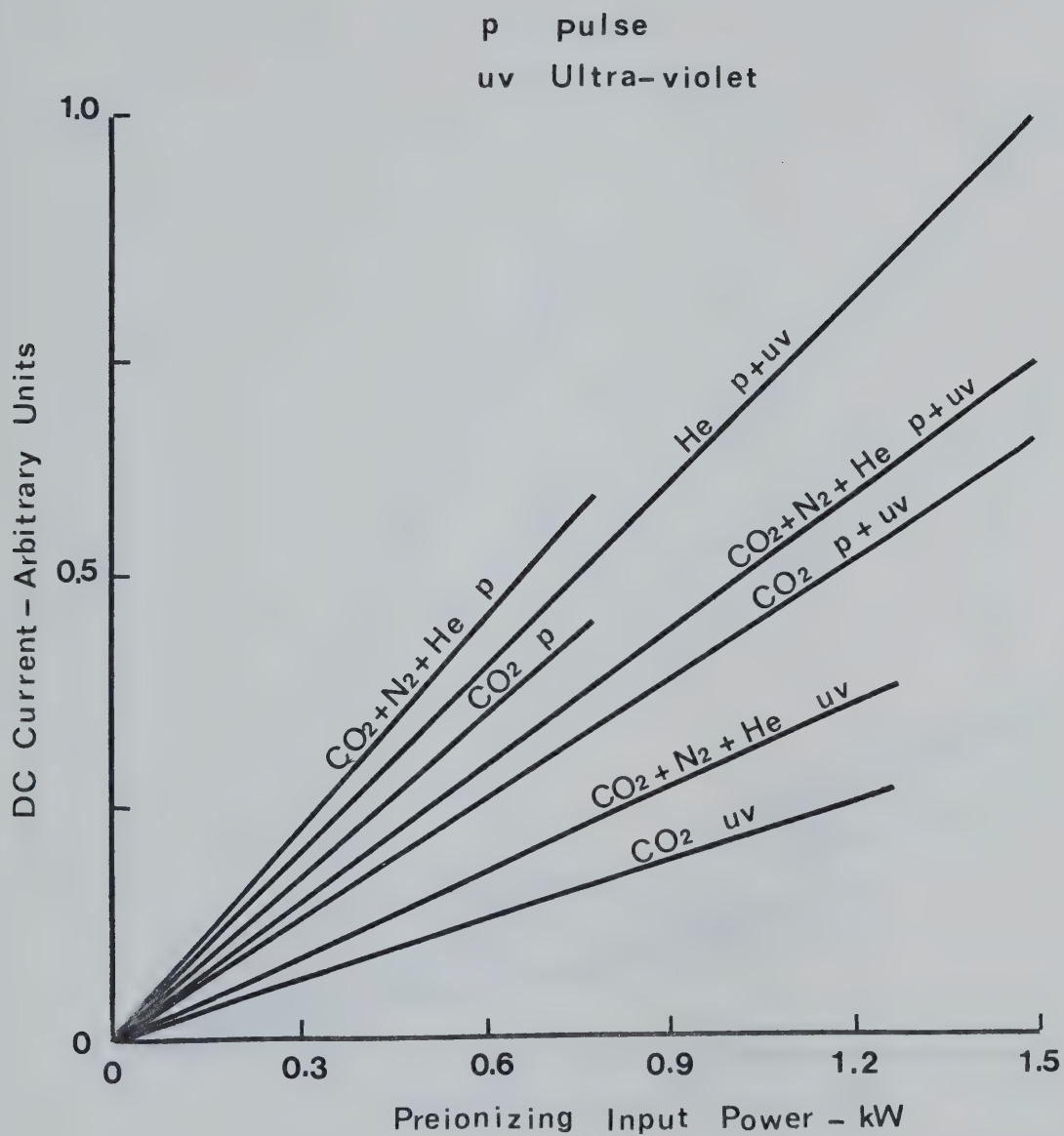


Figure 3-2 Relative Plasma Generation at 5 torr
Pulser - 13kV at 1~10kHz, dc - 300V,
 $E/N=2.6 \times 10^{-16} \text{V-cm}^2$

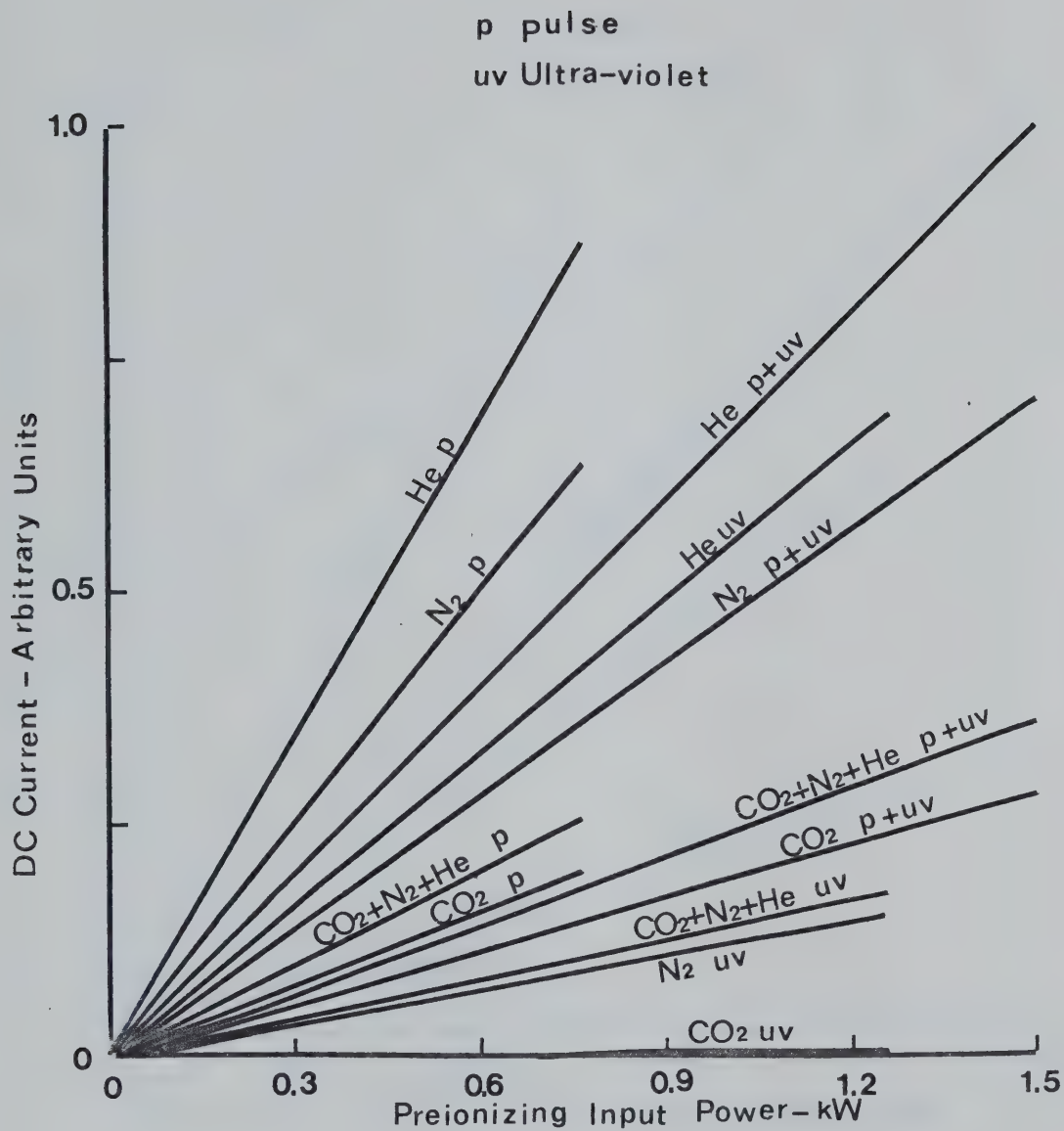


Figure 3-3 Relative Plasma Generation at 10 torr
Pulser -13kV at -10kHz, dc - 350V,
 $E/N - 1.5 \times 10^{-16} \text{ V-cm}^2$

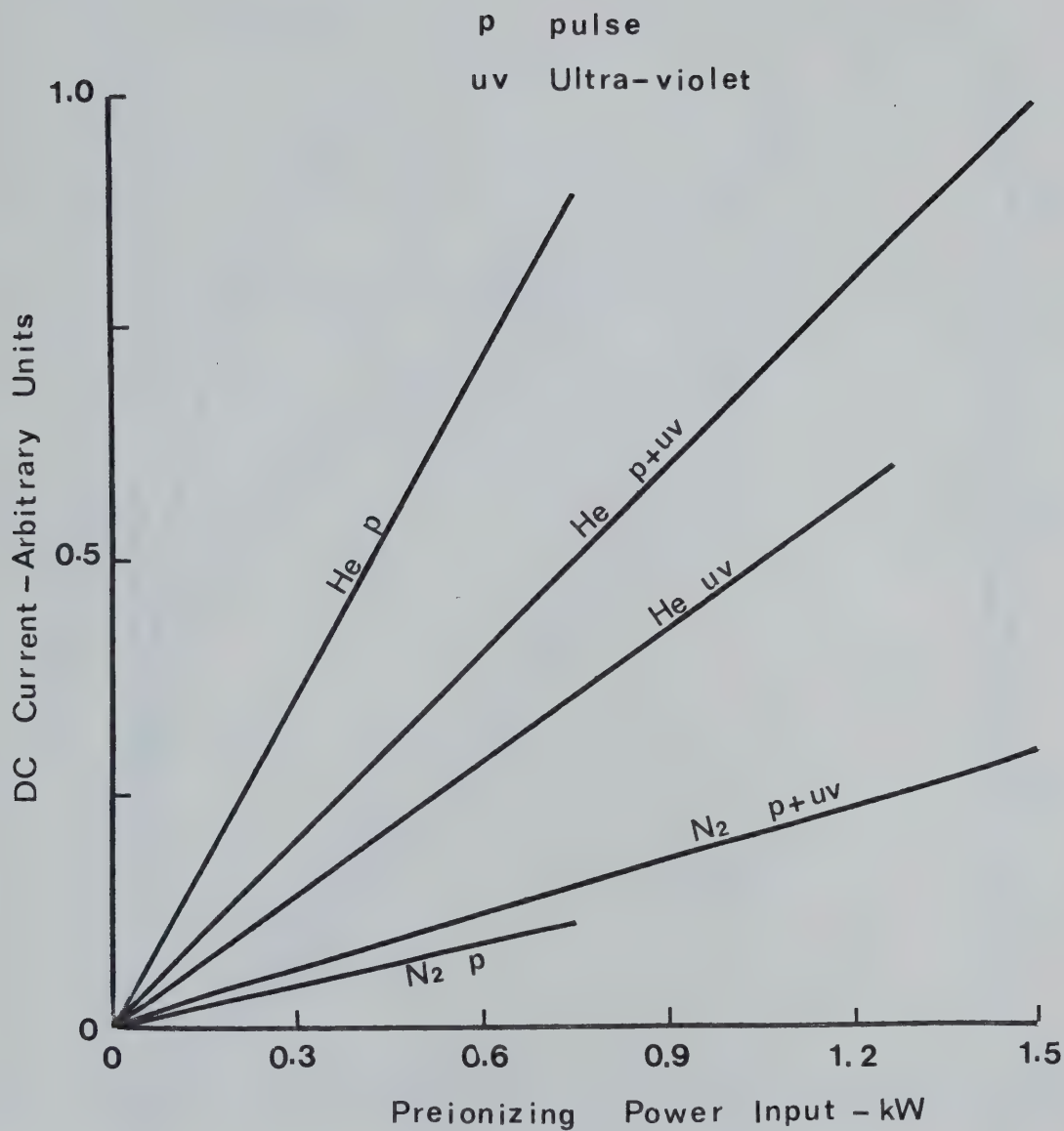


Figure 3-4 Relative Plasma Generation at 20 torr
 Pulser - 13kV at 1~10kHz, dc - 375V,
 $E/N - 8.2 \times 10^{-17} \text{ V-cm}^2$

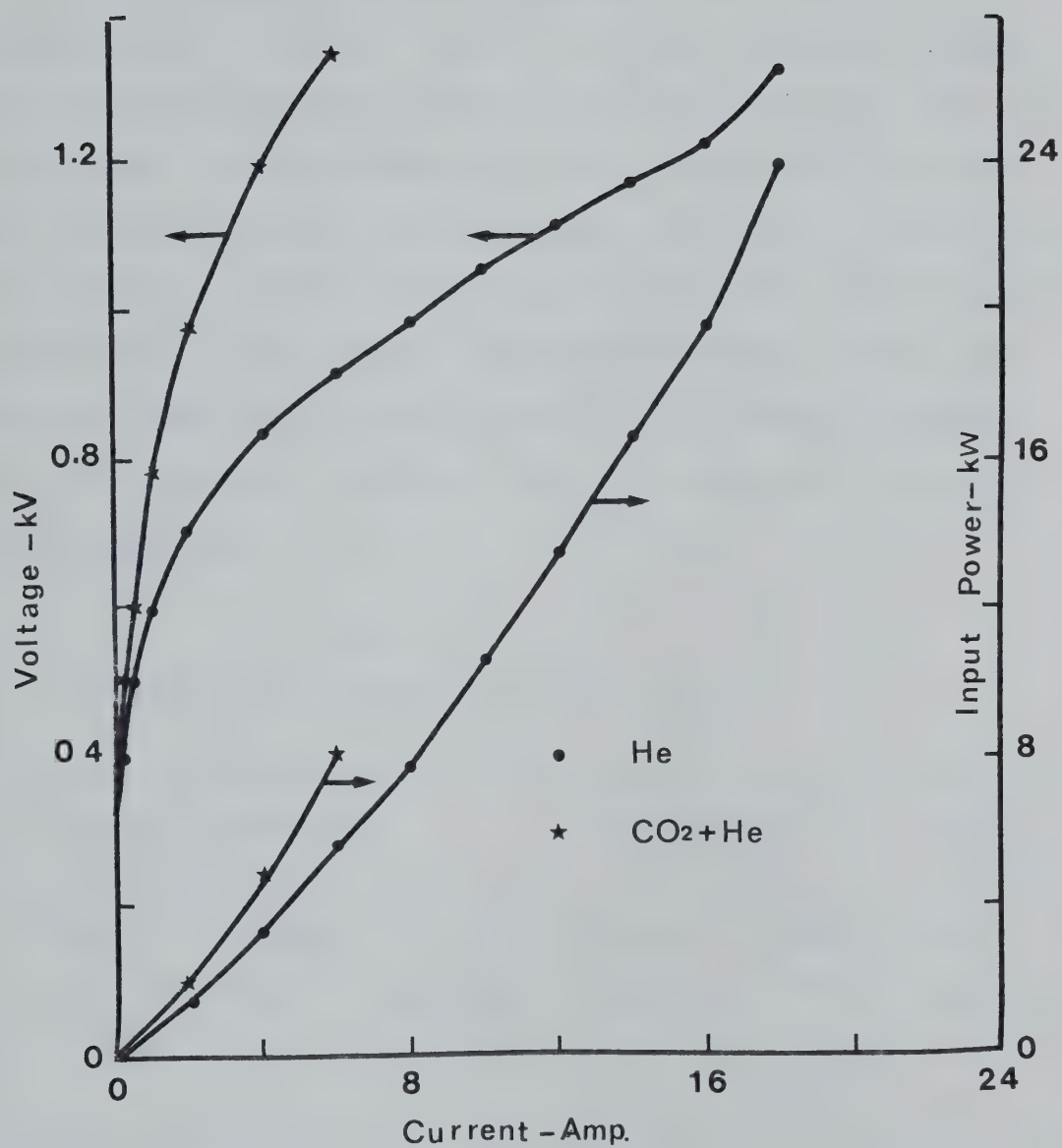


Figure 3-5 Discharge Characteristic in He and CO₂:He Mixture

1.5 torr of CO_2 was added. Because this phenomenon is very important in laser operation, a further discussion is presented below.

Table 3-1 presents the plasma parameters which contribute to the electron density or total dc current. The first and second Townsend coefficients of He are at least three times larger than that of CO_2 . On the other hand, the plasma decay rate of CO_2 is much faster than that of He. In order to compare the plasma decay rates of CO_2 , N_2 and He, data were obtained from three different figures of Reference 28 and presented in Figure 3-6R. Because of small Townsend coefficients and large recombination coefficient as shown in the table and figure, the plasma density in CO_2 is smaller than in He when the preionization conditions and E/N are the same.

Table 3-1

Ionization and Recombination Coefficients

Gas	Townsend Coefficient (Ref. (91))				Recombination Coefficient		Drift Velocity	
	press.	voltage	α	β	press.	coeff.	press.	vel.
CO_2	4 torr	350	2.24	~ 0	4.9 torr		4.9 torr	6.5×10^6
		700	9.28	~ 0		$\sim 10^{-5}$ (28)		(90)
N_2	4 torr	350	1.35	~ 0				
		700	7.08	0.049	5	1.6×10^{-6} (28)	5	3×10^6 (90)
He	6 torr	305	6.45	0.0436				
		772	10.8	0.36	6.1	$\sim 10^{-8}$ (28)	6.1	5×10^6 (90)

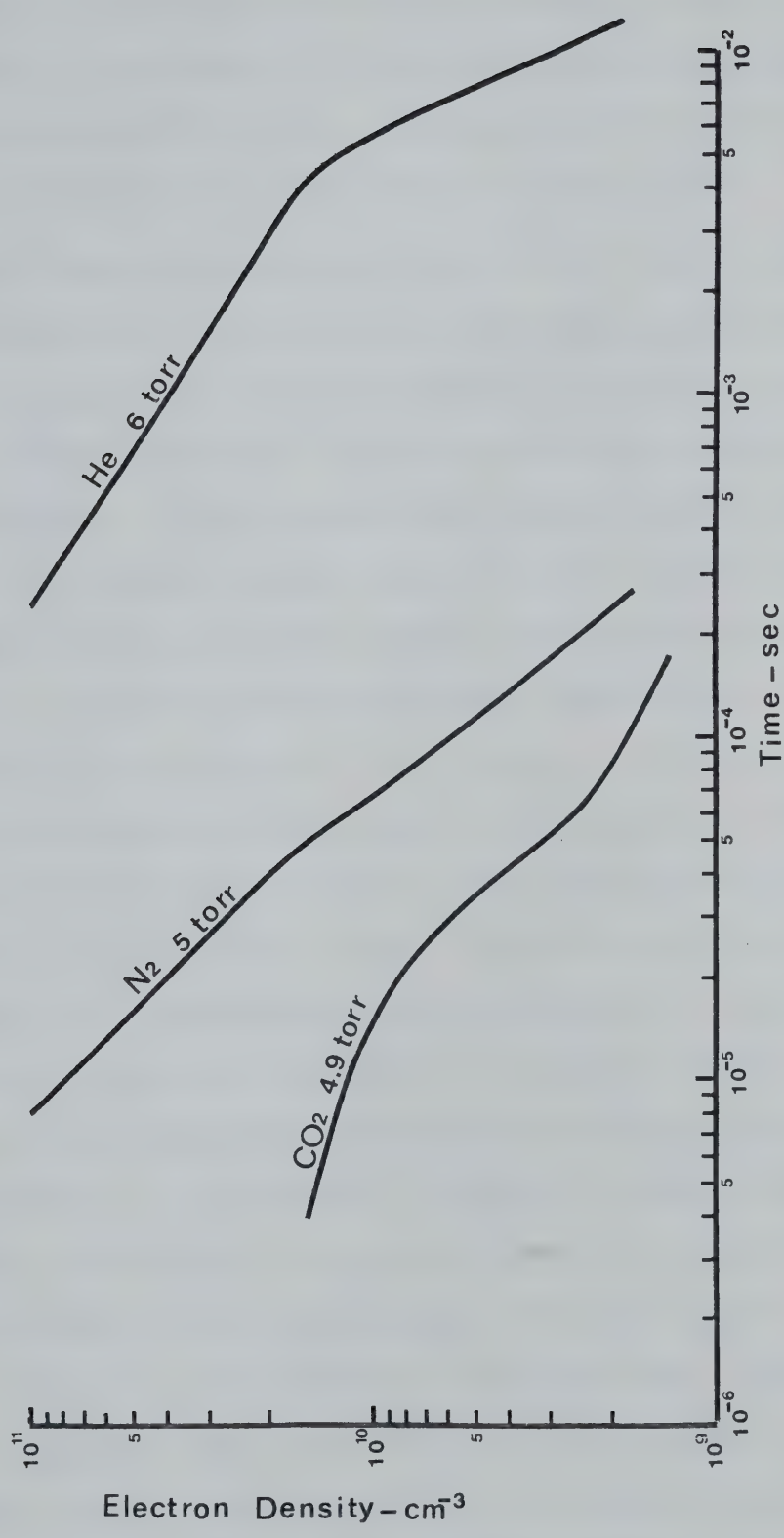
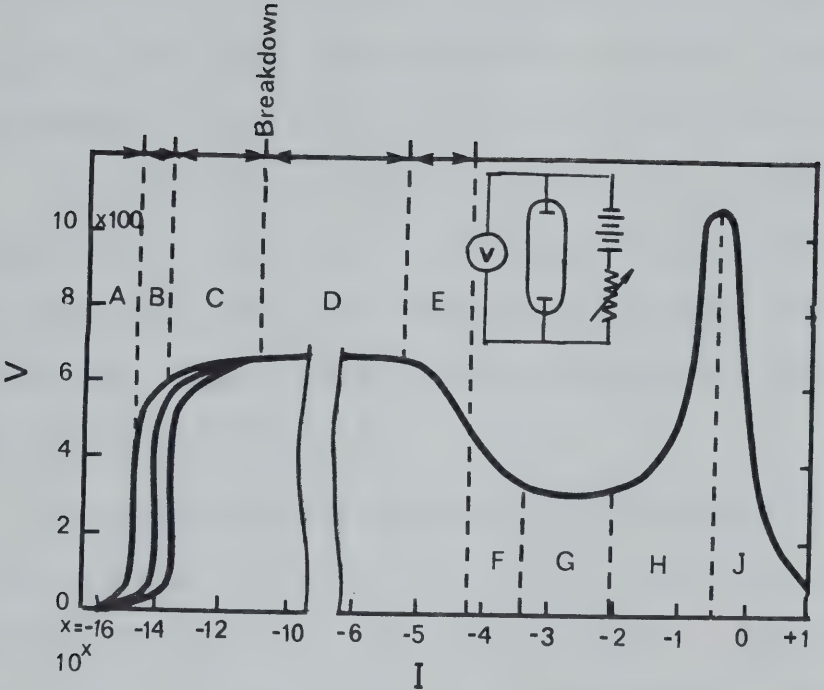


Figure 3-6R Plasma Decay in CO₂, N₂ and He (Ref. 28)

3-1-3 V-I Characteristics in Low Pressure P.I.E. Laser

In order to understand the V-I characteristics of the P.I.E. laser properly a knowledge of V-I characteristics of low pressure discharges without preionization is an asset. For convenience the latter has been excerpted from Reference 92 and presented in Figure 3-7R.

In this figure the Random burst pulses result from the free electrons produced by natural causes such as cosmic ray ionization. However, if enough free electrons are present in the gap as a consequence of external volume ionization, a steady current may be observed without onset of the pulses. Under a constant free electron density, the current increases as the voltage increases until it reaches a plateau known as the Saturation current. Here all available free electrons in the gap are collected. Increasing the voltage beyond a certain point, the current starts to increase again. This increase is exponential and this region is called the Townsend discharge. Further increase of the voltage leads to an over-exponential increase in the current followed by the collapse of the voltage across the gap. This abrupt transistion is known as Breakdown. It is characterized by an increase in the current of several orders of magnitude with almost no increase of voltage. Here the current becomes independent of the external ionizing source and is thus self-sustained. If the current is allowed to increase further, the voltage across the discharge begins to drop until it reaches a low level, known as Subnormal and Normal glow regions. The normal glow is characterized by a constant current density at the cathode and a constant voltage across the discharge. More specifically, the area occupied by the cathode glow increases proportionally with the current. The normal glow region terminates when the whole cathode flat surface is covered by



- | | |
|---------------------------|-------------------|
| A. Random burst pules | F. Subnormal glow |
| B. Saturation current | G. Normal glow |
| C. Townsend discharge | H. Abnormal glow |
| D. Self-sustained current | J. Arc |
| E. Corona | |

Discharge tube -- 2-cm dia. and 50-cm long

Figure 3-7R Typical Characteristics for Self Sustained Low Pressure Discharge (Ref. 92)

the cathode glow. If the current is forced to increase further the cathode glow establishes itself on any additional surface available, such as the metal leads or backside of the cathode. The discharge in this operating mode is known as the Abnormal glow and is characterized by an increase in both voltage and current. The termination of the abnormal glow is followed by another transition known as the arc. In the arc discharge the cathode glow constricts into a small and bright arc spot which carries about two orders of magnitude higher current than the glow discharge⁽⁹²⁾.

This knowledge of the selfsustained glow discharge is utilized to explain the V-I characteristics of the P.I.E. laser. The V-I characteristic curves are shown in Figure 3-8 as a function of the preionizing power. The preionizing power was changed by varying the pulse repetition rate at a constant charging voltage. The curve for a self-sustained glow discharge was obtained by measuring the voltage and the current without preionization. The dotted line represents the Townsend-to-glow transition. The saturation current was so small that meaningful measurements could not be made due to the equipment limitation. The breakdown voltage of about 850 V resulted in nearly 3A sustainer current after breakdown. As the sustainer voltage was lowered the sustainer current decreased to about 1.2A, at which point the glow disappeared. By definition, this curve shows only the normal glow (1.2 ~ 2.5A) and abnormal glow (2.5 ~ 14A) regions. When the gas is preionized by 1 kHz-10 kV pulses, the curve is modified considerably. The saturation current is increased by many orders of magnitude to about 15 mA. The resulting current of density of 0.025 mA/cm^2 is comparable to that of the subnormal glow region of Figure 3-7R. Consequently, the Townsend-to-glow transition does not show on the curve. As the voltage increases from the point of

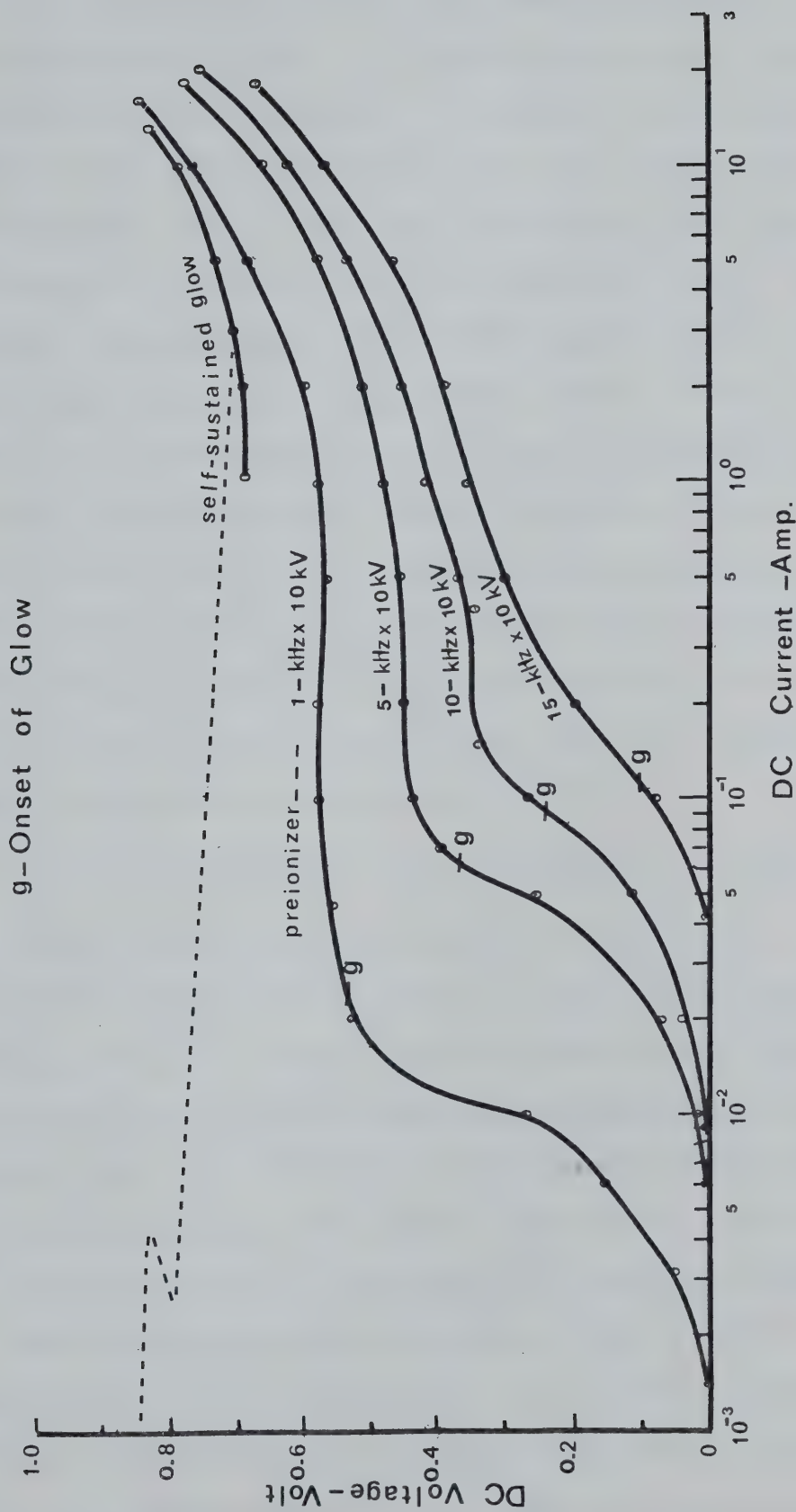


Figure 3-8 V-I Characteristics of Low Pressure P.I.E.

Laser

$\text{CO}_2:\text{N}_2:\text{He} = 1:1.2:13.2$ (torr)

Flow ~ 30 m/sec

glow onset, 'g' in Figure 3-8, the curve shows the extended normal glow and the abnormal glow regions. As the preionizing power is increased by increasing the pulser frequency, the saturation current also increases as expected. The regional boundaries became less distinct with more preionizing power input. This is well illustrated by the curve for 15 KHz operation which hardly shows the normal glow region. This phenomenon is characterized by the fact that most of the flat portion of the cathode is covered by thin glow upon onset of the glow. Further increase in the current from this point starts the abnormal glow discharge as shown. It should be noticed that the voltage for the glow onset becomes less significant as the preionizing power is increased. This signifies that the pulse discharge itself produces quasi-continuous cathode glow and the sustainer voltage intensifies the glow as well as expands the glow to the additional surface. This is an abnormal glow process in which the current increases with voltage.

3-1-4 The Gas Impedance of the Low Pressure P.I.E. Laser

The gas impedance of the laser plasma obtained from the V-I characteristics (Figure 3-8) is plotted in Figure 3-9 as a function of discharge current. The overall behavior of these curves reveals that preionization heavily controls the discharge characteristics at low sustainer current, and the effect of preionization gradually diminishes with increasing current. This signifies that as the current increases, some of the electrons must be generated by the sustainer discharge. Since these sustainer generated electrons are also subjected to pulse multiplication, the preionization still controls the discharge. The degree of preionization can be represented by the slope of an Impedance-Current curve and the departure of this curve from the self-sustained curve.

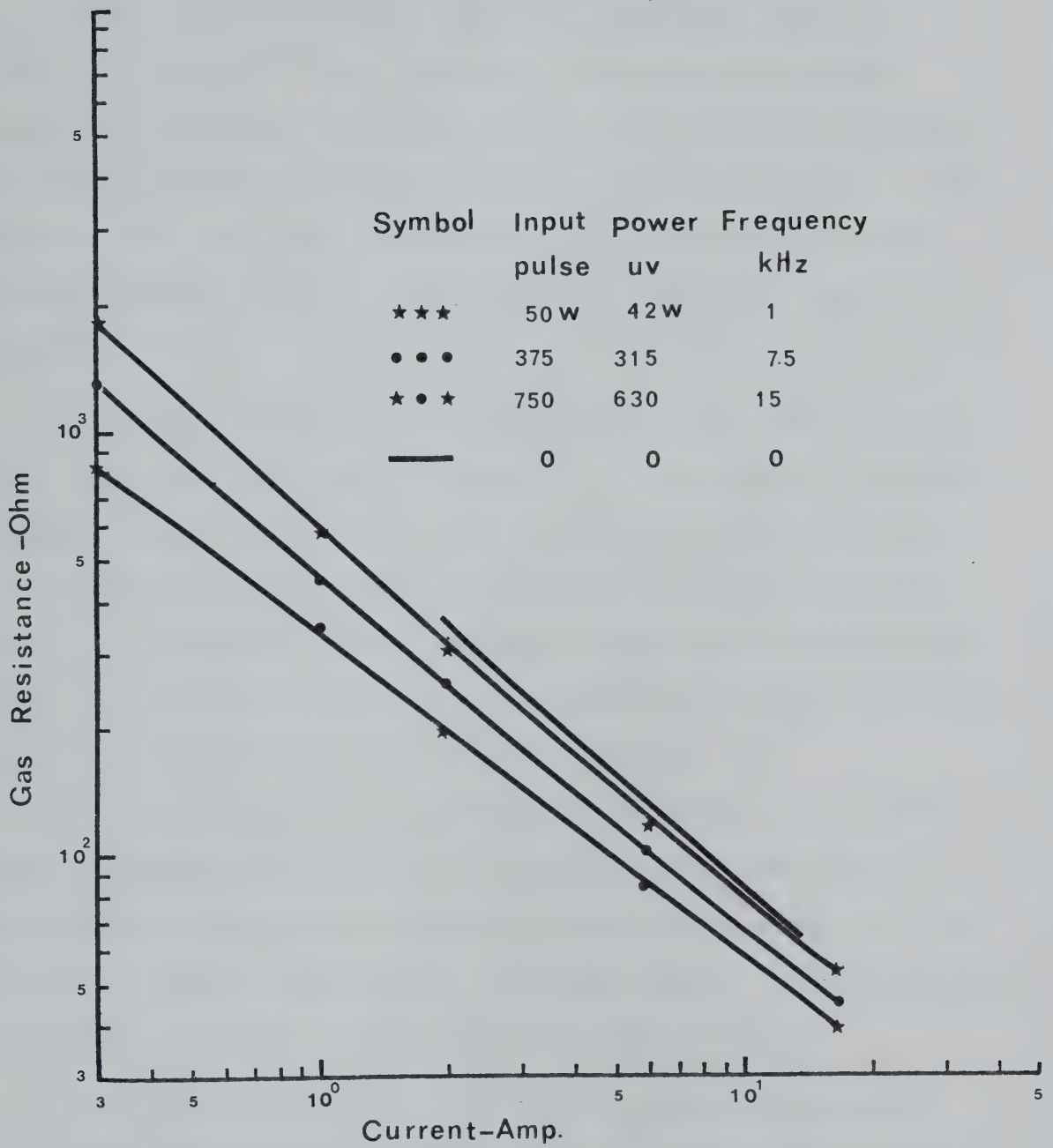


Figure 3-9 Total Gas Impedance vs. Total Current
 $\text{CO}_2:\text{N}_2:\text{He} = 1:1.2:13.2$ (torr),
 Flow - 30 m/s, Pulser - 10kV

3-1-5 Gain Measurements

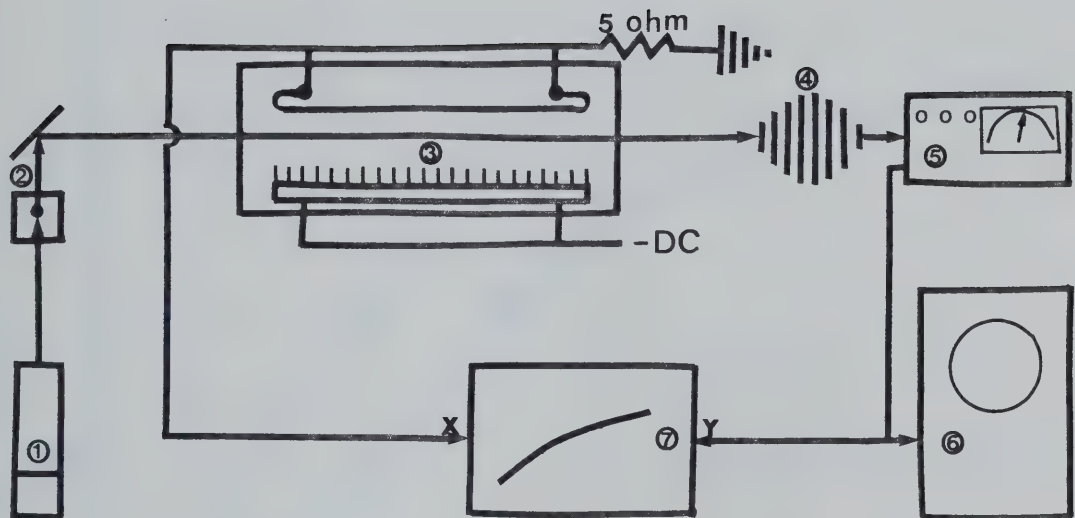
Except for the preliminary pulsed and "burst mode" data of Reilly⁽²³⁾ and Hill⁽²²⁾, the literature has provided little or no information on the gain characteristics of "pulser sustained" CO₂ lasers. This section therefore presents the results of gain measurements at lower pressure. The results of gain measurements for the second and third electrode configurations are given in Sections 3-3-3, and 3-4-2, respectively.

The gain was measured with the experimental setup shown in Figure 3-10. A low power CO₂ laser of less than 1.5 W was operated in the TEM fundamental mode. The spot size was 3 mm. This low power C.W. probe laser normally operated on the P(20) transition. The probe beam was directed by a two-mirror scanner and passed through the amplifying laser medium. The beam was detected with a thermopile and a Coherent Radiation power meter, both of which were placed in a shielding box.

Due to the electric noise generated by the pulser, measurements of parameters became quite difficult. As a solution to this problem, the shielding box was grounded to the common ground and the power meter was operated by a battery pack located in the meter casing. This arrangement reduced the noise level to less than a few percent of signal.

Error in gain measurements introduced by a possible probe laser level drift was eliminated by measuring the probe laser level before and after each reading. The averaged value of these two measurements was used in calculating the gain.

Figure 3-11 shows the single pass small signal gain coefficient measured at two different pressures and as a function of the input power density. The curve for the lower pressure discharge indicates a higher



- | | |
|------------------|--------------------|
| 1. probe Laser | 2. Scanning Mirror |
| 3. Active Medium | 4. Thermopile |
| 5. Detector | 6. Oscilloscope |
| 7. X-Y plotter | |

Figure 3-10 Equipment Layout for the Gain Measurements

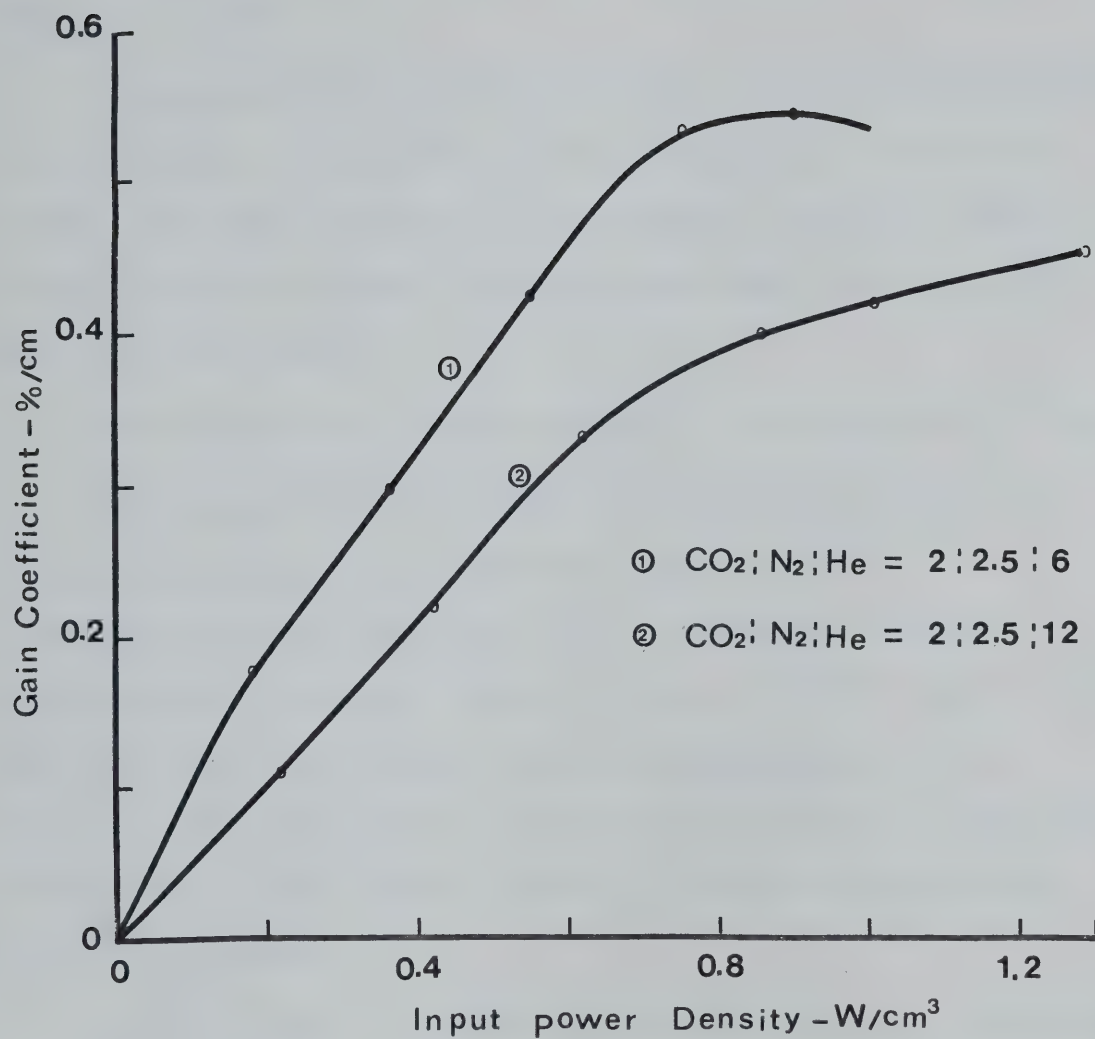


Figure 3-11 Gain Coefficient vs. Input Power Density
Pulser - 5kHz at 10kV
Flow - 30 m/sec

gain parameter than that obtained with the same input power density at higher pressure. This result generally agrees with the findings of References 35, 48 .

The figure also illustrates the tendency of earlier gain saturation at lower pressure. Since laser output is proportional to the product of small signal gain and saturation coefficients, the data of Figure 3-11 explains why the low pressure discharge yields higher gain yet produces lower laser output power.

3-1-6 Absorption of the Laser Energy by a Pulse Excited CO_2 Plasma

The phenomenon that a CO_2 plasma is cooled after absorption of a 10.6 μm laser pulse has been reported by Wood et al.⁽⁷¹⁾. The heating and cooling effects in CO_2 glow discharges perturbed by a 10.6 μm laser pulse have been reported by Aoki et al.⁽⁷³⁾. Gower et al.⁽⁷⁴⁾ have investigated laser induced current perturbations and used the results to obtain measurements of the V-T rates for the CO_2 lower (10^00) and upper (00^01) laser levels in various CO_2 10.6 μm amplifying and absorbing C.W. plasma.

A somewhat similar phenomenon was observed here in the pulse-ionized CO_2 plasma. A C.W. 10.6 μm probe laser beam was absorbed or amplified through the quasi-C.W. CO_2 plasma depending upon the operating pressure. Under no flow conditions this absorption usually occurred when the pressure was higher than ~ 4.0 torr. At lower pressures (< 4.0 torr) the CO_2 plasma amplified the probe beam. The degree of amplification or absorption depended upon the pulser input power. Figure 3-12 shows the single pass absorption as a function of the pulser input power.

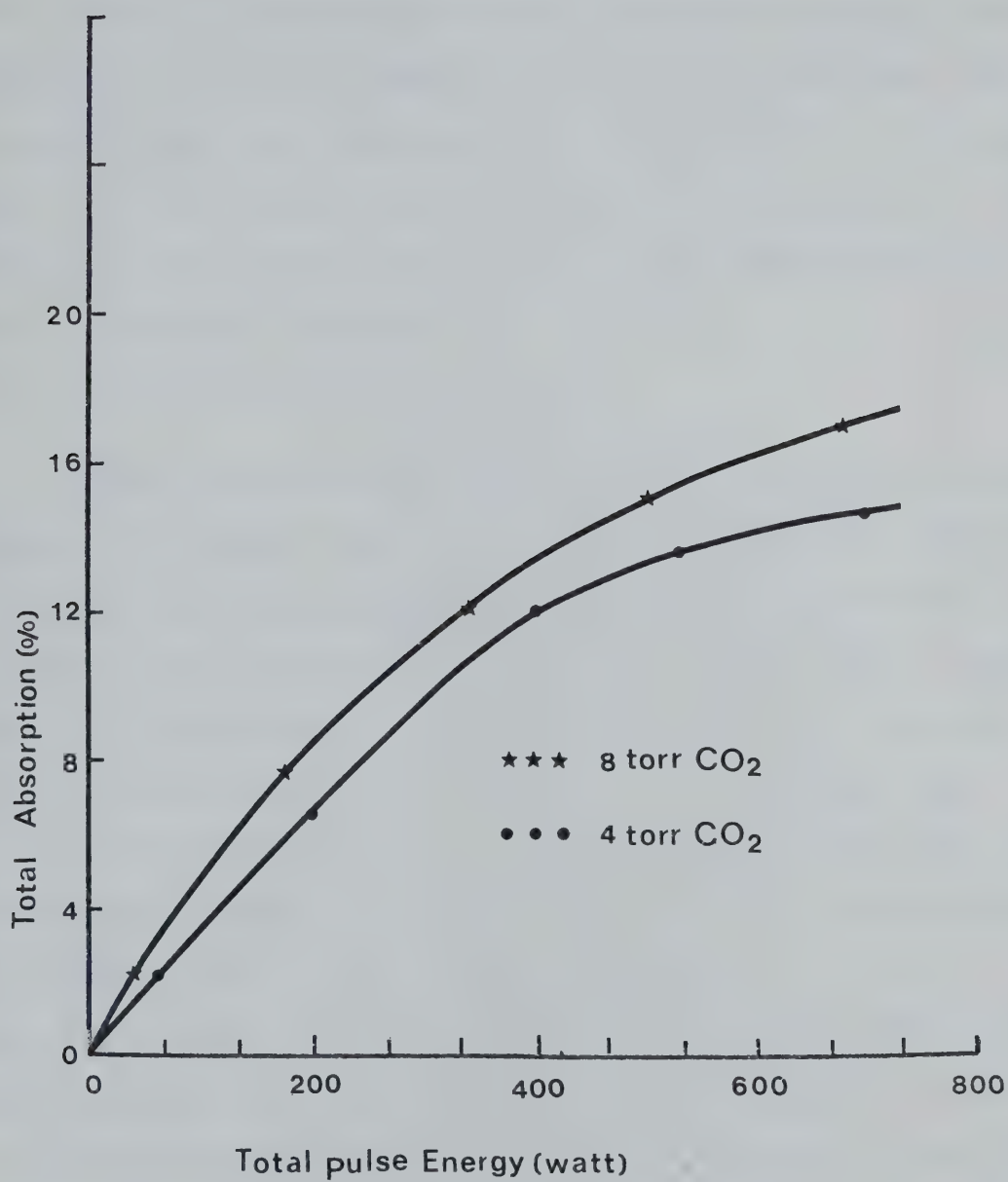


Figure 3-12 Total Laser Absorption vs. Pulse Power
No flow and no UV input

When the CO_2 gas was circulated at low speed, the absorption dropped to almost zero. The same result was achieved in static CO_2 by establishing a low current dc discharge in addition to the pulse discharge. The laser gas constituent, He or N_2 plasma did not absorb the probe beam. The absorption by the CO_2 plasma was reduced to zero when He or N_2 was added. These observations suggest that this absorption is primarily due to gas heating and the efficient excitation of the lower laser levels (10^00 , 02^00) by the pulsed discharge.

3-1-7 Output Power at Low Pressure

In this section the preionizing input power variation is directly related to the optical output power change. The preionizing input power was varied by changing the pulser repetition rate at a 10 kV fixed voltage. To obtain the V-I characteristic curve shown in Figure 3-13, the laser gas mixture was preionized with the pulses at 5 kHz and the sustainer voltage was increased gradually. At point 'a' the sustainer open circuit voltage was kept constant while the pulser repetition rate was varied gradually from 5 kHz to 1 kHz, from 1 kHz to 10 kHz and then from 10 kHz back to 5 kHz. This was repeated at points 'b', 'c' and 'd'. The result was plotted on an X-Y plotter. As shown in Figure 3-13 each V-I locus appeared as a straight line with an average slope of -0.047 A/V . At low pulser frequency the discharge voltage was higher and the current was lower than that at a high frequency. This observation was not unexpected.

The optical resonator, described in Section 2-3-2, was utilized for optical power extraction. The extracted beam from a 6.6% opening, hole-coupled mirror was partially focussed and detected by a Coherent Radiation Model 203 power meter. The detected signal and the sustainer

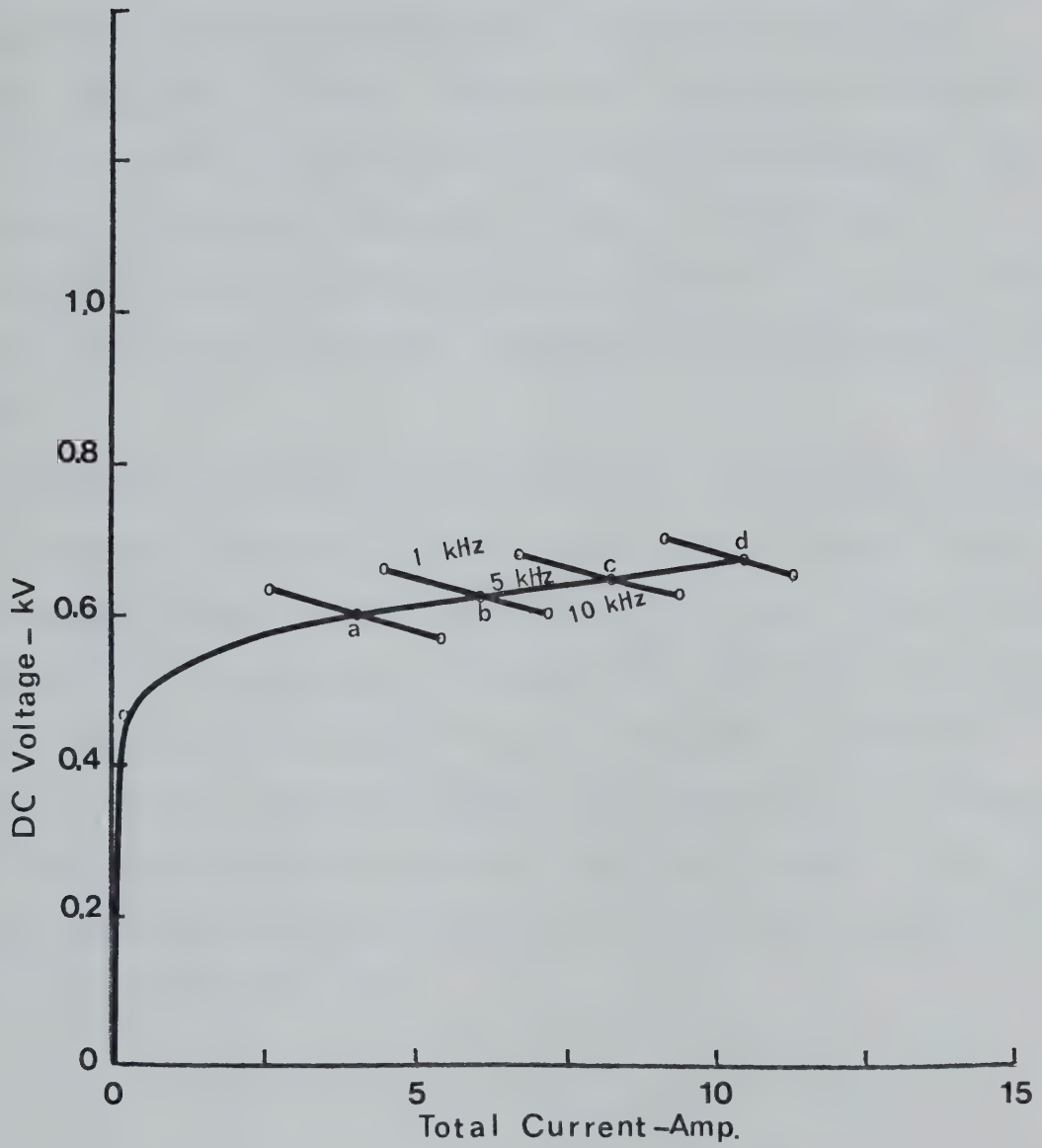


Figure 3-13 Variation of V-I Characteristic with
Preionizer Frequency
 $\text{CO}_2:\text{N}_2:\text{He} = 1.1:1.5:7.4$ (torr)
Pulser - 10kV x -
300pF pulse and 360 pF U.V. capacitors

voltage, V, were used to plot the V-P (power) characteristic curve on the second X-Y plotter. Thus obtained and presented curve, shown in Figure 3-14, can be directly related to the corresponding V-I curve in Figure 3-13. The optical output power increased with increasing pulser input power at low dc currents, but the opposite resulted at high dc currents. A satisfactory and detailed explanation for this phenomenon is presently unavailable. However, it may perhaps be a combined manifestation of an effective deactivation of the upper laser level ($00^{\circ}1$) by fast electrons, a decrease in E/N and gas heating by the pulser.

Maximum output power was achieved using a 2-pass optical resonator⁽³⁵⁾. This resonator consisted of a square plane mirror, a spherical folding mirror with a radius of curvature of 20.4 m, and a flat circular Ge output mirror with 6% transmission. The maximum input and output powers recorded at 25 torr ($\text{CO}_2:\text{N}_2:\text{He} = 2:2:20.8$) were 15 kW and 120 W respectively. Taking the optical volume efficiency of 13% (the ratio of the volume of the plasma occupied by the resonator to the total discharge volume), the power extraction efficiency was about 10.5%. This value is comparable to the result of Reference 35.

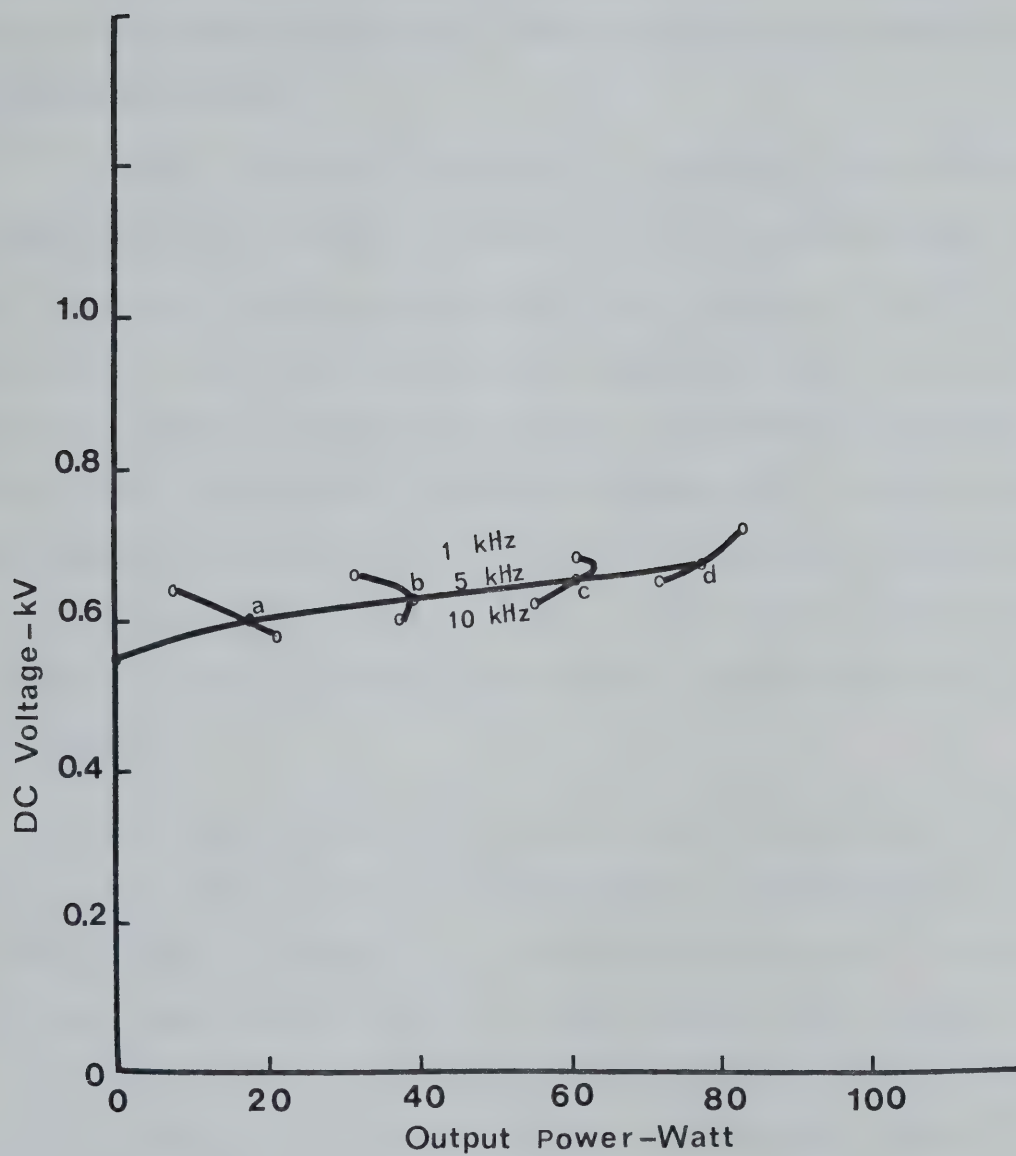


Figure 3-14 Voltage vs. Laser Output Power
 $\text{CO}_2:\text{N}_2:\text{He} = 1.1:1.5:7.4$ (torr),
Pulser - 10 kV

3-2 General Characteristics of Electrolytic Solution Ballasting

The solid cathode configuration initially used in the laser system provided satisfactory performance at low pressure (< 20 torr). However, as the operating pressure of the laser gas mixture was increased, several problems developed.

At higher pressure (> 20 torr) the preionizing pulse discharge tended to constrict easily. Accordingly the sustainer discharge operated in a critically stable state such that even a small perturbation resulted in an arc. Since there was no current limiting element in the sustainer circuit a stable glow discharge condition could never be restored. Furthermore, the sustainer and pulse discharges were so closely coupled that an arc in the discharge was followed by continuous conduction of the pulser switch (thyatron). Hence, an electrolytic solution ballasted multipin cathode was designed in an attempt to achieve an even discharge distribution.

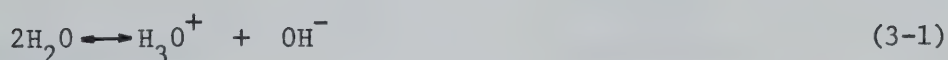
The concept of electrode pin ballasting with electrolytic solution has not been widely adopted in laser technology mainly because of such complications as excessive pin corrosion in the water, and the necessity for water tight seals. However, for this project, most of these problems have been solved and an electrolytic solution ballasted electrode design has been developed that appears suitable for industrial application.

In order to provide design information for solution ballasted electrodes, the following several sections are devoted to evaluation of material performance in the solution as well as the gas discharge.

3-2-1 Tap Water as a Ballasting Fluid

The most economical ballasting fluid is tap water. In this section

the use of tap water as a ballasting fluid and coolant for the laser cathode was investigated. As shown in Table 3-2 the City of Edmonton tap water is a dilute aqueous solution of various chemicals. At a low current density the cations and the anions from the chemicals in tap water carry the current. As the voltage across the water gap spacing increases (in this project, < 160 - 180 V) to raise the operating current, the water dissociates into H_3O^+ and OH^- .



Now the hydroxyl ions are attracted toward the anode and react with water molecules producing neutral oxygen gas molecules. It should be noted that in the water ballasted pin cathode, the pins act as anodes in the water. If the pin material is reactive in the oxygen environment, the pins will be oxidized and corrosion will occur. When materials such as brass, copper and copper alloys were used as anode materials, a greenish blue oxide film appeared on the anode tips, decreasing the current. This film continuously grew thicker and from time to time a part of the film was carried away by the flowing water.

With a similar process, hydrogen gas evolves in the vicinity of the cathode. The cathode also collected a jelly type compound which was presumed to be a collection of Mg, Na, Ca etc. These film deposits on the anode and cathode gradually decreased the current density when the operating voltage was kept constant. In addition, the gases generated by the electrolysis action were trapped around the electrodes (pins and buss bar) and decreased the electrode surface area (A_w), in contact with the water. This in turn decreased the current. The current in the water,

Table 3-2

THE CITY OF EDMONTON
ANALYSIS OF TREATED TAP WATER

	Summer Months May to Sept. Inclusive	Winter Months Oct. to April Inclusive
Calcium Bicarbonate $\text{Ca H}_2 \text{CO}_3$	38 p.p.m.	36 p.p.m.
Calcium Sulphate Ca SO_4	20 p.p.m.	12 p.p.m.
Magnesium Sulphate Mg SO_4	23 p.p.m.	33 p.p.m.
Magnesium Bicarbonate $\text{MgH}_4 \text{CO}_3$	0 p.p.m.	2 p.p.m.
Sodium Sulphate $\text{Na}_2 \text{SO}_4$	17 p.p.m.	47 p.p.m.
Sodium Chloride NaCl	5 p.p.m.	5 p.p.m.
Organic Matter	9 p.p.m.	13 p.p.m.
	<u>112 p.p.m.</u>	<u>148 p.p.m.</u>
Calcium Ca^{++}	20.16 p.p.m.	18.09 p.p.m.
Magnesium Mg^{++}	4.59 p.p.m.	7.07 p.p.m.
Sodium Na^+	7.49 p.p.m.	17.08 p.p.m.
Total Hardness	71.0 p.p.m.	77.0 p.p.m.
pH Value	9.1 p.p.m.	9.1 p.p.m.

I_w , is expressed by Ohm's law⁽⁸⁴⁾:

$$I_w = \frac{E_t - E_d}{R} = \frac{A_w \sigma_w}{d_w} V_w \quad (3-2)$$

where E_t is the terminal voltage between the electrodes (Volt) E_d is the decomposition (electrochemical) potential of the electrolytic solution (Volt), R is the total resistance (ohm) which is expressed by $R = \frac{d_w}{A_w \sigma_w}$, σ_w is the conductivity of the water, d_w is the mean water gap spacing, and V_w is the effective potential in volts ($=E_t - E_d$). Equation (3-2) indicates that the current can be controlled by the water contacting surface area. This fact takes on a very important role in suppressing arcs and will be discussed further later in this chapter.

The water temperature gradient, existing between upstream and downstream of the water flow, results in a lower ballasting resistance for the pins on the water downstream. Consequently the downstream pins easily initiate an instability. This problem can be solved by increasing the water flow.

3-2-2 Temperature Dependence of Water Resistance

In order to investigate the relationship between the water temperature and its resistance, tests have been made using the setup shown in Figure 3-15. In the device the water gap spacing, d_w , can be adjusted, and the water temperature is varied by changing the hot and cold water mixing ratio.

The test results are plotted in Figure 3-16 for stainless pins. The water resistance increases linearly with increasing gap spacing and decreases with increasing water temperature. The latter is attributed

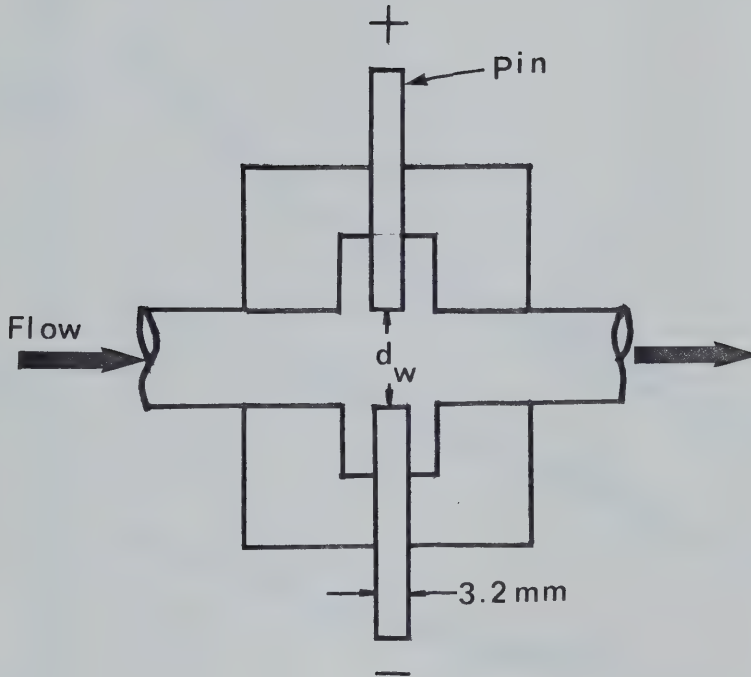


Figure 3-15 Water Discharge Test Device

to the fact that the dissolved salts dissociate more easily at higher temperature, increasing the density of charge carriers.

3-2-3 The Discharge Characteristics of Various Pin Materials in the Gas Discharge

The materials chosen for this experiment are those which can be easily, and economically obtained. The five different materials that have been tested are copper, brazing brass, aluminum, tungsten, and 304-stainless steel rods 3.2 mm in diameter. To evaluate the pin materials

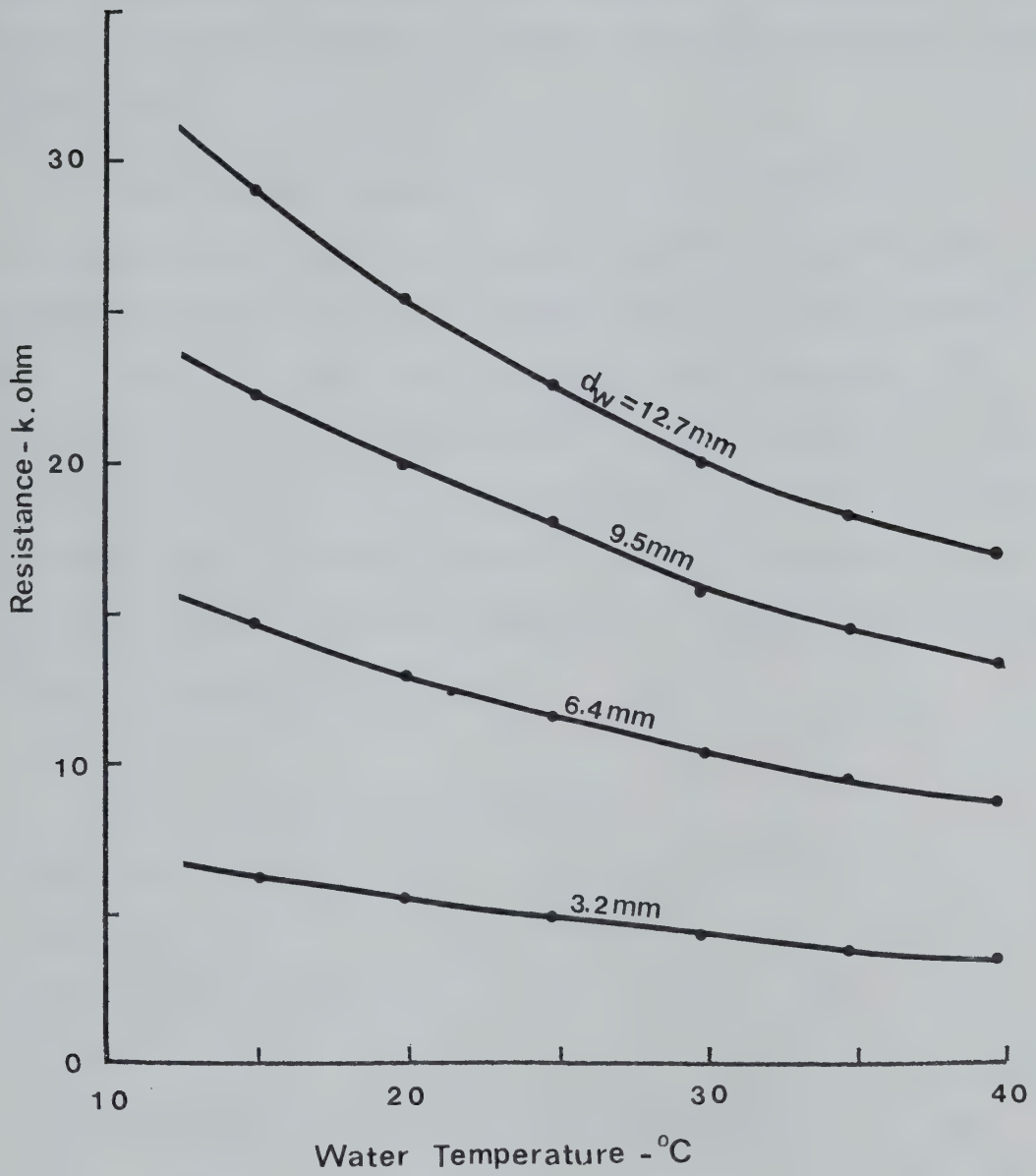


Figure 3-16 Resistance Change with Water Temperature

under actual laser operating conditions, the pins were installed in the electrode described in Section 2-1-9 of Chapter 2. Three pins of each material were arranged in such a way that each material could be tested simultaneously.

The glow discharge characteristics and the sputtering rate of the pins were of primary concern in the gas discharge. Since the glow discharge is directly related to the work function of the materials, a brief review of work function is made in the following. For quick reference, the work function data from the literature⁽⁴²⁾, has been reproduced in Table 3-3. The work function of a metal represents the minimum amount of energy that must be given to the fastest moving electron at the absolute zero of temperature in order for this electron to be able to escape from the metal.

Table 3-3 Work Functions

Material	Al	Cu	Fe	Sn	Zn	W
Thermionic, ϕ_o	-	4.38	4.77	-	-	4.46
Photoelectric, ϕ	3.57	4.3	4.5	4.38	3.5	4.66

The thermionic work function, ϕ_o is expressed by:

$$\phi_o = \frac{b_o k}{e} \text{ (Volt)} \quad (3-3)$$

where b_o is the constant of the emitting surface, k is the Boltzmann's constant, and e is the electron charge.

The photoelectric work function, ϕ is expressed by:

$$\phi = \frac{h\nu_o}{e} = \frac{12336}{\lambda_o} \quad (\text{Volt}) \quad (3-4)$$

Where ν_o is the threshold frequency, h is the Planck's constant, and λ_o is the threshold wavelength in Angstroms. The photoelectric work function is more important for a cold cathode discharge.

At low pressure, aluminum, with the smallest work function, started to glow at the lowest sustainer voltage. As the voltage was increased, the glow which appeared on each pin was almost the same, regardless of the pin material. The tungsten pins which have the largest work function were an exception however. They did not exhibit any observable glow.

The characteristics of the glow at higher pressure, (80 torr) ($\text{CO}_2 : \text{N}_2 : \text{He} - 10 : 10 : 60$) proved to be somewhat dependent on the pin material. Copper and brass pins supported glows which were similar in appearance. A weak glow covered the tip of the pins and extended downward on the downstream side of each pin. When observed along the optical axis, the glow appeared in the shape of an inverted right triangle. Aluminum pins yielded the most intense glow which however covered the smallest area on the downstream side of the tip. The glow on stainless steel entirely covered the tip of the pins. The glow was thicker than that on the other pins. Tungsten pins did not produce any glow at higher pressure, as was also the case in the lower pressure region.

After an hour of operation, the system was opened for examination. The copper and brass surfaces were clean due to sputtering action. Ring shaped deposits around the pins on the ceramic insulating plate indicated that copper pins were more susceptible to sputtering than brass. The

relative sputtering rates reproduced in Table 3-4 are consistent with the above observations.

Table 3-4 Relative Sputtering Rate in H_2 ⁽⁴²⁾

Al	W	Fe	Sn	Cu	Zn
8	18	19	55	84	95

However, because of concentrated glow activity on the aluminum pin the sputtering was also localized. Consequently, except for the glow spot the pin was covered with a very hard and black film deposit. An insulating characteristic of this film deposit prevented a glow from appearing through the film even at low pressure. The stainless steel pin was covered with a thin, dark brown film which, however, did not impede a glow discharge. Since tungsten pins produced no glow activity, the surface was unaffected.

Consequently, aluminum and tungsten were disqualified as high power laser cathode materials. This evaluation was made on the basis of performance in the gas discharge.

3-2-4 The Performance of Various Pin Materials in Tap Water

The previous section already disqualified tungsten and aluminum as cathode materials. However, the performance in water of these materials was still of interest. Therefore, they were included in the evaluation. Every material tested suffered corrosion in a tap water discharge, but to a different degree. Copper pins were affected most, and marginally more than the brass pins. Both copper and brass pins were covered with a reddish powder which was easily removed by the flowing water.

The part of the aluminum pin that had been in tap water was covered with a very hard, dark-grey, and porous deposit. The deposit was non-conductive and could not easily be removed by abrasion. Consequently, the current path must have been through pores. The tungsten pin was not noticeably corroded but was covered with a greenish-yellow deposit which was assumed to be a by-product liberated from the copper and brass pins. There was no deposit or oxide film on the surface of the stainless steel pin. Instead the surface was polished by an electrolytic polishing action. At a high current density, about 100 mA/pin or up, the polishing action was so pronounced that the surface appeared mirror-like.

On the basis of the above and the previous section, only stainless steel was considered as a suitable material for use in a water ballasted cathode. The quantitative and comparative performance tests in various solutions, reported in the following section, revealed that stainless steel pins behave well both in water and aqueous solutions as well as in the gas discharge.

The analysis of the compositions of the 304 stainless steel is provided in Table 3-5 for reference.

Table 3-5 Composition of 304 Stainless Steel

C	0.08%	Si	1.2%	Cu	0.5%
Mn	2.0	Cr	20.0	Mo	0.5
P	0.045	Ni	10.5	Fe	65.15
S	0.03				

3-2-5 The Use of Electrolytic Aqueous Solutions for Ballasting

Despite the satisfactory performance of tap water for ballasting and cooling, the possibility of using other solutions was studied. Utilization of a proper solution protects the pins from corrosion and results in convenient control of the resistivity by varying the concentration of the solution. Distilled water has been used throughout the test as the solvent and several solutes have been tested. The test structure was the same as described in Figure 3-15.

The first solute chosen was cupric sulfate (CuSO_4) which has been used successfully for making liquid resistors. The passage of the D.C. current through the solution resulted in the generation of excessive gases. These gases were trapped in numerous bubbles and the bubbles accumulated continuously. Gas production was accelerated when copper, brass or any copper alloy was used as electrodes. Similar results were obtained with a solution of cleaning ammonia (ammonium-hydroxide). An additional disadvantage of ammonia was an objectionable odor.

A test with an aqueous solution of Preston antifreeze, known to be a corrosion inhibitor and good electrical conductor, showed a unique behavior. A black film deposited on the anode pin surface and grew so thick that eventually arcs developed in the water gap. This indicated that the discharge took place by puncturing through the film deposit.

An aqueous solution of potassium carbonate crystal ($\text{K}_2\text{CO}_3 \cdot \frac{1}{2}\text{H}_2\text{O}$ - simply referred to as, potassium carbonate, in this thesis), has been tested with great success. It does not generate too much gas, the bubbles do not accumulate, and there is no objectionable odor. Moreover it provides the stainless steel pins with a thin, brown passive film

which slows down the corrosion rate under normal operating conditions. Potassium carbonate can be handled safely with minimum care. As will be shown in the following section, the concentration of potassium carbonate in the solution is so small that it can be used in laser systems with little hazard. Potassium dichromate ($K_2Cr_2O_7$) was also tested for its ability as a corrosion inhibitor. However, dark brown spots developed on the stainless steel pins instead of a uniform protective film. So further use of potassium dichromate was not made.

Since the potassium carbonate solution and the stainless steel pins complemented each other well, a further analysis was made to evaluate their performance in the laser system.

3-2-6 Stainless Steel Pin Performance in Potassium Carbonate

($K_2CO_3 \cdot \frac{1}{2}H_2O$) Solution

Further studies of the performance of stainless steel pin electrodes in potassium carbonate solutions were undertaken to quantitatively determine the corrosion rate so as to provide data for predicting the operating lifetime of the pins. To evaluate the absolute and relative corrosion rate of stainless steel, several materials listed in Table 3-6 were tested at the same time.

One pin of each of the materials was placed in a solution 1.3 centimeters away from a common stainless steel cathode. The solution consisted of 2 cc potassium carbonate dissolved in 3000 cc distilled water. The ends of pins not in the solution were connected together and joined to an adjustable 0-300 V dc power supply. Because the corrosion rate depends more on the current than on voltage, the total current was kept at 3 amperes. To maintain this current, the voltage had to be decreased

in the course of the experiment to counteract the decrease in impedance due to a temperature increase in the solution. The fraction of the total current passing through a particular pin varied during the experiment because of the different degree of surface passivation (surface becomes inactive because of the deposit). The experimental results, tabulated in Table 3-6, and plotted in Figure 3-17, show that the relative weight loss rate (weight loss/current) of stainless steel is about an order of magnitude smaller than that of other materials. Nickel (welding rod) and monel pins corroded somewhat faster even though they developed relatively thick films. These two materials developed numerous pits in the passive film, which may have accelerated the corrosion rate. The tungsten pins carried a much lower current due to its high work function which resulted in an effective resistance of $2k\Omega$ at 75V.

The weight loss rate of brass was reduced by an excessive passivation of the surface, as shown in Figure 3-18. The excessive passivation that reduces the operating current is not a desirable feature in cathode pin performance, as it will upset the ballasting resistance, eventually causing degradation of the gas discharge. Copper developed the thickest passive film. This film however came off easily. The estimated film resistance was about 200 ohms. The film that developed on the brass pin was thin but very tough and very resistive, about 800 ohms.

Figure 3-19 shows the V-I characteristics for the tungsten and the stainless steel pins. It is interesting to find that at 50 mA discharge current the tungsten pin yielded a $2.4k\Omega$ effective resistance while that of the stainless steel pins was only 360Ω . This is perhaps the main reason why the tungsten pins did not support a glow discharge when used

Table 3-6 Comparison of the Corrosion Rate Exhibited
by Different Materials

Material Description	Copper	Brass	Nickel	Monel	Tungsten	Stainless Steel
Weight						
loss (mg)	107	72	148	143	50	39
<u>Current</u>						
final (mA)	320	90	550	660	4	1550
<u>Weight/current</u>						
mg/mA	0.3	0.80	0.27	0.22	12.5	0.025
<u>Film deposit</u>						
Color	Black	Black	Black	Black	Gray	Brown
Thickness	Thick	Thick	Thin	Thick	Thin	Thin
Hardness	Medium	Hard	Hard	Hard	Hard	Hard

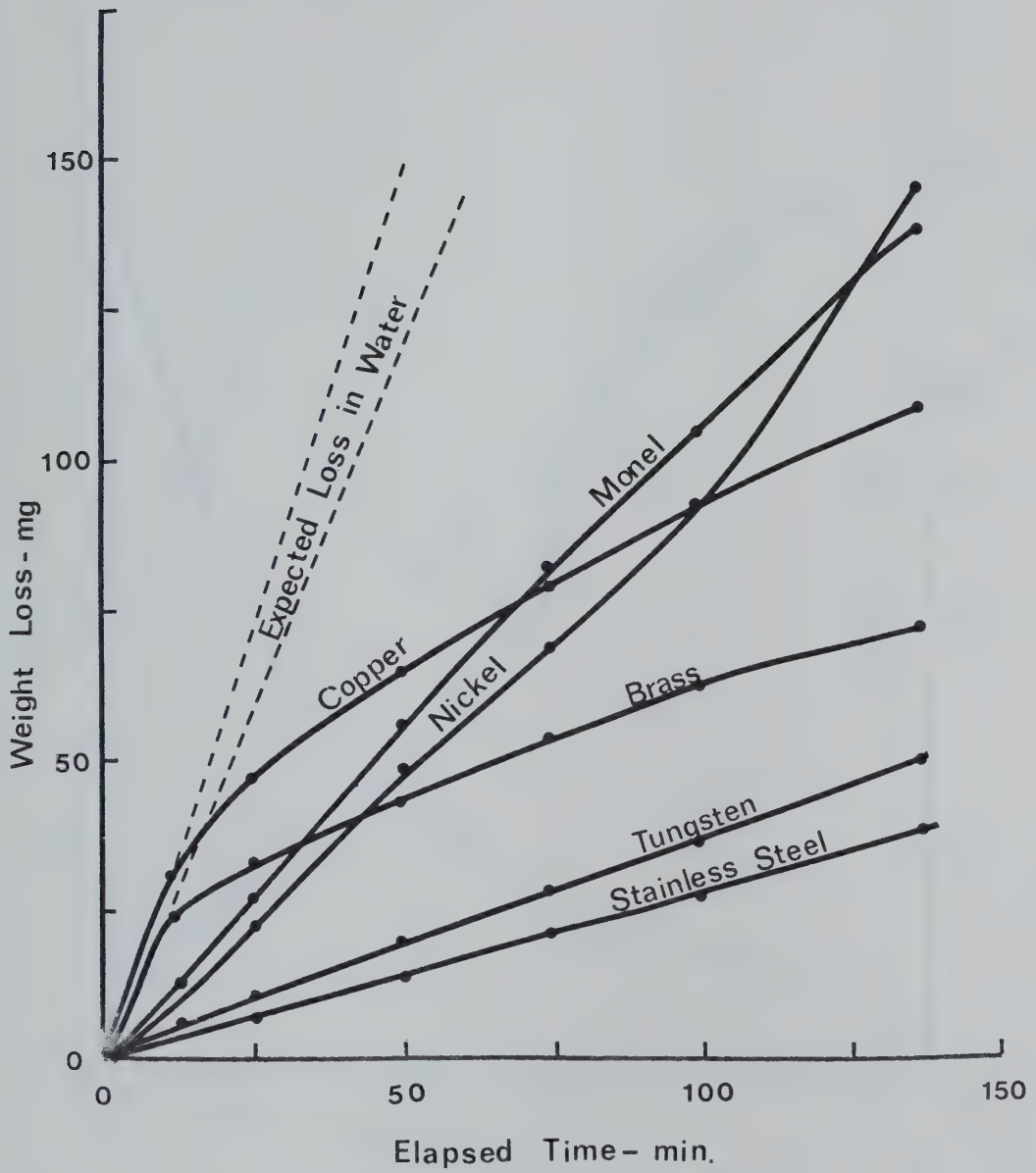


Figure 3-17 Corrosion Rates of Different Metals in Potassium Carbonate Solution
 Electrolyte concentration - 0.7 gm/l
 Gap - 1.3cm,
 Dc Voltage - 75V

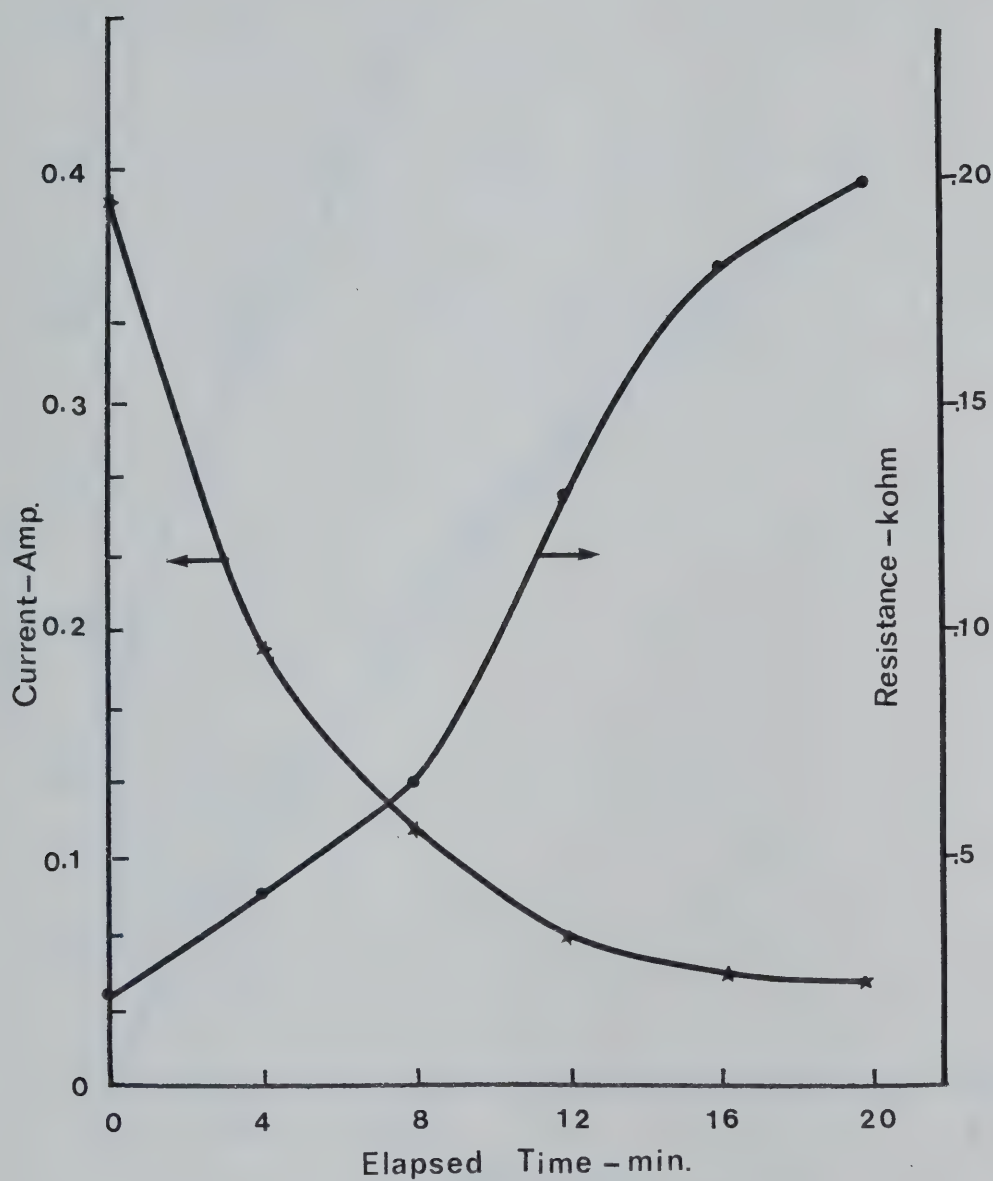


Figure 3-18 Brass Pin Passivation Rate
Electrolyte concentration - 0.7 gm/l
Gap - 13 cm
Dc Voltage - 75V

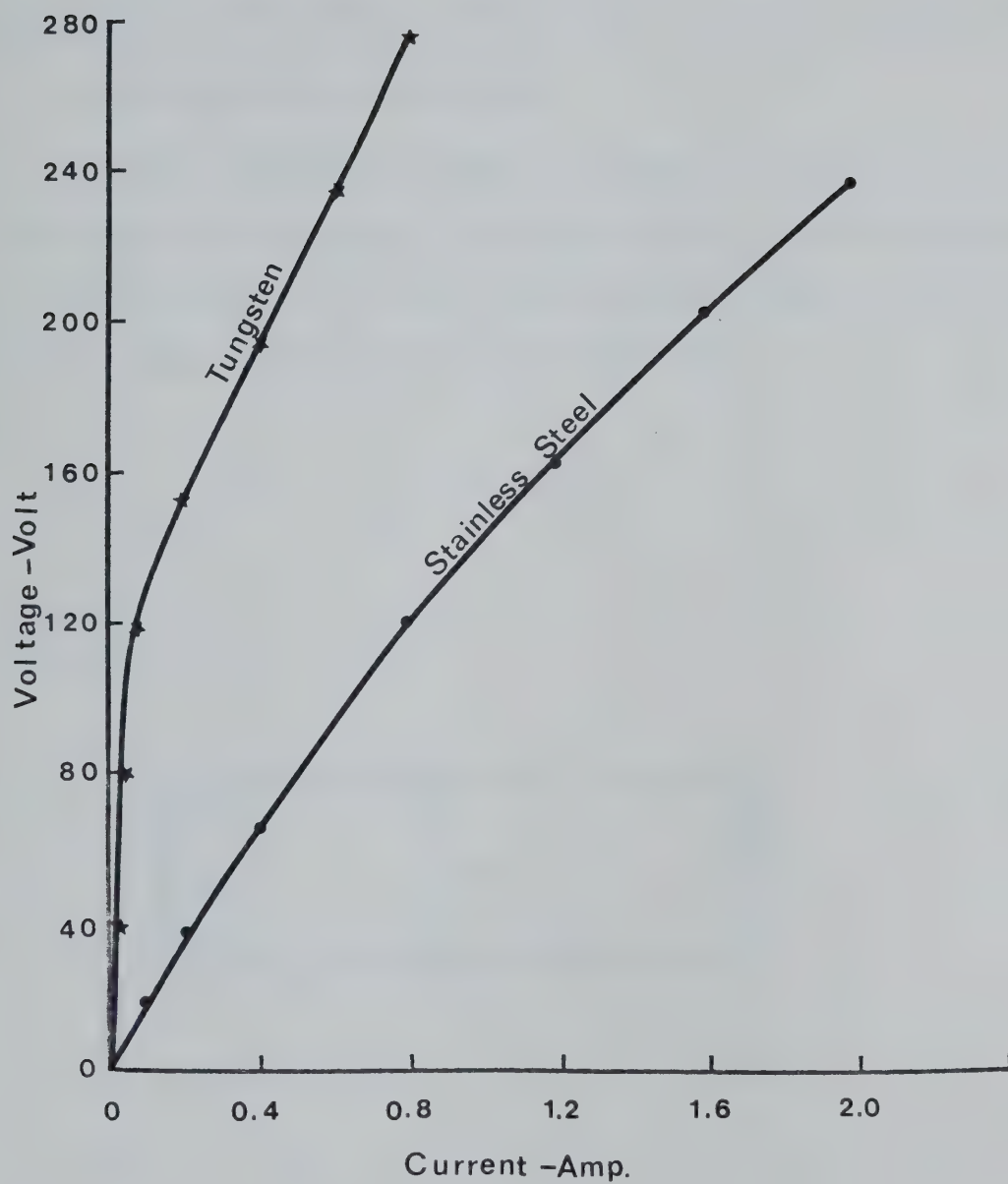


Figure 3-19 V-I Characteristic in Potassium Carbonate Solution
Electrolyte concentration - 0.7 gm/l
Gap - 1.3 cm

in the actual electrode described in Section 3-2-1.

These tests quantitatively confirmed that stainless steel pins in a potassium carbonate solution were the best choice for the laser cathode.

3-2-7 Estimation of Pin Lifetime

A further evaluation was made to estimate the working lifetime of a stainless steel pin cathode. It is assumed that a 3.2 mm diameter pin with flat ends is to be used. The pin length will not be affected until the edge rounds off as shown in Figure 3-20.

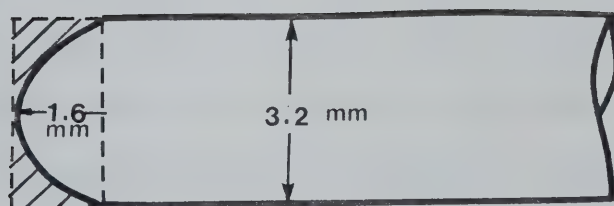


Figure 3-20 Edge Round-off

This is because the sharp edge produces an enhanced electric field and consequently the corrosion rate is greater at this edge. Eventually the edge rounds off.

Figure 3-21 shows the relationship between the weight loss (mg) and the operating time (hr.) at a current density of 120 mA/pin. This value is approximately three times larger than the maximum current density under normal operation of the laser system under consideration. According to the experimental results obtained with the electrode described in Section 2-1-19, the electrode can be operated until the pin becomes shortened by ~ 6 mm. The working lifetime of a pin, calculated on the basis of the above information and Figure 3-21, is approximately 1100 hours. This lifetime can be extended by using larger pins and/or lowering the current density per pin.

Figure 3-22 is a plot of the relationship between the operating time and the reduction in the pin length, measured at a current density of 120 mA/pin. There is no loss in the pin length for up to 33 hours of operation as a result of the rounding off process.

3-2-8 Concentration of Potassium Carbonate and Resistances of the Solution

Studies were made to provide design criteria for solution ballasted electrodes by using the test device illustrated in Figure 3-15. It was arranged so that approximately 6 mm of both the cathode and anode were immersed in the solution. The resulting resistance can be directly related to the water gap spacing.

Various concentrations of the solution were tested for resistivity changes with 6.4 mm gap spacing and the results are illustrated in Figures

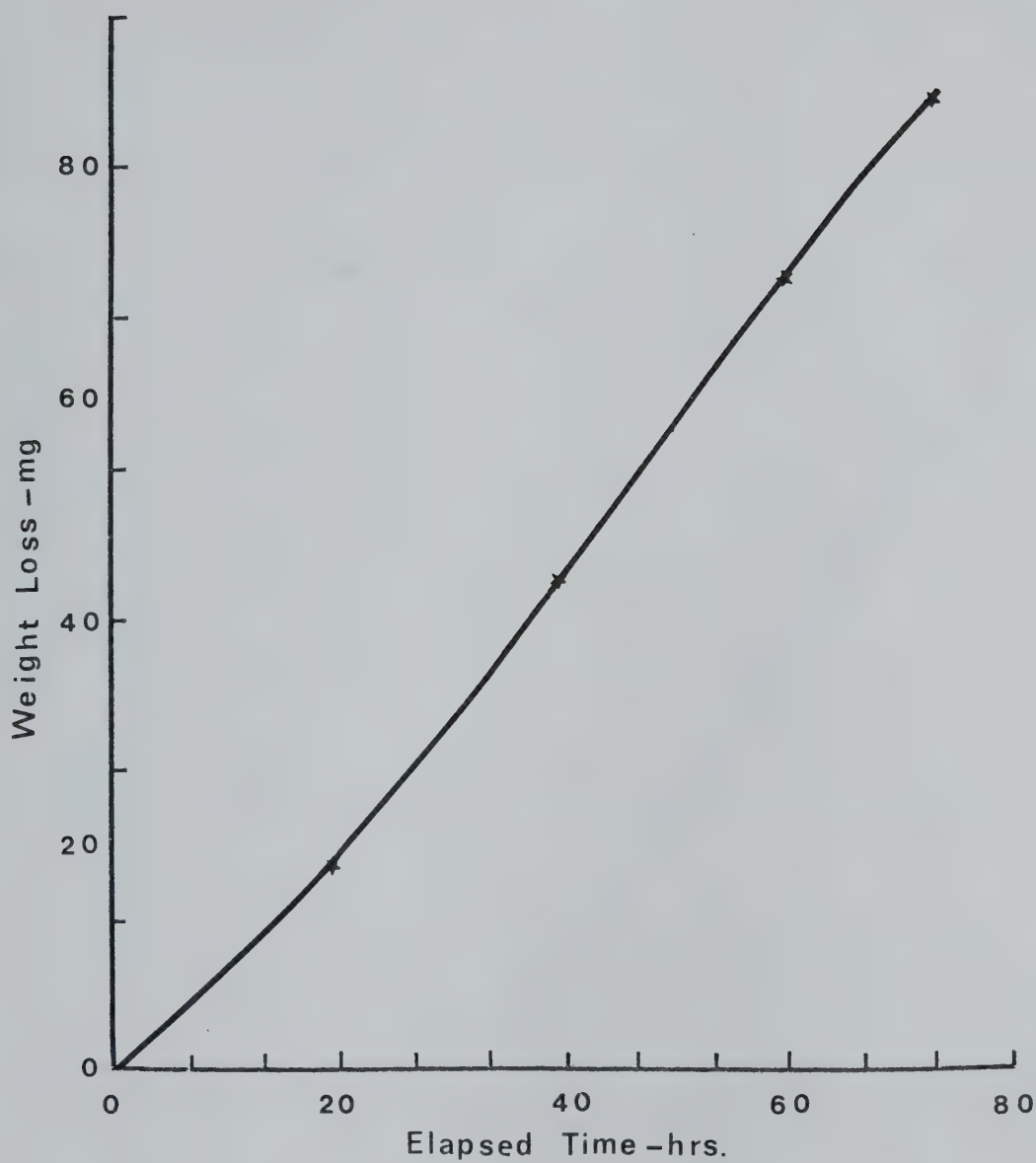


Figure 3-21 Corrosion Rate of 304 Stainless Steel Pin
Electrolyte concentration - 0.83 gm/l
Gap - 1.3 cm
Dc - 100 V and 120 mA

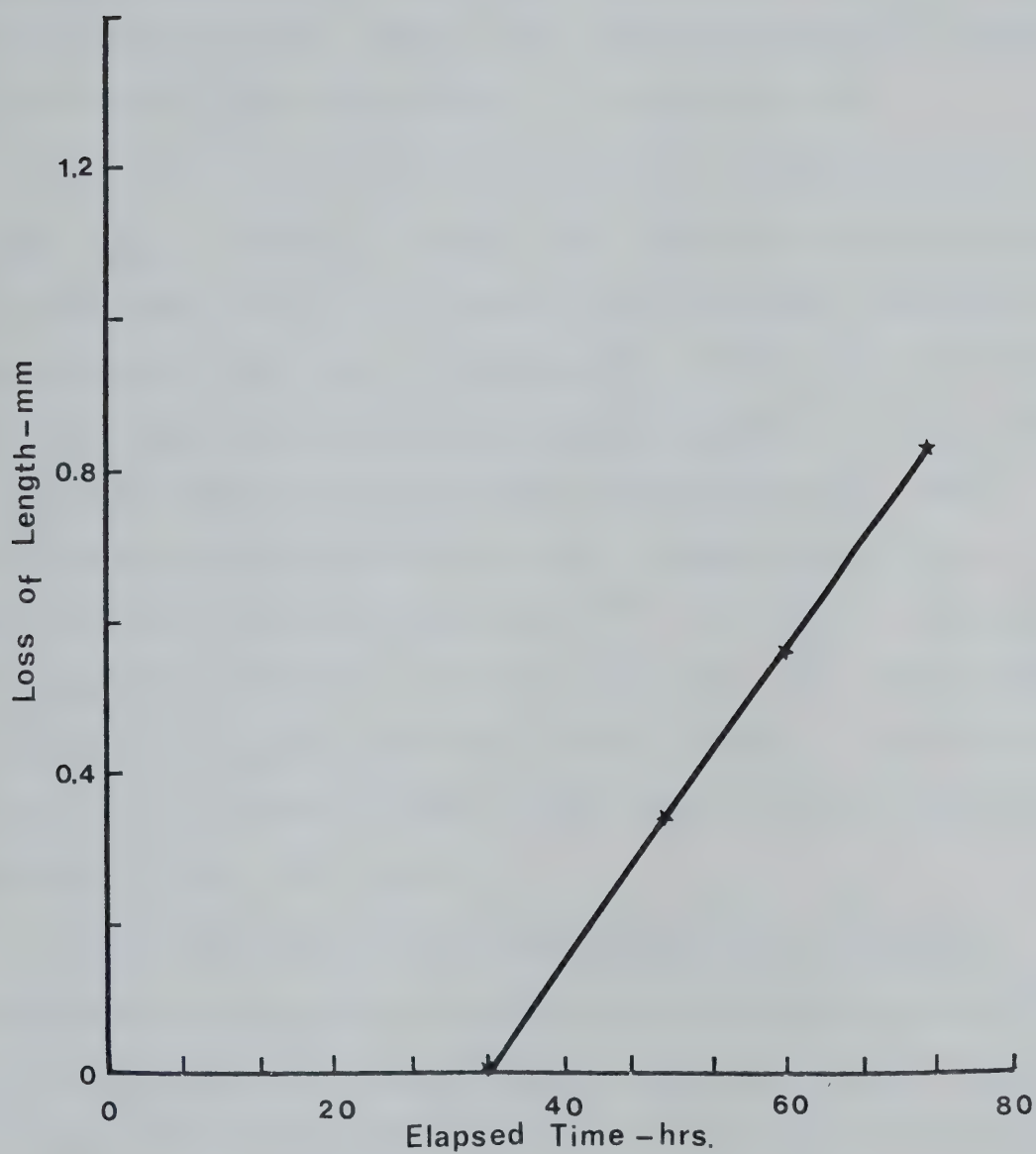


Figure 3-22 Pin Length Loss vs. Operating Time
Electrolyte concentration - 0.83 gm/l
Gap - 1.3 cm
Dc - 100V and 120 mA

3-23 and 3-24. These results reveal a number of features. For a fixed gap spacing the resistance is inversely proportional to the concentration of potassium carbonate. However, this inverse proportionality deviates at very low and high concentrations of potassium carbonate.

Also, for low concentration the resistance decreases somewhat over a wide range of increasing voltage. This effect may be partially caused by various impurities having different dissociation and ionization potentials. Such impurities could play an important role in the current carrying activity. The effect of impurities would be expected to be more pronounced at low concentrations of potassium carbonate where the ratio of impurity to potassium carbonate is high. A common impurity found in distilled water is carbonic acid, H_2CO_3 ⁽⁸²⁾. This acid is formed when CO_2 from the air dissolves in the distilled water. The solution heating effect may be partially responsible for the deviation. The heating effect is higher in a low concentration solution because much more power is dissipated within the solution.

Figure 3-25 shows the resistance presented by an individual subelectrode as a function of the fluid gap spacing. The data were taken at 200 Volts on a 3 mm diameter stainless steel pin immersed 6 mm into varying concentrations of K_2CO_3 solution. It is clear from these data that a wide range of elemental resistance is obtainable in this manner. In actual cathode fabrication, it is expedient to design for a constant channel size with a uniformly increasing fluid gap and decreasing pin immersion length in the direction of gas flow. This arrangement provides better current distribution over the electrode surface and thus results in a more uniform gain profile.

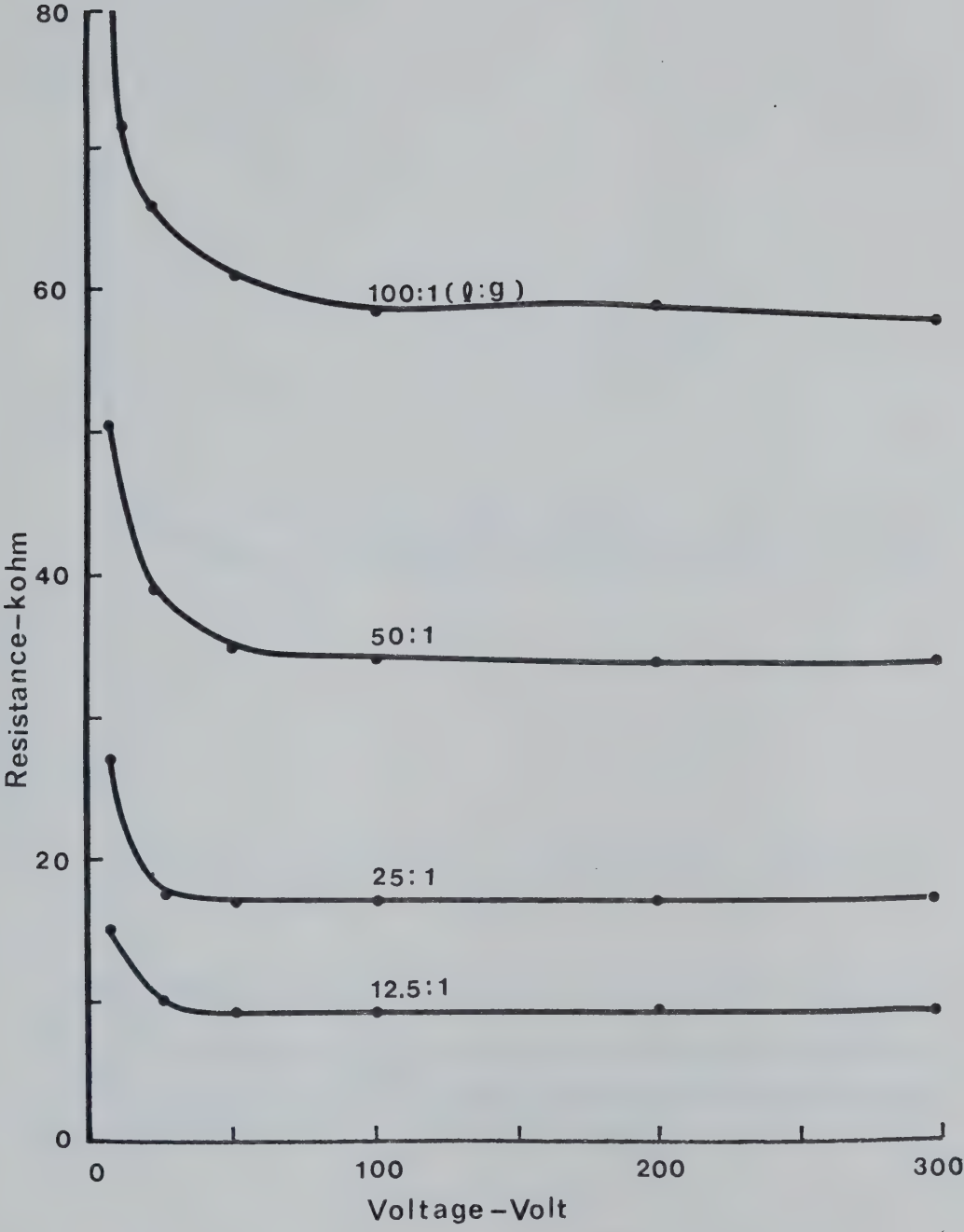


Figure 3-23 Electrolytic Solution Resistance vs.
Operating Voltage at Low Concentration
Gap - 6.3 mm, pin protrusions - 6.3 mm

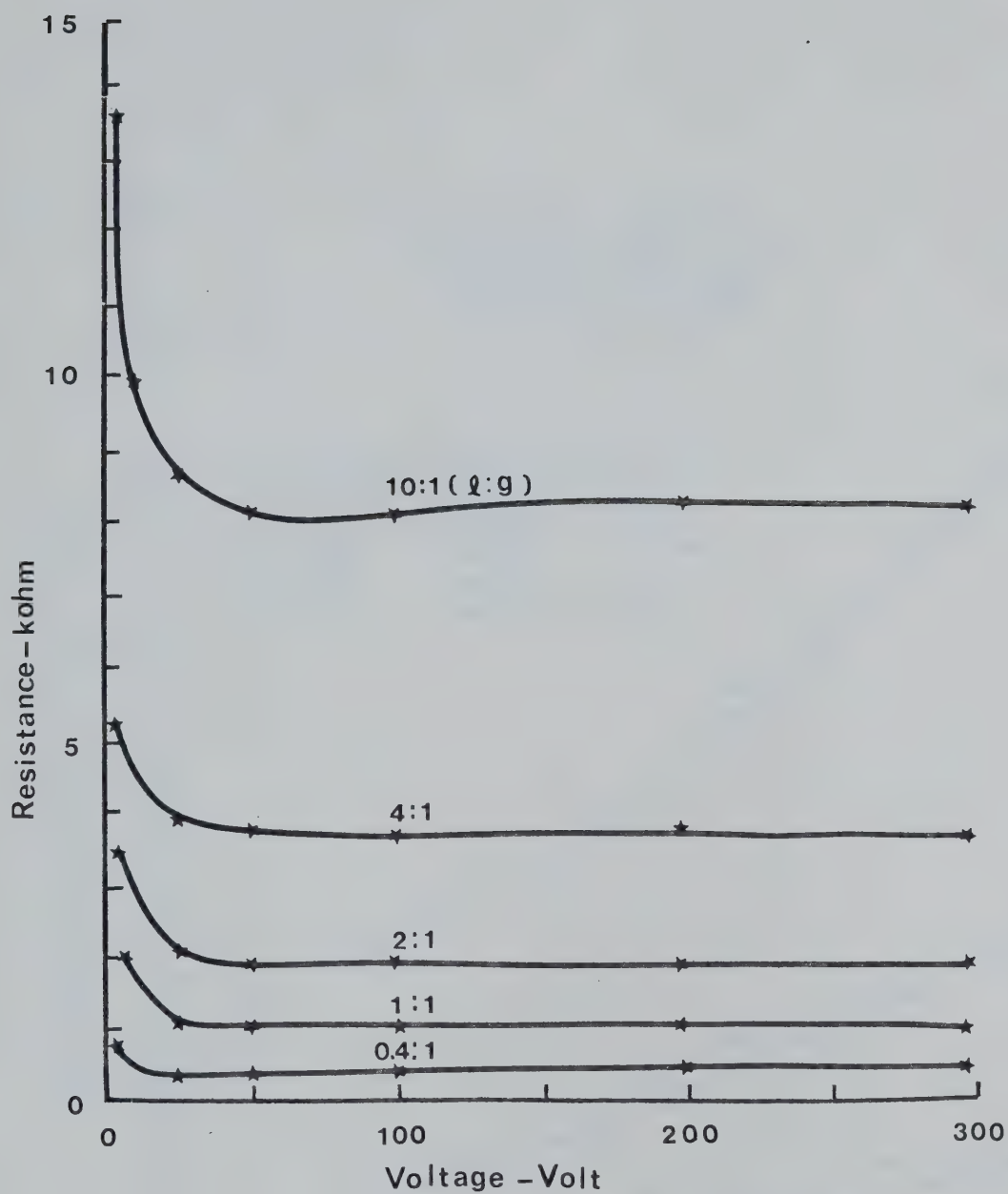


Figure 3-24 Electrolytic Solution Resistance vs. Operating Voltage at High Concentration
Gap - 6.3 mm, pin protrusions - 6.3 mm

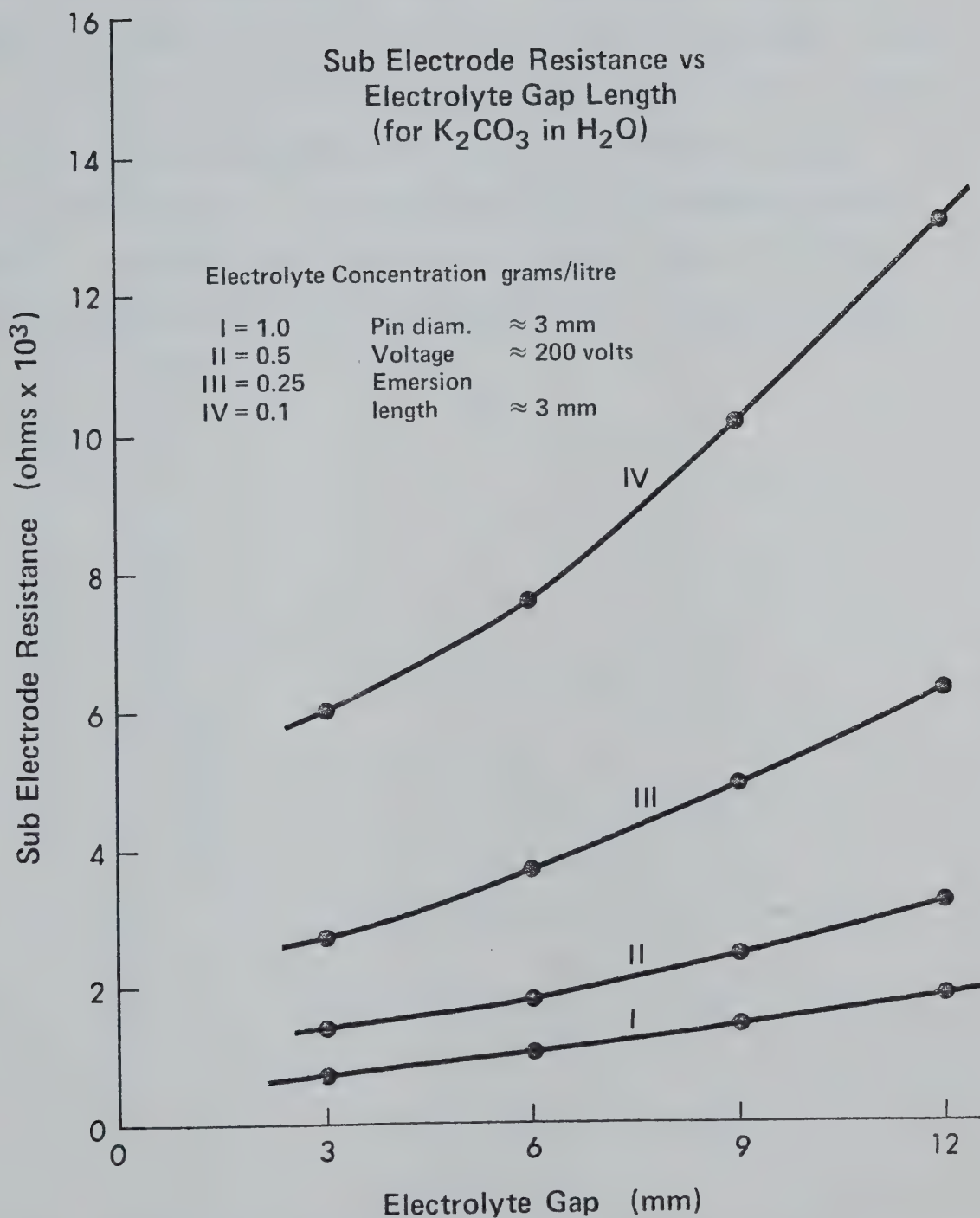


Figure 3-25 Subelectrode Resistance vs. Gap Spacing in the Solution

A typical resistance-current characteristic exhibited by a multi-pin cathode (with 512 pin) is given in Figure 3-26. This initial high valued nonlinear effective resistance, quickly drops to a constant low value, independent of discharge current. The resistance decrease of a single pin (Figure 3-23) was very much amplified in this figure. This is quite understandable since the former effect was magnified about 500 times. These measurements were conducted over a short period; about 5 sec. per curve. If the measuring time is prolonged one should expect a resistance curve deviation at the high current end due to a solution heating effect. The resistance curve for high concentration may also be affected.

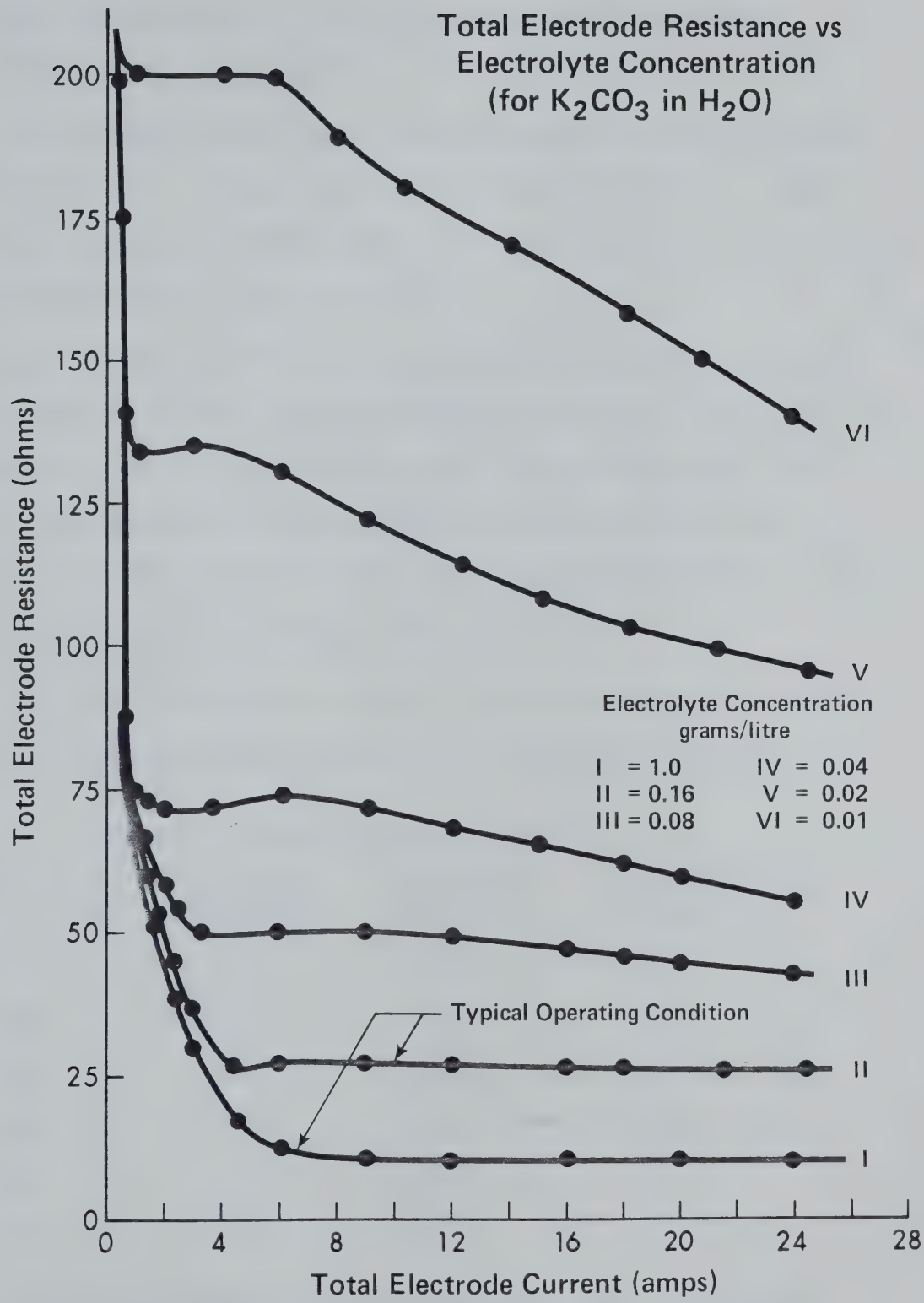


Figure 3-26 Total Electrode Resistance vs. Total Current

3-3 Laser Operation with 276 Pin , Tap Water Ballasted Cathode;

2nd Electrode Configuration

The detailed construction of this electrode is given in Chapter 2, Section 2-1-9. It has 6 rows of pins, and each row has 46 pins with a 1.2 cm distance between pins. The row spacing of 2.5 cm resulted in a pin density of 1 pin per 2.6 cm^2 .

All of the results in this section were obtained using tap water as the ballasting fluid unless otherwise specified. The first test was made with $\sim 3 \text{ mm}$ water gap spacings and $\sim 5 \text{ mm}$ pin immersion in the water. The maximum of 5 kW input power was achieved at 60 torr (CO_2 : N_2 :He = 10:10:40) pressure. A power input limiting instability eventually started from the pins in the gas downstream row.

In order to minimize the problem, the water gap spacings and pin protrusion length into the discharge were arranged as per Table 3-7.

Table 3-7 Electrode Pin Arrangement

Row No.	Water Gap Spacing (mm)	Resistance $\text{k}\Omega/\text{pin}$	Pin Protrusion in Gas (mm)
1st	4.8	13.0	14.3
2nd	5.6	15.0	13.5
3rd	6.4	17.0	12.7
4th	7.1	19.5	11.9
5th	7.9	22.0	11.1
6th	8.7	25.0	10.3

With this arrangement, the maximum input power obtained was 12.6 kW at the same pressure, and with the same mixing ratio as in the first test.

3-3-1 The Relationship Between Pulser and dc Input Powers

Since the pulser input power is a function of three parameters; the storage capacitance, the charging voltage and the operating frequency, variations in dc input power were studied as functions of these three parameters. The results are plotted in Figures 3-27 and 3-28. Termination of a curve in Figure 3-27 at the frequency lower than 20 kHz indicates that further power input was not possible due to arc development. This situation was improved when the pulser was operated at higher voltage as shown in Figure 3-28. A maximum dc input power was achieved when the pulser was operated at 15 kV and with a storage capacitance of 830 pF. However, each curve has its own maximum which is a strong function of frequency. Further increase in frequency, after the maximum is obtained, decreases the dc input power as shown in Figure 3-28.

Besides the parameters mentioned above, other parameters such as rise time and pulse duration also affected the maximum dc input. Since these two parameters are mainly influenced by the discharge circuit geometry it is very important to maintain the discharge loop at minimum length, in order to obtain a narrow pulse with fast rise time. In this test structure the pulse width was typically less than 100 nanoseconds with a rise time of near 30 nanoseconds. The pulser output voltage and current waveforms, obtained when driving the electrodes, are illustrated in Figure 3-29. The current spike of Figure 3-29b is near 150 amps, with a duration of 50 nsec. Electrical pick up accounts for much of the high frequency oscillations superimposed on the current waveform of Figure 3-29b.

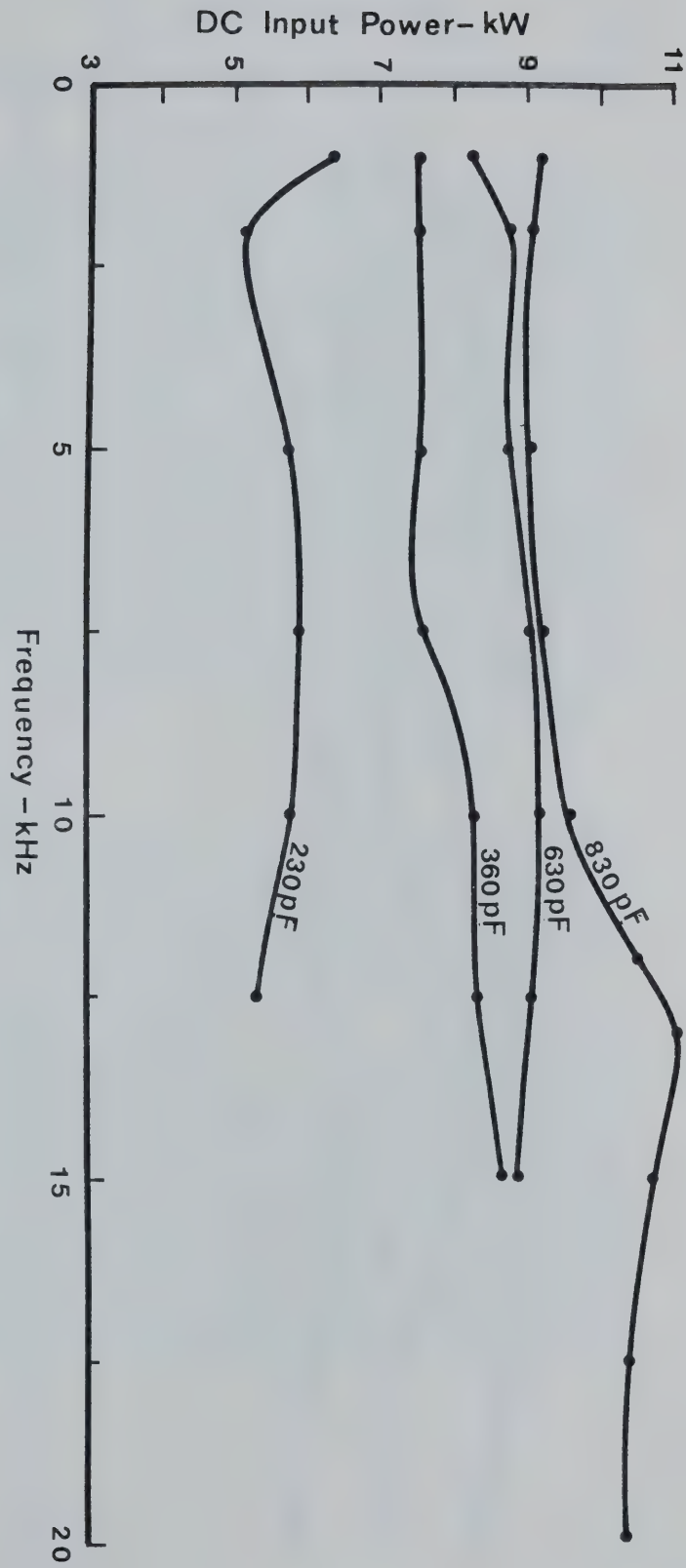


Figure 3-27 Input Power vs. Preionizer Frequency at 10kV
CO₂:N₂:He = 10:10:40 (torr), without U.V.

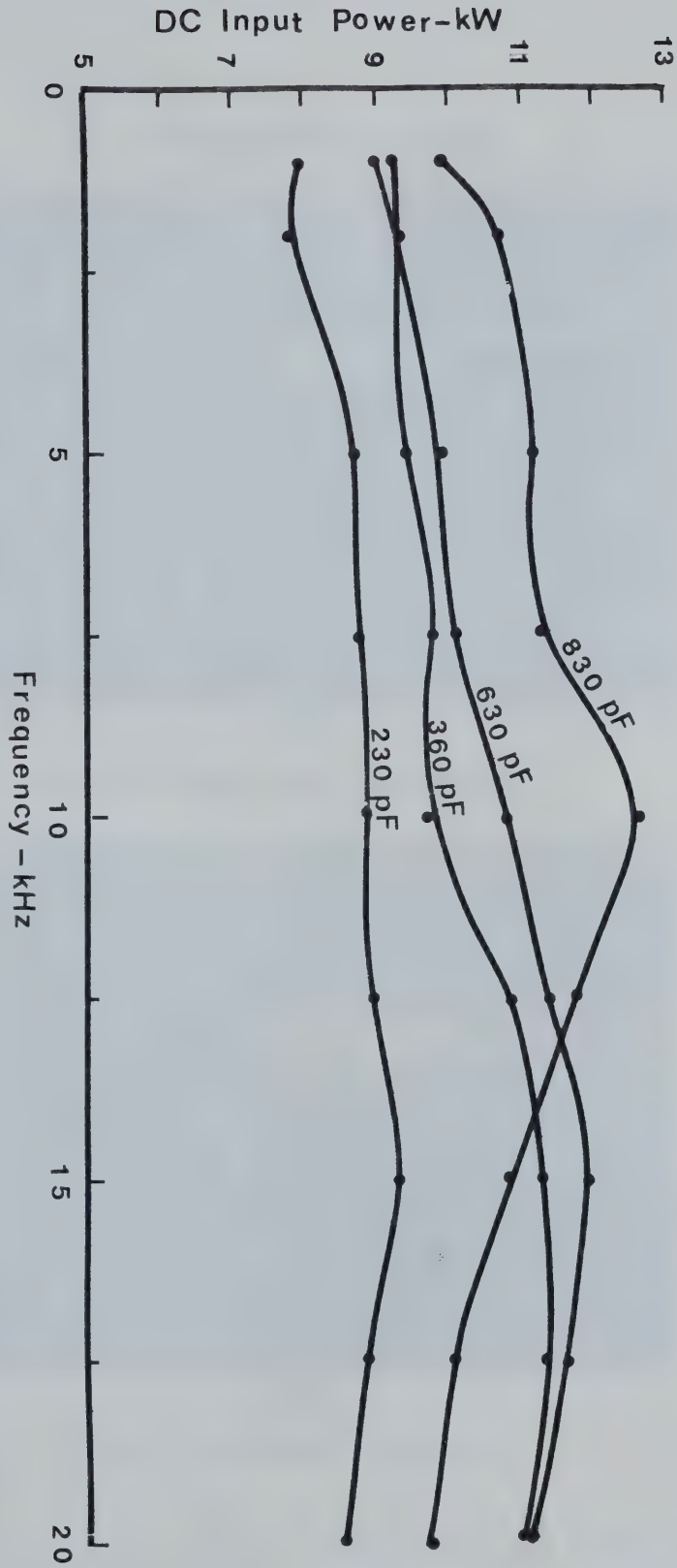
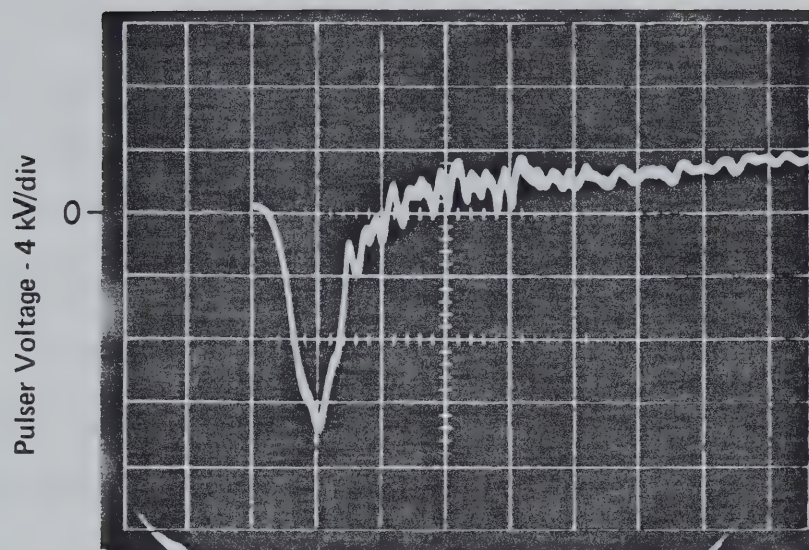
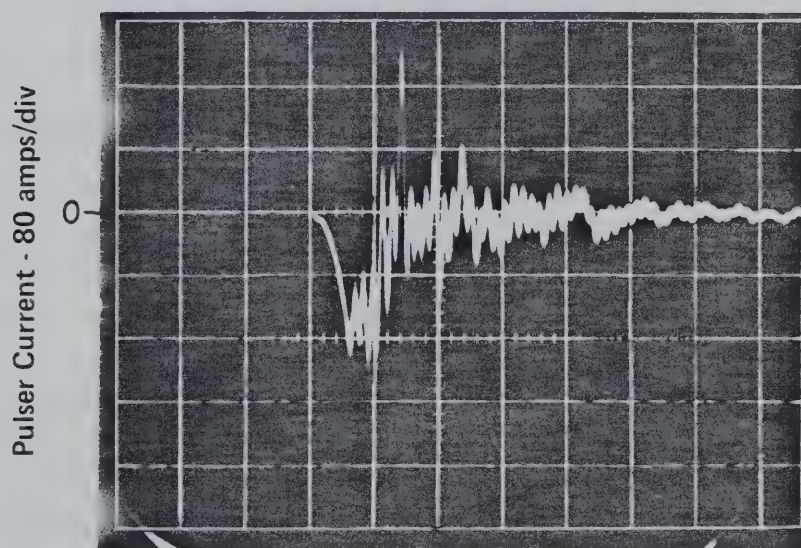


Figure 3-28 Input Power vs. Preionizer Frequency at 15 kV
 $\text{CO}_2:\text{N}_2:\text{He} = 10:10:40$ (torr), without U.V.

Pulser Waveforms



Sweep Speed - 100 nsec/div



Sweep Speed - 100 nsec/div

Figure 3-29 Pulser Output Voltage and Current Waveforms

Generally, improved dc power loading was achieved when the laser gas mixture was preionized with a pulse having narrower width and higher voltage. This is because the prolonged pulse tail may act as an increased sustainer voltage and the ionization cross section increases with an increasing electric field intensity⁽⁹²⁾. For most of the tests performed here, the optimum storage capacitance was found to be approximately 700 pF, while the best frequency range was $7 \sim 15$ KHz.

3-3-2 General Discharge Characteristic of 2nd Electrode Configuration

Initially, the pin materials were chosen to be copper and brass. The copper pins were mounted in the first, fifth and sixth rows while the brass pins were used for the rest of the rows. These pins had been employed for about a year with actual operating time of ~ 300 hours. In the gas discharge, both pins behaved similarly even though the copper pins appeared to sputter more. The sputtered materials seemed to deposit on the ceramic plate around each pin, in a circular fashion and with a long tail in the flow direction. These deposit tails reveal the flow behavior in the vicinity of the cathode surface. No adverse effect attributable to these sputter deposits have yet been observed.

The glow discharge obtained with this electrode configuration at 45 torr is shown in Figure 3-30. Six rows of the cathode pins are clearly shown with thirteen glow strips of anode bars. Two of the anode bars are not shown in this picture. Several glow spots above the anode bars are due to spark plug U.V. sources. As can be seen the upstream pins are not fully covered with glow. This suggests that the pin lengths in the discharge may be slightly too long. However, glow



Figure 3-30 Photo of Glow Discharge at 45 torr ($\text{CO}_2:\text{N}_2:\text{He}=1.7:7.3:36$)

1. U.V. Source
2. Anode
3. Cathode

nonuniformity found within the second row may be attributed to gas trapping around the pin ends immersed in the recirculating fluid. This latter effect has been confirmed by the observation that the nonuniformity moved with the ballasting fluid flow. An important parameter appears to be subelectrode protrusion length into the discharge region. A limited experimentation with different pin lengths has shown that 6 mm or less pin protrusion beyond the cathode's upper ceramic surface is adequate. With an excessive protrusion, the pin interaction becomes a limiting factor. Ideally, the subelectrodes should be near flush mounted and have a surface area selected to provide the desired current density. Several intense discharge columns can be observed against a uniform background glow. These columns are caused by different discharge conditions experienced by each pin due to nonuniformities in construction. These areas may develop into an arc at high power loading. However, thanks to the self-optimizing nature of this solution ballasted electrode, the discharge gradually becomes more and more uniform with operating time.

When using the P.I.E. excitation technique with this electrode configuration a maximum 33 kW was deposited into a 3.7ℓ discharge volume. This is equivalent to an input power density of 8.8W/cm^3 and as such is slightly higher than the thermal limit of 7.9W/cm^3 of References 75 and 76 for a 2.3ms gas residence time. Considering the flow rate of 50m/s and the operating pressure of 45 torr ($\text{CO}_2:\text{N}_2:\text{He} = 1.7:7.3:36$), the specific input power is 190 kW/lb. This value represents an improvement over 140 kW/lb of Reference 35. The specific input power of 190 kW/lb is also close to the thermal limit of 200 ~ 300 kW/lb of Reference 15.

3-3-3 Small Signal Gain Measurements

The equipment and experimental procedure for small signal gain

measurements are outlined in Section 3-1-5.

a) Spatial Gain Variation

The probe laser beam was scanned across the gain aperture approximately 1 cm below the anode-cathode midplane. Figure 3-31 shows the total small signal gain variation with downstream distance as a function of pressure. As can be seen the gain parameter decreases with increasing pressure. This result is consistent with the findings of low pressure measurement in Section 3-1-5, and the result of Reference 48 . Generally in the ballasted pin system, spatial uniformity of the discharge in the flow direction is assumed. However, as expected there are still gain variations between the rows; with local minimum directly above each row and local maximum in between the rows. This is because the discharge column from each pin was blown downstream. The variation in small signal gain transverse to the gas flow direction is displayed in Figure 3-32. The curve reveals a large variation in gain, especially in the vicinity of the electrodes. Such performance is perhaps not unexpected in a C.W. device⁽³⁵⁾ where nonuniform gas heating is likely to be present. This aspect should be particularly manifest in this test laser system, which has a high specific discharge power loading but only a relatively low gas flow velocity. With such a corresponding long gas residence time heating in the cathode-fall region could well dominate the transverse gain dependence.

Further investigations were made on the relationship between gain variation and current density at 25 torr. The result was plotted in Figure 3-33. It was observed that the spatial gain variation became smaller as the current density increased. This signifies that the laser medium is more uniformly excited as the current increases due to growing

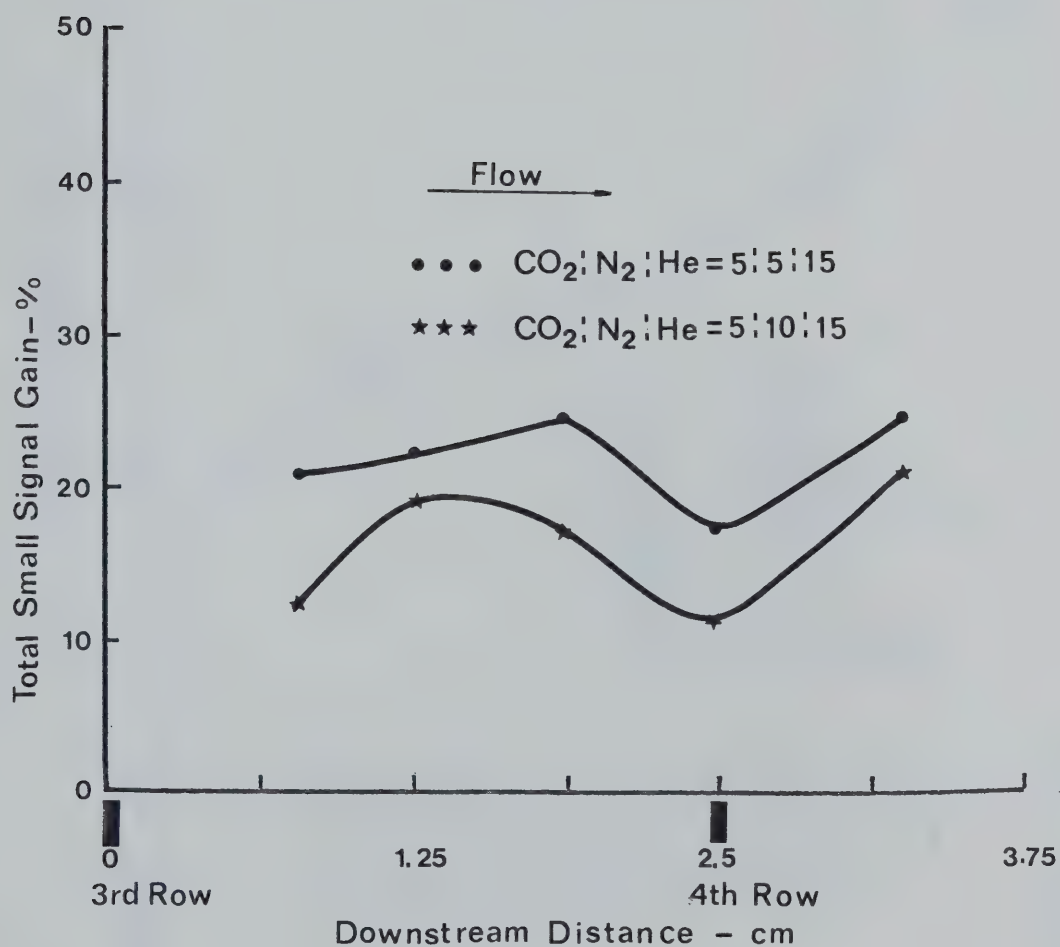


Figure 3-31 Spatial Small Signal Gain Profile Between the Rows
 Pulser - 10kHz at 10kV , - Total current - 5A
 Current density - 18mA/pin

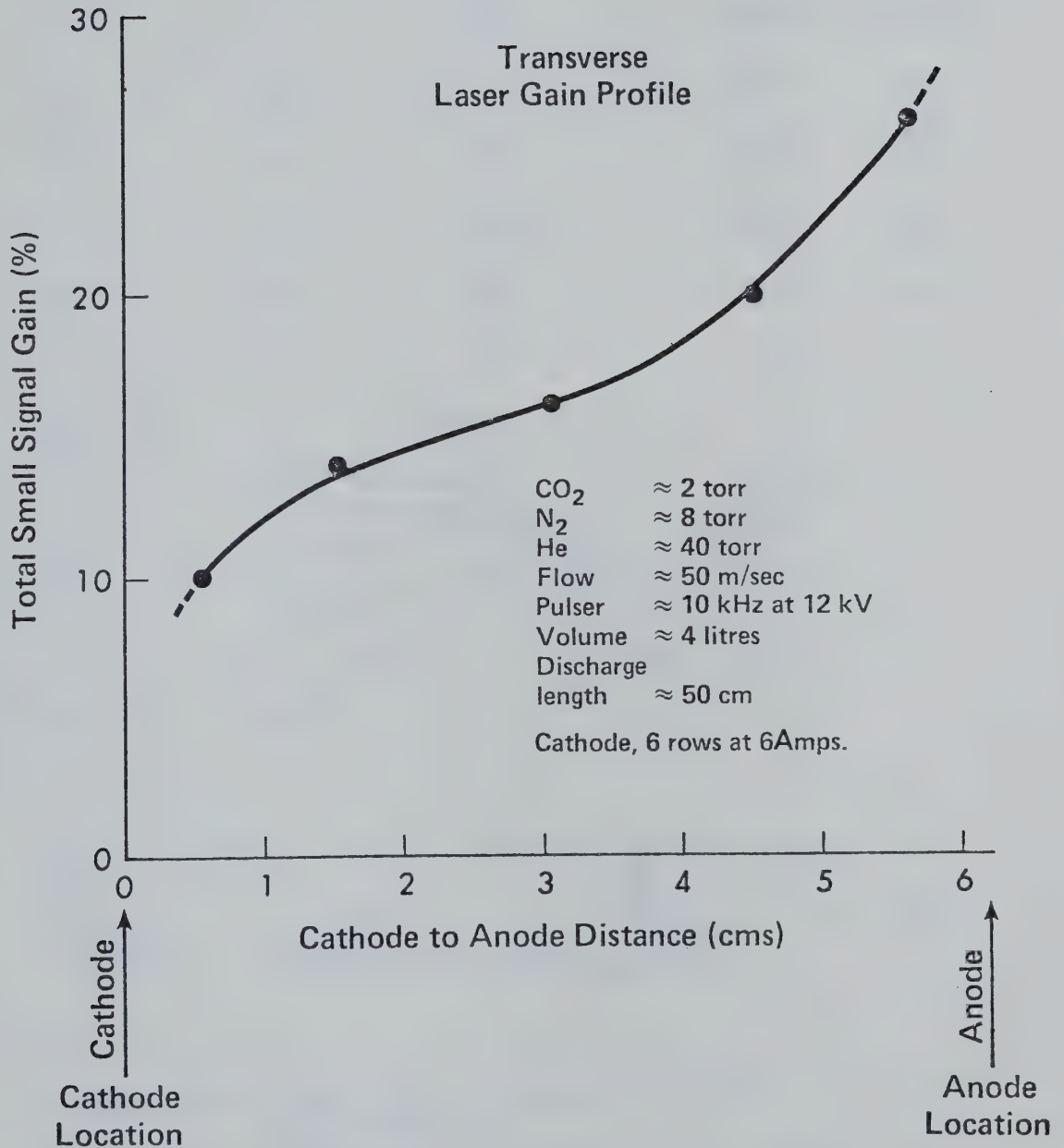


Figure 3-32 Variation in Small Signal Gain from Cathode to Anode
 CO₂:N₂:He = 5:5:15 (torr)
 Flow - 30m/sec
 Pulser - 10kHz at 10 kV

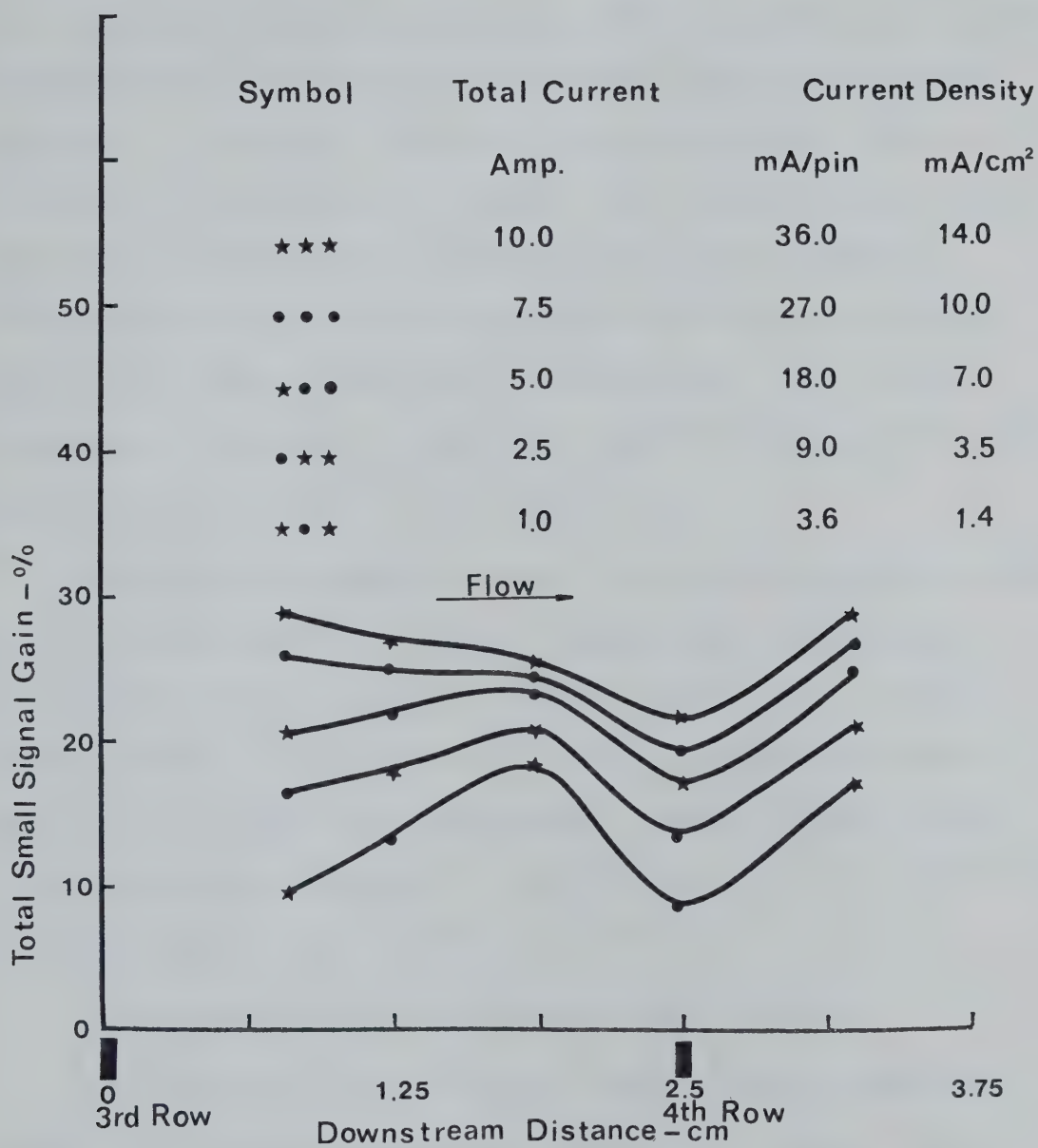


Figure 3-33 Spatial Gain Variations at Different Current Densities
 $\text{CO}_2:\text{N}_2:\text{He} = 5:5:15$ (torr), Flow - 30m/sec
 Pulser - 10kHz at 10kV

cathode glow area and consequent discharge column from each pin.

Better spatial gain uniformity existed near the anodes. Figure 3-34 is a plot of the small signal gain profile measured along 1 cm above the anode-cathode midplane in the output-power optimized-gas mixture ($\text{CO}_2:\text{N}_2:\text{He} = 1.7:7.3:36$). This gain profile is relatively uniform and as such is an improvement over Reference 48. The improvement in the gain profile is attributed to a more uniform current distribution provided by the multipin cathode. It is also shown that the upstream pins pump the laser mixture as well as condition it. This is quite different from References 13 and 48 in which the sole purpose of the upstream pins is to condition the laser gas mixture.

The gain maximum appearing between the fifth and sixth rows suggests that the fifth row carries a somewhat larger current than necessary. This condition can be corrected by a slight readjustment of the pin immersion lengths. Unfortunately, the design precluded measurement of individual row currents with this cathode. However, judging from the gain profile and the luminosity of the discharge, the current must be well distributed among the rows except for the 5th row.

b) Gain Variation with the Current and Flow Velocity

Figure 3-35 shows the near linear relationship observed between the small signal gain coefficient and the total dc current. Even at the maximum test current of 12 A, which is equivalent to a current density of 44 mA/pin or 16.5 mA/cm^2 , this linear relationship is still maintained. This suggests that the system can be operated at still higher total current. The near linear dependence observed in this figure is similar to that reported for self-sustained devices⁽⁴⁸⁾.

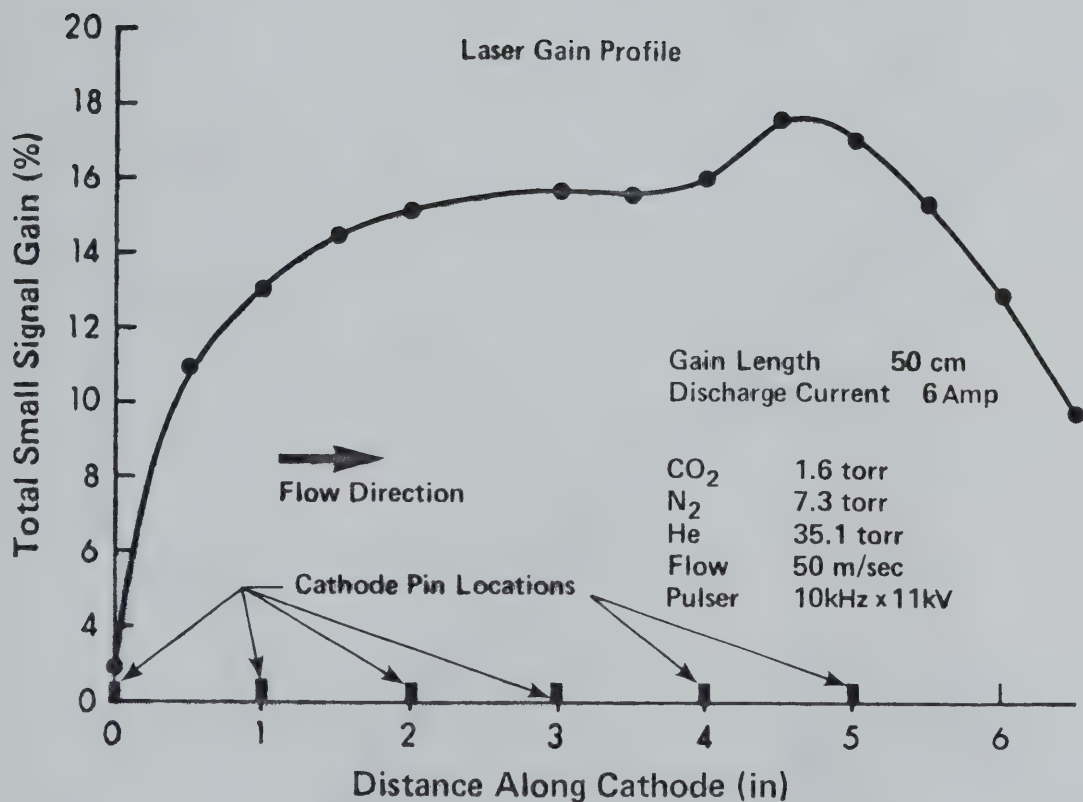


Figure 3-34 Spatial Gain Profile in the Direction of Flow

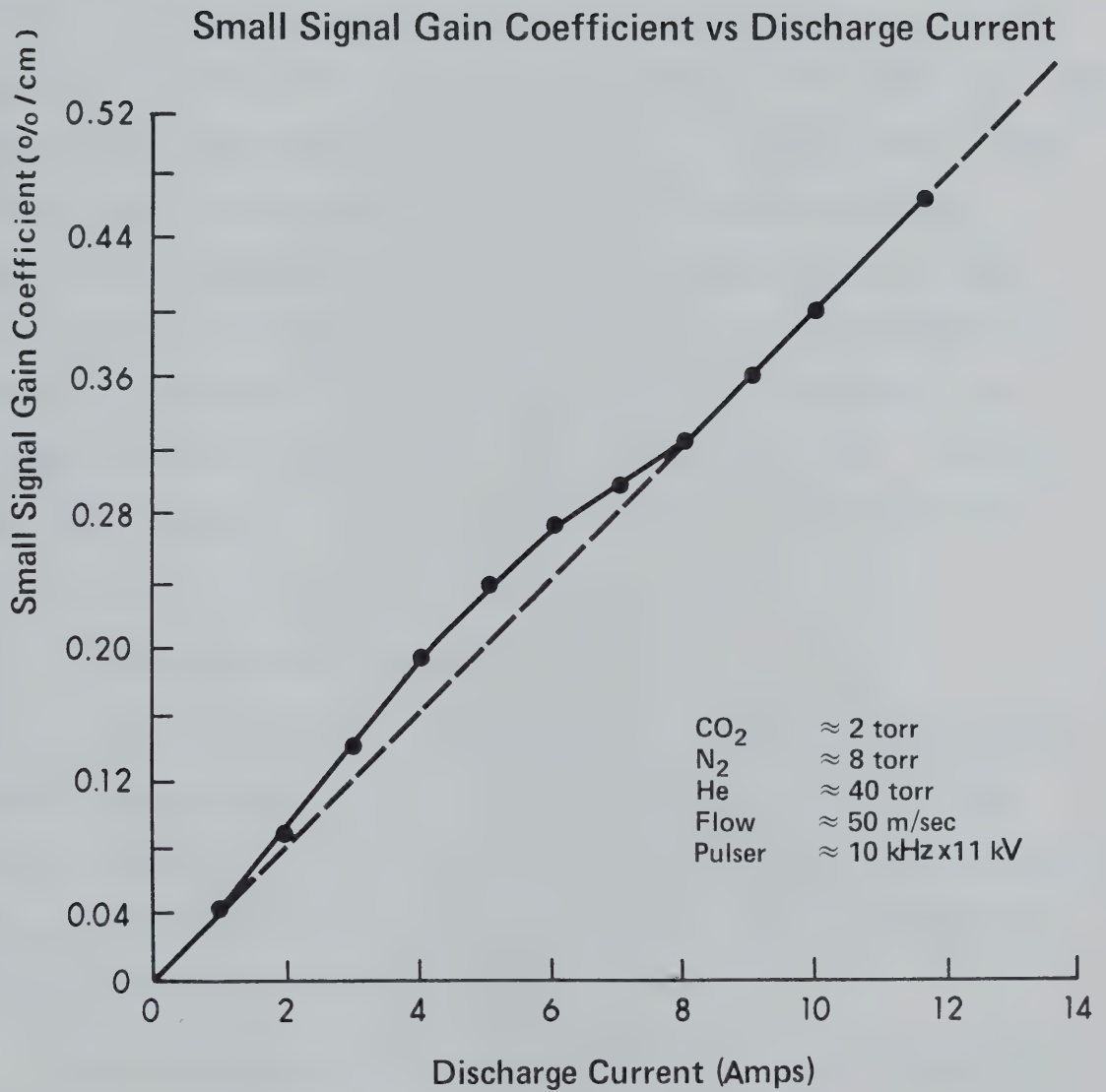


Figure 3-35 Small Signal Gain Coefficient
vs. Total Current

Gas flow assumes a very important role in enhancing gain by lowering the gas temperature and by removing contaminants from the discharge volume. Even a slow flow can increase the gain by a factor of two⁽¹⁰⁾. In the laser system described here, the gain increases rapidly for gas flows faster than 12 m/s as shown in Figure 3-36. This behavior may be due to improper mixing of the gases at slow flow speeds. CO₂ gas has a tendency to settle to the lower part of the system, around the heat exchanger, while helium gas tends to rise to the upper part of the system, which forms the laser box. This assumption was somewhat confirmed from observation of discharge color variations at low flow speed. When the flow rate is about 15 m/s (flow speed through the heat exchanger ~ 3 m/s) more effective mixing takes place, increasing the CO₂ partial pressure in the active volume and hence the gain. At still higher flow velocity the gain continues to rise with increasing flow speed because of the cooling effect of the gas flow.

c) Gain Optimization by Partial Pressure

In order to study the variations in gain with the partial pressure of each laser gas constituent, a two step optimization procedure was employed. Initially the CO₂ partial pressure was approximately optimized by first fixing the N₂ and He partial pressures. Next N₂, and finally the He partial pressure was optimized.

The above procedure was repeated several times using the previous optimization data as a starting point. The final results are shown in Figure 3-37. Care should be taken in interpreting the data obtained. This is because the discharge parameters are also affected by changes in pressure. Consequently, it is very difficult to conduct a consistent

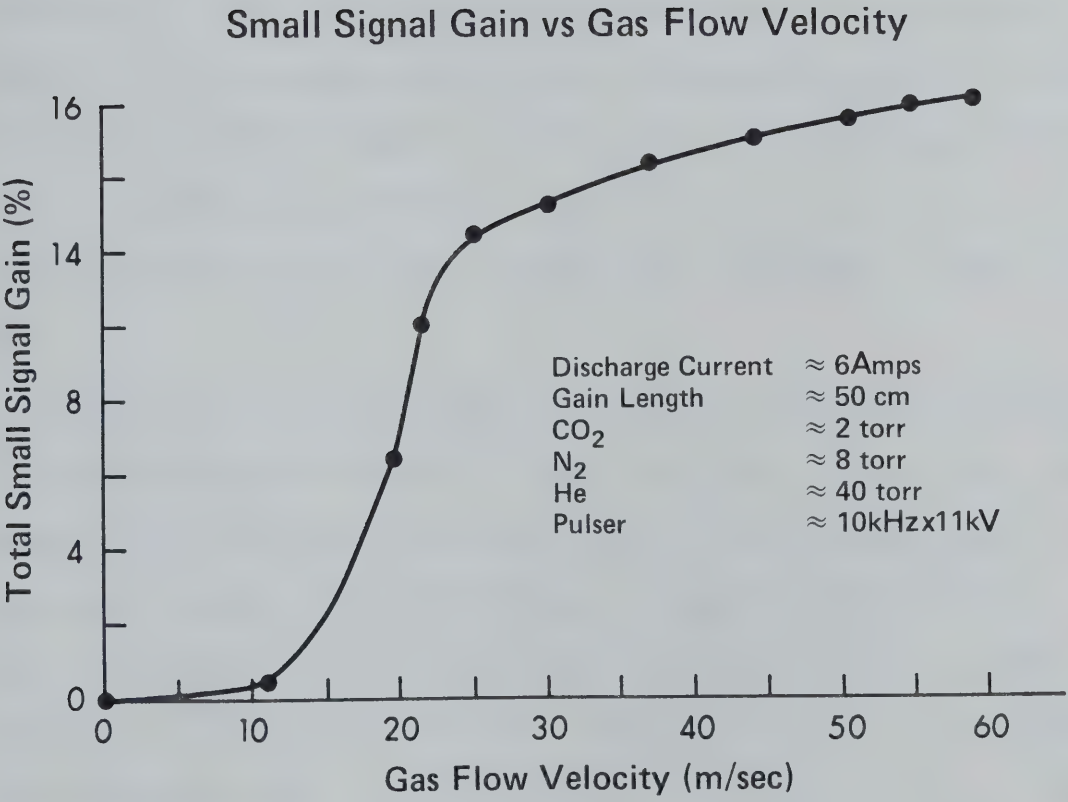


Figure 3-36 Total Small Signal Gain vs. Gas Flow Velocity

test with varying pressure. In an effort to overcome some of this ambiguity a new parameter has been introduced. The parameter, termed the "specific gain coefficient" is here defined as the ratio of the measured small signal gain coefficient to the specific input power density. This new parameter has units of $\% - \text{cm}^2/\text{watt}$ and as such provides a very meaningful comparison of device operation over a wide range of pressure and discharge conditions.

Figure 3-37 illustrates the results of the laser mixture optimization for CO_2 and N_2 , expressed in terms of this new specific gain coefficient. When N_2 and He partial pressures were 7.3 torr and 35.2 torr respectively, the maximum specific gain coefficient occurred at 2.5 torr CO_2 partial pressure. When 2.5 torr CO_2 , and 35.0 torr He were used the maximum specific gain coefficient occurred at 2.5 torr N_2 pressure. In both cases the magnitude of the specific gain coefficient is almost the same.

Figure 3-38 shows the change of the specific gain coefficient with the partial pressure of He, at 1.7 torr of CO_2 and 7.3 torr of N_2 . The maximum occurs at a very low pressure and decreases gradually with pressure in a near exponential fashion. A similar test was made to study the behavior of the specific gain coefficient with air pressure. The result is plotted in Figure 3-39. The reduction rate of the specific gain coefficient with partial pressure was greatest for CO_2 . Next in following order was air, N_2 and He.

Because this new performance parameter, defined in this thesis, has to date not appeared in the literature, the author is unable to make further comparisons in this line.

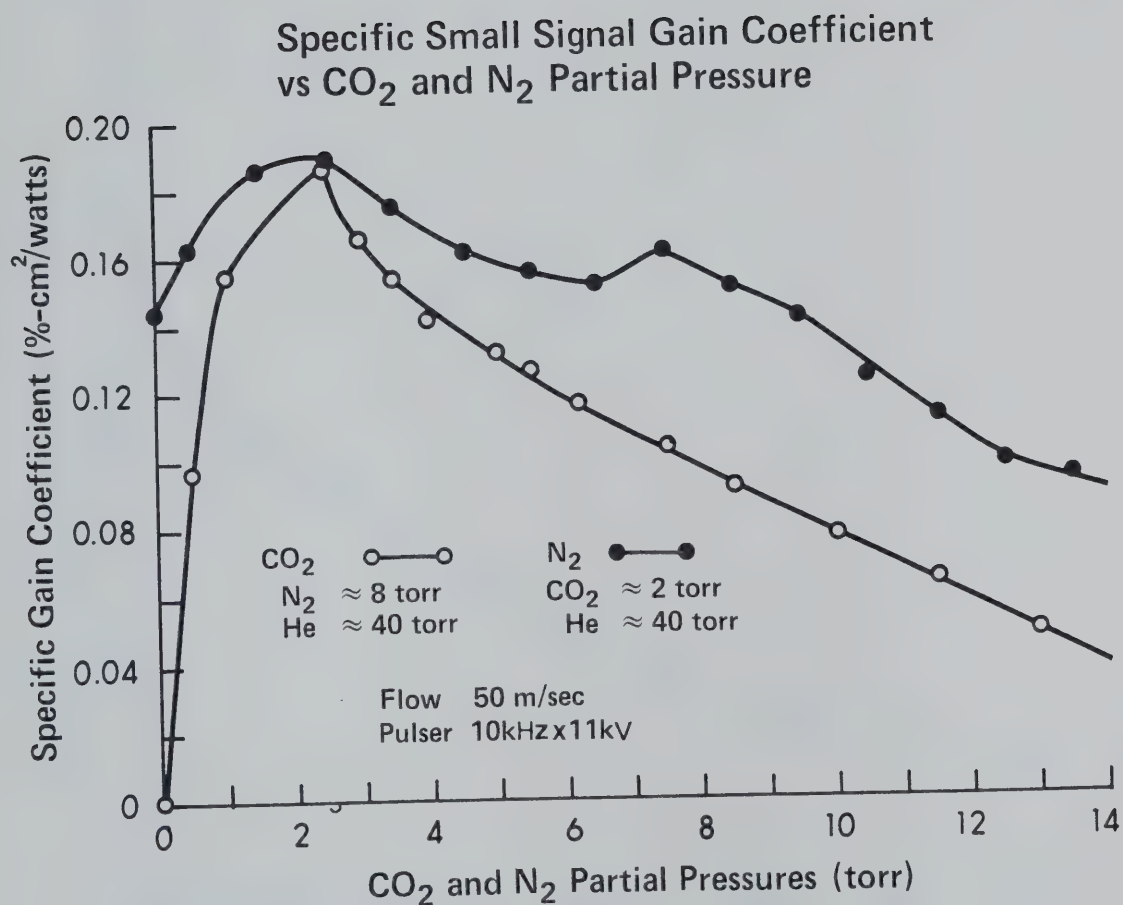


Figure 3-37 Specific Gain Coefficient vs. CO₂ and N₂ Partial Pressures

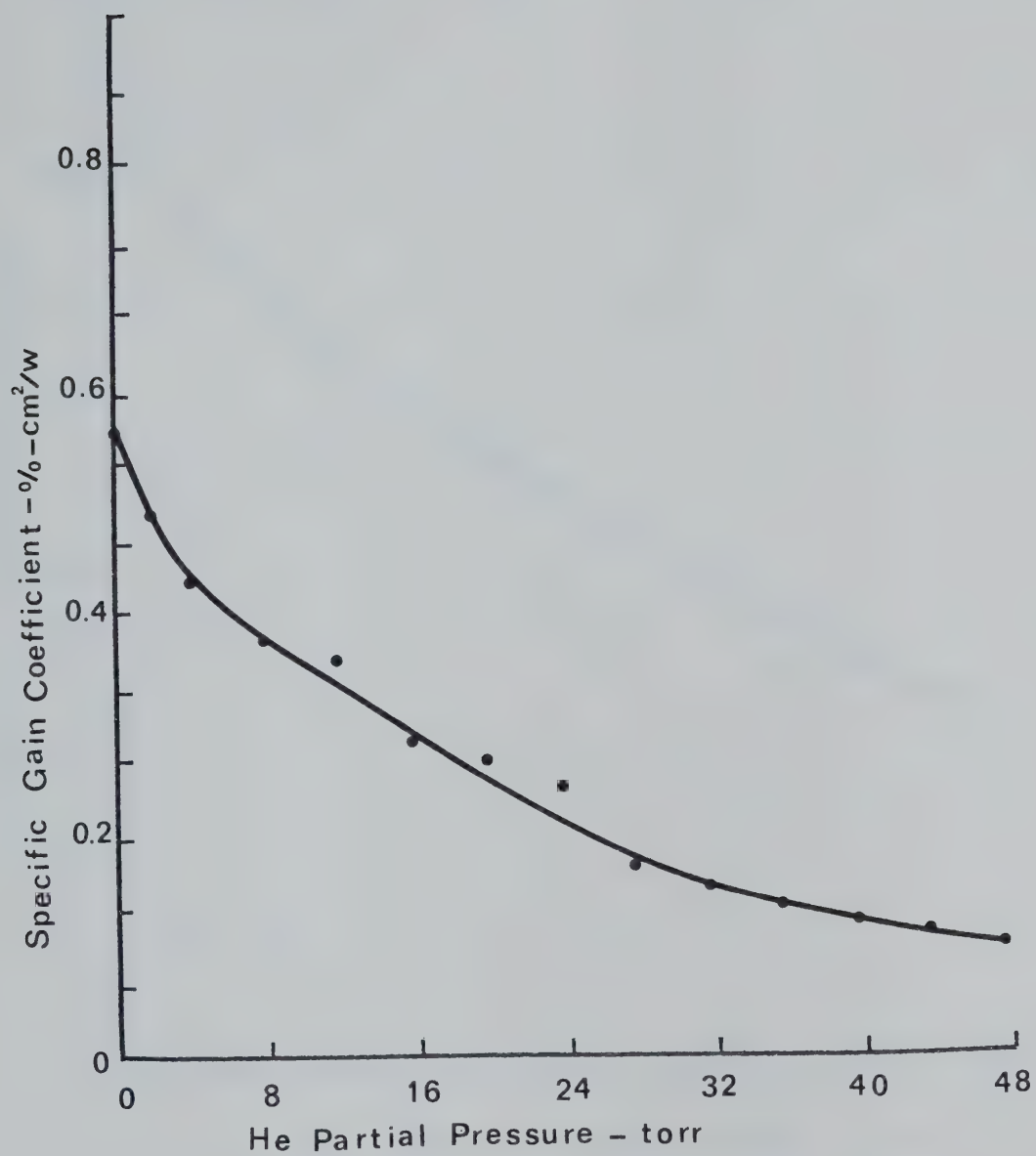


Figure 3-38 Specific Gain Coefficient vs. He Partial Pressure
 $\text{CO}_2:\text{N}_2:\text{He} = 1.7:7.3:\sim$ (torr), Flow - 50 m/sec
Pulser - 10kHz at 11kV, Total current - 6A

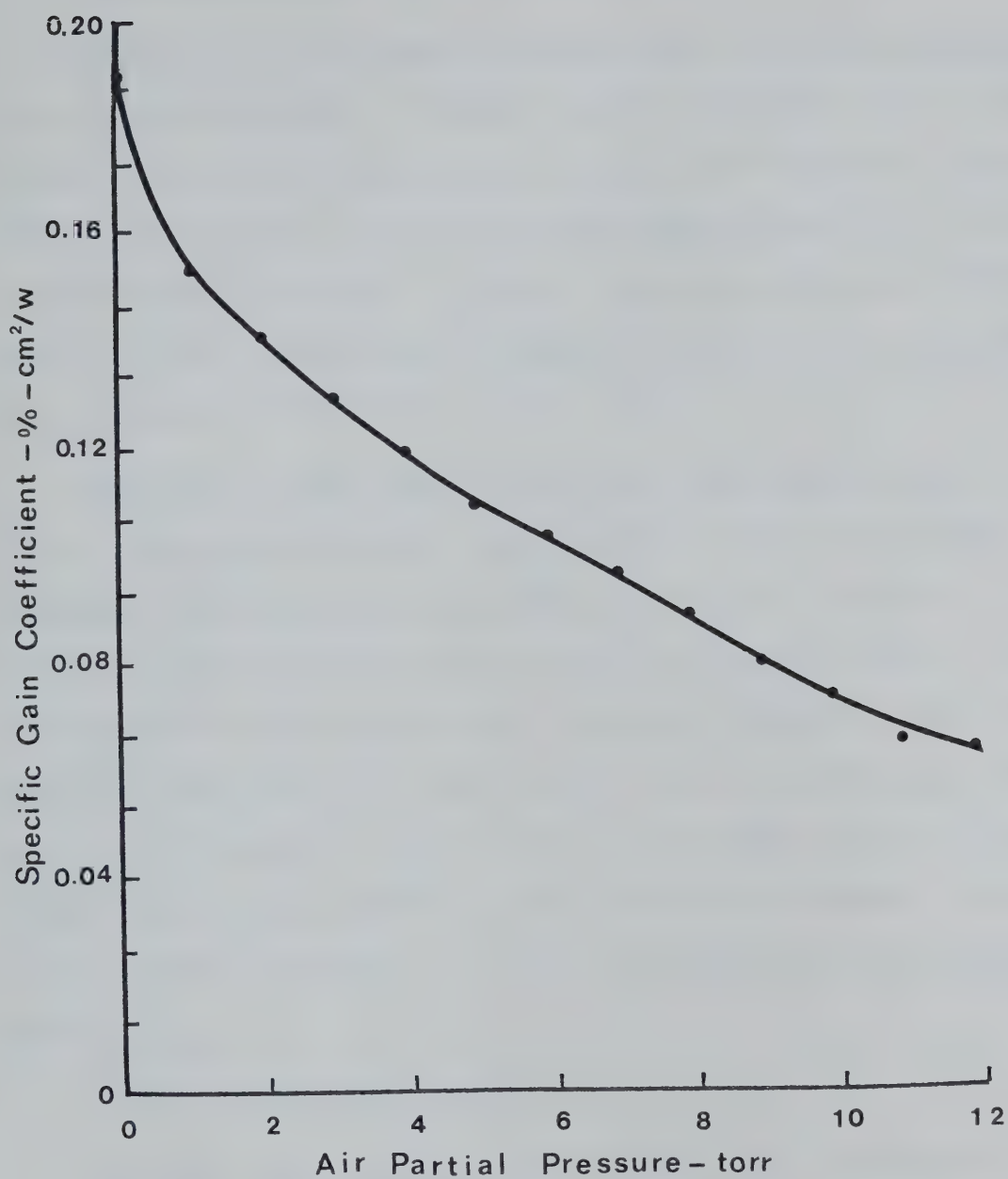


Figure 3-39 Specific Gain Coefficient vs. Air Partial Pressure
CO₂:N₂:He = 1.7:7.3:36 (torr), Flow - 50 m/sec
Pulser - 10kHz at 11kV, Total Current - 6A

3-3-4 Optical Output Power Characteristic

The final and perhaps most important aspect of any laser operation is output power extraction. A system capable of high input power loading but that produces little output power is practically worthless. Often high input power can be achieved by using a mixture containing a lot of He but a very small amount of CO_2 and N_2 . In this condition the output power extraction cannot be high, as there is an insufficient vibrational energy reservoir.

This being the case, most of the output characteristics reported in this thesis were evaluated or measured under optimum output power conditions. The output power was always monitored by a Coherent Radiation detector connected to an X-Y plotter. The other input to the plotter was total discharge current. A second X-Y plotter was used to monitor and record the V-I characteristics. Two calibrated multimeters were employed to measure discharge current and voltage, and to provide a cross-check with the plotted V-I data. With this arrangement, input current, voltage, input power, and output power were easily and accurately measured.

a) Output Power Optimization

The output power was optimized for maximum power extraction by varying the partial pressure of the individual laser gases. The optical system employed was previously described in Section 2-3-2. Figure 3-40 is the result of output power optimization by varying the CO_2 partial pressure. The optimum partial pressure range (that produced more than 90% of the maximum output power) is from 1.0 to 2.5 torr. The most

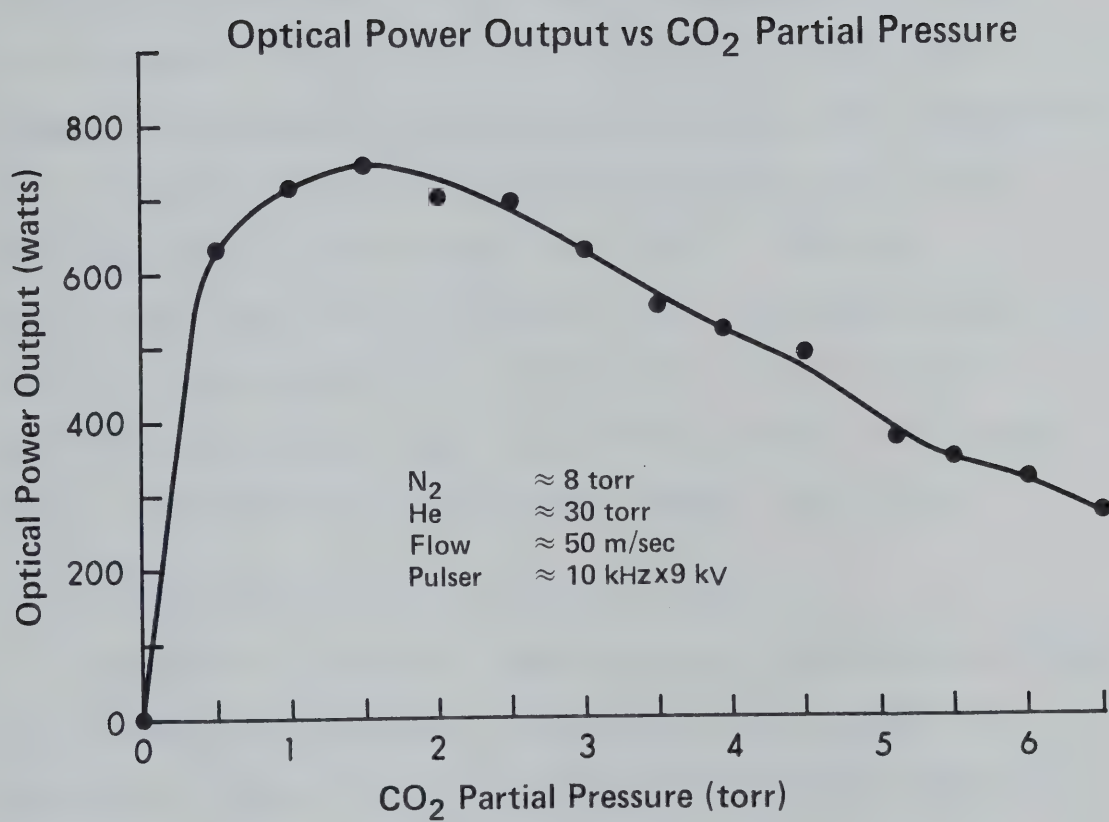


Figure 3-40 Dependence of Laser Power Output with CO₂ Partial Pressure
 CO₂:N₂:He = 1.7:7.3:36 (torr), Flow - 50m/sec

favourable pressure is 1.7 torr. As mentioned earlier, the partial pressure of CO_2 is quite small compared with the other constituent gases; N_2 and He. This result is consistent with References 8 and 13 .

As illustrated in Figure 3-41a the optimum N_2 partial pressure range was 5-10 torr with the maximum output power occurring at 7.3 torr. When the N_2 pressure was zero, the laser operated as a CO_2 - He laser with an output of 210 watt. This result can be compared with that of Figure 3-41b where the output power was optimized by varying the He partial pressure. When the partial pressure of He was zero, which was equivalent to CO_2 - N_2 laser operation, the maximum output power was 215 watt. These results are in good agreement with those of Reference 11 . It should be noted that the total pressure of CO_2 - N_2 operation (8.5 torr) is quite low compared with the total pressure of CO_2 - He operation (31.5 torr). The optimum range for He partial pressure was broad (24 - 48 torr). The most favorable He partial pressure was 36 torr.

b) Output Power Decrease with Air Leakage

Experience has shown that laser operation is considerably affected by air leakage into the system. Air leakage affects overall laser performance by changing both the total operating pressure and the gas composition. This affect has been investigated for two cases; one for natural leakage and the other for induced leakage. The system had a rather large leakage rate of half a torr per hour. This value is termed "natural leakage" to differentiate it from the "induced leakage", in which the leakage was artificially introduced.

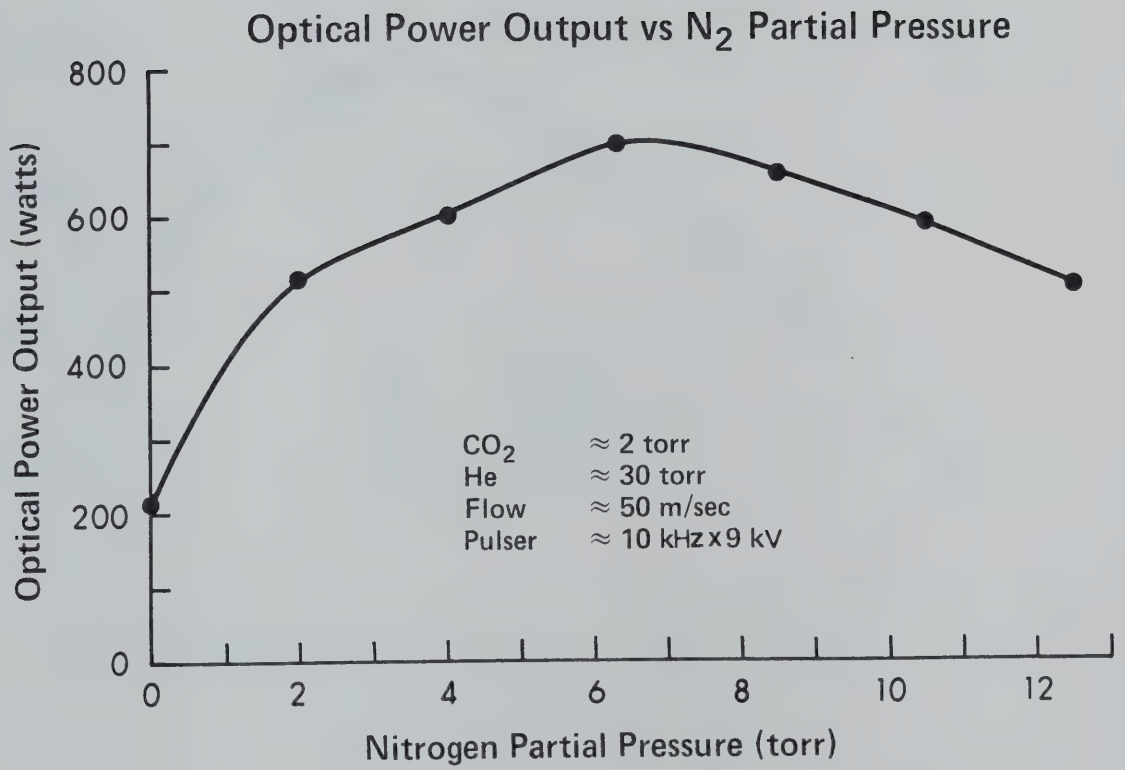


Figure 3-41a Dependence of Laser Power Output with N₂ Partial Pressure

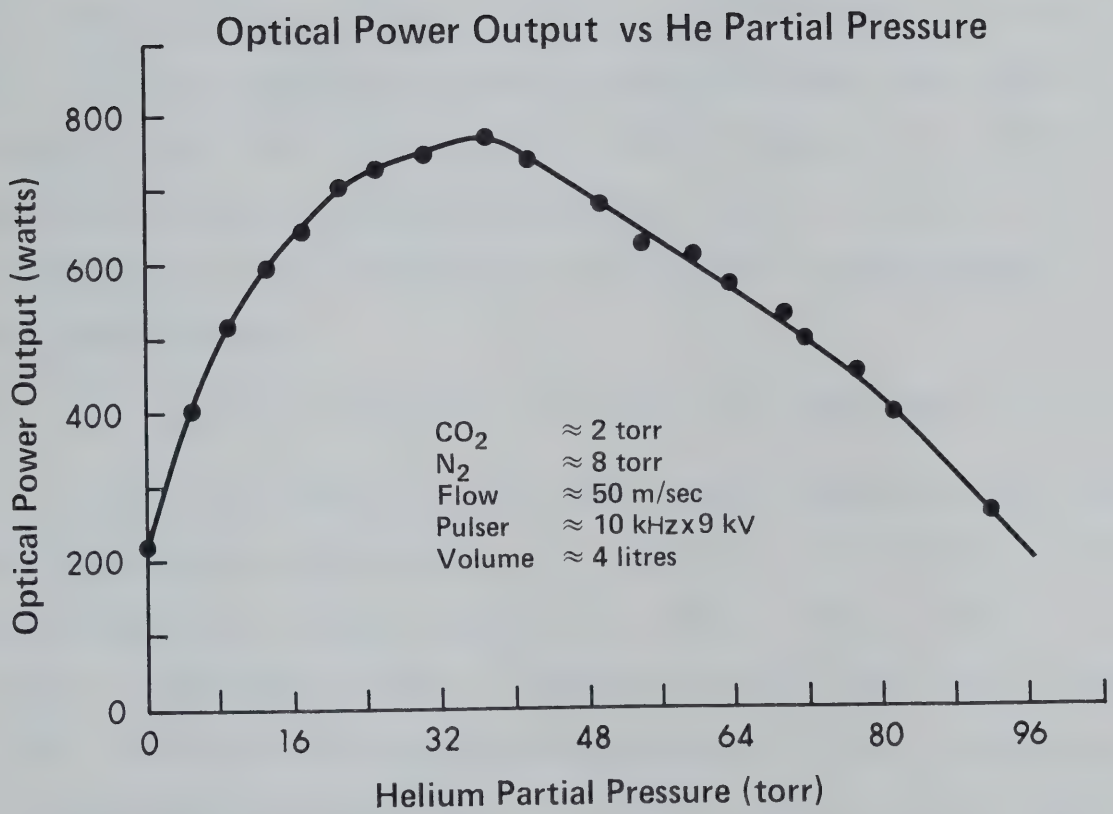


Figure 3-41b Dependence of Laser Power Output with He Partial Pressure

Both results were plotted in Figure 3-42 for comparison. The test with natural leakage was conducted over seven hours. The output power decreased linearly with increasing air partial pressure. The decreasing rate in power output was 91.4 watt per torr which is more than twice as high as 42.1 watt per torr of the induced air leakage. The rate discrepancy between the two results can be attributed to oil vapor from the high speed drive-box, and outgassing from the organic material inside the system which would have a larger effect on performance than natural leakage. The time period for the natural leakage was seven hours which is about 14 times longer than that of the induced leakage test. Therefore, the concentration of contaminants had enough time to build up in the system for the natural leakage test thus resulting in high absorption of the laser radiation.

c) Output Power Dependence on Gas Flow and Pulser Repetition Rate

Figure 3-43 shows the optical power output dependence on gas flow, and preionization at the maximum dc power input. The abscissa is the relative gas flow velocity expressed in percent. 100% is equivalent to 50 m/s. Recalling the result of the gain measurement with flow of Figure 3-36, the increase in gain for speeds greater than 10 m/s is equivalent to the increase in output power at 20% relative speed. At the maximum flow, the highest preionizing input power (780W) increased the optical output power by more than 120 watt over the lowest preionizing input power case (80W).

The preionizing input power was varied by changing the operating frequency and the resulting optical output power was plotted in Figure 3-44. From this figure it appears that a 10kHz pulser repetition rate

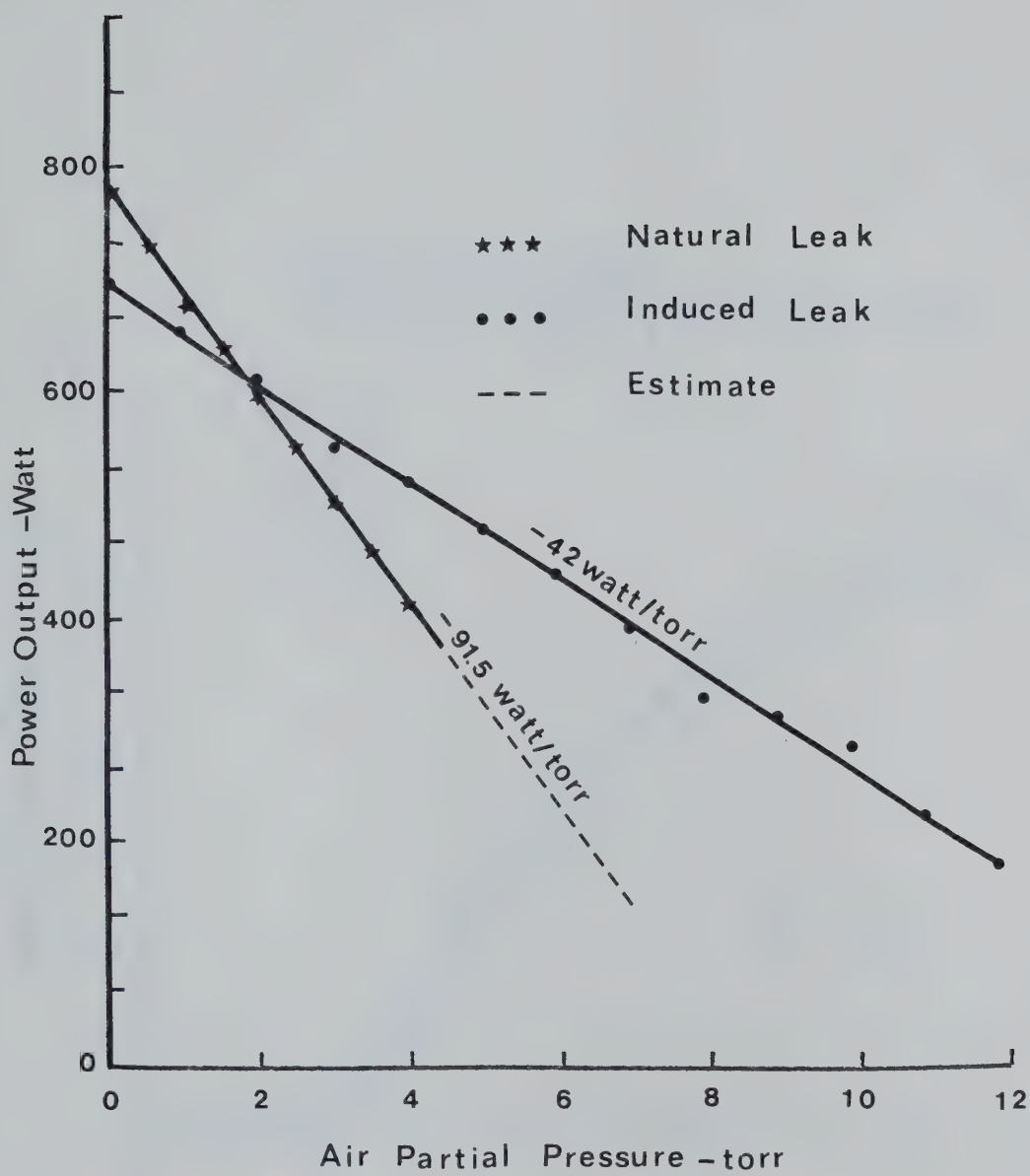


Figure 3-42 Dependence of Laser Power Output with Partial Air Pressure

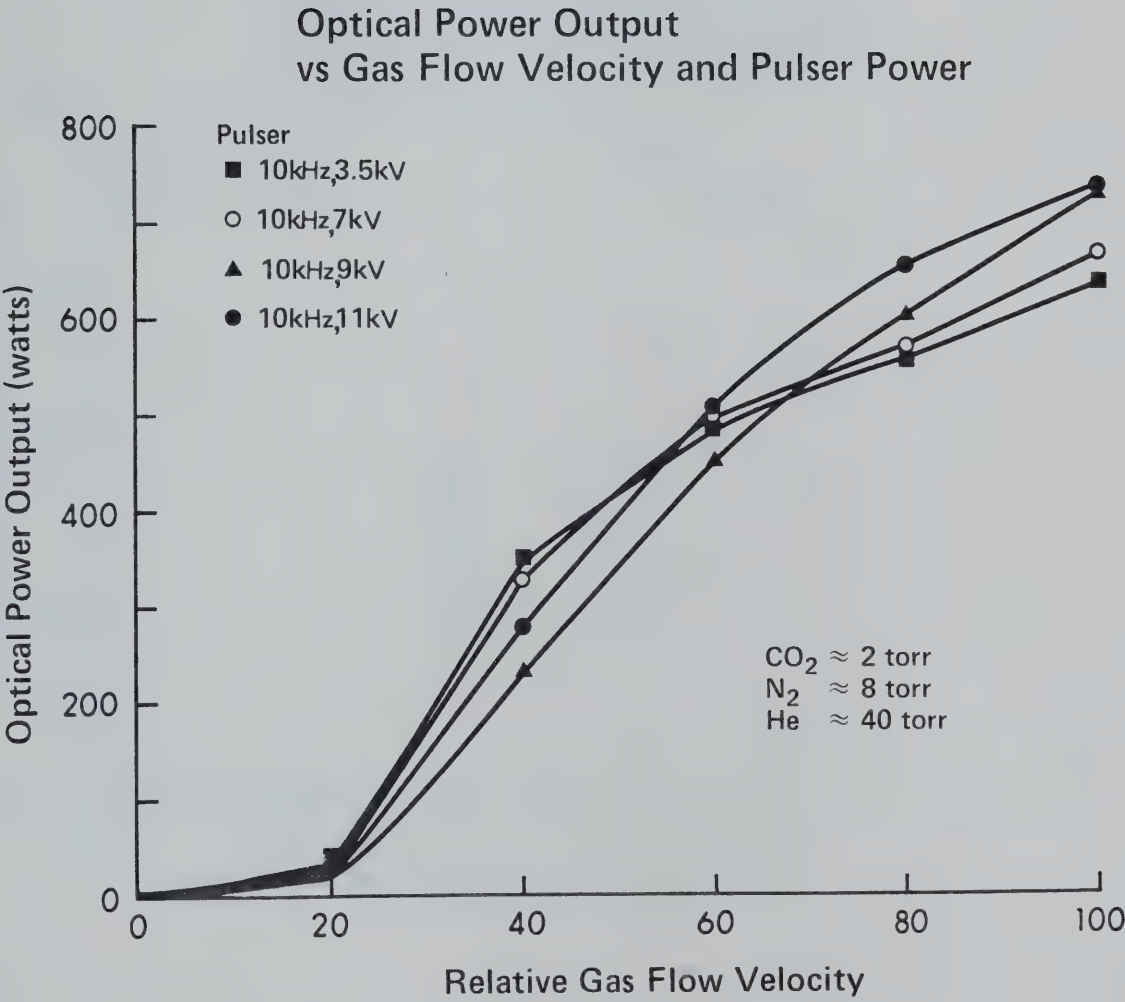


Figure 3-43 Dependence of Laser Power Output on Gas Flow Velocity

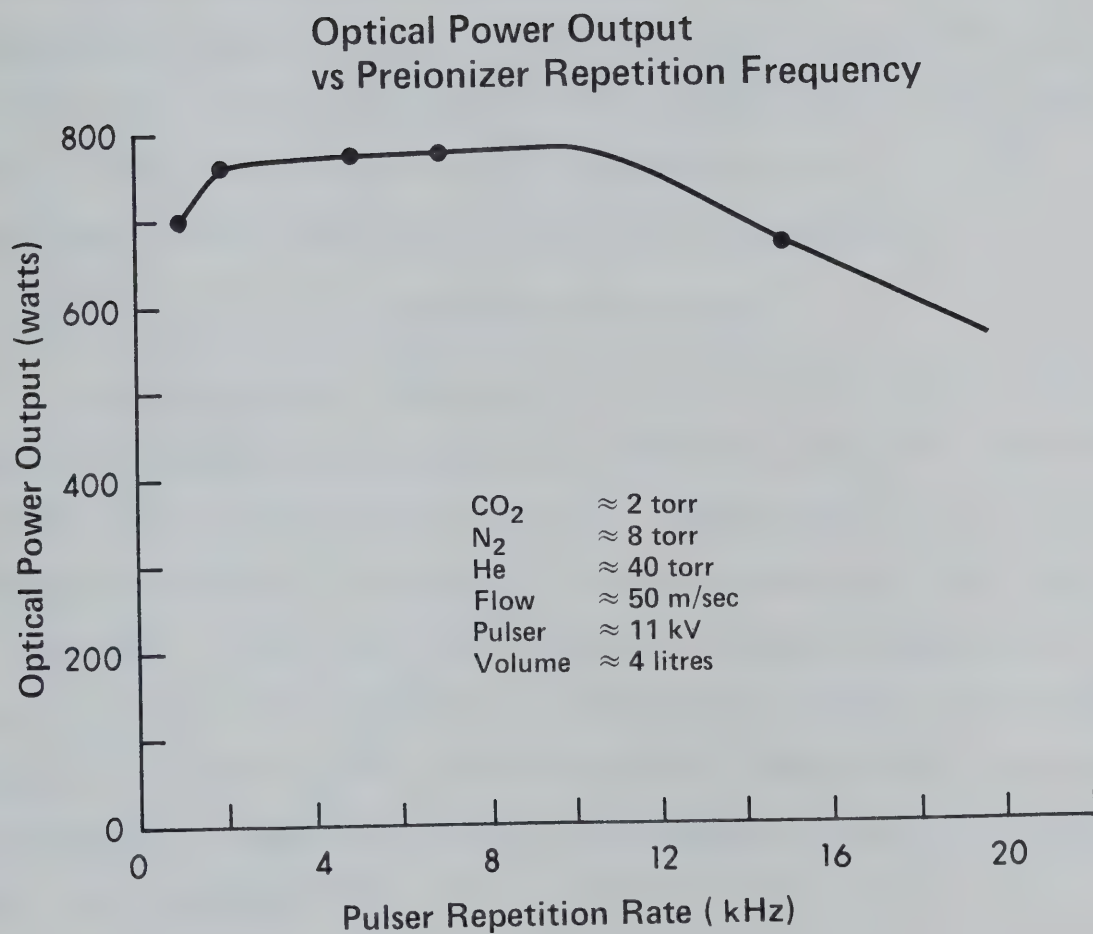


Figure 3-44 Dependence of Laser Power Output
on Pulsed Repetition Rate

is as high as desirable in this system. Performance, however is not a strong function of pulser frequency, in that essentially the same output power is obtained from 10 kHz down to as low as 3 kHz.

d) Comparison of Self-sustained and Preionizer Maintained Modes

The substantial input and output power gains that were achieved by using the preionizing technique instead of the self-sustained glow discharge is shown in Figure 3-45. With less than 1 kW preionizer input power, about 10 kW sustainer input power and 520 W optical output power improvements were achieved over glow discharge operation. The 100% increase in power output justifies the use of the preionizer.

3-3-5 Translational Temperature Measurements

The translational temperature of the laser medium should be kept as low as possible for efficient laser performance since the lower laser levels (10^00 , 02^00) thermally populate at a high temperature and form a thermal bottleneck. The population inversion between the $10.6\mu\text{m}$ transitions (00^01 - 10^00) goes to zero at 680°K , terminating laser action⁽⁵⁾. Another effect is the reduction of the stimulated emission cross section due to the increase of the collision-broadened linewidth with increasing temperature. Assuming equilibrium, the temperature rise in the discharge ΔT , can be expressed by:

$$\Delta T = \frac{P_e - P_L - P_c}{4.2 \rho C_p \frac{U}{x} V_c} \quad (3-5)$$

where the symbols are as follows:

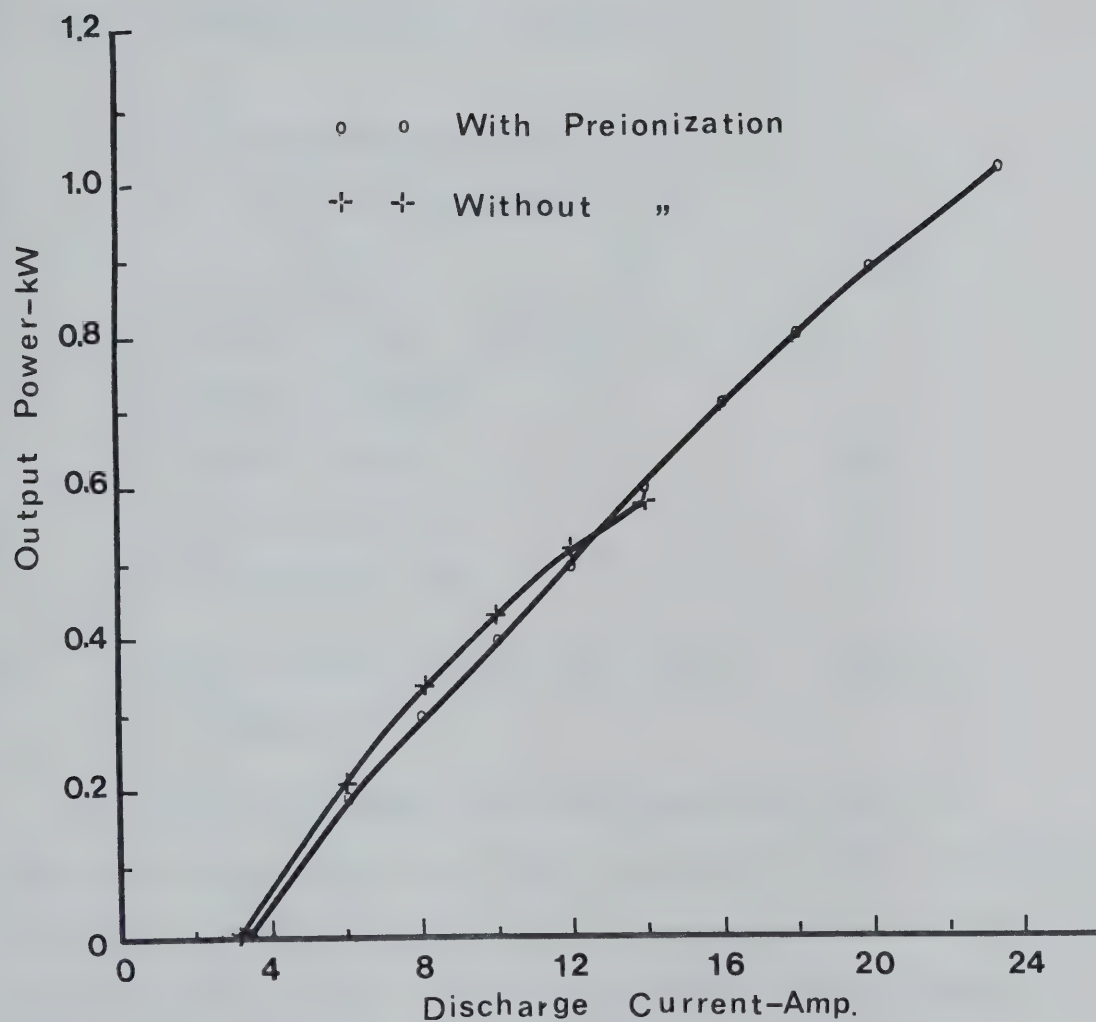


Figure 3-45 Optical Power Output vs. Discharge Input Power
With and Without Preionization
 $\text{CO}_2:\text{N}_2:\text{He} = 1.7:7.3:36$ (torr), Flow -50m/sec
Pulser - 10kHz at 12kV

Symbol	Description	Unit
P_e	Electrical power Input	Watt
P_L	Laser output	Watt
P_c	Power loss by cooling	Watt
ΔT	Temperature change °K between	°K
T_1	The upstream temperature	°K
T_2	The downstream temperature	°K
ρ	The gas density	gm/cm ³
C_p	The specific heat of the gas (constant pressure)	—
U	The flow velocity	cm/s
x	The electrode width	cm
V_L	The discharge volume	cm ³
4.2	The conversion constant from Joules to degree Kelvin	J/gm-°K

For a given input power and laser output power the power removal by cooling should be as large as possible in order to maintain a small ΔT . It should be noted that P_c does not include the heat loss through the heat exchanger. Most of parameters are predetermined by the design and operational conditions. The most easily variable parameter is the flow velocity.

Due to the discharge interaction with the measuring probe, especially during pulser operation, the translational temperature was measured 14 cm downstream using a thermometer. Normally, the hot gas from the discharge extends far downstream⁽³⁵⁾, consequently the measure-

ments should closely approximate the discharge temperature.

In order to determine the thermal behavior of helium and nitrogen, discharges were made in gas mixtures consisting of CO_2 and either helium or nitrogen. The temperature rise per unit input power (W/cm^3) was found to be $0.014\text{ }^\circ\text{K}/\text{W}$ with a $\text{CO}_2:\text{N}_2$ mixture and $0.0044\text{ }^\circ\text{K}/\text{W}$ with a $\text{CO}_2:\text{He}$ mixture. This simple test illustrates the effective cooling of the electric discharge by helium.

Figure 3-46 shows the translational temperature change with D.C. input power. The temperature has been measured under actual laser operating conditions. At higher input power, the temperature gradually levels off because the entire structure begins to take part in the heat radiating action.

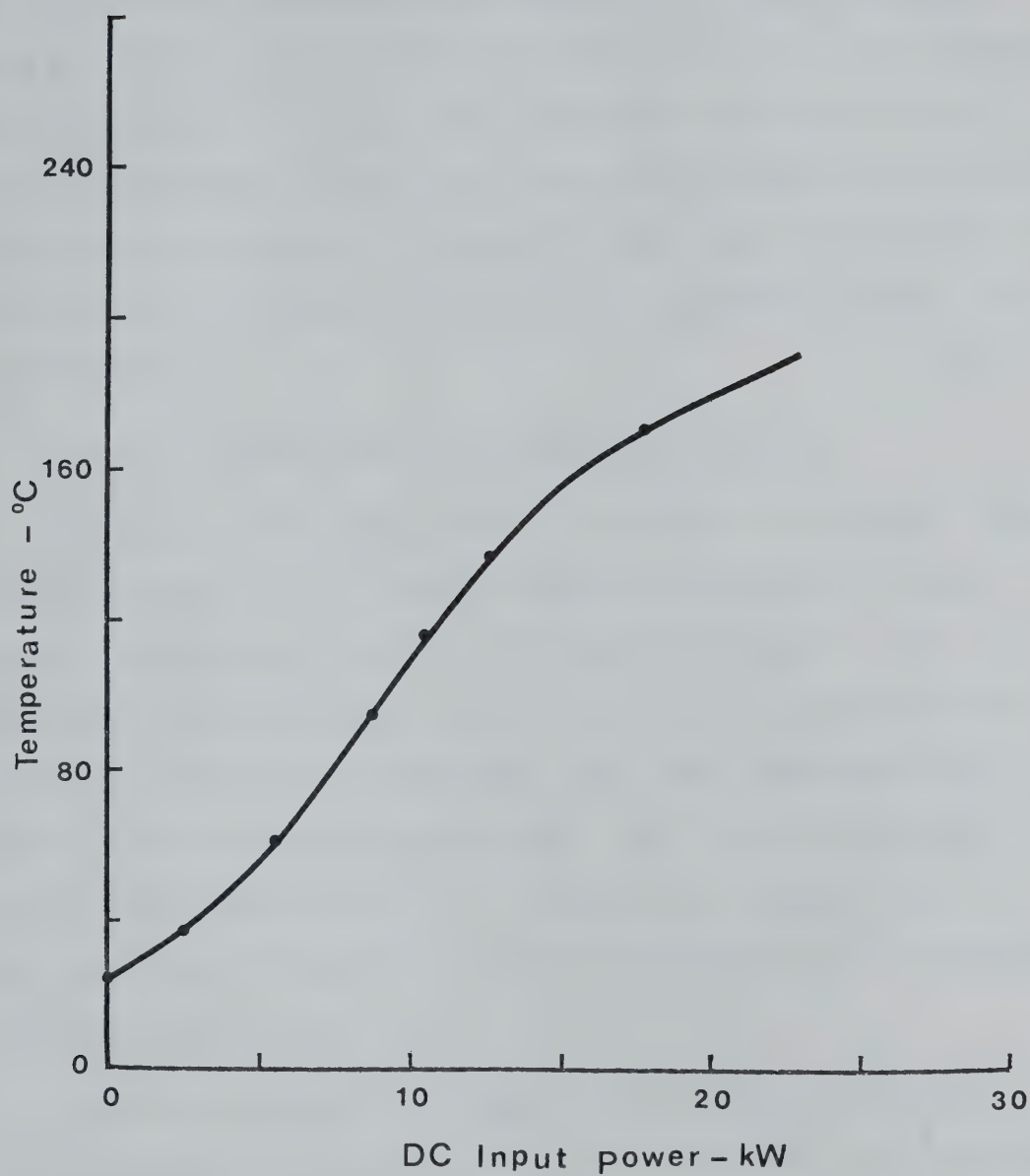


Figure 3-46 Translational Temperature Change with Input Power
 $\text{CO}_2:\text{N}_2:\text{He} = 1.7:7.3:36$ (torr), Flow - 50m/sec
Pulser - 10kHz at 13kV

3-4 Laser Operation with 512-Pin Cathode: 3rd Electrode Configuration

Significant improvements were achieved in overall performance using the 512 - pin cathode with a potassium carbonate aqueous solution, and 304 stainless steel pins. This combination exhibited not only a negligible corrosion rate but more importantly provided a gentle cleansing electro-chemical reaction at the metal - electrolytic solution interface when current density was high (> 40 mA/pin); and a protective film at a low current density.

3-4-1 V-I Characteristics and Operating Impedances

The V-I characteristics shown in Figure 3-47 are somewhat similar to those obtained with the second electrode configuration (276-pin cathode). However, in this case the operating voltage was about 30% lower than that of the previous case because of its lower ballasting impedance (~ 20 ohm). No significant input power improvement has been obtained with the increased pin density. This result is consistent with the findings of Wutzke et al.⁽⁴⁸⁾. However, it is expected that the input power will be improved by the self-optimization of the electrode as described in Section 2-1-9.

Each curve in Figure 3-47 shows the V-I characteristic under different preionization conditions. Curve I signifies a photo-impulse preionization operation. Here the sustainer voltage is well below breakdown, and the discharge is kept running by both photo and impulse ionizations. This preionization produces an extremely uniform and stable plasma. Curve II represents operation with only impulse ionization. Although operation without U.V. preionization is stable, discharge

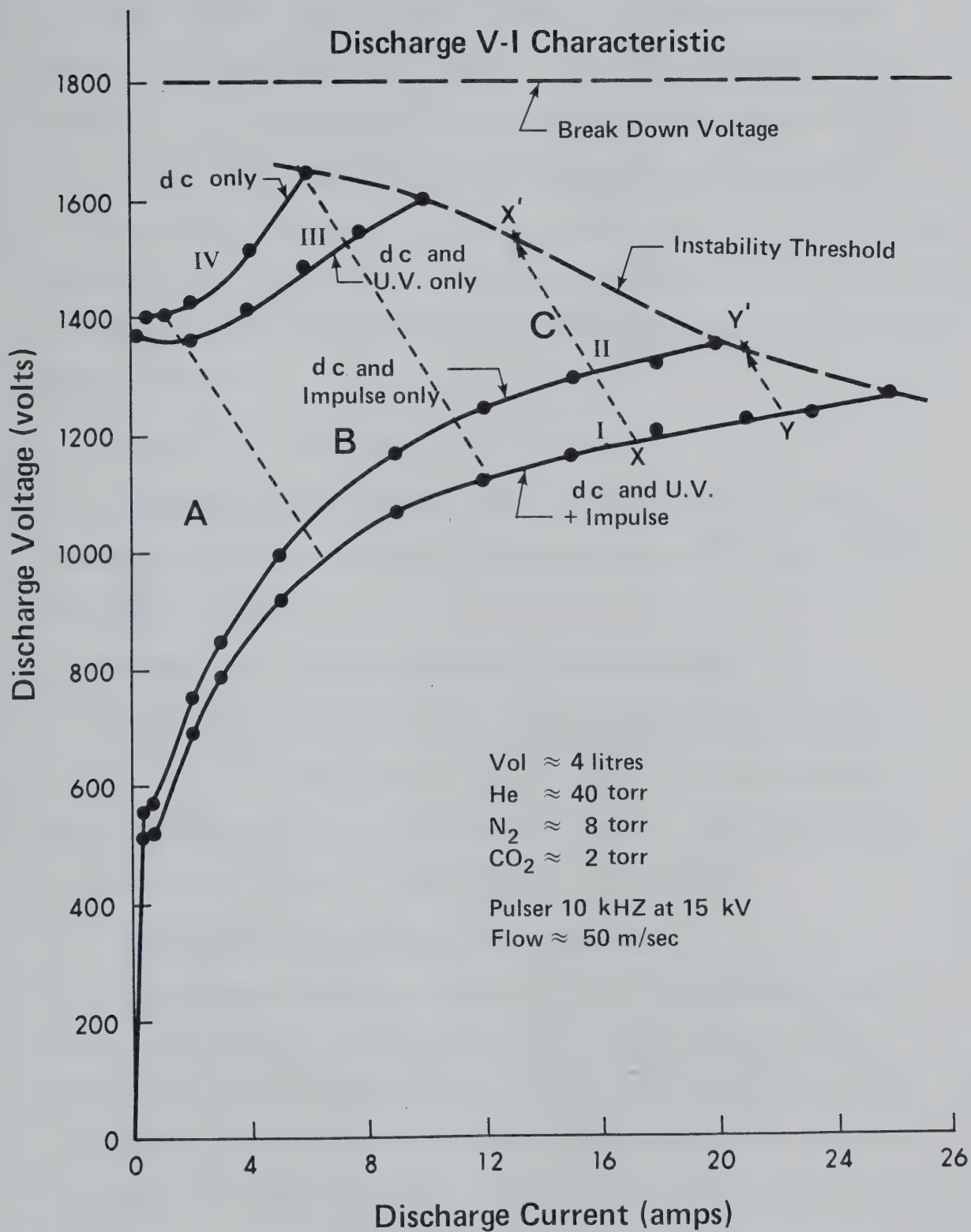


Figure 3-47 V-I Characteristics of P.I.E. Discharge in High Pressure

uniformity becomes degraded, with a tendency for downstream blowing. Maximum power loading is also reduced. Curve III demonstrates the influence of U.V. preionization on the self-sustained V-I characteristic.

Fully self-sustained performance without photo or impulse ionization, is characterized by curve IV. In this narrow and comparatively unstable regime, the discharge is highly nonuniform and blows considerably downstream. The dotted lines extended from curve IV bound the different modes of operation:

Region "A" - preionization sustained mode;

Removing the preionization from this region results in the termination of the discharge and the electrode potential jumps to the open circuit voltage.

Region "B" - self-sustained glow discharge mode;

Complete elimination of preionization from this region ends up on curve IV for a self-sustained glow discharge. The preionization in this region keeps the discharge uniformly spread. The self-sustained glow discharge is usually constricted to a small volume.

Region "C" - Preionization maintained mode;

The plasma uniformity maintained by the preionization creates an extra stable region "C" which would be an unstable region otherwise. Therefore, absence of preionization in this region means eventual arc development. Note that gradual removal of preionization by changing frequency from x or y on curve I results in an arc at x' or y' respectively.

Some insight into this P.I.E. type discharge behavior may be provided through re-examination of the "photo-impulse" V-I characteristic curve I in Figure 3-47. Figure 3-48 represents this same curve plotted

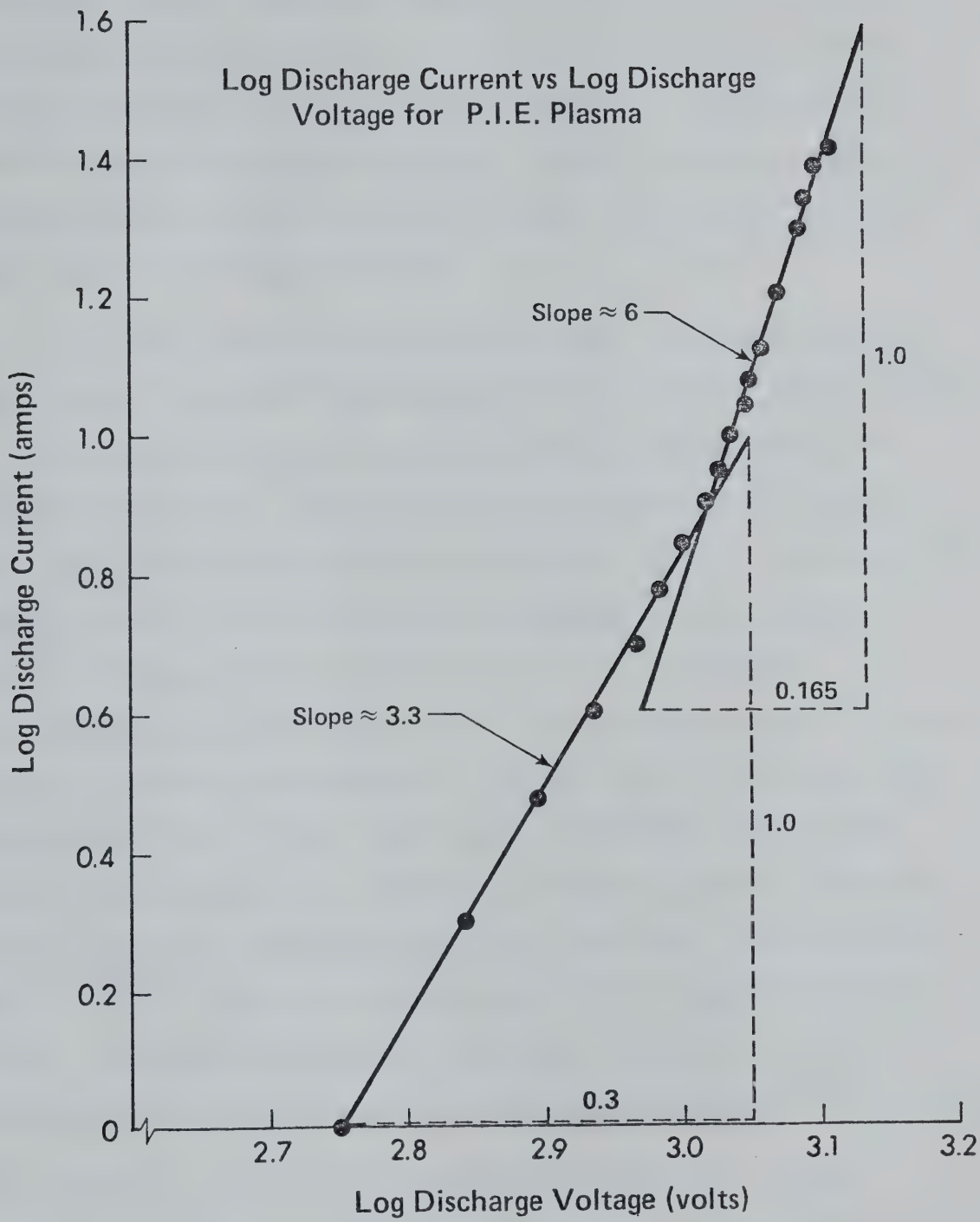


Figure 3-48 Log-Log Plot of V-I Characteristics of the P.I.E. Laser

on a log-log format. The data is seen to be well fitted by two lines of considerably different slope. For discharge currents up to about 7 amps. the sustainer current is proportional to $V^{3.3}$. Above this level V^6 fits the experimental data well. Where V is the sustainer discharge voltage. This 7A is on the boundary of the pulser sustained region and the self-sustained region.

The initial slope is somewhat remote from a linear V-I characteristic expected in a true "pulser-sustained" mode. The experimental result, $V^{3.3}$, could be the influence of a plasma density gradient within the interelectrode region. Nonuniform U.V. illumination and the relatively short range photoionization process could account for this discrepancy⁽²⁸⁾. However, the near abrupt transition in discharge current dependence of V^6 near 1 kV is more difficult to interpret. It is nevertheless conceivable, even in this relatively low field-pressure regime (2.3 kV/cm-atmos.) of operation and especially in the vicinity of the cathode, that the sustainer field-strength could provide sufficient energy via the cathode fall potential for collisional ionization by cathode electrons. Such a process would provide an additional source term in the electron swarm^(93, 104). This term is combined with the U.V. source term and jointly multiplied by the impulse discharge. The glow on the pin ballasted cathode exhibits an abnormal glow characteristic upon first appearance. This can be understood by recalling the definition of an abnormal glow⁽⁹²⁾ which is presented in Section 3-1-3, and the shape of each pin. Each pin has a negligible flat portion. Consequently, the current dependence of V^6 can be attributed to the abnormal glow process. This result is consistent with that of the abnormal glow discharge of Reference 92.

Figure 3-49 shows the plasma and the ballasting impedance changes with current. It reveals that the ballasting impedance was much less than that of the second electrode configuration (276 pin cathode). However, the plasma impedance remained the same. This result suggests that the pin density does not change the plasma impedance very much as long as the current density (A/cm^2) is maintained the same.

3-4-2 Spatial Gain Profile and Discharge Characteristics

The spatial gain profile, measured in the flow direction, is illustrated in Figure 3-50. Curve 'A' represents the gain profile measured with the third electrode configuration. Curve 'B', the gain profile for the second electrode configuration is redrawn from Figure 3-34 for comparison purpose. The gain profiles of Figure 3-50 can be altered at will by adjustment of the fluid gap spacing.

The decrease in the total gain in the downstream direction coincides with the current distribution profile shown in Figure 3-51. This result is compared with that of other workers^(35,48) in which the downstream side of the electrodes carry the greater part of the discharge current. However, in this case the current on the downstream side is unnecessarily small due too much incremental ballasting resistance in the flow

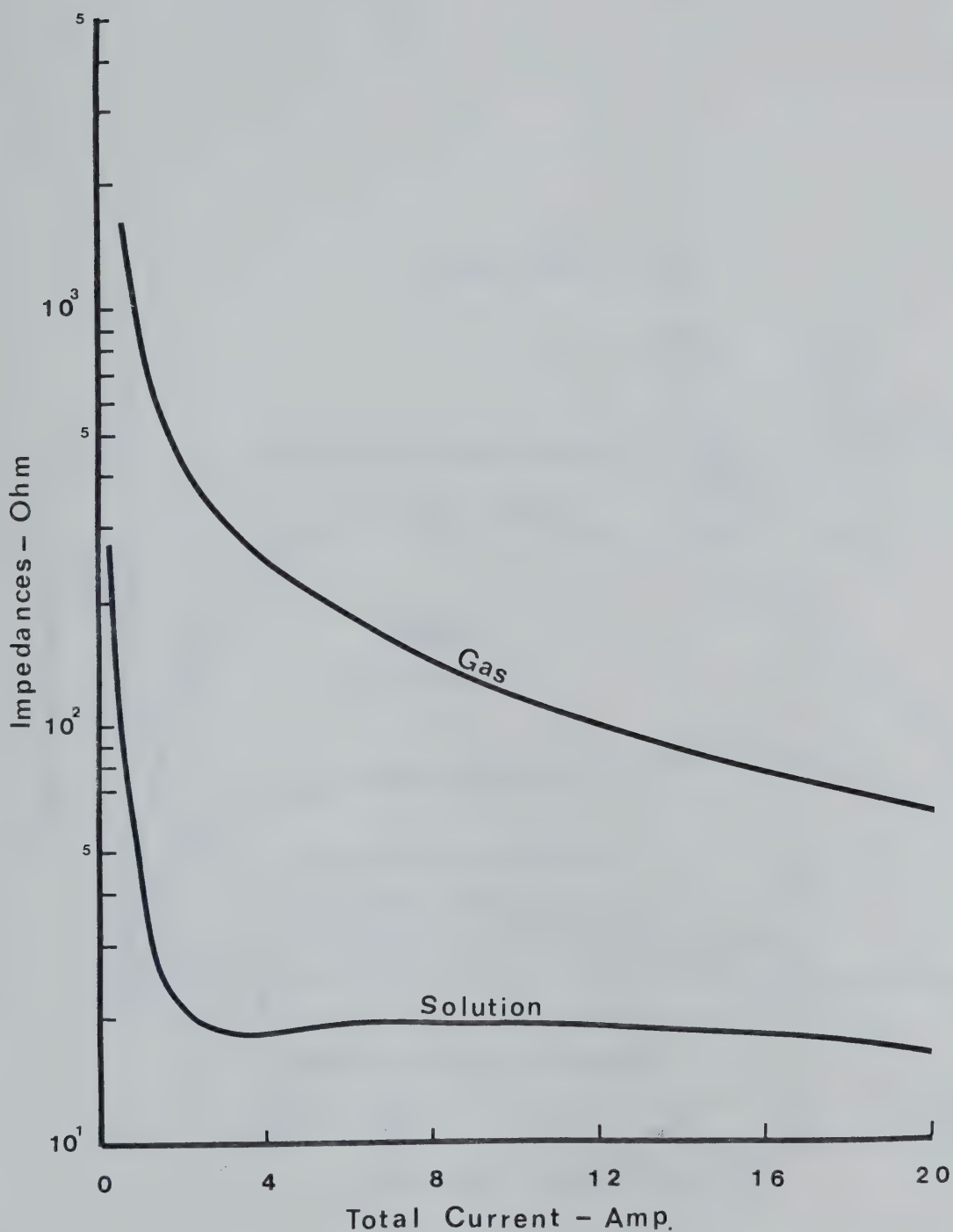


Figure 3-49 Laser Plasma Impedance vs. Discharge Current
 $\text{CO}_2:\text{N}_2:\text{He} = 1.7:7.3:36$ (torr), Flow - 50m/sec
Pulser - 10kHz at 11kV

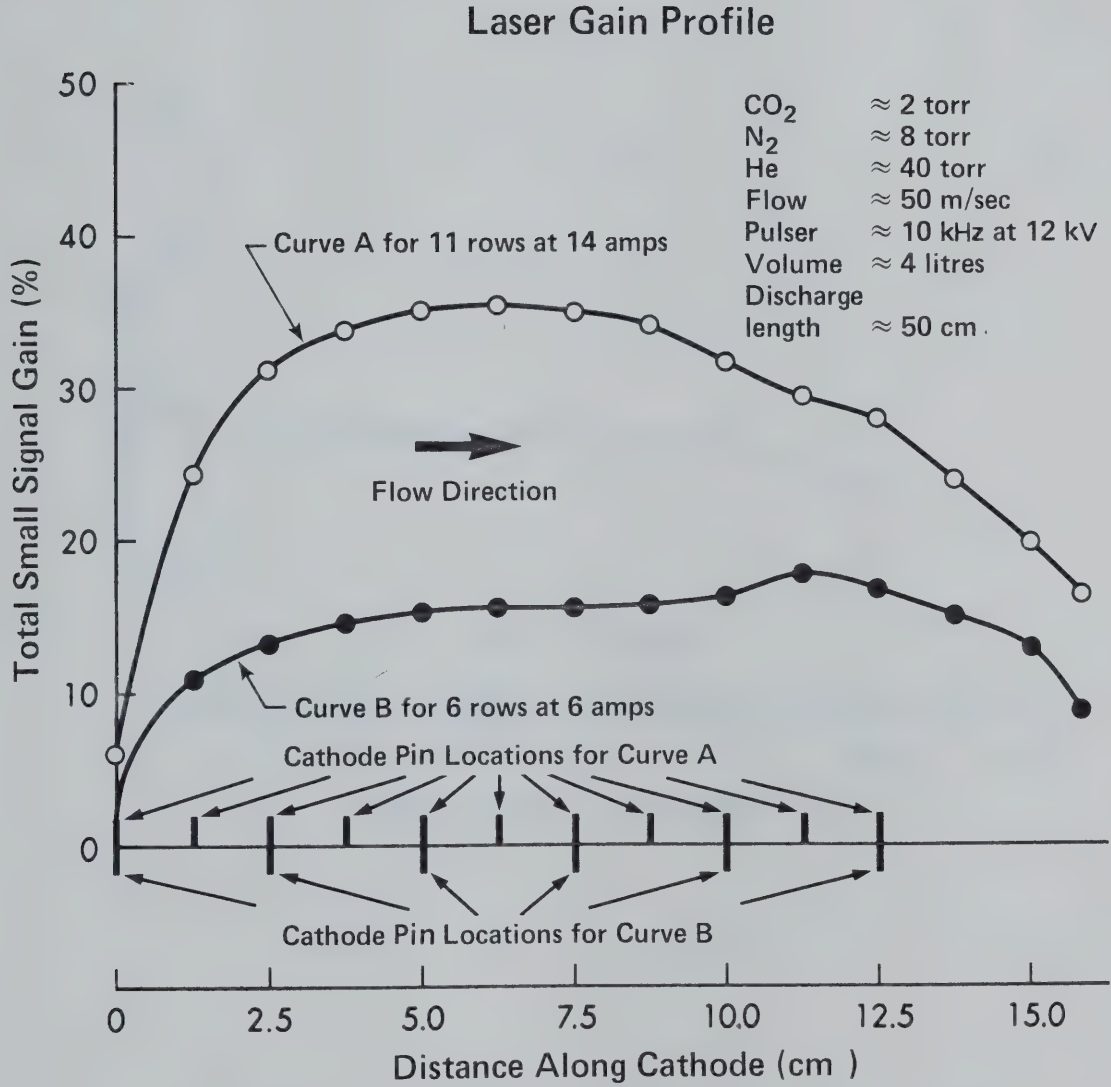


Figure 3-50 Spatial Gain Profile in the Direction of Flow

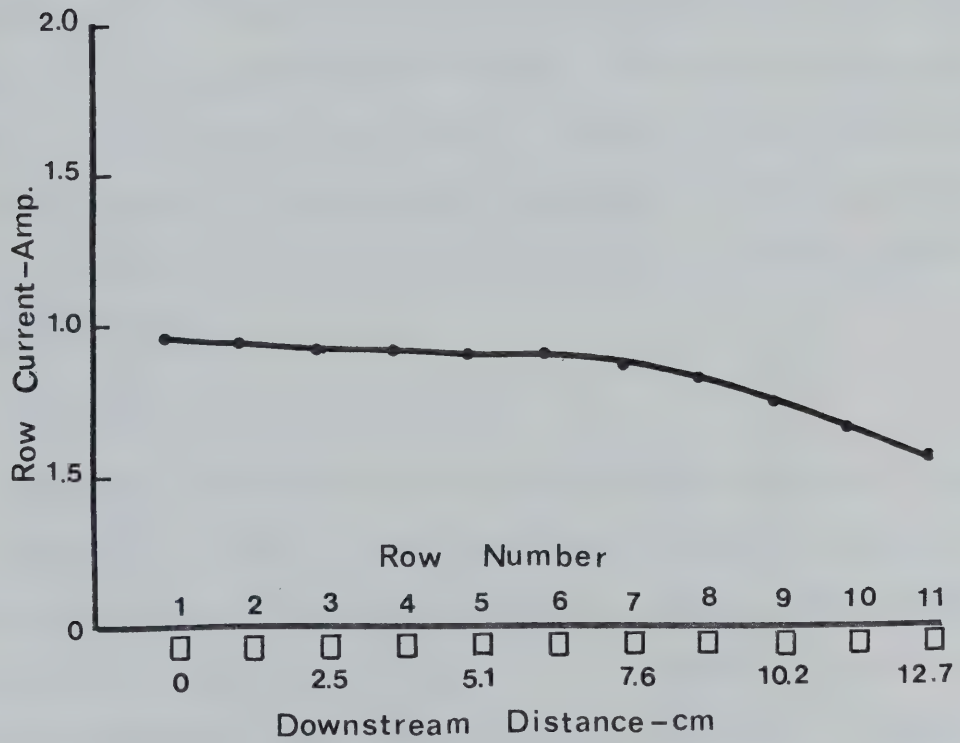


Figure 3-51 Spatial Current Distribution
 $\text{CO}_2:\text{N}_2:\text{He} = 1.7:7.3:40$ (torr), Flow - 50m/sec
 Pulser - 10 kHz at 13kV, Total current - 10A

direction. The current distribution and consequent gain profile will be improved with time by the self-optimizing tendency as explained in Section 2-1-9.

The current distribution profile is understood by reviewing the distribution of the ballasting resistance. Figure 3-52 shows the ballasting resistance per pin as a function of the gap spacing. The nonlinearity of the ballasting resistance is mainly caused by the different pin surface area immersed into the solution. No adverse effect due to the nonlinear distribution has been observed. However, if one wants to have linear distribution of the ballasting resistance, the fluid gap spacing should be adjusted by moving the current buss instead of changing the pin immersed lengths.

3-4-3 Output Power Characteristics

The temporal behavior of the sustainer current is shown in Figure 3-53. The impulse current is seen here to be negligible in comparison to the steady state dc sustainer component. The dc current shows a small perturbation for about 250 ns after the initiation of each pulse. The resulting optical output power waveform is illustrated in Figure 3-54. The small spike appearing on the dc level indicates that the laser pumping by the pulser is almost negligible so that the optical output power can be assumed as C.W.

A further investigation was made on the long range temporal behaviors of the input power, the output power, and the laser extracting efficiency. The results are plotted in Figure 3-55. The output power dropped off approximately 1% per minute for a 3 minute test period. This is attributed to the input power decrease which resulted from the inclusion of small gas bubbles in the solution and the gas impedance change.

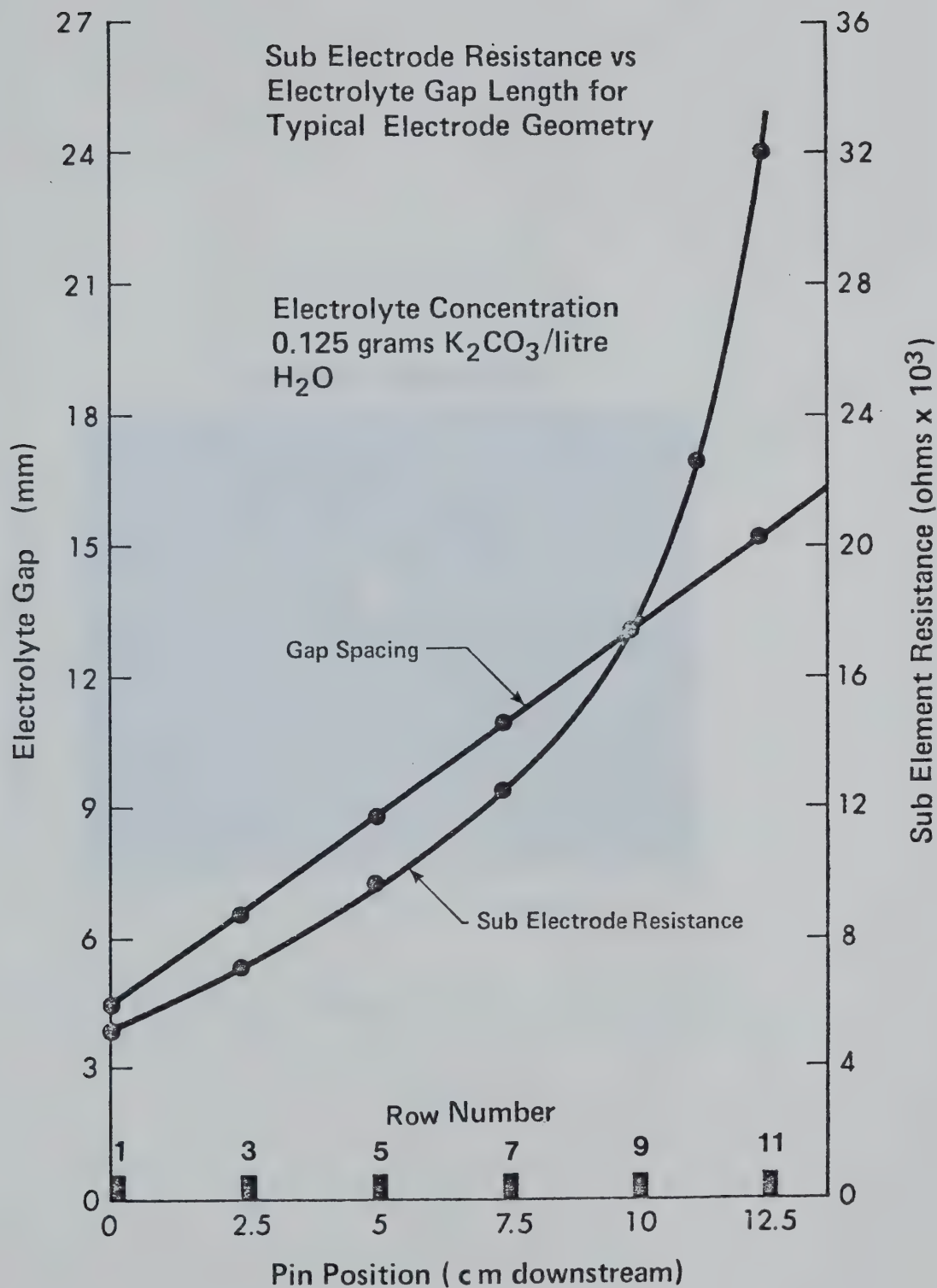


Figure 3-52 Subelement Ballasting Resistance and Fluid Gap Spacings

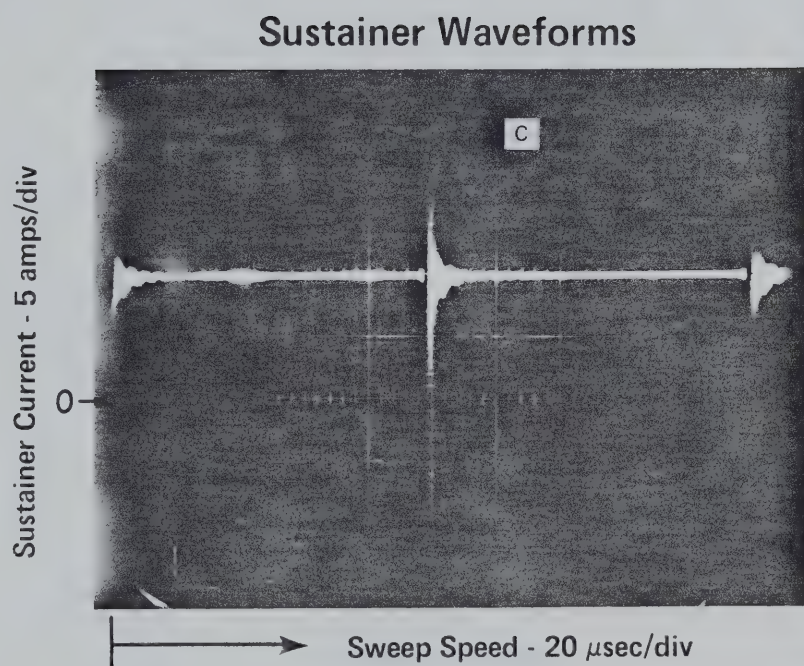


Figure 3-53 Temporal Behavior of Sustainer Current (Long)

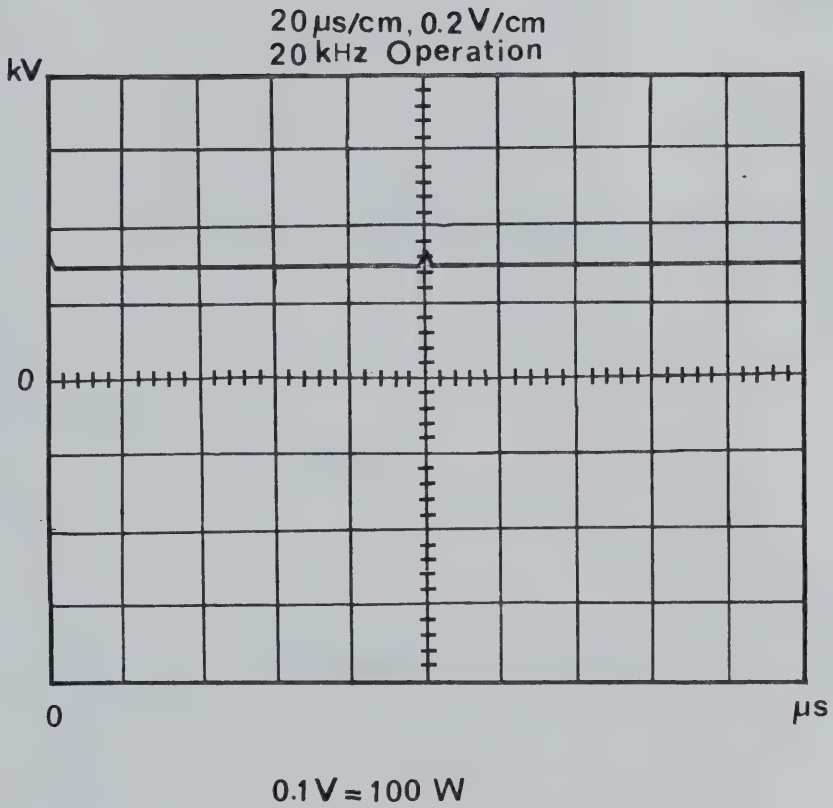


Figure 3-54 Temporal Behavior of Laser Power Output (Long)

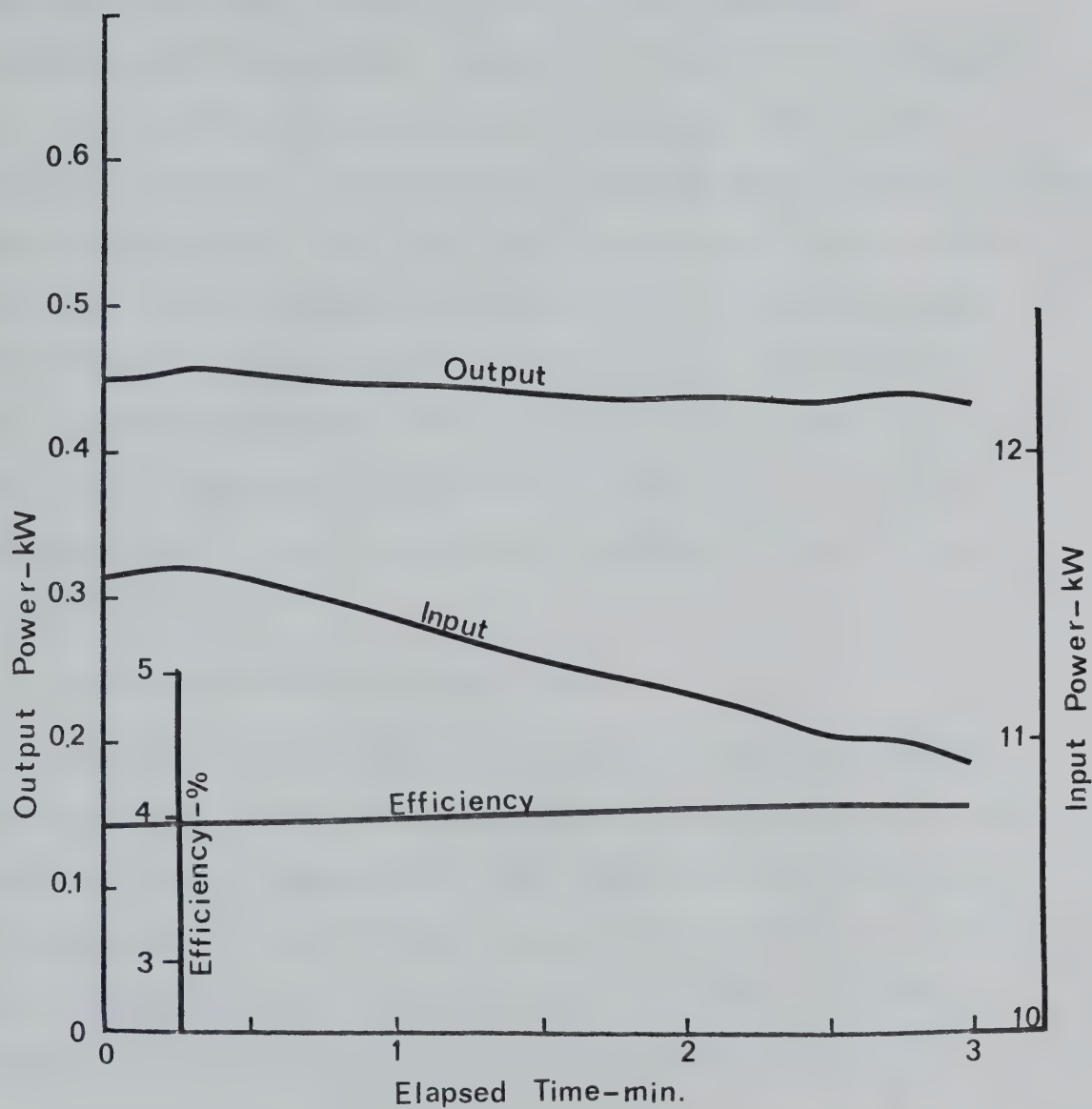


Figure 3-55 Temporal Behavior of Input Power, Output Power and Efficiency
 $\text{CO}_2:\text{N}_2:\text{He} = 1.7:7.3:40$ (torr), Flow - 50m/sec
 Pulser - 10 kHz at 13 kV

However, the power extraction efficiency remained the same. This clearly indicates that under this operating condition, neither contaminants nor temperature plays an important role in laser operation.

Considering that the system was operated in a closed cycle configuration, the constant efficiency is an asset of this system. The low power extraction efficiency is due to the water damaged mirror surfaces and reasons described previously. The linear relationship between the input power and output power is illustrated in Figure 3-56. The maximum output power of 1200 W obtained with 25 kW discharge input power yields 5% power extraction efficiency. The improvement in this case is due to better mirror alignment and a repolished output mirror. The linear dependence suggests that the system can be operated at higher input-output power levels.

3-4-4 Material Processing Experiments

The "Material Processing" mainly includes cutting, welding and drilling in this section. The acceptance by industry of the high power laser for material processing was first reported in the United States by Locke et al.⁽⁷⁷⁾, and a further progress report was made in 1974⁽⁷⁹⁾. More recently, the United States Air Force justified the economics of laser cutting over conventional aerospace cutting methods⁽⁸⁰⁾.

In order to demonstrate the potential of lasers for material processing, various qualitative experiments were conducted utilizing the laser developed for this project. The optical system used for the experiments was the basic 5-pass optical resonator with a Zn-Se output mirror, and an NaCl lens with a 50cm focal length. The beam was focused to a diameter of approximately 1.0 mm, resulting in a power density of $1.3 \times 10^5 \text{ W/cm}^2$.

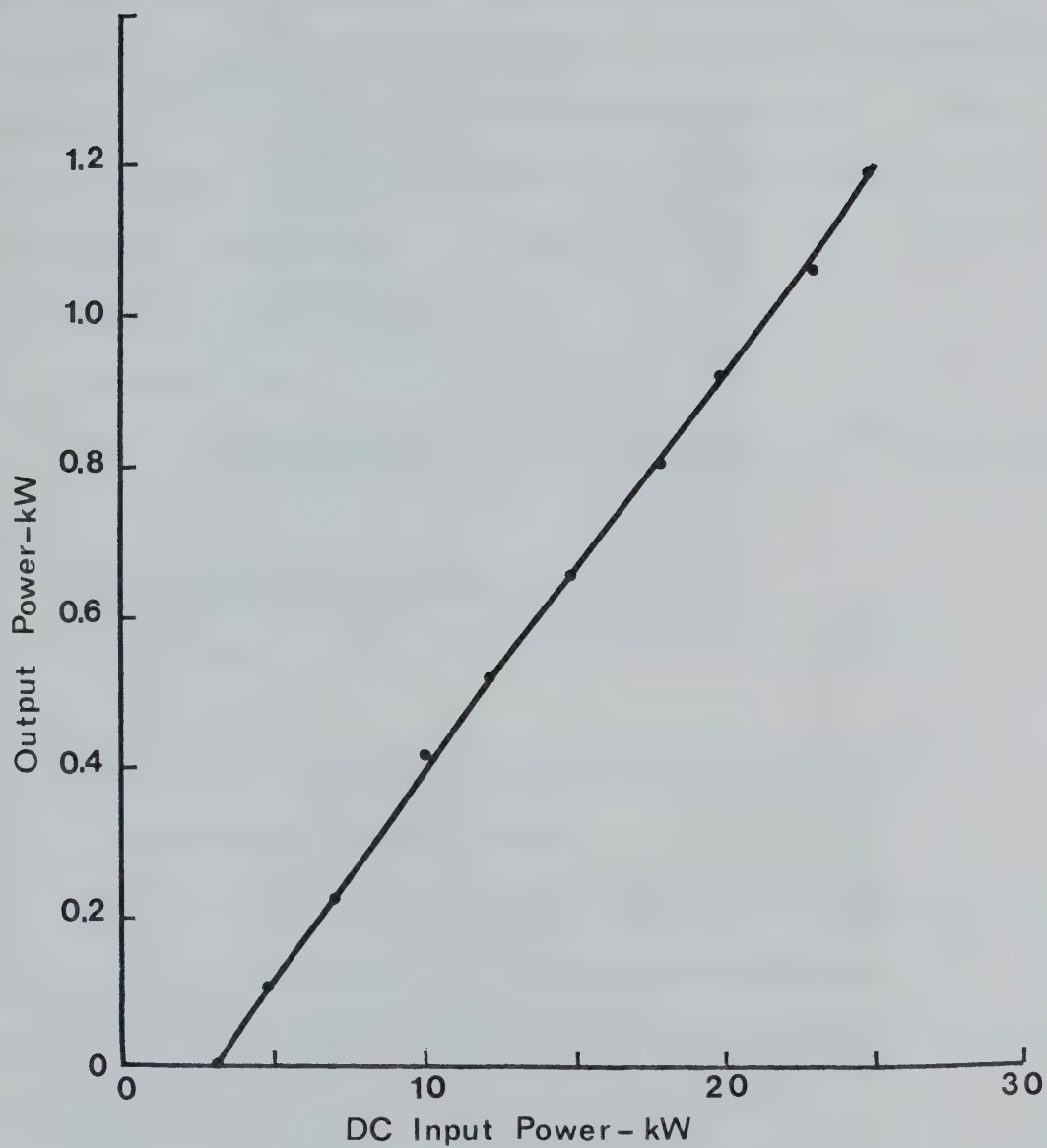


Figure 3-56 Input-Output Power Characteristic
 $\text{CO}_2:\text{N}_2:\text{He} = 1.7:7.3:36$ (torr), Flow - 50m/sec
Pulser - 10kHz at 13kV

In these experiments, the laser beam was brought to the focusing NaCl lens, which was 1.5 m away from the output mirror, through the atmosphere. A funnel designed to supply a working gas to the work-piece, enclosed the laser beam up to 2 cm before the focal point. A remote control adjustment allowed the work piece to be moved vertically or horizontally perpendicular to the laser beam axis. Also, a rotating chuck was provided for welding.

a) Laser Cutting

The three techniques for high power laser cutting⁽⁷⁹⁾ are listed below:

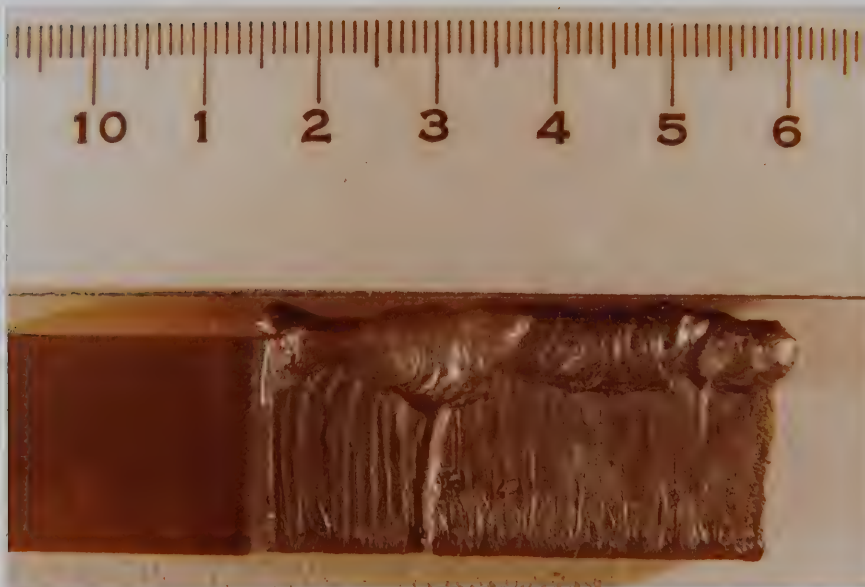
- 1) Vaporizing the cut region.
- 2) Melting and blowing away the molten material with an inert gas.
- 3) Melting and blowing away the molten material with a reactive gas, usually oxygen.

The third technique is the most effective since extra energy is generated from an exothermic reaction between an active gas and the hot metal. For this reason the third technique was mainly used for metal cutting.

Figure 3-57 shows the photos of the laser cutting and cut-edge of 2 cm thick carbon steel. An oxygen jet was used to cut this thickness at a speed of ~ 30 cm/min. When the first technique was used the maximum thickness that could be cut was about 0.5 cm. The considerable slag adhesion to the opposite edge of the beam signifies that the oxygen jet stream was not fast enough. The low jet stream is attributed to the low pressure used and $\sim 30^\circ$ jet angle to the cutting edge. The work



(a)



(b)

Figure 3-57 Laser Cutting of 2 cm Carbon Steel

a) Cutting Operation

b) Cut Edge

piece was fed manually. The cut-edge will become smoother with automatic feeding.

Fire brick, concrete block, glass and ceramic plate exhibit almost the same characteristics in laser cutting. The molten puddle assumed a highly reflective glass-like state and further penetration of the laser beam was difficult. Therefore, for effective cutting of these materials, a blowing gas or a mechanical means of removing molten material was required. Laser cutting may also have potential in surgery, especially amputation surgery as verified by tests on a meat bone. A 2 cm thick bone was cut at a speed of 60 cm/min.

b) Laser Welding

Laser welding is known to be very effective because of the ability for deep penetration and high speed welds. The penetration depth can be compared with an electron beam weld, however, laser welding is considered to be superior to electron beam welding in the sense that the laser beam can be transmitted through the atmosphere, or through various gases without much attenuation⁽⁷⁹⁾.

Figure 3-58 is a photo of a laser weld conducted with 3 mm wall stainless steel pipe. The butt-joint was welded in a vertical position. The complete fusion penetration welding was performed at a speed of 10 cm/min. The weld does not show any sign of beading. The probability of impurity inclusion is very low, since filler metals were not used in this laser welding process. The heat affected zone is very narrow (<1 cm) and this situation will be still more improved with higher power density.

The problems encountered in laser welding are the reflection of the beam from the metal surface and energy absorption by the plume of

vaporized material. Fortunately, as the temperature of the surface increases, reflectivity generally decreases with a corresponding increase in absorptivity⁽⁵⁶⁾. The absorptivity can also be improved by coating the work piece. The plume of vaporized material can be deflected to avoid the incoming laser beam by flushing the working surface with a shielding gas.

c) Laser Drilling

A laser drilling process is simple but potentially important for industrial applications. The results of early investigations of hole drilling are well documented in Reference 56.

A common characteristic of the laser drilled holes found in this experiment, is that the holes are tapered with a larger diameter at the entrance. This effect is much more pronounced in deep holes. This fact can be explained by assuming a laser beam impinging on the surface of the work piece with uniform power density. After a small incremental time, Δt , the laser beam is specified to have drilled a depth of Δh . Here after the beam power at the boundary acts on the hole surface ($2\pi r \Delta h$) as well as the beam front. As a result, the hole becomes slightly tapered. The situation is more aggravated as the hole deepens because the side wall behaves as a "light pipe" that causes refocusing of the beam. This effect was experimentally verified by 13 cm deep holes drilling through a perspex plate.

Figure 3-59 shows the holes pierced through 2.5 cm thick asbestos plate. Two holes perpendicular to the paper are 2.5 cm deep. The deep hole drilled parallel with the paper is demonstrated by a rod passing through it. Deep hole drilling was performed on a concrete block

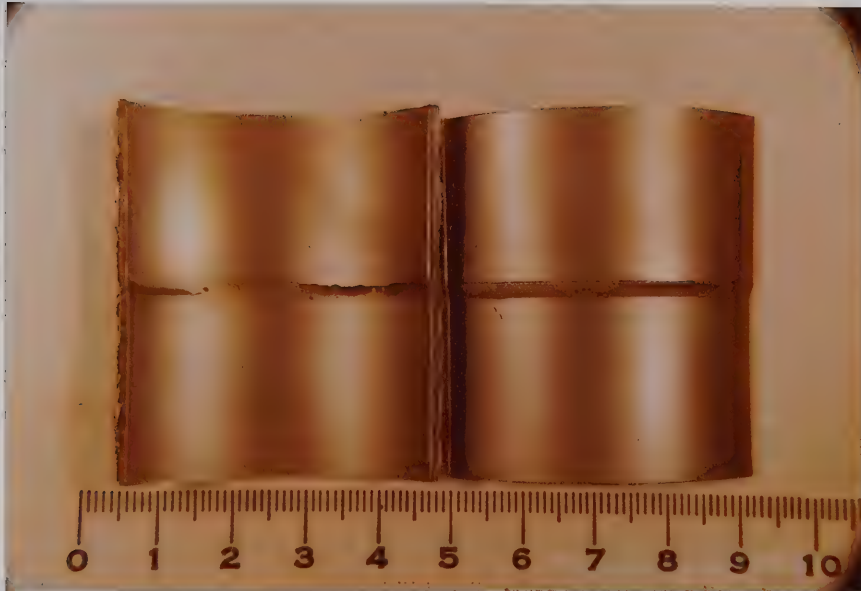


Figure 3-58 Photo of Butt-joint Laser Weld - 1 pass
3 mm Wall Stainless Steel Pipe

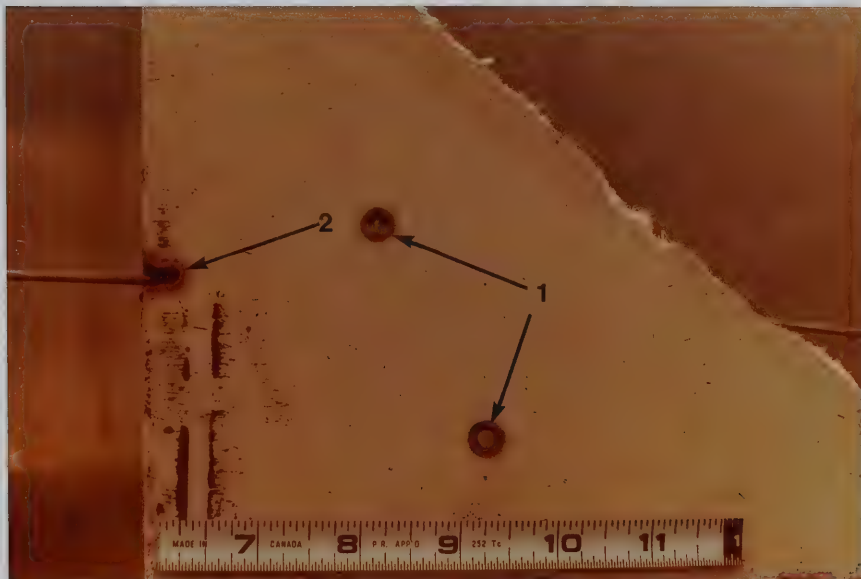


Figure 3-59 Photo of Laser Drilled Asbestos Plate

1. Perpendicular to Paper
2. Parallel With Paper

(~ 6 cm), a perspex plate (~ 13 cm), a salt block (~ 14 cm), and a coal chunk (~ 15 cm). For concrete drilling, the molten material was removed by mechanical means. To drill a clean hole through organic material (perspex or coal) extra care should be exercised. Otherwise the gasified organic materials will burn fiercely, damaging the entrance aperture. An NaCl block in its natural state was found to be completely opaque to the $10.6\text{ }\mu\text{m}$ laser beam. More than 90% of the material vaporized and escaped from the hole. As the hole deepened, the molten material was spewed out with these vapors like a volcanic eruption. The vapors did not seem to absorb laser energy significantly, and re-crystallized outside the hole.

The general trend of the deep hole drilling action is illustrated in Figure 3-60. The maximum depth achievable with a given laser power density depends upon the material and working environment. The working environment such as temperature or drilling position is important for efficient drilling. At the maximum depth the energy removed by loss mechanisms balances the incident laser energy, and the curve becomes flat signifying that no further drilling is achieved.

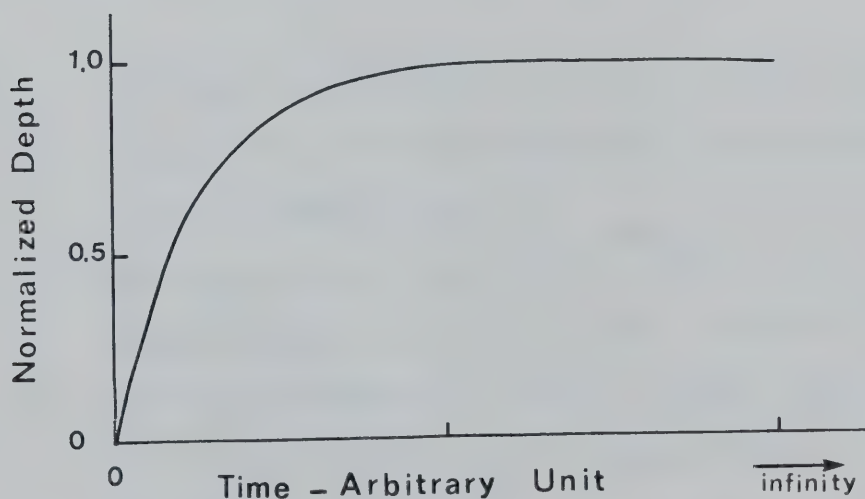


Figure 3-60 Hole Depth vs. Drilling Time

CHAPTER 4

P.I.E. LASER THEORETICAL MODELING

This P.I.E. laser model presented here, is based on the five temperature model of Manes and Seguin⁽⁹⁴⁾, with an extension for the effect of CO produced by the CO_2 dissociation in the electric discharge^(37,97). The CO concentration under continuous electric discharge can reach as high as 50% in a closed system⁽³⁷⁾, and 10% in a flow system⁽⁷²⁾. In order to reflect the substantial translational temperature gradient in the flow direction under C.W. operation, each relaxation coefficient includes the translational temperature term⁽⁹⁷⁾. The characteristics of the active medium of a continuous-flow CO_2 laser are included to describe the spatial dependence of the gain parameter along the flow direction. The cavity field intensity equation is modified to include the effect of the flow, the output coupling, and losses of the multipass optic system.

4-1 Approximations Made for the Theoretical Modeling

To simplify the calculations, the following approximations are made:

1. The energy exchange among the levels of a mode is so rapid that Boltzmann equilibrium can be assumed for each vibrational mode⁽⁹⁴⁾.
2. The heated gas has enough time to expand so that the gas pressure is constant in time and space⁽⁴⁸⁾.
3. Spontaneous emission and particle diffusion rates are so small that they can be neglected except for the initial radiation⁽⁴⁸⁾.

4. The electron density is uniform in the direction transverse to electron drift and gas flow⁽³⁵⁾.
5. Each vibrational mode can be represented as a perfect harmonic oscillator⁽¹¹⁾.
6. The flow is fast enough to prevent building up of quenching molecules that reduce the N_2 metastable or 2-step ionization of N_2 ⁽¹⁰⁾.
7. Ionization and dissociation of CO_2 from the upper laser level by the pulse discharge is comparable to that from the lower laser level.
8. The water content can be neglected.
9. The preionizing input power is so small that (typically less than 5% of the sustainer input power) the parameter variation with time can be neglected.

4-2 Energy Balance Equations

The five-temperature model for a time-dependent TEA laser has been modified for a continuous-flow P.I.E. laser by incorporating terms describing the effects of flow velocity, translational temperature and CO. It can be assumed that the time dependent electron density is spatially uniform because the pulse preionizing energy is adjusted such that current density is uniform in the flow direction. However, due to the non-zero relaxation times, the rate of change in the stored energy of each vibrational mode is spatially dependent. Consequently, the energy balance equations should include two independent variables; the downstream distance, x , and the time, t . Assuming that the energy density $E_i(x,t)$ (erg/cm³) of the "i" species is a function of time and the downstream distance, the rate of change in the energy density is the total derivative expressed by:

$$\begin{aligned} \frac{d E_i(x,t)}{dt} &= \frac{\partial E_i(x,t)}{\partial t} + \frac{\partial E_i(x,t)}{\partial x} \frac{dx}{dt} \\ &= \frac{\partial E_i(x,t)}{\partial t} + \frac{\partial E_i(x,t)}{\partial x} U \end{aligned} \quad (4-1)$$

where U represents the flow velocity. This equation constitutes the left hand side of the energy balance equations. In the energy balance equations $E_i(x,t)$ is denoted by E_i for convenience.

The time rate of change of the vibrational energy, E_i , of each mode of oscillation is described by the Landau Teller equation as follows⁽⁹⁸⁾:

$$\frac{d E_i}{dt} = \frac{E_i - E_i^e(T_i)}{\tau} \quad (4-2)$$

where $E_i^e(T_i)$ is the equilibrium energy at the vibrational temperature T_i , and τ is the time required for the difference $E_i - E_i^e(T_i)$ to fall to $1/e$ of its initial value. The equation (4-2) shows that the vibrational energy always tends toward an equilibrium value.

E_1 represents the energy per unit volume (erg/cm^3) stored in the CO_2 symmetrical mode which contains the lower laser level, (10^0) . The rest of the symbols will be defined later.

$$\begin{aligned} U \left[\frac{\partial E_1}{\partial x} \right] + \frac{\partial E_1}{\partial t} = & N_e(x,t) F_{N_{\text{CO}_2}} h\nu_1 X_1 - \frac{E_1 - E_1^e(T)}{\tau_{10}(T)} \\ & - \frac{E_1 - E_1^e(T_2)}{\tau_{12}(T_2)} + \left(\frac{h\nu_1}{h\nu_3} \right) \left[\frac{E_3 - E_3^e(T, T_1, T_2)}{\tau_3(T, T_1, T_2)} \right] \\ & + \frac{h\nu_1}{h\nu_5} \left[\frac{E_5 - E_5^e(T, T_1, T_2)}{\tau_5(T, T_1, T_2)} \right] + h\nu_1 \Delta N W I_v \end{aligned} \quad (4-3)$$

The first term on the right hand side represents the energy gain of the symmetric vibrational mode by electron pumping. The energy gained through vibrational-vibrational (V-V) relaxation into this mode from the higher vibrational modes is added to the electron pumping energy. The energy loss through V-T (vibrational-translational) and V-V relaxation is represented by the second and third terms. Stimulated emission also contributes to the energy gain of the

symmetrical vibrational mode and is represented in the equation by the last term. The rate of energy density change of the CO_2 bending mode (E_2) is expressed as follows:

$$\begin{aligned}
 U \left(\frac{\partial E_2}{\partial x} \right) + \frac{\partial E_2}{\partial t} = & N_e(x,t) F N_{\text{CO}_2} h\nu_2 X_2 + \frac{E_1 - E_1^e(T_2)}{\tau_{12}(T_2)} \\
 & - \frac{E_2 - E_2^e(T)}{\tau_{20}(T)} + \frac{h\nu_2}{h\nu_3} \left[\frac{E_3 - E_3^e(T, T_1, T_2)}{\tau_3(T, T_1, T_2)} \right] \\
 & + \frac{h\nu_2}{h\nu_5} \left[\frac{E_5 - E_5^e(T, T_1, T_2)}{\tau_5(T, T_1, T_2)} \right] \quad (4-4)
 \end{aligned}$$

On the right hand side, the second term is the energy obtained from fermi-resonant symmetric mode, the third term is the energy released to the translational state by the V-T relaxation and the fourth and fifth are the energies obtained through V-V relaxations from the upper laser level, and CO at $V=1$ respectively.

The energy density (erg/cm^3) stored in the CO_2 asymmetric mode is designated by E_3 . The rate equation for E_3 is expressed by:

$$\begin{aligned}
 U \left(\frac{\partial E_3}{\partial x} \right) + \frac{\partial E_3}{\partial t} = & N_e(x,t) F N_{\text{CO}_2} h\nu_3 X_3 - \frac{E_3 - E_3^e(T, T_1, T_2)}{\tau_3(T, T_1, T_2)} \\
 & + \frac{E_4 - E_4^e(T_3)}{\tau_{43}(T)} + \frac{h\nu_3}{h\nu_5} \left[\frac{E_5 - E_5^e(T, T_3)}{\tau_{53}(T, T_3)} \right] \\
 & - h\nu_3 \Delta N W I_v \quad (4-5)
 \end{aligned}$$

Energy contributions are made by electron pumping, resonant transfer from the first vibrational mode of N_2 ($V=1$), and the V-V relaxation of first vibrational mode of CO ($v=1$). The main energy drain processes are V-V relaxation to the lower laser levels and stimulated emission.

The energy density for N_2 , E_4 , decays dominantly by resonant transfer to the CO_2 asymmetric mode. Other relaxation processes are neglected without much error.

$$U\left(\frac{\partial E_4}{\partial x}\right) + \frac{\partial E_4}{\partial t} = N_e(x,t) N_{N_2} h\nu_4 X_4 - \frac{E_4 - E_4^e(T_3)}{\tau_{43}(T)} + \frac{h\nu_4}{h\nu_5} \left[\frac{E_5 - E_5^e(T, T_4)}{\tau_{54}(T, T_4)} \right] \quad (4-6)$$

E_5 is the energy density (erg/cm^3) stored in the CO vibrational mode.

$$U\left(\frac{\partial E_5}{\partial x}\right) + \frac{\partial E_5}{\partial t} = N_e(x,t) (1-F) N_{CO_2} h\nu_5 X_5 - \frac{E_5 - E_5^e(T, T_3)}{\tau_{53}(T, T_3)} - \frac{E_5 - E_5^e(T, T_1, T_2)}{\tau_5(T, T_1, T_2)} - \frac{E_5 - E_5^e(T, T_4)}{\tau_{54}(T, T_4)} \quad (4-7)$$

Electron pumping is the only contribution to the energy gain of E_5 mode while the stored energy decays to all relevant modes through V-V,

or V-T relaxation processes.

Equations (4-3) through (4-7) describe the energy exchange rates among the relevant levels of the gas transport C.W. P.I.E. laser. In order to complete the model, the kinetic energy and the radiation intensity equations are needed.

The total kinetic energy per unit volume, E , can be expressed in terms of the translational temperature, T , as follows^(97,99):

$$E = \left(\frac{5}{2} N_{N_2} + \frac{5}{2} N_{CO_2} + \frac{3}{2} N_{He} \right) kT \quad (4-8)$$

Its rate of change is due to the V-T relaxation of each vibrational mode, the energy defect in V-V relaxation, and direct heating from the gas discharge.

$$\begin{aligned} U \left(\frac{\partial E}{\partial x} \right) + \frac{\partial E}{\partial t} = & \frac{E_1 - E_1^e(T)}{\tau_{10}(T)} + \frac{E_2 - E_2^e(T)}{\tau_{20}(T)} + h \left(\frac{\nu_3 - \nu_2 - \nu_1}{h\nu_3} \right) \\ & \left[\frac{E_3 - E_3^e(T, T_1, T_2)}{\tau_3(T, T_1, T_2)} \right] + h \left(\frac{\nu_5 - \nu_2 - \nu_1}{h\nu_5} \right) \\ & \left[\frac{E_5 - E_5^e(T, T_1, T_2)}{\tau_5(T, T_1, T_2)} \right] + h \left(\frac{\nu_5 - \nu_3}{h\nu_5} \right) \left[\frac{E_5 - E_5^e(T, T_3)}{\tau_{53}(T, T_3)} \right] \\ & + h \left(\frac{\nu_5 - \nu_4}{h\nu_5} \right) \left[\frac{E_5 - E_5^e(T, T_4)}{\tau_{54}(T, T_4)} \right] \end{aligned} \quad (4-9)$$

In a typical pin ballasted laser discharge direct heating is less than 10% of the total heating whereas V-T and V-V heating is over 90% of the total heating⁽⁴⁸⁾. In the P.I.E. laser system under consideration, electrode cooling may compensate, or surpass the direct heating.

For this reason the direct heating and cooling effects were not considered in Equation (4-9).

The cavity radiation intensity, I_v , is expressed by:

$$U \frac{\partial I_v}{\partial x} + \frac{dI_v}{dt} = c v_L \Delta N W I_v - \frac{I_v}{\tau_c} + c h v_c N_{001}^0 P(J) \frac{\lambda_0^2 2 \Delta v_2}{\tau_{sp} A \pi \Delta v_{sp}} \quad (4-10)$$

The last term represents the spontaneous emission which is negligible under continuous operation.

The translational temperature can be calculated by using Equations (4-8) and (4-9). This translational temperature is expected to increase with increasing downstream distance. Consequently, the gas experiences changes of its parameters such as gas density and flow velocity. Since the preionizing input power is less than 5% of the sustainer input, the time dependent influence of the preionizer is neglected. The spatial pressure variation can also be neglected. This is because the gas has enough time to expand in moving a distance of the order of the spatial resolution of the measurements.

This assumption simplifies the variation of gas density and flow velocity with downstream distance, x , so that they can be calculated by the following equations:

$$N_a(x) = N_a(0) \frac{T(0)}{T(x)} \quad (4-11)$$

where $N_a(0)$ and $N_a(x)$ are the number densities of the gas species 'a' at the downstream distance '0' and 'x' respectively. $T(0)$ and $T(x)$ are the translational temperatures:

$$U(x) = U(0) \frac{T(x)}{T(0)} \quad (4-12)$$

where $U(0)$ and $U(x)$ are the flow velocities at the discharge inlet and at a downstream distance 'x'. These gas dynamic equations are incorporated with the energy balance equations to describe the P.I.E. discharge.

4-3 Description of Symbols

The terms appearing in the energy balance equations are explained in the appearing order:

<u>Symbol</u>	<u>Description</u>	<u>Unit</u>
U	Gas flow velocity	cm/sec
x	Downstream distance from the upstream cathode edge	cm
t	Time	sec
E_i	Energy per unit volume stored in the "i" vibrational mode; $E_i(x,t)$ i vibrational mode 1 CO ₂ symmetric 2 CO ₂ bending 3 CO ₂ asymmetric 4 N ₂ vibrational (V=1) 5 CO vibrational (V=1)	erg/cm ³
$N_e(x,t)$	Time and spatial dependent electron density	cm ⁻³
F	$\frac{N_{CO_2} - N_{CO}}{N_{CO_2}}$ CO ₂ fraction	No unit
N_J	Number density of J species J Species CO ₂ CO ₂ N ₂ N ₂ He He CO CO	cm ⁻³

h 6.6252×10^{-27} Planck's constant erg/sec

ν_i Vibrational frequency of Hz

"i" Vibrational mode

ν_1 4.16×10^{13}

ν_2 2.0×10^{13}

ν_3 7.04×10^{13}

ν_4 6.984×10^{13}

ν_5 6.425×10^{13}

ν_L 2.83×10^{13}

X_i Effective electron vibrational excitation rate of "i" mode cm^3/sec

θ_i $h\nu_i/k$ characteristic temperature of "i" mode $^\circ\text{K}$

$E_1^e(T_n)$ $\frac{h\nu_1^{\text{FNCO}_2}}{\exp(\theta_1/T_n) - 1}$ erg/cm^3

the equilibrium value of E_1 at temperature T_n where $n=0$ or 2

$\tau_{mn}(T)$ $\left\{ \sum_{a=1}^4 N_a k_{mn}^a [\exp(-\theta_m/T) - 1] \right\}^{-1}$ sec

the relaxation times which are

expressed as a function of pressure

and temperature from Reference 97 .

The kinetic rate constants,

k_{mn}^a ,s used in this work are summarized

in Table 4-1, where "a" denotes the

gas species;

a Gas Species

1 CO₂

2 N₂

3 He

4 CO

and "mn" represents the
initial and final levels
respectively, involved in
V-V or V-T relaxation.

k 1.38054x10⁻¹⁶ erg/°K

Boltzmann's constant

$\tau_{12}(T_2)$
$$\frac{1 - \exp(-\theta_2/T_2)}{2 \sum_{a=1}^4 N_a k_{12}^a [1 + \exp(-\theta_2/T)]}$$
 sec

Relaxation time associated with
the Fermi resonance between the
CO₂ symmetric and bending modes

T_1
$$\frac{\theta_1}{\ln[\text{FN}_{\text{CO}_2} (h\nu_1/E_1) + 1]}$$
 °K

Effective temperature of the
symmetric mode

T_2
$$\frac{\theta_2}{\ln[\text{FN}_{\text{CO}_2} (2h\nu_2/E_2) + 1]}$$
 °K

Effective temperature of the
bending mode

$$T_3 = \frac{\theta_3}{\ln[FN_{CO_2} (h\nu_3/E_3)+1]} \quad ^\circ K$$

Effective temperature of the a-symmetric mode

$$E_3^e(T, T_1, T_2) = \frac{FN_{CO_2} k \theta_3}{\exp(\frac{\theta_1}{T_1} + \frac{\theta_2}{T_2} + \frac{\theta_3 - \theta_2 - \theta_1}{T}) - 1} \quad \text{erg/cm}^3$$

The equilibrium value of E_3

$$E_5^e(T, T_1, T_2) = \frac{(1-F)N_{CO_2} k \theta_5}{\exp(\frac{\theta_1}{T_1} + \frac{\theta_2}{T_2} + \frac{\theta_5 - \theta_2 - \theta_1}{T}) - 1} \quad \text{erg/cm}^3$$

The equilibrium value of E_5

$$\tau_3(T, T_1, T_2) = \frac{[\exp(\frac{\theta_1}{T_1}) - 1][\exp(\frac{\theta_2}{T_2}) - 1]}{A_3 [\exp(\frac{\theta_1}{T_1} + \frac{\theta_2}{T_2} + \frac{\theta_3 - \theta_2 - \theta_1}{T}) - 1]} \quad \text{sec}$$

The relaxation time of the a-symmetric mode

$$\tau_5(T, T_1, T_2) = \frac{[\exp(\frac{\theta_1}{T_1}) - 1][\exp(\frac{\theta_2}{T_2}) - 1]}{A_5 [\exp(\frac{\theta_1}{T_1} + \frac{\theta_2}{T_2} + \frac{\theta_5 - \theta_2 - \theta_1}{T}) - 1]} \quad \text{sec}$$

The relaxation time of the CO($v=1$) mode

$$A_3 = F \sum_{a=1}^4 N_a k_3^a \quad \text{a constant}$$

$$A_5 = (1-F)k_5 N_{CO_2} \quad \text{a constant}$$

$$\Delta N = N_{00^\circ 1} P(J) - \frac{2J+1}{2J+3} N_{10^\circ 0} P(J+1) \quad \text{cm}^{-3}$$

Number density difference

$$N_{00^{\circ}1} \quad F N_{\text{CO}_2} \exp\left(-\frac{\theta_3}{T_3}\right) \left[1 - \exp\left(-\frac{\theta_1}{T_1}\right)\right] \quad \text{cm}^{-3}$$

$$\times \left[1 - \exp\left(-\frac{\theta_2}{T_2}\right)\right]^2 \left[1 - \exp\left(-\frac{\theta_3}{T_3}\right)\right]$$

Number density of the upper laser
level

$$N_{10^{\circ}0} \quad F N_{\text{CO}_2} \exp\left(-\frac{\theta_1}{T_1}\right) \left[1 - \exp\left(-\frac{\theta_1}{T_1}\right)\right] \quad \text{cm}^{-3}$$

$$\times \left[1 - \exp\left(-\frac{\theta_2}{T_2}\right)\right]^2 \left[1 - \exp\left(-\frac{\theta_3}{T_3}\right)\right]$$

Number density of the lower laser
level

$$w \quad \frac{S_f \lambda_L^2}{4\pi^2 h\nu_2 \tau_{sp} \Delta\nu_L} \quad \text{cm}^2$$

The stimulated emission rate
on the line
center

$$S_f \quad \frac{\text{gain medium volume}}{\text{optical volume}}$$

$$\lambda_L \quad 10.6 \times 10^{-4} \quad \text{laser wavelength} \quad \text{cm}$$

$$\nu_L \quad \frac{c}{\lambda_L} = \frac{2.997926 \times 10^{10}}{10.6 \times 10^{-4}} = 2.828 \times 10^{13} \quad \text{Hz}$$

The laser frequency

$$c \quad 2.997926 \times 10^{10} \quad \text{Speed of light} \quad \text{cm/sec}$$

$$\tau_{sp} \quad 5 \quad \text{sec}$$

Spontaneous relaxation time

$$\Delta \nu_L = \sum_{a=1}^4 \frac{N_a Q_a}{\pi} \left(\frac{8kT}{\pi \mu_t} \right)^{1/2} \quad \text{Hz}$$

The laser transition homogeneous
line width

Q_a	a	species	cm^2
	1	CO_2	1.3×10^{-14}
	2	N_2	1.14×10^{-14}
	3	He	3.7×10^{-15}
	4	CO	1.14×10^{-14}

The collision cross section for
gas species, 'a'

$$\mu_t = \frac{M_{\text{CO}_2} M_a}{(M_{\text{CO}_2} + M_a)} \quad \text{Reduced mass} \quad \text{g}$$

$$M_{\text{CO}_2} = 7.3 \times 10^{-23} \quad \text{g}$$

$$M_{\text{N}_2} = 4.6 \times 10^{-23} \quad \text{g}$$

$$M_{\text{He}} = 4.6 \times 10^{-23} \quad \text{g}$$

$$M_{\text{CO}} = 4.65 \times 10^{-23} \quad \text{g}$$

$$I_v = \text{Cavity field intensity} \quad \text{erg/sec.cm}^2$$

$$\tau_{43}(T) = \{F N_{\text{CO}_2} k_{43}(T)\}^{-1} \quad \text{sec}$$

V-V relaxation time from $\text{N}_2(v=1)$
to upper laser level $\text{CO}_2(00^{\circ}1)$

$$E_4^e(T_3) = \frac{N_{\text{N}_2} \theta_4 k}{\exp(E_4/T_3) - 1} \quad \text{erg/cm}^3$$

the equilibrium value of E_4

$$E_5^e(T, T_b) = \frac{(1-F)N_{CO_2} \theta_5 k}{\exp\left(\frac{\theta_b}{T_b} - \frac{\theta_b - \theta_5}{T}\right) - 1} \quad \text{erg/cm}^3$$

where $b = 3$ or 4

the equilibrium value of E_5

at T_3 or T_4

$$\tau_{5b}(T, T_b) = \frac{\exp\left(\frac{\theta_b}{T_b}\right) - 1}{F N_{CO_2} E_{5b}(T) \left[\exp\left(\frac{\theta_b - \theta_5}{T}\right)\right] \left[\exp\left(\frac{\theta_b}{T_b} + \frac{\theta_5 - \theta_b}{T}\right) - 1\right]} \quad \text{sec}$$

$$P(J) = (2hcB/kT) (2J+1) \exp[-hcBJ(J+1)/kT] \quad -$$

$$P(J+1) = (2hcB/kT) (2J+3) \exp[-hcB(J+1)(2J+3)/kT] \quad -$$

where J is the rotational quantum number,

and B is the rotational constant, 0.389 cm^{-1}

The Boltzmann distribution factors

$$\tau_c = \left(-\frac{2L}{c}\right) \ln R \quad \text{sec}$$

The laser cavity lifetime where

' L ' is the laser cavity length.

For an n -pass system, L becomes $L=n\ell$

where ' ℓ ' is the single path

length. ' R ' is the reflectivity

of the mirrors including the out-

put coupling and is expressed by⁽¹⁰⁰⁾

$$R = (1 - t_r - \ell_{so})(1 - \ell_{s1}) \dots (1 - \ell_{s(n-1)})$$

where t_r is the effective trans-

mittivity of the output mirror,

ℓ_{so} is the mirror loss at the
output mirror and $\ell_{s(n-1)}$ is the
loss at the n_{th} mirror or n_{th} re-
flection

A $0.201^{(48)} \text{ sec}^{-1}$
 $0.187^{(103)}$

The spontaneous transition rate

$\Delta\nu_{sp}$ The spontaneous transition linewidth Hz

TABLE 4-1

TEMPERATURE DEPENDENT RATE CONSTANTS

τ	k_{CO_2}	k_{N_2}	k_{H_2}	k_{CO}
τ_{10}	$2.07 \times 10^{-9} \times \exp(-77/T^{1/3})$	$4.32 \times 10^{-10} \times \exp(-77/T^{1/3})$	$3.65 \times 10^{-10} \times \exp(-77/T^{1/3})$	$3.07 \times 10^{-7} \times \exp(-77/T^{1/3})$
τ_{12}	$8.65 \times 10^{-15} \times T^{3/2}$	$3.68 \times 10^{-16} \times T^{3/2}$	$4.23 \times 10^{-17} \times T^{3/2}$	$3.68 \times 10^{-16} \times T^{3/2}$
τ_{20}	$4.6 \times 10^{-10} \times \exp(-77/T^{1/3})$	$9.6 \times 10^{-11} \times \exp(-77/T^{1/3})$	$8.1 \times 10^{-11} \times \exp(-77/T^{1/3})$	$6.82 \times 10^{-8} \times \exp(-77/T^{1/3})$
τ_3	$9.6 \times 10^{23} \times T^{-5.89} \times F(T)$	$6.87 \times 10^{23} \times T^{-5.89} \times F(T)$	$2.43 \times 10^{23} \times T^{-5.89} \times F(T)$	$6.87 \times 10^{23} \times T^{-5.89} \times F(T)$
<hr/>				
	$k_{CO_2-CO_2}$	$k_{N_2-CO_2}$	$k_{H_2-CO_2}$	k_{CO-CO_2}
τ_1	$8.65 \times 10^{-15} \times T^{3/2}$			
<hr/>				
τ_{43}	Choose Larger One	$1.71 \times 10^{-6} \exp(-175.3/T^{1/3})$		
		$6.07 \times 10^{-14} \exp(15.3/T^{1/3})$		
τ_5				$5.96 \times 10^{-22} \times T^{-5.86} \times F(T)$
τ_{53}				$1.56 \times 10^{-11} \times \exp(-30/T^{1/3})$
τ_{54}			Choose Larger One	$1.78 \times 10^{-6} \exp(-210/T^{1/3})$ $6.98 \times 10^{-13} \exp(25.6/T^{1/3})$

Where $F(T) = \exp\{-4223/T - 672.7/T^{1/3} + 2683/T^{2/3}\}$

4-4 Computer Simulation of the P.I.E. Laser Model

In the preceding sections, the energy balance equations, and the modeling procedures for a continuous wave CO₂ P.I.E. laser have been presented. In this section a procedure of numerical solution of these equations by using System/360, Continuous System Modeling Program (CSMP) is briefly discussed. A detailed description of the method of programming is found in Reference 106. More information was summarized in Appendix A. The program structural segmentation is illustrated in Figure 4-1. The structure statements within the INITIAL segment are calculated only once at 'x' equals zero. Each gas number density, translational and vibrational temperatures, corresponding energies, and all parameters that do not change through the discharge volume are calculated, or are assigned values under the heading of CONSTANT in this segment for initialization.

The structure statements within the DYNAMIC segment describe the dynamics of this model, and the corresponding computations are performed repeatedly, under control of the selected integration routine (Runge-Kutta method), during each run. The temperature dependent rate constants of Table 4-1 are computed with the initial temperature. With the computed rate constants, the relaxation times are calculated. These results and the parameters obtained from the INITIAL segment allow the differential equations to be solved. Upon completion of the energy calculation for each mode, the population inversion, ΔN , and the stimulated emission rate, W , are computed. The small signal gain coefficient, α_0 , is obtained by the following equation:

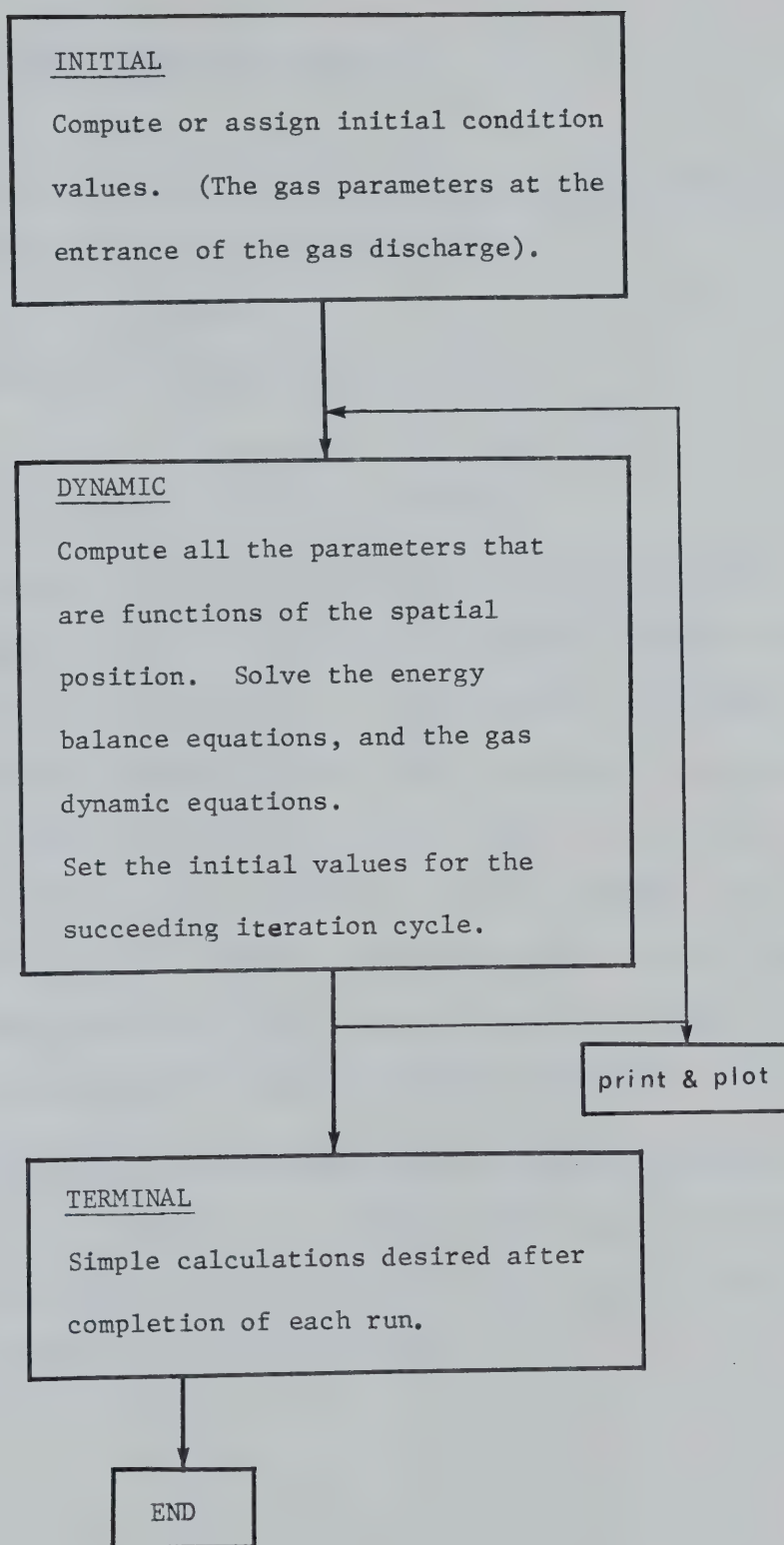


Figure 4-1 CSMP Program Structure

$$\alpha_o = h\nu_L W \Delta N \times 100 \text{ (\%/cm)} \quad (4-13)$$

The symbols are explained in the previous section. The total gain, GAIN, is defined by the following equation:

$$\text{GAIN} = \frac{I_P (e^{\alpha_o L/100} - 1)}{I_P} \times 100 \text{ (\%)} \quad (4-14)$$

where I_P is the probe laser beam intensity.

Before starting the next iteration cycle, the print interval, PREDEL, under TIMER control is tested, and the requested outputs (T , T_1 , T_3 , α_o , GAIN, N_{10^0} , N_{00^1} and ΔN) are printed. Further evaluation for the translational and vibrational temperatures, flow velocity, and number densities is performed. The parameter values obtained in the current iteration cycle are assigned to be input data for the next iteration cycle. The computation recycles with the integration increment, DELT. The recycling terminates when the independent variable, x , meets the maximum condition, FINTIM.

The structure statements within the TERMINAL segment describe the computation or action to be performed upon completion of each simulation run. This segment is automatically entered when the TIME equals FINTIM or any finish condition is satisfied.

4-5 Comparison of the Results With the Experimental Measurements

A good method for testing a laser kinetic model and computer code is to compare the theoretical calculations with the measured values. In this section the previously measured data was replotted to compare with the computer plotted curves. Although the calculation produces many output parameters only several of them were printed and plotted for comparison purposes. The first calculation was conducted with the following conditions. In this calculation CO effects were excluded simply because the degree of dissociation was not known. The simulation was made with the same discharge parameters as used for Figure 3-34. These parameters are summarized as follows:

Electrode Configuration	2nd
Discharge Volume	4ℓ
Electrode Spacing	6cm
CO ₂ :N ₂ :He = 1.7:7.3:36 (torr)	
Sustainer Current	6A
Current Distribution	
actual	unknown
assumption	spatially-uniform
Resonator Status	no mirror

Both calculated and measured total gains were plotted as a function of downstream distance in Figure 4-2. The calculated data was presented in Appendix A under data 1. As shown in Figure 4-2, poor agreement is seen in the vicinity of upstream and downstream pins. The measured results suggest that the upstream and downstream pins carried more than the average current. Unfortunately, individual row currents could

not be measured with this cathode. Except for these two extreme regions the calculated total gain agrees very well with the measured data. This good agreement through a wide spatial range (from 2 to 10 cm) suggests that CO generation by CO_2 dissociation must be small under these discharge conditions.

The second computer calculation was made with the same conditions as for the first calculation, except for the current density, and the electrode configuration:

Electrode configuration	3rd
Sustainer current	14A

Figure 4-3 compares the measured and computed translational temperatures for two different discharge conditions. It is seen from Figure 4-3 that a fair amount of heating energy is removed by electrode cooling, especially for the 14A case. Therefore, the measured translational temperature was used as an input to the program for the second calculation. At this point it is obvious that a cooling energy term should be included in Equation (4-9), however, no attempt was made due to the complexity of estimating the cooling term. The gas flow velocity, expressed by Equation (4-12), is proportional to the gas temperature and therefore the flow velocity can be deduced from Figure 4-3 by replacing 300°K with 50 m/s.

Figure 4-4 shows the computer plotted total gain curve for the P(20) transition along with the measured data curve reproduced from Figure 3-50. The corresponding small signal gain coefficients are illustrated in Figure 4-5. The theoretical and experimental values agree very well, except for the upstream region in which the theoretical

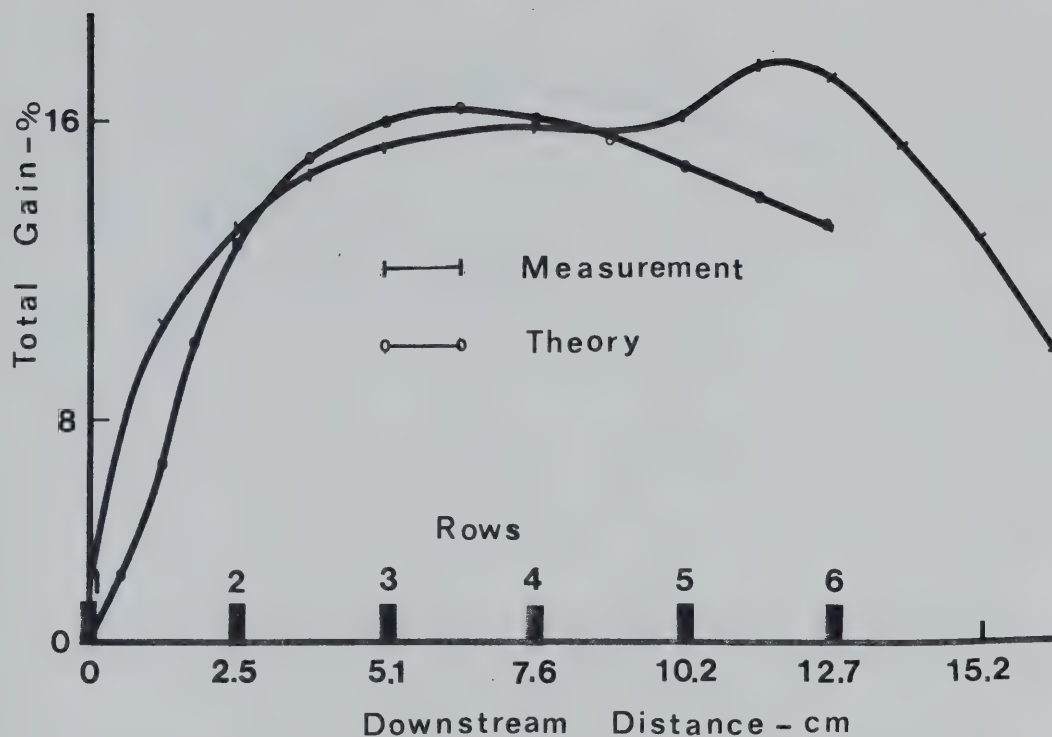


Figure 4-2 Comparison of the Measured Total Signal With the Computed Value

Electrode configuration - 2nd

Discharge volume - 4ℓ

Electrode spacing - 6 cm

$\text{CO}_2:\text{N}_2:\text{He} = 1.7:7.3:36$ (torr)

Total current - 6A

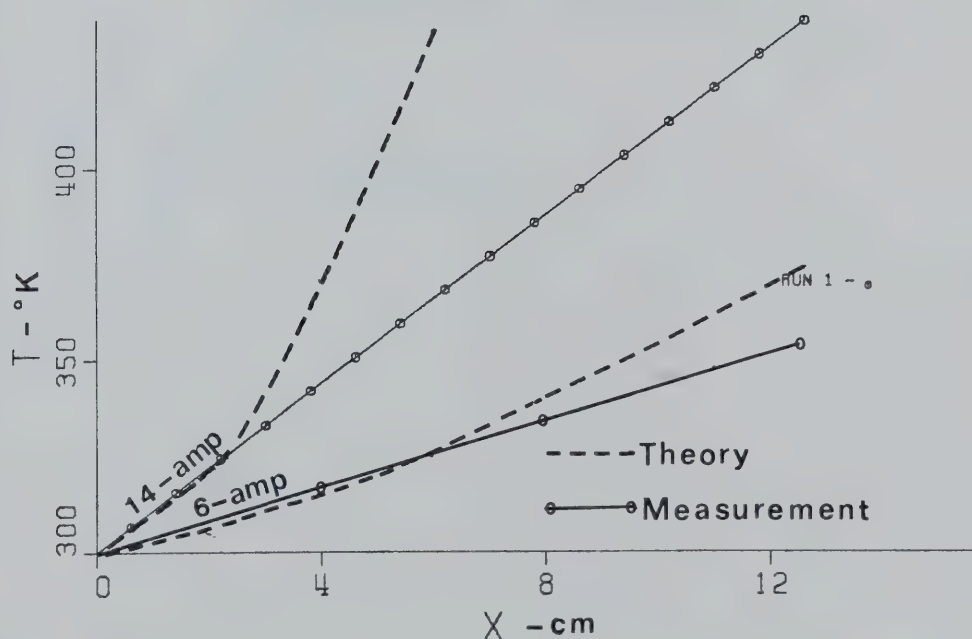


Figure 4-3 Comparison of the Measured Translational Temperature with the Computed Value

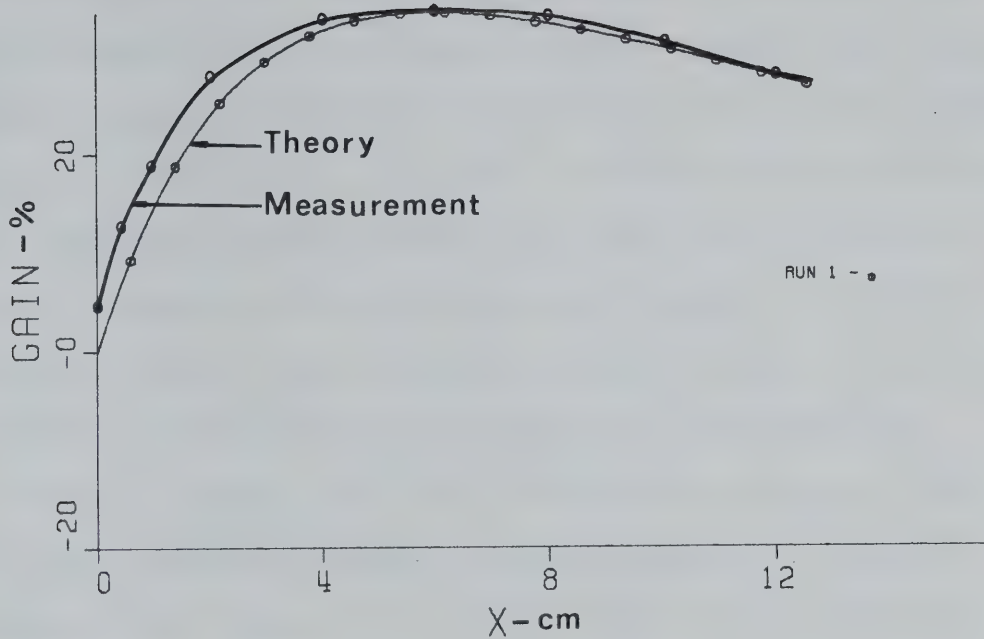


Figure 4-4 Comparison of the Measured Total Signal Gain with Computed Value
 Electrode configuration - 3rd
 Total current - 14A

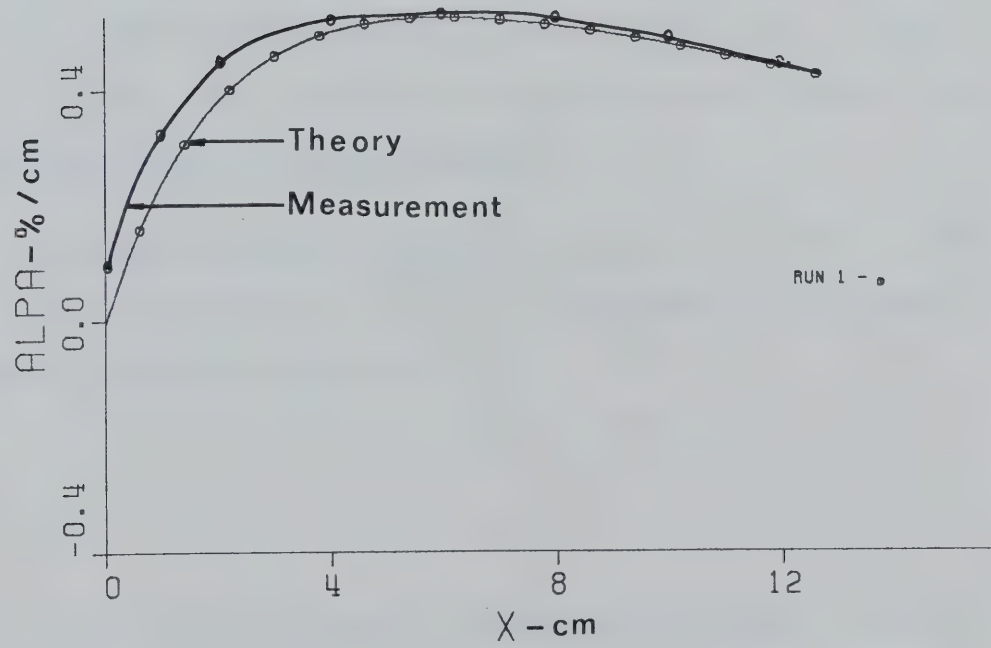


Figure 4-5 Comparison of the Measured Small Signal Coefficient with the Computed Values

values are somewhat low. This discrepancy might have resulted from the underestimation of the upstream-row-current resulting from approximating the measured current distribution (Figure 3-51), by the average current for the calculation. The effect of CO, which was not included in this calculation may also account for a part of this discrepancy. The better agreement on the downstream may be related to the improved E/N as shown in Figure 4-6. A spatially dependent E-field in the discharge can be calculated from the measured current and resistance data of Figures 3-51 and 3-52, while the temperature dependent number density can be estimated from the measured temperature of Figure 4-3 and Equation(4-11). Figure 4-6 is a plot of E/N and input power density as a function of downstream distance, x . Normally the E/N value for this P.I.E. laser is about $1.6 \times 10^{-16} \text{ V-cm}^2$, which is lower than $2 \times 10^{-16} \text{ V-cm}^2$ of COFFEE laser and $3.0 \times 10^{-16} \text{ V-cm}^2$ of the non-flowing self-sustained laser⁽⁴⁸⁾. Figure 4-6 also reveals that the input power density decreases with increasing downstream distance. This situation may be ideal for better operation since the reduced number density may cause a gain saturation at lower values of intensity.

The cavity radiation intensity, I_v in equation 4-10, is made up of the two components, I^+ and I^- , in the positive and negative optical axis (Z-axis) respectively.

$$I_v = I^+ + I^- \quad (4-15)$$

In this optical resonator, the positive direction is defined as the direction from the output mirror to the rear mirror. The 4-mirror 5-pass optical resonator results in a fairly complicated steady-

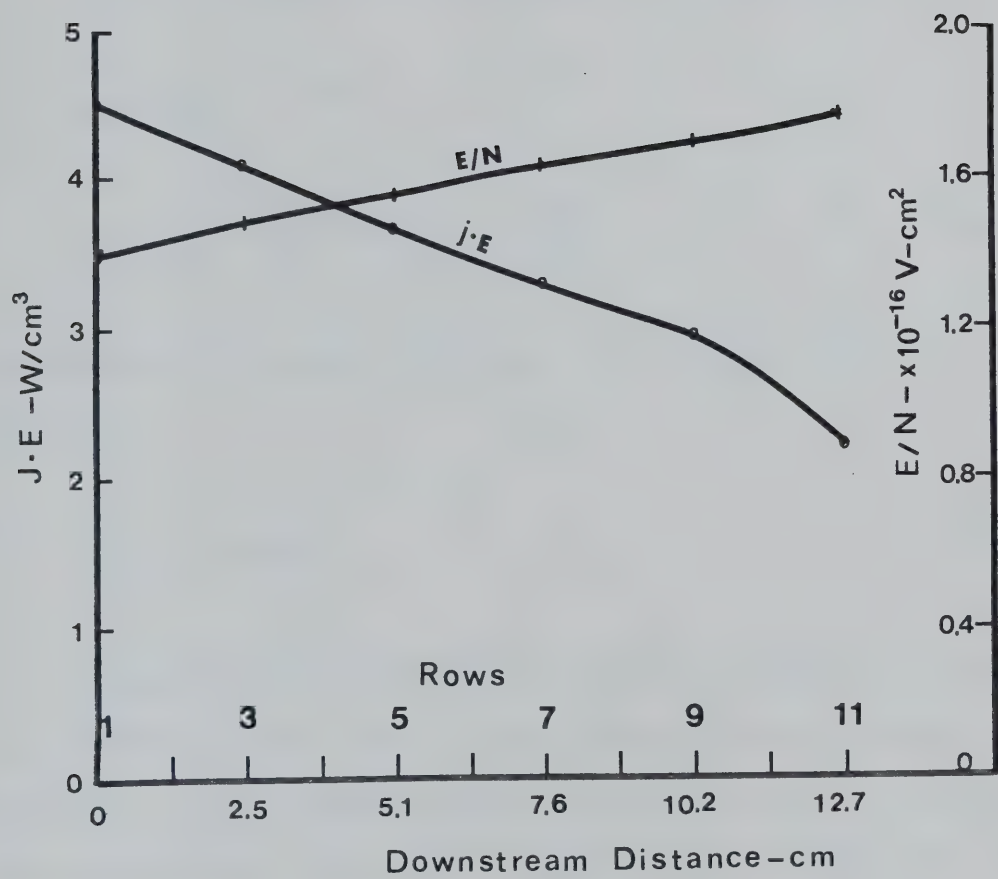


Figure 4-6 Spatial Dependence of E/N and $j \cdot E$

state intensity diagram, as shown in Figure 4-7. Assuming homogeneous laser transitions, the relationships governing laser oscillations in the Rigrod's⁽¹⁰⁰⁾ and Cool's⁽¹⁰²⁾ single-pass laser resonators are generally applicable to this multi-pass system.

The small signal gain coefficient, α , is given by⁽¹⁰²⁾

$$\alpha = h\nu\Delta Nw$$

$$= \left(\frac{1}{I^+} \right) \left(\frac{\partial I^+}{\partial Z} \right) = - \left(\frac{1}{I^-} \right) \left(\frac{\partial I^-}{\partial Z} \right) \quad (4-16)$$

The symbols are described in Section 4-3. From equation (4-16) it is seen that

$$I^+ I^- = \text{Constant} \quad (4-17)$$

Figure 4-7 also shows that the radiation intensities are reduced at each mirror surface due to mirror absorption and scattering. The absorption loss is greatly increased by the intermediate folding mirrors since the radiation intensity at these mirrors is nearly twice that at the output or the rear mirror. Under steady-state oscillation the following relationship exists.

$$\left(\frac{I_L^+}{I_L^-} \right) \gamma_2 = \left(\frac{I_o^-}{I_o^+} \right) \gamma_1 = 1 \quad (4-18)$$

Where 'o' and 'L' denote $Z=0$ and $Z=L$ respectively. γ_1 and γ_2 are the effective reflectances of the output and the rear mirrors respectively.

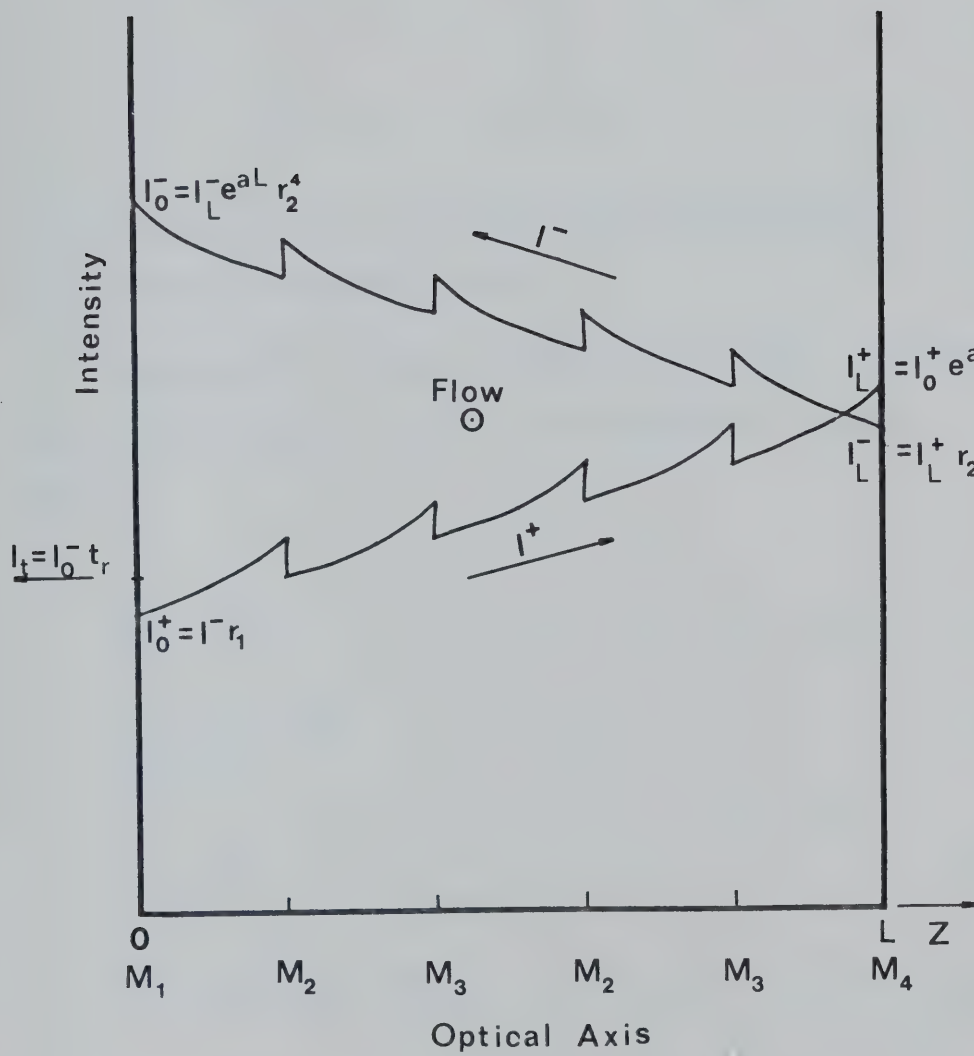


Figure 4-7 Schematic Diagram of the
Normalized Radiation Intensity for a
Steady-State Stimulated Emission in the
4-Mirror 5-Pass Resonator

In this 5-pass optical resonator, the mirrors are so designed that each mirror has constant reflectance⁽¹⁰⁴⁾ with the same loss factor, ℓ_o .

$$\gamma_1 = 1 - \ell_o - t_r \quad (4-19)$$

$$\gamma_2 = 1 - \ell_o$$

γ_2 is also applicable to the intermediate folding mirrors. T_r is the transmittance of the output mirror.

Assuming that the gain medium is homogeneous, the intensities at the output and the rear mirrors can be expressed in terms of α , γ_1 , γ_2 and I_o^+ .

$$I_o^+ = I_o^- \gamma_1 \quad (4-20)$$

$$I_o^- = I_o^+ \cdot e^{2\alpha L} \cdot \gamma_2^8 \cdot \gamma_1 \quad (4-21)$$

$$I_L^+ = I_o^+ \cdot e^{\alpha L} \cdot \gamma_2^4 \quad (4-22)$$

$$I_L^- = I_o^+ \cdot e^{\alpha L} \cdot \gamma_2^5 \quad (4-23)$$

The transmitted intensity, I_t , is represented by

$$I_t = I_o^- \cdot t_r = I_o^+ \cdot e^{2\alpha L} \cdot \gamma_2^8 \cdot t_r \quad (4-24)$$

From equations (4-20) and (4-21), the steady-state oscillation condition can be deduced as follows:

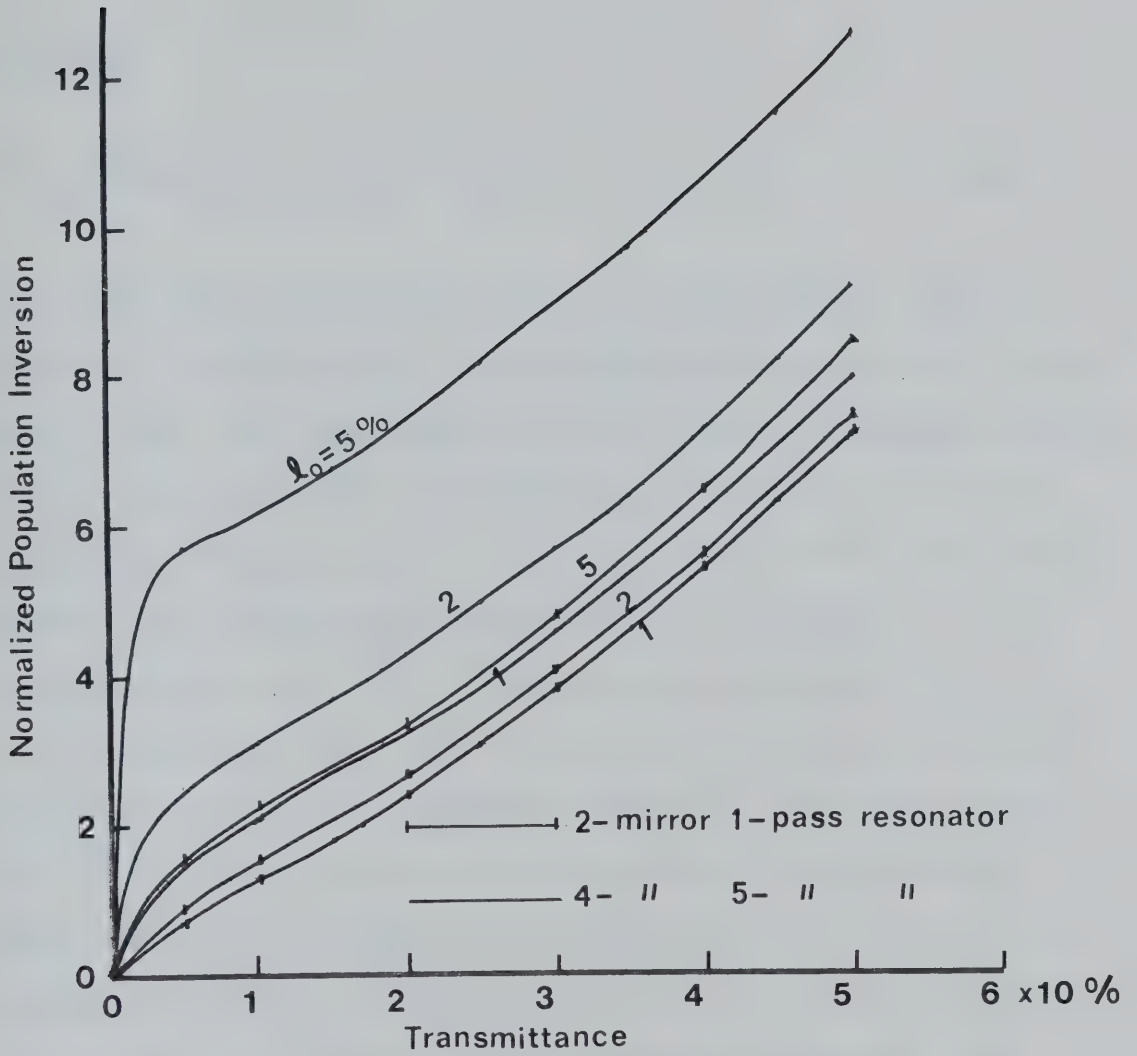


Figure 4-8 Schematic Diagram of the Normalized Steady-State Oscillation Conditions; A 4-mirror 5-pass Resonator is compared with a 2-mirror 1-pass Resonator. l_0 is the mirror loss

$$I_o^+ = I_o^+ \cdot e^{2\alpha L} \cdot \gamma_2^9 \cdot \gamma_1 \quad (4-25)$$

This gives

$$\int_0^L \alpha dZ = \alpha L = -\frac{1}{2} \ln(1 - \ell_o)^9 \cdot (1 - \ell_o - t_r) \quad (4-26)$$

This is plotted in Figure 4-8 by varying ℓ_o and t_r , for a 2-mirror 1-pass and a 4-mirror 5-pass resonators with the same effective active medium length. The result shows the effect of mirror absorption clearly. With the same reflectances and transmittances of mirrors, the single-pass resonator requires much less population inversion than the 5-pass resonator for a steady-state oscillation. The optimization of transmittance against mirror loss is well treated in Reference 102.

In conclusion, the P.I.E. laser model and computer code based on Manes and Seguin's five temperature model⁽⁹⁴⁾, and Davies' refined model⁽⁹⁷⁾, results in good parameter predictions. In this computer calculation the pulser effect was excluded on the grounds that the preionizing input power is less than 5% of the sustainer input power. However, for a P.I.E. laser with much more preionizing input power, the inclusion of pulser effect is important. More preionizing input power may degrade the pumping efficiency because it lowers the E/N value below that of this P.I.E. laser.

The parameters such as vibrational temperatures, upper and lower laser level number densities, and population inversion were also printed and plotted. The measurements of these parameters are out of the scope of this thesis. However, the computed values and curves are presented in Appendix A for reference purposes (Data 2).

CHAPTER 5

CONCLUSIONS AND SUGGESTIONS

The main objective of this project has been to develop a high power C.W. laser (at least 1 kW) for industrial application, and to conduct a detailed parametric study of the system.

A kilowatt P.I.E. (Photo-initiated, Impulse-enhanced, Electrically Excited) CO_2 C.W. laser system has been constructed and successfully operated. The pumping mechanism of the P.I.E. CO_2 laser is not different from that of a conventional CO_2 laser. However, the purpose of the P.I.E. laser system is to improve the input power loading by employing a double preionization technique; U.V. initiation and impulse enhancement.

In Chapter 1 a historical review of the operating principles and pumping mechanisms of high power CO_2 lasers was made. Selective pumping of the CO_2 upper laser level (00^01) by energy coincidence with N_2 and selective relaxation of the lower laser level (10^00) by collisional relaxation with He are two major mechanisms used to establish a population inversion in a CO_2 laser gas mixture. A larger population inversion for a fixed laser gas mixture is achieved by increasing the input power within the gain saturation limit. The input power loading can be improved by utilizing a proper preionization technique which eliminates or extends the arc limit.

The spark sources (J77 spark plugs) employed have a broad U.V. spectrum. However, one-step photoionization of a CO_2 laser gas mixture is precluded by the fact that CO_2 heavily absorbs for $\lambda < 1700\text{\AA}$ except for a narrow window at $\lambda = 1200\text{\AA}$. The one-step photoionization wavelengths of the laser gas constituents are considerably below this^(27,28,45,47).

The wide frequency spectrum of the U.V. source and the narrower bandwidth of photoionization results in a low overall preionization efficiency. The efficiency is defined as the ratio of resulting sustainer current to the preionizing power input. The preionization can be enhanced by direct impulse multiplication⁽²²⁾.

Chapter 2 provides a detailed description of the P.I.E. laser system constructed for this thesis. The system has been designed for TF (tranverse flow), and TE operation in which the electric field, gas flow and the optical axis are mutually orthogonal.

The laser box accommodating the main electrodes, optical resonator, U.V. sources and a flow guide, provides easy access so that the electrode configuration can be quickly changed. A turbo blower provides a maximum flow velocity of 50 m/s through the discharge volume; which is equivalent to an 1800 l/s flow rate. This flow rate exchanges the discharge volume 490 times per second and develops a 2.3 ms gas residence time.

Three different cathode materials, graphite, aluminum and copper machined to assume approximate Rogowski profiles, were tested. The graphite cathode proved to be unsatisfactory since the surface was eroded by repetitive impulses, and the resulting dust contaminated the system. The localized oxide film on the aluminum cathode surface distorted the discharge uniformity and eventual arc formation resulted in pits. These pits initiated arcs for subsequent tests. For the reasons mentioned above, the graphite and aluminum cathodes were exempted from further experiments. The copper cathode performed well for operation at lower pressures (< 20 torr). The thin wall of this cathode provided very efficient cooling.

In P.I.E. laser operation the space charges appear to take an important role in limiting the input power loading. A small disturbance in the uniform discharge of a continuous surface cathode may cause an arc and the restoration to a glow discharge is impossible without decreasing the sustainer voltage. This prompted the design of a multi-element cathode in which each subelectrode is ballasted by a circulating fluid; tap water or potassium carbonate (K_2CO_3) solution. Much more effective row ballasting is achieved by increasing the fluid gap in the gas flow downstream direction. The self-optimization characteristic of current distribution, resulting from electrode corrosion in the fluid, gradually improves the input power loading with the operating time. After 100 hours of operation the input power was improved by a factor of three. Also, in the event of an arc in the discharge the increased elemental current causes localized heating and vaporization of the conducting fluid. The high resistance gas bubbles, momentarily so formed, then acts to extinguish the arc. Uniform current distribution is therefore resumed without experiencing component damage.

The most effective anode was found to be a grate-type, made of 6.3mm copper tubes. The tubes were spaced 6.3mm apart so that 50% U.V. transmission was obtained.

The preionizer is composed of two units; a trigger unit and a pulser unit. The trigger unit provides 1.6 kV positive triggering pulses to the grid of a thyratron, HY1802, in the pulser unit. D.C. charging of the pulser unit is accomplished through a set of saturable inductors. A typical value of inductance varies from 1.2 henry non-saturated to 34 millihenry saturated. This variation imposes very slow

initial charging (typically 12 μ s) and very fast main charging (6 μ s). This saturable inductor and a charging diode unit provides a resonant charging condition for a frequency less than twice that of the natural frequency. The resonant charging is characterized by the fact that the pulse voltage is almost twice the power supply voltage. This efficient pulser provides 10 megawatt pulses at a rate of 20 kHz at 20 kV.

Most of the experimental results are presented and discussed in Chapter 3. The experiments are subgrouped into three different categories. The initial experiments were conducted with a continuous surface cathode at lower pressures (< 20 torr). Subsequent experiments were devised to evaluate the solution ballasting technique, and to provide design criteria for solution ballasted electrodes. The final experiments involved two solution ballasted multipin cathodes.

In this P.I.E. laser system U.V. initiation is proven to be quite important in establishing a uniform discharge. U.V. light provides uniformly distributed background electrons which are multiplied by the immediately following impulse. The preionization efficiency is the largest for the impulse and smallest for the U.V. A slightly lower efficiency is achieved with U.V. initiation and impulse enhancement, however, the largest sustainer current is obtained.

V-I characteristic curves for this P.I.E. laser system were interpreted with the aid of those obtained in a low pressure self-sustained discharge⁽⁹²⁾. Under normal operating conditions the high background electron density from preionization causes the Townsend discharge region in the V-I characteristic curve to be absent. However, at relatively low preionization levels a V-I characteristic curve somewhat similar to

the normal glow characteristic is detected. With lower preionization, the Townsend discharge region also is detected. The glow initiation voltage gradually decreases with increasing preionization. As the preionizing power is increased a quasi-continuous glow is established without the sustainer voltage. The high current end of each curve shows the abnormal glow characteristic. In this region the sustainer voltage creates some electron-ion pairs and these are subjected to impulse multiplication. It is estimated that about 2×10^9 electrons are generated with 10kHz at 15 kV preionization. This is an order of magnitude smaller than the required density of 3×10^{10} for 20 A operation.

In connection with the V-I characteristics three modes of P.I.E. laser operation have been realized. In the preionizer sustained mode the sustainer voltage merely collects the charged particles without contributing to the plasma generation. Removal of preionization results in termination of the discharge. The self-sustained glow mode is an intermediate region where sufficient ionization to sustain a glow discharge is achieved by the sustainer voltage when the preionization is removed. In the pulser maintained mode the sustainer contributes a large part of the ionization and preionization stabilizes the discharge. When uniform background electrons are removed, E/P increases rapidly due partly to the poor sustainer power supply regulation and partly to the decreased ionization. This results in an arc.

Much improved input power loading has been achieved by utilizing both types of solution ballasted cathodes. Input power loading of 8.8 W/cc and 190 kW /lb are the thermal limits reported by Nighan⁽⁷⁵⁾, and Eckbreth⁽¹⁵⁾ respectively. Increasing pin density from 1 pin/2.6 cm² to 1 pin/1.4 cm² did not improve the power loading significantly. However,

the increased pin density decreases the current density per pin and the total ballasting resistance. Tap water can be used as a ballasting fluid. However, an electrolytic solution is more useful, since the fluid resistance may be changed with ease. A series of tests with easily obtainable compounds revealed that potassium carbonate solution is suitable for practical application. Among several pin materials tested, such as tungsten, brass, copper, aluminum, nickel, monel and stainless steel, only stainless steel showed satisfactory performance in both gas and fluid discharges. The rest of the materials performed poorly in gas and/or fluid. Moreover, stainless steel and potassium carbonate solution complemented each other so well that a cathode consisting of 3 mm diameter stainless steel pins will operate for more than a thousand hours.

The optimum CO_2 partial pressure in the laser gas mixture is found to be low (~ 2 torr out of 50 torr of total pressure). This is in good agreement with the literature^(8,13). Computer calculation shows that less than 10% of the CO_2 molecules are excited to the upper laser level. This suggests that the partial pressure of CO_2 should not be unnecessarily high because of its adverse effect on the discharge stability. The small signal gain coefficient (%/cm) is comparable to that of Reference 48. However, a direct comparison with the existing data is limited due to the unspecified discharge parameters. More meaningful comparison may be made with the "specific gain coefficient" ($\% \text{ cm}^2/\text{watt}$) which is defined as the ratio of the small signal gain coefficient to the input power density.

The small signal gain measurement also shows that the gain profile can be improved by using the differential fluid gap spacing concept, i.e.

the idea of compensating the lower plasma impedance on the gas downstream side by introducing more ballasting resistance to the downstream pins. The spatial gain variation between the cathode and anode shows a rapid change near the electrodes. The gain enhancement near the anode is in good agreement with References 35, 101. The gain variation between the rows is large near the cathode and small near the anode. This variation is also dependent on the sustainer current. At higher currents the variation is smaller. This signifies that the gas is more uniformly excited due to the fact that the discharge column from each pin grows larger with increasing current. The temporal gain variation is almost negligible since the preionizing input power is less than 5%, and the sustainer current fluctuation is small under normal operation.

A 5-pass optical resonator with a hole coupled output mirror was used to extract a maximum laser output power of 1200 watts continuous wave at 10.6 μm . This yielded approximately a 5% discharge efficiency and a 3.5% overall efficiency. This relatively low efficiency is attributed to the high reflection loss of the multipass system employed. A theoretical calculation shows that at best only 50% extraction of the available power can be achieved with this 5-pass system. This situation could be improved by designing a longer laser cavity and utilizing a resonator making fewer passes. This argument is supported by the fact that, for a lower pressure discharge (< 20 torr), the 5-pass optical resonator extracted only 4% of the discharge power, while a 2-pass resonator achieved a 10.5% efficiency.

The quality of the laser beam obtained with the hole coupled mirror is low in the sense that the focused beam size is too large (typically

~ 5 mm diameter). The reason for this is that most of the beam power is extracted by refraction. This problem can be solved by using a dielectric mirror within the threshold power density. The focused beam size was reduced to approximately 1 mm by using a ITRAN IV (Zinc Selenide) output mirror. This is equivalent to a power density of $1.3 \times 10^5 \text{ W/cm}^2$ when the output power is 1 kW. This power density is capable of cutting 2 cm thick mild steel, and of penetrating welding 3 mm thick stainless steel. The device also proved to be capable of drilling deep holes in such materials as concrete, NaCl, coal, ceramic, and asbestos.

The P.I.E. laser modeling was performed in Chapter 4. Manes and Seguin's five temperature model⁽⁹⁴⁾ was refined to include the effects of CO and the change of the translational temperature in the discharge by Davis et al⁽⁹⁷⁾. This model has been further extended to represent the C.W. P.I.E. laser developed for this thesis. The time evolution of the energy stored in each vibrational mode is also a spatial dependent in this P.I.E. laser system. The left hand side of each energy balance equation is modified to include two independent variables and the gas flow velocity.

Five vibrational energy equations, the time rate of change of the total gas kinetic energy equation, and the time evolution of the radiation intensity were solved by using System/360 Continuous System Modeling Program language which has eight built-in integration routines. This program can produce many outputs such as the gain coefficient, gain, number densities, vibrational temperatures, translational temperature and power output. Due to the limited space only several parameters are calculated, and the results are included in Appendix A. The results are in good agreement with the measured data.

The P.I.E. C.W. laser system developed for this thesis may be utilized in industry as a basic unit of a high power laser system. A building block concept, in which a system is scaled up by stacking the unit system in series, may be useful. A simple calculation in this connection shows that a 3 m long system (6 units) will easily produce a 10 kW C.W. laser. In this scaling method, no uncertainty factors are involved. The anode developed in this project may be utilized in very high power laser systems. The potassium carbonate solution ballasted, stainless steel pin cathode appears readily scalable to very large size and power levels. This pair of electrodes and the P.I.E. technique have constituted a firm basis for stable, durable and controllable high power laser operation.

Investigation is required on the mirror curvature arrangement, and the reflectivity of the output mirror to obtain the maximum optical power extraction efficiency. In this connection, the focused beam quality has to be studied for efficient material processing.

An automatic or semi-automatic control system is required to correct the gradual misalignment of the optical resonator during operation. The misalignment may occur by such mechanical causes as systems' vibration and mirror surface heating.

Also a high power beam monitoring and controlling device is needed for fully controlled material processing. The above suggestions cover only a part of many research topics related to industrial application of a P.I.E. laser.

REFERENCES

1. C.K.N. Patel, "Continuous Wave Laser Action on Vibrational Transitions of CO_2 ", Phys. Rev. Lett., Vol. 336A, pp. 1187-1193, Nov. 1964.
2. C.K.N. Patel, "Selective Excitation Through Vibrational Energy Transfer and Optical Laser Action in $\text{N}_2\text{-CO}_2$ " Phys. Rev. Lett., Vol. 13, pp. 617-619, Nov. 1964.
3. G. Moeller and J.D. Rigden, "High Power Laser Action in $\text{CO}_2\text{-He}$ Mixtures", Appl. Phys. Lett., Vol. 7, pp. 274-279, Nov. 1965.
4. W.B. Tiffany, R. Targ, and J.D. Foster, "Kilowatt CO_2 Gas Transport Laser", Appl. Phys. Lett., Vol. 15, pp. 91-93, Aug. 1969.
5. A.J. Demaria, "Review of C.W. High-power CO_2 Lasers", Proc. IEEE Vol. 61, No. 6, June 1973.
6. A.C. Eckbreth, J.W. Davis and E.A. Pinsley, "Investigations of a CO_2 Laser Pulse Amplifier", Appl. Phys. Lett., Vol. 18, No. 3, pp. 73-75, Feb. 1971.
7. A.C. Eckbreth and J.W. Davis, "Cross Beam Electric-discharge Convection Laser", Appl. Phys. Lett., Vol. 19, No. 4, pp. 101-103, Aug. 1971.
8. A.E. Hill, "Uniform Electrical Excitation of Large High Pressure Nearsonic $\text{CO}_2\text{-N}_2\text{-He}$ Flow Stream", Appl. Phys. Lett., Vol. 18, No. 5, pp. 194-197, Mar. 1971.
9. E.T. Gerry, "Gas Dynamic Lasers", IEEE Spectrum Vol. 7, pp. 51-58, 1970.

10. E.V. Locke, R. Hella and L. Westra, "Performance of an Unstable Oscillator on a 30 K.W. C.W. Gas Dynamic Laser, Appl. Phys. Lett., Vol. 21, No. 1, pp. 25-27, July 1972.
11. P.K. Cheo, "CO₂ Lasers", Lasers, Vol. 3, Marcel Dekker, New York, 1971.
12. R.D. Hake and A.V. Phelps, "Momentum Transfer and Inelastic-collision Cross Sections for Electrons in O₂, CO, and CO₂", Phys. Rev. Vol. 18, p. 70, 1967.
13. R.B. Lancashire, D.L. Arger, E.J. Manista, G.J. Slaby, J.W. Dunning and R.M. Stubbs, "The NASA High Power Carbon Dioxide Laser - A Versatile Tool for Laser Application", Proc. Soc. Photo Opt. Inst. Eng. Vol. 86, pp. 11-19, Aug. 1976.
14. A.K. LaFlamme, "Double Discharge Excitation for Atmospheric Pressure CO₂ Lasers", Rev. Sci. Instrum., Vol. 43, pp. 995-998, July 1972.
15. A.C. Eckbreth and J.W. Davis, RF Augmentation in CO₂ Closed Cycle D.C. Electric Discharge Convection Lasers", Appl. Phys. Lett., Vol. 21, No. 1, p. 101 July 1972.
16. H.J. Seguin and J. Tulip, "Photo Initiated and Photo Sustained Lasers", Appl. Phys. Lett., Vol. 21, pp. 414-415, Nov. 1972.
17. D. Yu Zaroslov et al., "Plasma Jet CO₂ Lasers", JETP Lett., Vol. 15, pp. 470-472, June 1972.
18. H.G. Ahlstrom et al., "Cold Cathode Electron Beam Controlled CO₂ Laser Amplifier", Appl. Phys. Lett., Vol. 21, pp. 492-494, Nov. 1972.

19. W.L. Nighan, "Electron Energy Distributions and Collision Rates in Electrically Excited N_2 , CO_2 and CO ", Phys. Rev. Ser. A. Vol. 2, pp. 1989-2000, Nov. 1970.
20. M.J. Boness and G.J. Schulz, "Vibrational Excitation of CO_2 by Electron Impact", Phys. Rev. Lett., Vol. 21, p. 1031, 1968.
21. U.E. Hochuli and T.P. Sciacca Jr., "Cold Cathodes for Sealed-off CO_2 Lasers", IEEE Journal of Quantum Electronics, Vol. QE-10, No. 2, Feb. 1974.
22. A.E. Hill, "Continuous Uniform Excitation of Medium-pressure CO_2 Laser Plasmas by Means of Controlled Avalanche Ionization", Appl. Phys. Lett., Vol. 22, No. 12, pp. 670-673, June 1973.
23. J.P. Reilly, "Pulsed/Sustainer Electric Discharge Laser", J. Appl. Phys., Vol. 43, No. 8, pp. 3441-3446, Aug. 1972.
24. J.S. Levine and A. Javan, "Observations of Laser Oscillation in a 1 atm. CO_2 - N_2 -He Laser Pumped by an Electrically Heated Plasma Generated Via Photoionization", Appl. Phys. Lett., Vol. 22, No. 2, pp. 55-57, Jan. 1973.
25. O.P. Judd, "An Efficient Electrical CO_2 Laser Using Preionization by Ultra-violet Radiation", Appl. Phys. Lett., Vol. 22, No. 3, pp. 95-96, Feb. 1973.
26. D.B. Cohn and E.R. Ault, "Photoinitiated Transversely Sustained CO_2 Laser", Appl. Phys. Lett., Vol. 22, No. 4, pp. 138-140, Feb. 1973.
27. O.P. Judd and J.Y. Wada, "Investigations of a U.V. Preionized Electrical Discharge and CO_2 Laser", IEEE J. Quant. Elect., Vol. QE-10, No. 1, pp. 12-20, Jan. 1974.

28. D. McKen, "A Study of U.V. Photo-ionization for CO₂ Laser",
Ph.D. Thesis, Univ. of Alberta, 1976.
29. G.N. Glasoe and J.V. Lebacqz, The Hydrogen Thyatron in "Pulse
Generator", pp. 335-380, Dover Publications, Inc., N.Y. 1965.
30. F. Früngel, "Quenching Spark Gaps as Trigger Elements in High-
speed Cinematography", Tech. Report.
31. E. Panarella and V. Guty, "A Kiloampere Current Diode Based
on the Quenched Spark Principle" Journal of Phys. E:
Sci. Instrum., Vol.7, 1974.
32. R. Cappi, "A High Repetition Rate Pulse Generator Using a
Hydrogen Ceramic Thyatron", Cern/mps/co 69-17, Oct. 1967.
33. G.J. Scoles and B.P. Newton, "Very High Frequency Pulse Generators
Using Hydrogen Thyatrons", Eleventh Modulator Symposium,
Sept. 1973.
34. H.J. Seguin and G. Sedgwick, "Low Voltage Gas Transport TE CO₂
Laser", Appl. Opt., Vol. 11, pp. 745-748, Apr. 1972.
35. G. Sedgwick, "Transverse C.W. CO₂ Laser Systems", Ph.D. Thesis,
Univ. of Alberta, 1974.
36. W.J. Wiegand and W.L. Nighan, "Plasma Chemistry of CO₂-N₂-He
Discharges", Appl. Phys. Lett., Vol. 22, No. 11, pp. 583-
585, June 1973.
37. P.D. Tannen, P. Bletzinger and A. Garscadden, "Species Composition
in the CO₂ Discharge Laser", IEEE J. of Quantum Electron. Vol.
QE-10, No. 1, pp. 6-11, Jan. 1974.
38. P.K. Cheo and H.G. Cooper, "Gain Characteristics of CO₂ Laser
Amplifiers at 10.6 microns", IEEE J. of Quantum Electron.
Vol. QE-3, pp. 79-84, Feb. 1967.

39. O.G. Feil, "Van Systems for Very Wide Angle Subsonic Diffusers",
Trans. of the ASME J. of Basic Engrg., pp. 759-764, Dec. 1964.
40. A.C. Eckbreth and F.S. Owen, "Flow Conditioning in Electric
Discharge Connection Lasers", Rev. Sci. Instr., 43, pp. 995-
998, 1972.
41. A.J. Chapman and W.F. Walker, "Introductory Gas Dynamics", Holt
Publication, 1971, pp. 149-104 and 442-447.
42. J.D. Cobine, "Gaseous Conductors", Dover Publications Inc., New
York, pp. 177-181.
43. F.M. Penning, "Electrical Discharges in Gases", Philips Technical
Library, Holland, 1957.
44. W.M. Clark Jr., and R.C. Lind, "Space and Time Resolved Gain
Measurements of a U.V.-sustained CO₂ Laser", Appl. Phys.
Lett., Vol. 25, No. 5, Sept., 1974.
45. R.C. Lind, J.Y. Wada, G.J. Dunning and W.M. Clark Jr., "A Long-
pulse High-energy CO₂ Laser Pumped by an Ultra-violet
Sustained Electric Discharge", IEEE J. of Quant., Electron.,
Vol. QE-10, pp. 818-821, Oct. 1974.
46. E. Locke, "Multikilowatt Industrial CO₂ Lasers", Proc. Soc. pho.
opt. inst., Eng. Vol. 86, pp. 2-10, Aug. 1976.
47. R.C. Lind, "High Energy CO₂ Laser Pumped by a U.V. Sustained
Discharge", IEEE J. of Quant. Electron., Vol. QE-11, p. 710,
Sept. 1975.
48. S.A. Wutzke, L.H. Taylor, J.L. Pack, T.V. George and L.A. Weaver,
"C.W. Pin Discharge Laser Final Technical Report", Nov. 1974.

49. A.M. Prokhorov, "Molecular Amplifier and Generator for Submillimeter Waves", JETP (USSR), Vol. 34, pp. 1658-1659, June 1958.
50. A.L. Schawlow and C.H. Townes, "Infrared and Optical Masers", Phys. Rev., Vol. 29, pp. 1940-1949, Dec. 1958.
51. A.G. Fox and T. Li, "Resonant Modes in an Optical Maser", Proc. IRE., Vol. 48, pp. 1904-1905, Nov. 1960, "Resonant Modes in a Maser Interferometer", Bell Syst. Tech. J., Vol. 40, pp. 453-488, Mar. 1961.
52. G.D. Boyd and J.P. Gordon, "Contocal Multimode Resonator for Millimeter Through Optical Wave-length Masers", Bell Syst. Tech., J., Vol. 40, pp. 489-508, Mar. 1961.
53. G.D. Boyd and J. Cogelnik, "Generalized Confocal Resonator Theory", Bell Syst. Tech. J., Vol. 41 pp. 1347-1368, July 1962.
54. A.E. Siegman, "Unstable Optical Resonators for Laser Applications", IEEE Proc., Vol. 53, pp. 277-287, Mar. 1965.
55. H. Kogelnik and T. Li, "Laser Beams and Resonators", Appl. Opt., Vol. 5, No. 10, Oct. 1966.
56. S.S. Charschan, "Lasers in Industry", Vannostranal Reinhold Co., N.Y.
57. C.K.N. Patel, "C.W. High Power Laser Action in CO_2 -He Mixture", Appl. Phys. Lett., Vol. 7, No. 10, pp. 274-276, Nov. 1965.
58. C.K.N. Patel, P.K. Tien and J.H. McFee, "C.W. High Power CO_2 - N_2 -He Laser", Appl. Phys. Lett., Vol. 7, No. 11, pp. 290-292, Dec. 1965.
59. J.R. Meyer-Ardent, "Introduction to Classical and Modern Optics", Prentice Hall, N.J., 1972.

60. R. Ulrich, T.J. Bridges and M.A. Pollack, "Variable Metal Mesh Coupler for Infrared Lasers", Appl. Opt., Vol. 9, No. 11, p. 2511 Nov. 1970.
61. E.A. Philips, J.P. Reilly, and D.B. Norman, "Off Axis Unstable Laser Resonator; Operations", Appl. Opt., Vol. 15, No. 9, p. 2159, Sept. 1976.
62. DE. McCumber, "Eigenmodes of a Symmetric Cylindrical Confocal Laser Resonator and Their Perturbation by Output Coupling Apertures", Bell. Syst. Tech. J., Vol. 44, No. 2, pp. 333-363, Feb. 1965.
63. D.E. McCumber, "Eigenmodes of an Asymmetric Confocal Laser Resonator with a Single Output Coupling Aperture", Bell Syst. Tech. J., Vol. 48, No.3 p. 1919, 1969.
64. R. Ulrich, K.F. Renk and L. Genzel, IEEE Trans. MTT-11, p. 363, 1963.
65. R.A. Wood, N. Brignall, C.R. Pidgeon and F. Alberkdal, "An Optically Pumped Wave Guide Laser with Mesh Reflectors", Opt. Comm., Vol. 14, No. 3, pp. 301-303, July 1975.
66. D.J. Spencer, H. Mirrels, T.A. Jacobs and R.W.E. Gross, "Preliminary Performance of a C.W. Chemical Laser", Appl. Phys. Lett., Vol. 16, No. 6, p. 235, 1970.
67. D.J. Spencer, D.A. Durraw and H.A. Bixler, "Continuous-Chemical-Laser Cavity Study", Appl. Phys. Lett., Vol. 20, p. 164, 1972.
68. H.C. Wright, "Infrared Techniques", pp. 1-20, Oxford, 1973.

69. A. Javan and J.S. Levine, "The Possibility of Producing Laser Plasmas Via Photoionization", IEEE J. of Quant. Elect., Vol. QE-8, No. 11, pp. 827-832, 1972.
70. P.K. Cheo, "Effects of Gas Flow on Gain of 10.6 Micron CO₂ Laser Amplifiers", IEEE J. of Quant. Elect., Vol. QE-3, No. 12, pp. 683-689, Dec. 1967.
71. A.D. Wood, M. Camac and E.T. Gerry, "Effects of 10.6 μ m Laser Induced Air Chemistry on Atmospheric Refractive Index", Appl. Opt. Vol. 10, p. 1877, 1971.
72. P.K. Cheo and H.G. Cooper, "Gain Characteristics of CO₂ Laser Amplifier at 10.6 Microns", IEEE J. of Quant. Elect., Vol. QE-3, p. 79, 1967.
73. T. Aoki, C. Yamada, and M. Katayama, "Impulsive Optic Acoustic Effect of CO₂, SF₆ and NH₂ Molecules", Jap. J. Appl. Phys. Vol. 10, p. 1303, 1971.
74. M.C. Gower and A.I. Carswell, "Vibration-translation Rates in CO₂ Glow Discharges", Appl. Phys. Lett., Vol. 22, No. 7, Apr. 1973.
75. W.L. Nighan and W.J. Wiegand, "Causes of Arching in C.W. CO₂ Convention Laser Discharge", Appl. Phys. Lett., 25, p. 633, 1974.
76. J. Tulip and H. Seguin, "High Pressure Glow Discharge Using Differentially Pumped Cathode", Applied Phys. Lett., Vol. 27, No. 1, p. 15, July 1975.
77. E.V. Locke, E.D. Hoag and R.A. Hella, "Deep Penetration Welding With High Power CO₂ Lasers", IEEE J. of Quant. Elect. Vol.

QE-8, pp. 132-135, Feb. 1972.

78. D.J. Baordsen, D.J. Schmatz, and R.E. Bisaro, "High Speed Welding of Sheet Steel with a CO₂ Laser", Welding J., Vol. 52, Apr. 1973.
79. E.V. Locke and R.A. Hella, "Metal Processing with a High Power CO₂ Laser", IEEE J. Quant. Elect., Vol. QE-10, No. 2, Feb. 1974.
80. J.R. Williamson, "Summary of Air Force Programs in Laser Cutting", Proc. Soc. Photo Opt. Inst. Eng., Vol. 86, pp. 40-46, 1976.
81. E.H. Newman, "Electrolytic Conduction", Chapman and Hall Ltd., pp. 36-96, 1930.
82. H.P. Talbot and A.A. Boanchard, "Electrolytic Dissociation Theory", The MacMillan Co., N.Y. 1915.
83. C.T. Kingzett, "Chemical Encyclopedia", pp. 146-147, 1932.
84. D. Dobos, "Electrochemical Data", Elsevier Scientific Publishing Co., N.Y. pp. 19-53, 1975.
85. P.V. Shchigolev, "Electrolytic and Chemical Polishing of Metals", Holon, Israel, 1970.
86. F.L. LaQue and H.R. Copson, "Corrosion Resistance of Metals and Alloys", Reinhold Publishing Corporation, N.Y., pp. 375-456, 1963.
87. B.C. Conway, "Theory and Principles of Electrode Processes", The Ronald Press Co., N.Y. pp. 13-42 and 183-218, 1965.
88. H.R. Thirsk and J.A. Harrison, "A Guide to the Study of Electrode Kinetics", Academic Press, N.Y., pp. 1-6, 1972.
89. P. Delahay, "Double Layer and Electrode Kinetics", Interscience, N.Y. 1965.

90. O.P. Judd, "The Effect of Gas Mixture on the Electron Kinetics in the Electrical CO₂ Gas Lasers", J. Appl. Phys., Vol. 45, No. 10, p. 4572, 1974.
91. L.B. Loeb, "Fundamental Processes of Electrical Discharge in Gases", John Wiley and Sons Inc., N.Y. 1939.
92. E. Nasser, "Fundamentals of Gaseous Ionization and Plasma Electronics", A Division of John Wiley and Sons Inc., N.Y. 1971.
93. L.J. Denes and J.J. Locke, "V-I Characteristic of Pulsed CO₂ Laser Discharge", Appl. Phys. Lett., Vol. 23, No. 3, pp. 130-132, Aug. 1973.
94. K.R. Manes and H.J. Seguin, "Analysis of the CO₂ TEA Laser", J. Appl. Phys., Vol. 43, No. 12, p. 2038, 1972.
95. E.N. Bazarov, G.A. Geraimov and Yu. I. Posudin, "Chemical Reactions During Electric Discharges in Molecular Gas", Sov. J. Quant. Electron., Vol. 5, No. 11, p. 1351, 1975.
96. A.R. Davies, "Calculation on Output Pulse Shapes, Gain Pulse Profiles, Gain Limitation in the CO₂ TEA Laser", J. Appl. Phys. Vol. 47, No. 5, 1976.
97. A.R. Davies, K. Smith and R.M. Thomson, "Tlaser - A CO₂ Laser Kinetics Code", Comput. Phys. Commun. 10, p. 117, 1975.
98. W.G. Vincent and G.H. Kruger, "Introduction to Physical Gas Dynamics", McGraw-Hill Book Co., N.Y.
99. P.A. Thomson, "Compressible Fluid Dynamics", McGraw-Hill Book Co., N.Y.
100. A.A. Vednov, A.F. Vitshas, A.P. Napartovinch, and V.P. Panchenko, "Calculation of the Energy Characteristics of an Electric

- Discharge CO₂ Laser", Sov. J. Quant. Electron., Vol. 5,
No. 12. pp. 1404-1408, 1976.
101. J.M. Hoffman, F.W. Bingham, and J.B. Moreno, "Parametric
Experimental and Theoretical Study of a Cold-Cathode
Electron Beam Controlled CO₂ Laser",
J. Appl. Phys., Vol. 45, No. 4, p.1798, 1974.
 102. T.A. Cool, "Power and Gain Characteristics of High Speed Flow
Lasers", J. of Appl. Phys., Vol. 40, No. 9, Aug. 1969.
 103. W.J. Witteman, Philips Res. Rep., Suppl., 2 p 58 1963.
 104. C.S. Kakshminarasimba, J. Lucas, J.L. Moruzzi and J.J. Spalding
"Electron Swarm Parameters in CO₂ Laser Gas Mixture",
J. Phys. D:, Appl. Phys., Vol. 9, p. 1727, 1976.
 105. L.J. Denes, L.E. Kline, M.J. Pechersky, R.J. Spreadbury and
L.H. Taylor "Ultraviolet-initiated CO₂ Laser Research"
Technical Report #76-902
 106. CSMP User's Manual, IBM. U of A Library ID No.
CH20-0367-4.

APPENDIX A

Computer Program

The program provides an application-oriented language that allows the problems to be prepared directly from a set of ordinary differential equations.

Two important features of S/360 CSMP are statement sequencing and a choice of integration methods. With few exceptions, structure statements may be written in any order and, at the user's option, may be sorted automatically (or not sorted) by the system to establish the correct information flow. Centralized integration is used to ensure that all integrator outputs are computed simultaneously at the end of the iteration cycle. A choice may be made among the fifth-order Milm predictor-corrector, fourth-order Runge-Kutta, Simpson's, second-order Adams, trapezoidal, and rectangular integration methods.

FORTRAN IV (Level G) is used as the source language. With the proper MTS (Michigan Terminal System) command language explained in Reference 105, the CSMP source program is translated, executed, printed, plotted or punched.

Normally the independent variable is time, t . However, in this case the independent variable is downstream distance, x . For this reason, the time is renamed to x before the INITIAL segment. The program is immediately followed. The data 1 and data 2 are the computed results for the first and second computation respectively. The graphs are computer plots for some of the second computation outputs.

CW PIE LASER

DATA1

RKS

INTEGRATION

X	CM	T	K	T1	K	T2	K	ALPHA	GAIN	V1000 CM ³	V0001 CM ³	DELM CM ³
0.0		3.0000E 02		3.0000E 02		3.0000E 02		-4.6827E-05	9.9738E-01	7.1005E 13	7.0663E 11	-2.1969E+12
2.0000E-01		3.0003E 02		3.0113E 02		3.0097E 02		2.0280E-04	1.0114E 00	7.2511E 13	1.6531E 14	9.5151E+12
4.0000E-01		3.0019E 02		3.0201E 02		3.0177E 02		4.5521E-04	1.0250E 00	7.3655E 13	3.3170E 14	2.1363E+13
6.0000E-01		3.0044E 02		3.0294E 02		3.0261E 02		6.8639E-04	1.0392E 00	7.4886E 13	4.8446E 14	3.2226E+13
8.0000E-01		3.0079E 02		3.0389E 02		3.0350E 02		8.9748E-04	1.0516E 00	7.6188E 13	6.2451E 14	4.2170E+13
1.0000E 00		3.0121E 02		3.0487E 02		3.0441E 02		1.0906E-03	1.0630E 00	7.7549E 13	7.5292E 14	5.1270E+13
1.2000E 00		3.0170E 02		3.0586E 02		3.0535E 02		1.2648E-03	1.0735E 00	7.8969E 13	8.7075E 14	5.9601E+13
1.4000E 00		3.0226E 02		3.0687E 02		3.0631E 02		1.4275E-03	1.0832E 00	8.0436E 13	9.7885E 14	6.7223E+13
1.6000E 00		3.0289E 02		3.0790E 02		3.0730E 02		1.5737E-03	1.0921E 00	8.1974E 13	1.0779E 15	7.4188E+13
1.8000E 00		3.0358E 02		3.0895E 02		3.0832E 02		1.7043E-03	1.1003E 00	8.3572E 13	1.1685E 15	8.0529E+13
2.0000E 00		3.0433E 02		3.1002E 02		3.0935E 02		1.8247E-03	1.1077E 00	8.5217E 13	1.2515E 15	8.6317E+13
2.2000E 00		3.0514E 02		3.1110E 02		3.1041E 02		1.9358E-03	1.1145E 00	8.6924E 13	1.3276E 15	9.1596E+13
2.4000E 00		3.0599E 02		3.1219E 02		3.1148E 02		2.0345E-03	1.1207E 00	8.8679E 13	1.3972E 15	9.6395E+13
2.6000E 00		3.0688E 02		3.1330E 02		3.1257E 02		2.1236E-03	1.1263E 00	9.0488E 13	1.4609E 15	1.0076E+14
2.8000E 00		3.0782E 02		3.1441E 02		3.1368E 02		2.2037E-03	1.1313E 00	9.2348E 13	1.5191E 15	1.0472E+14
3.0000E 00		3.0880E 02		3.1554E 02		3.1480E 02		2.2757E-03	1.1359E 00	9.4252E 13	1.5723E 15	1.0832E+14
3.2000E 00		3.0981E 02		3.1668E 02		3.1593E 02		2.3399E-03	1.1400E 00	9.6218E 13	1.6207E 15	1.1156E+14
3.4000E 00		3.1083E 02		3.1781E 02		3.1706E 02		2.3971E-03	1.1437E 00	9.8195E 13	1.6647E 15	1.1448E+14
3.6000E 00		3.1191E 02		3.1895E 02		3.1820E 02		2.4480E-03	1.1469E 00	1.0024E 14	1.7048E 15	1.1711E+14
3.8000E 00		3.1302E 02		3.2013E 02		3.1939E 02		2.4928E-03	1.1498E 00	1.0237E 14	1.7412E 15	1.1946E+14
4.0000E 00		3.1417E 02		3.2132E 02		3.2057E 02		2.5321E-03	1.1523E 00	1.0455E 14	1.7743E 15	1.2157E+14
4.2000E 00		3.1534E 02		3.2252E 02		3.2178E 02		2.5663E-03	1.1546E 00	1.0679E 14	1.8042E 15	1.2344E+14
4.4000E 00		3.1653E 02		3.2373E 02		3.2299E 02		2.5957E-03	1.1565E 00	1.0909E 14	1.8311E 15	1.2509E+14
4.6000E 00		3.1774E 02		3.2494E 02		3.2421E 02		2.6209E-03	1.1581E 00	1.1143E 14	1.8554E 15	1.2655E+14
4.8000E 00		3.1898E 02		3.2617E 02		3.2545E 02		2.6421E-03	1.1595E 00	1.1383E 14	1.8771E 15	1.2782E+14
5.0000E 00		3.2024E 02		3.2740E 02		3.2670E 02		2.6594E-03	1.1606E 00	1.1630E 14	1.8964E 15	1.2894E+14
5.2000E 00		3.2151E 02		3.2864E 02		3.2795E 02		2.6734E-03	1.1615E 00	1.1880E 14	1.9137E 15	1.2984E+14
5.4000E 00		3.2280E 02		3.2989E 02		3.2921E 02		2.6843E-03	1.1622E 00	1.2135E 14	1.9290E 15	1.3063E+14
5.6000E 00		3.2408E 02		3.3113E 02		3.3046E 02		2.6925E-03	1.1627E 00	1.2393E 14	1.9424E 15	1.3129E+14
5.8000E 00		3.2537E 02		3.3236E 02		3.3172E 02		2.6981E-03	1.1631E 00	1.2656E 14	1.9541E 15	1.3183E+14
6.0000E 00		3.2668E 02		3.3363E 02		3.3299E 02		2.7011E-03	1.1633E 00	1.2924E 14	1.9642E 15	1.3224E+14
6.2000E 00		3.2802E 02		3.3491E 02		3.3427E 02		2.7016E-03	1.1633E 00	1.3201E 14	1.9727E 15	1.3253E+14
6.4000E 00		3.2936E 02		3.3619E 02		3.3557E 02		2.7002E-03	1.1632E 00	1.3482E 14	1.9799E 15	1.3273E+14
6.6000E 00		3.3072E 02		3.3748E 02		3.3687E 02		2.6968E-03	1.1630E 00	1.3769E 14	1.9859E 15	1.3284E+14
6.8000E 00		3.3209E 02		3.3878E 02		3.3818E 02		2.6915E-03	1.1627E 00	1.4063E 14	1.9905E 15	1.3285E+14
7.0000E 00		3.3349E 02		3.4010E 02		3.3952E 02		2.6843E-03	1.1622E 00	1.4367E 14	1.9941E 15	1.3278E+14
7.2000E 00		3.3489E 02		3.4142E 02		3.4085E 02		2.6756E-03	1.1616E 00	1.4674E 14	1.9966E 15	1.3263E+14
7.4000E 00		3.3629E 02		3.4275E 02		3.4220E 02		2.6657E-03	1.1610E 00	1.4986E 14	1.9981E 15	1.3241E+14
7.6000E 00		3.3767E 02		3.4405E 02		3.4351E 02		2.6547E-03	1.1603E 00	1.5297E 14	1.9988E 15	1.3214E+14
7.8000E 00		3.3910E 02		3.4539E 02		3.4486E 02		2.6422E-03	1.1595E 00	1.5621E 14	1.9986E 15	1.3179E+14
8.0000E 00		3.4052E 02		3.4674E 02		3.4622E 02		2.6286E-03	1.1586E 00	1.5951E 14	1.9977E 15	1.3139E+14
8.2000E 00		3.4191E 02		3.4805E 02		3.4755E 02		2.6145E-03	1.1577E 00	1.6276E 14	1.9960E 15	1.3095E+14
8.4000E 00		3.4332E 02		3.4938E 02		3.4889E 02		2.5994E-03	1.1567E 00	1.6609E 14	1.9938E 15	1.3046E+14
8.6000E 00		3.4476E 02		3.5073E 02		3.5025E 02		2.5832E-03	1.1556E 00	1.6953E 14	1.9908E 15	1.2992E+14
8.8000E 00		3.4619E 02		3.5208E 02		3.5161E 02		2.5661E-03	1.1545E 00	1.7301E 14	1.9872E 15	1.2933E+14
9.0000E 00		3.4763E 02		3.5344E 02		3.5298E 02		2.5484E-03	1.1534E 00	1.7655E 14	1.9831E 15	1.2870E+14
9.2000E 00		3.4908E 02		3.5481E 02		3.5437E 02		2.5301E-03	1.1522E 00	1.8017E 14	1.9785E 15	1.2804E+14
9.4000E 00		3.5051E 02		3.5616E 02		3.5573E 02		2.5113E-03	1.1510E 00	1.8377E 14	1.9734E 15	1.2735E+14
9.6000E 00		3.5199E 02		3.5755E 02		3.5713E 02		2.4915E-03	1.1497E 00	1.8753E 14	1.9678E 15	1.2661E+14
9.8000E 00		3.5339E 02		3.5888E 02		3.5847E 02		2.4720E-03	1.1485E 00	1.9117E 14	1.9619E 15	1.2587E+14
1.0000E 01		3.5482E 02		3.6023E 02		3.5983E 02		2.4520E-03	1.1472E 00	1.9491E 14	1.9558E 15	1.2511E+14
1.0200E 01		3.5632E 02		3.6164E 02		3.6125E 02		2.4310E-03	1.1458E 00	1.9884E 14	1.9491E 15	1.2430E+14
1.0400E 01		3.5780E 02		3.6305E 02		3.6267E 02		2.4096E-03	1.1445E 00	2.0283E 14	1.9421E 15	1.2346E+14
1.0600E 01		3.5924E 02		3.6441E 02		3.6404E 02		2.3883E-03	1.1431E 00	2.0673E 14	1.9347E 15	1.2261E+14
1.0800E 01		3.6068E 02		3.6578E 02		3.6542E 02		2.3669E-03	1.1417E 00	2.1068E 14	1.9273E 15	1.2176E+14
1.1000E 01		3.6215E 02		3.6717E 02		3.6682E 02		2.3451E-03	1.1403E 00	2.1475E 14	1.9196E 15	1.2088E+14
1.1200E 01		3.6365E 02		3.6859E 02		3.6825E 02		2.3226E-03	1.1389E 00	2.1895E 14	1.9115E 15	1.1997E+14
1.1400E 01		3.6512E 02		3.7000E 02		3.6966E 02		2.3000E-03	1.1375E 00	2.2315E 14	1.9032E 15	1.1905E+14
1.1600E 01		3.6658E 02		3.7139E 02		3.7106E 02		2.2774E-03	1.1360E 00	2.2736E 14	1.8946E 15	1.1811E+14
1.1800E 01		3.6804E 02		3.7277E 02		3.7246E 02		2.2548E-03	1.1346E 00	2.3159E 14	1.8858E 15	1.1717E+14
1.2000E 01		3.6953E 02		3.7420E 02		3.7389E 02		2.2316E-03	1.1331E 00	2.3597E 14	1.8769E 15	1.1620E+14
1.2200E 01		3.7098E 02		3.7557E 02		3.7527E 02		2.2092E-03	1.1317E 00	2.4026E 14	1.8681E 15	1.1525E+14
1.2400E 01		3.7246E 02		3.7699E 02		3.7670E 02		2.1858E-03	1.1302E 00	2.4472E 14	1.8587E 15	1.1426E+14
1.2600E 01		3.7391E 02		3.7838E 02		3.7809E 02		2.1629E-03	1.1288E 00	2.4913E 14	1.8494E 15	1.1329E+14

PROBLEM DURATION 0.0

TO 1.2600E 01

VARIABLE	MINIMUM	X	MAXIMUM	X	TIMER VARIABLES
T	3.0000E 02	0.0	3.7391E 02	1.2600E 01	DELT = 1.0000E-02
ALPHA	-4.6827E-05	0.0	2.7017E-03	6.1489E 00	DELMIN= 1.2700E-04
GAIN	9.9738E-01	0.0	1.1633E 00	6.1264E 00	FINTIM= 1.2600E 01
V1000	7.1005E 13	0.0	2.4913E 14	1.2600E 01	PRDEL = 2.0000E-01
V0001	7.0663E 11	0.0	1.9988E 15	7.6766E 00	OUTDEL = 2.0000E-01
DELM	-2.1969E 12	0.0	1.3286E 14	6.7158E 00	

SAMPLE PROGRAM

****CONTINUOUS SYSTEM MODELING PROGRAM****

PROBLEM INPUT STATEMENTS

TITLE CW PIE LASER

RENAME TIME=X

INITIAL

```

VC020=PC02*Z
VN20 =FN2 *Z
VHE0 =PHE *Z
TAC  =-ALOG(RE)*2.*AL/C
SF=GMV/OTV
EE0  =T*R*(5.*VN2/2.+5.*VC02/2.+3.*VHE/2.)
E100 =TH1*R*F*VC02/(EXP(TH1/T0)-1.)
E200 =2.*TH2*R*F*VC02/(EXP(TH2/T0)-1.)
E300 =TH3*R*F*VC02/(EXP(TH3/T0)-1.)
E400 =TH4*R*VN2/(EXP(TH4/T0)-1.)
VE    =AI/(1.602E-19*VD*AR)
T      =T0
T1     =T10
T2     =T20
T3     =T30
T4     =T40
VC02   =VC020
VN2    =VN20
U       =U0
VHE    =VHE0

```

CONSTANT	X1 =4.0E-09,	X2 =4.0E-09,	X3 =5.0E-09,...
	X4 =2.0E-08,	X5 =3.0E-08,	PC02 =1.7,...
	FN2 =7.3,	PHE =36.0,	GMV =4500.0,...
	OTV =4500.0,	F =1.0,	XJ =19.0,...
	VD =1.0E07,	RE =0.63,	XH =6.62E-27,...
	AL =56.0,	AI =14.0,	AR =700.0,...
	XMC02=7.3E-23,	XMN2 =4.6E-23,	XMHE =6.7E-24
CONSTANT	R =1.38E-16,	C =2.998E10,	AMDL =10.6E-04,...
	RHE =3.7E-15,	T0 =300.0,	TH1 =1997.0,...
	TH2 =960.0,	TH3 =3380.0,	TH4 =3354.0,...
	THL =1380.0,	Z =3.536E16,...	
	B =0.386,	QC02 =1.3E-14,	QN2 =1.14E-14,...
	TASP =5.0,	DINU =0.0,	U0 =5000.0,...
	T10 =300.0,	T20 =300.0,	T30 =300.0,
			T40 =300.0

DYNAMIC

```

R1C02=8.65E-15*T**1.5
R10C02=2.07E-09*EXP(-77./T**(1./3.))
R10HE =3.65E-10*EXP(-45./T**(1./3.))
R10N2 =4.32E-10*EXP(-77./T**(1./3.))
R12C02=R1C02
R12N2 =3.68E-16*T**1.5
R12HE =4.23E-17*T**1.5
R20C02=R10C02/4.5
R20N2 =R10N2/4.5
R20HE =R10HE/4.5
FT=EXP(-4223./T-672.7/T**(1./3.)+2683./T**(2./3.))
R3C02=9.6E23*T**(-5.89)*FT
R3N2 =6.87E23*T**(-5.89)*FT
R3HE =2.43E23*T**(-5.89)*FT
R43  =6.07E-14*EXP(15.3/T**(1./3.))

```


CON'D

```

EX1  =1.-EXP(-TH1/T)
TA10 =1./((F*VCO2*R10CO2+VN2*R10N2+VHE*R10HE)*EX1)
EX2  =1.-EXP(-TH2/T)
TA20 =1./((F*VCO2*R20CO2+VN2*R20N2+VHE*R20HE)*EX2)
EX3  =(1.-EXP(-TH2/T2))/(1.+EXP(-TH2/T2))
TA12 =EX3/(2.*(F*VCO2*R12CO2+VN2*R12N2+VHE*R12HE))
EX4  =EXP(TH1/T1)-1.
EX5  =EXP(TH2/T2)-1.
EX6  =EXP(TH1/T1+TH2/T2+(TH3-TH2-TH1)/T)-1.
TA3  =EX4*EX5/(EX6*A3)
A3   =F*(VCO2*R3CO2+VN2*R3N2+VHE*R3HE)
TA43 =1./(F*VCO2*R43)
E1E0 =TH1*R*F*VCO2/(EXP(TH1/T)-1.)
E1E2 =TH1*R*F*VCO2/(EXP(TH1/T2)-1.)
E2E0 =2.*F*VCO2*TH2*R/(EXP(TH2/T)-1.)
E3E210=F*VCO2*TH3*R/(EXP(TH1/T1+TH2/T2+(TH3-TH2-TH1)/T)-1.)
E4E3 =VN2*TH4*R/(EXP(TH4/T3)-1.)
PJ    =2.*XH*C*B/(R*T)*(2.*XJ+1.)*EXP(-XH*C*B*XJ*(XJ+1.)/(R*T))
PJ1   =2.*XH*C*B/(R*T)*(2.*XJ+3.)*EXP(-XH*C*B*(XJ+1.))*...
      *(2.*XJ+3.)/(R*T))
EX14 =1.-EXP(-TH1/T1)
EX15 =1.-EXP(-TH2/T2)
EX16 =1.-EXP(-TH3/T3)
V0001=F*VCO2*EXP(-TH3/T3)*EX14*EX15**2.*EX16
V1000=F*VCO2*EXP(-TH1/T1)*EX14*EX15**2.*EX16
DELN =V0001*PJ-(2.*XJ+1.)/(2.*XJ+3.)*V1000*PJ1
EX17 =4.*F*VCO2*QC02/3.14*(R*T/(3.14*XMCO2))*0.5
EX18 =VN2*QN2/3.14*(8.*R*T/3.14*(1./XMCO2+1./XMN2))*0.5
EX19 =VHE*QHE/3.14*(8.*R*T/3.14*(1./XMCO2+1./XMHE))*0.5
DENUL =EX17+EX18+EX19
W      =SF*AMDL**2./(4.*3.14**2.*THL*R*TASP*DENUL)
E1DOT=(VE*F*VCO2*TH1*R*X1-(E1-E1E0)/TA10-(E1-E1E2)/TA12+TH1...
      /TH3*(E3-E3E210)/TA3+TH1*R*DELN*W*DINU)/U
E1     =INTGRL(E100, E1DOT)
E2DOT=(VE*F*VCO2*TH2*R*X2-(E2-E2E0)/TA20+(E1-E1E2)...
      /TA12+TH2/TH3*(E3-E3E210)/TA3)/U
E2     =INTGRL(E200, E2DOT)
E3DOT=(VE*F*VCO2*TH3*R*X3-(E3-E3E210)/TA3+(E4-E4E3)...
      /TA43-TH3*R*DELN*W*DINU)/U
E3     =INTGRL(E300, E3DOT)
E4DOT=(VE*VN2*TH4*R*X4-(E4-E4E3)/TA43)/U
E4     =INTGRL(E400, E4DOT)
U      =U0*T/T0
VCO2   =VCO20*T0/T
VN2    =VN20*T0/T
VHE    =VHE0*T0/T
T      =300.0+140.0/12.7*X
T1     =TH1/ALOG(F*VCO2*TH1*R/ABS(E1)+1.)
NDSORT
XX     =2.*F*VCO2*TH2*R/ABS(E2)
IF(ABS(XX).LT.10.E-5) GO TO 2
T2=TH2/ALOG(XX+1.)
GO TO 3
2 T2   =TH2/XX
3 CONTINUE
SORT
T3     =TH3/ALOG(F*VCO2*TH3*R/ABS(E3)+1.)
T4     =TH4/ALOG(VN2*TH4*R/ABS(E4)+1.)
ALPHA  =THL*R*DELN*W*100.0
GAIN   =(EXP(ALPHA/100.0*AL)-1.0)*100.0
TIMER  DELT=0.01, FINTIM=12.6
TIMER  PRDEL=0.2
      PREPAR  T, T1, T3, ALPHA, GAIN, V1000, V0001, DELN
PRINT  T, T1, T3, ALPHA, GAIN, V1000, V0001, DELN
TERMINAL
END
STOP

```


CW PIE LASER										DATA 2		RKS		INTEGRATION			
X	CM	T	°K	T1	°K	T3	°K	ALPHA	°/CM	GAIN	°	U1000	CM ⁻³	U0001	CM ⁻³	DELN	CM ⁻³
0.0	3.0000E 02	3.0000E 02	3.0000E 02	3.0000E 02	3.0000E 02	3.0000E 02	3.0000E 02	-4.6827E-03	-2.6189E-01	7.1005E 13	7.0663E 11	-2.1969E 12					
2.0000E-01	3.0220E 02	3.0447E 02	3.0689E 02	3.0932E 02	3.1180E 02	3.1432E 02	3.1689E 02	5.2554E-02	2.9868E 00	7.6876E 13	3.7885E 14	2.4566E 13					
4.0000E-01	3.0441E 02	3.0682E 02	3.0932E 02	3.1180E 02	3.1432E 02	3.1689E 02	3.1946E 02	1.0658E-01	6.2690E 00	8.1832E 13	7.4759E 14	5.0569E 13					
6.0000E-01	3.0661E 02	3.1180E 02	3.1432E 02	3.1689E 02	3.1946E 02	3.2203E 02	3.2460E 02	1.5829E-01	9.2690E 00	8.6618E 13	1.0740E 15	7.3457E 13					
8.0000E-01	3.0882E 02	3.1518E 02	3.1775E 02	3.2032E 02	3.2289E 02	3.2546E 02	3.2803E 02	2.0241E-01	1.2002E 01	9.1243E 13	1.3631E 15	9.3596E 13					
1.0000E 00	3.1102E 02	3.1839E 02	3.2096E 02	3.2353E 02	3.2610E 02	3.2867E 02	3.3124E 02	2.4161E-01	1.4488E 01	9.5731E 13	1.6193E 15	1.1133E 14					
1.2000E 00	3.1322E 02	3.2146E 02	3.2403E 02	3.2660E 02	3.2917E 02	3.3174E 02	3.3431E 02	2.7651E-01	1.6748E 01	1.0010E 14	1.8469E 15	1.2696E 14					
1.4000E 00	3.1543E 02	3.2441E 02	3.2698E 02	3.2955E 02	3.3212E 02	3.3469E 02	3.3726E 02	3.0753E-01	1.8794E 01	1.0436E 14	2.0488E 15	1.4071E 14					
1.6000E 00	3.1764E 02	3.2726E 02	3.2983E 02	3.3240E 02	3.3497E 02	3.3754E 02	3.4011E 02	3.3523E-01	2.0850E 01	1.0852E 14	2.2288E 15	1.5284E 14					
1.8000E 00	3.1984E 02	3.3001E 02	3.3258E 02	3.3515E 02	3.3772E 02	3.4029E 02	3.4286E 02	3.5982E-01	2.2323E 01	1.1261E 14	2.3980E 15	1.6349E 14					
2.0000E 00	3.2205E 02	3.3268E 02	3.3525E 02	3.3782E 02	3.4039E 02	3.4296E 02	3.4553E 02	3.8174E-01	2.3834E 01	1.1662E 14	2.5297E 15	1.7286E 14					
2.2000E 00	3.2425E 02	3.3529E 02	3.3786E 02	3.4043E 02	3.4300E 02	3.4557E 02	3.4814E 02	4.0129E-01	2.5198E 01	1.2058E 14	2.6559E 15	1.8109E 14					
2.4000E 00	3.2646E 02	3.3783E 02	3.4040E 02	3.4297E 02	3.4554E 02	3.4811E 02	3.5068E 02	4.1866E-01	2.6421E 01	1.2448E 14	2.7678E 15	1.8929E 14					
2.6000E 00	3.2866E 02	3.4031E 02	3.4288E 02	3.4545E 02	3.4802E 02	3.5059E 02	3.5316E 02	4.3413E-01	2.7521E 01	1.2835E 14	2.8673E 15	1.9459E 14					
2.8000E 00	3.3087E 02	3.4275E 02	3.4532E 02	3.4789E 02	3.5046E 02	3.5303E 02	3.5560E 02	4.4786E-01	2.8506E 01	1.3218E 14	2.9555E 15	2.0008E 14					
3.0000E 00	3.3307E 02	3.4514E 02	3.4771E 02	3.5028E 02	3.5285E 02	3.5542E 02	3.5799E 02	4.6003E-01	2.9384E 01	1.3598E 14	3.0336E 15	2.0483E 14					
3.2000E 00	3.3528E 02	3.4750E 02	3.5007E 02	3.5264E 02	3.5521E 02	3.5778E 02	3.6035E 02	4.7077E-01	3.0165E 01	1.3977E 14	3.1024E 15	2.0892E 14					
3.4000E 00	3.3748E 02	3.4982E 02	3.5239E 02	3.5496E 02	3.5753E 02	3.6010E 02	3.6267E 02	4.8020E-01	3.0854E 01	1.4353E 14	3.1628E 15	2.1241E 14					
3.6000E 00	3.3968E 02	3.5212E 02	3.5469E 02	3.5726E 02	3.5983E 02	3.6240E 02	3.6497E 02	4.8848E-01	3.1462E 01	1.4729E 14	3.2157E 15	2.1537E 14					
3.8000E 00	3.4189E 02	3.5439E 02	3.5696E 02	3.5953E 02	3.6210E 02	3.6467E 02	3.6724E 02	4.9571E-01	3.1995E 01	1.5104E 14	3.2620E 15	2.1785E 14					
4.0000E 00	3.4409E 02	3.5664E 02	3.5921E 02	3.6178E 02	3.6435E 02	3.6692E 02	3.6949E 02	5.0198E-01	3.2460E 01	1.5479E 14	3.3021E 15	2.1990E 14					
4.2000E 00	3.4630E 02	3.5886E 02	3.6143E 02	3.6400E 02	3.6657E 02	3.6914E 02	3.7171E 02	5.0736E-01	3.2859E 01	1.5853E 14	3.3365E 15	2.2155E 14					
4.4000E 00	3.4850E 02	3.6107E 02	3.6364E 02	3.6621E 02	3.6878E 02	3.7135E 02	3.7392E 02	5.1195E-01	3.3201E 01	1.6229E 14	3.3660E 15	2.2294E 14					
4.6000E 00	3.5071E 02	3.6326E 02	3.6583E 02	3.6840E 02	3.7097E 02	3.7354E 02	3.7611E 02	5.1581E-01	3.3489E 01	1.6604E 14	3.3908E 15	2.2382E 14					
4.8000E 00	3.5291E 02	3.6544E 02	3.6801E 02	3.7058E 02	3.7315E 02	3.7572E 02	3.7829E 02	5.1999E-01	3.3727E 01	1.6981E 14	3.4114E 15	2.2449E 14					
5.0000E 00	3.5512E 02	3.6761E 02	3.7018E 02	3.7275E 02	3.7532E 02	3.7789E 02	3.8046E 02	5.2154E-01	3.3919E 01	1.7358E 14	3.4280E 15	2.2489E 14					
5.2000E 00	3.5732E 02	3.6977E 02	3.7234E 02	3.7491E 02	3.7748E 02	3.8005E 02	3.8262E 02	5.2355E-01	3.4069E 01	1.7737E 14	3.4413E 15	2.2506E 14					
5.4000E 00	3.5953E 02	3.7192E 02	3.7449E 02	3.7706E 02	3.7963E 02	3.8220E 02	3.8477E 02	5.2503E-01	3.4180E 01	1.8117E 14	3.4512E 15	2.2501E 14					
5.6000E 00	3.6173E 02	3.7405E 02	3.7662E 02	3.7919E 02	3.8176E 02	3.8433E 02	3.8690E 02	5.2603E-01	3.4256E 01	1.8498E 14	3.4582E 15	2.2475E 14					
5.8000E 00	3.6394E 02	3.7619E 02	3.7876E 02	3.8133E 02	3.8390E 02	3.8647E 02	3.8904E 02	5.2660E-01	3.4299E 01	1.8881E 14	3.4625E 15	2.2431E 14					
6.0000E 00	3.6614E 02	3.7831E 02	3.8088E 02	3.8345E 02	3.8602E 02	3.8859E 02	3.9116E 02	5.2676E-01	3.4311E 01	1.9266E 14	3.4643E 15	2.2370E 14					
6.2000E 00	3.6835E 02	3.8043E 02	3.8300E 02	3.8557E 02	3.8814E 02	3.9071E 02	3.9328E 02	5.2655E-01	3.4295E 01	1.9652E 14	3.4639E 15	2.2294E 14					
6.4000E 00	3.7055E 02	3.8255E 02	3.8512E 02	3.8769E 02	3.9026E 02	3.9283E 02	3.9540E 02	5.2599E-01	3.4253E 01	2.0040E 14	3.4613E 15	2.2204E 14					
6.6000E 00	3.7276E 02	3.8466E 02	3.8723E 02	3.8980E 02	3.9237E 02	3.9494E 02	3.9751E 02	5.2512E-01	3.4187E 01	2.0430E 14	3.4568E 15	2.2101E 14					
6.8000E 00	3.7496E 02	3.8677E 02	3.8934E 02	3.9191E 02	3.9448E 02	3.9705E 02	3.9962E 02	5.2395E-01	3.4100E 01	2.0821E 14	3.4505E 15	2.1988E 14					
7.0000E 00	3.7717E 02	3.8888E 02	3.9145E 02	3.9402E 02	3.9659E 02	3.9916E 02	4.0173E 02	5.2252E-01	3.3992E 01	2.1215E 14	3.4427E 15	2.1863E 14					
7.2000E 00	3.7937E 02	3.9099E 02	3.9356E 02	3.9613E 02	3.9870E 02	4.0127E 02	4.0384E 02	5.2083E-01	3.3866E 01	2.1611E 14	3.4333E 15	2.1729E 14					
7.4000E 00	3.8157E 02	3.9309E 02	3.9566E 02	3.9823E 02	4.0080E 02	4.0337E 02	4.0594E 02	5.1892E-01	3.3722E 01	2.2008E 14	3.4226E 15	2.1587E 14					
7.6000E 00	3.8378E 02	3.9519E 02	3.9776E 02	4.0033E 02	4.0290E 02	4.0547E 02	4.0804E 02	5.1748E-01	3.3562E 01	2.2407E 14	3.4105E 15	2.1436E 14					
7.8000E 00	3.8598E 02	3.9729E 02	3.9986E 02	4.0243E 02	4.0500E 02	4.0757E 02	4.1014E 02	5.1581E-01	3.3388E 01	2.2808E 14	3.3973E 15	2.1278E 14					
8.0000E 00	3.8819E 02	3.9939E 02	4.0196E 02	4.0453E 02	4.0710E 02	4.0967E 02	4.1224E 02	5.1194E-01	3.3201E 01	2.3211E 14	3.3831E 15	2.1114E 14					
8.2000E 00	3.9039E 02	4.0149E 02	4.0406E 02	4.0663E 02	4.0920E 02	4.1177E 02	4.1434E 02	5.0927E-01	3.3001E 01	2.3616E 14	3.3679E 15	2.0945E 14					
8.4000E 00	3.9260E 02	4.0358E 02	4.0615E 02	4.0872E 02	4.1129E 02	4.1386E 02	4.1643E 02	5.0644E-01	3.2791E 01	2.4022E 14	3.3518E 15	2.0770E 14					
8.6000E 00	3.9480E 02	4.0566E 02	4.0823E 02	4.1080E 02	4.1337E 02	4.1594E 02	4.1851E 02	5.0345E-01	3.2569E 01	2.4431E 14	3.3348E 15	2.0589E 14					
8.8000E 00	3.9701E 02	4.0779E 02	4.1036E 02	4.1293E 02	4.1550E 02	4.1807E 02	4.2064E 02	5.0033E-01	3.2338E 01	2.4841E 14	3.3171E 15	2.0405E 14					
9.0000E 00	3.9921E 02	4.0988E 02	4.1245E 02	4.1502E 02	4.1759E 02	4.2016E 02	4.2273E 02	4.9709E-01	3.2098E 01	2.5253E 14	3.2986E 15	2.0217E 14					
9.2000E 00	4.0142E 02	4.0988E 02	4.1245E 02	4.1502E 02	4.1759E 02	4.2016E 02	4.2273E 02	4.9375E-01	3.1850E 01	2.5667E 14	3.2796E 15	2.0026E 14					
9.4000E 00	4.0362E 02	4.1408E 02	4.1665E 02	4.1922E 02	4.2179E 02	4.2436E 02	4.2693E 02	4.9029E-01	3.1596E 01	2.6082E 14	3.2599E 15	1.9831E 14					
9.6000E 00	4.0583E 02	4.1618E 02	4.1875E 02	4.2132E 02	4.2389E 02	4.2646E 02	4.2903E 02	4.8673E-01	3.1334E 01	2.6498E 14	3.2397E 15	1.9634E 14					
9.8000E 00	4.0803E 02	4.1828E 02	4.1985E 02	4.2242E 02	4.2499E 02	4.2756E 02	4.3013E 02	4.8310E-01	3.1067E 01	2.6916E 14	3.2191E 15	1.9434E 14					
1.0000E 01	4.1024E 02	4.2038E 02	4.2195E 02	4.2452E 02	4.2709E 02	4.2966E 02	4.3223E 02	4.7937E-01	3.0793E 01	2.7336E 14	3.1979E 15	1.9232E 14					
1.0200E 01	4.1244E 02	4.2246E 02	4.2403E 02	4.2660E 02	4.2917E 02	4.3174E 02	4.3431E 02	4.7558E-01	3.0516E 01	2.7756E 14	3.1764E 15	1.9029E 14					
1.0400E 01	4.1465E 02	4.2458E 02	4.2615E 02	4.2872E 02	4.3129E 02	4.3386E 02	4.3643E 02	4.7170E-01	3.0232E 01	2.8179E 14	3.1544E 15	1.8824E 14					
1.0600E 01	4.1685E 02	4.2669E 02	4.2826E 02	4.3083E 02	4.3340E 02	4.3597E 02	4.3854E 02	4.6777E-01	2.9946E 01	2.8602E 14	3.1322E 15	1.8617E 14					
1.0800E 01	4.1905E 02	4.2879E 02	4.3036E 02	4.3293E 02	4.3550E 02	4.3807E 02	4.4064E 02	4.63									

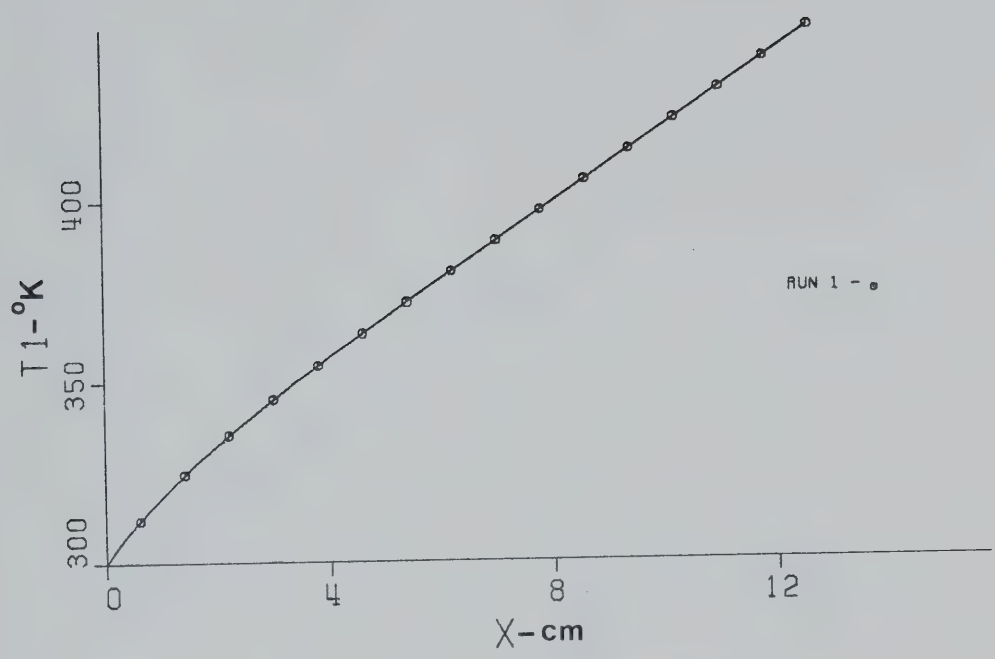


Figure APX1 Vibrational Temperature - Computed(100)

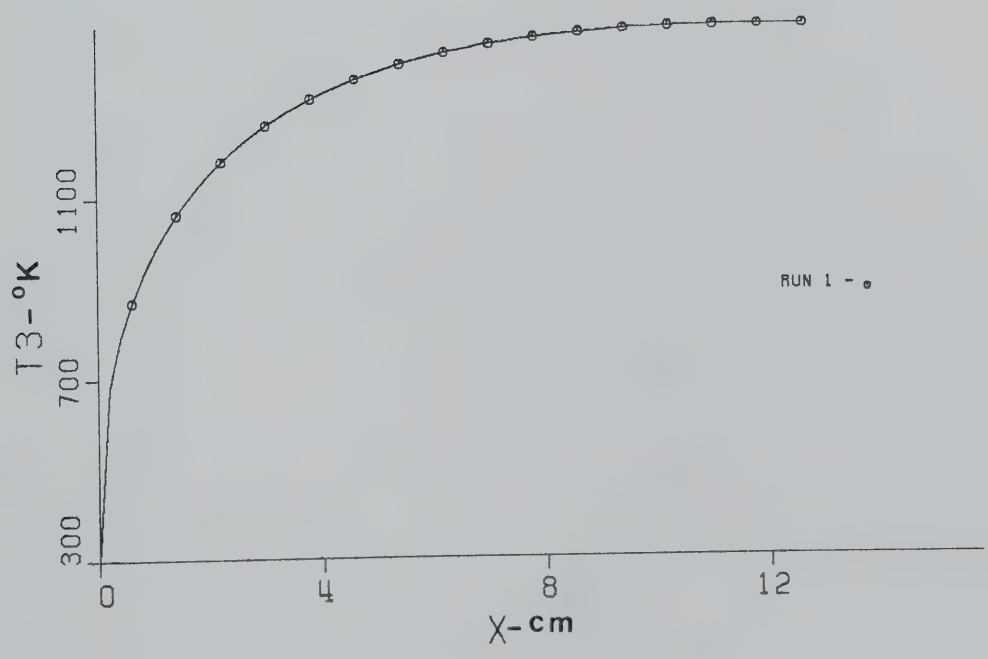


Figure APX2 Vibrational Temperature - Computed(001)

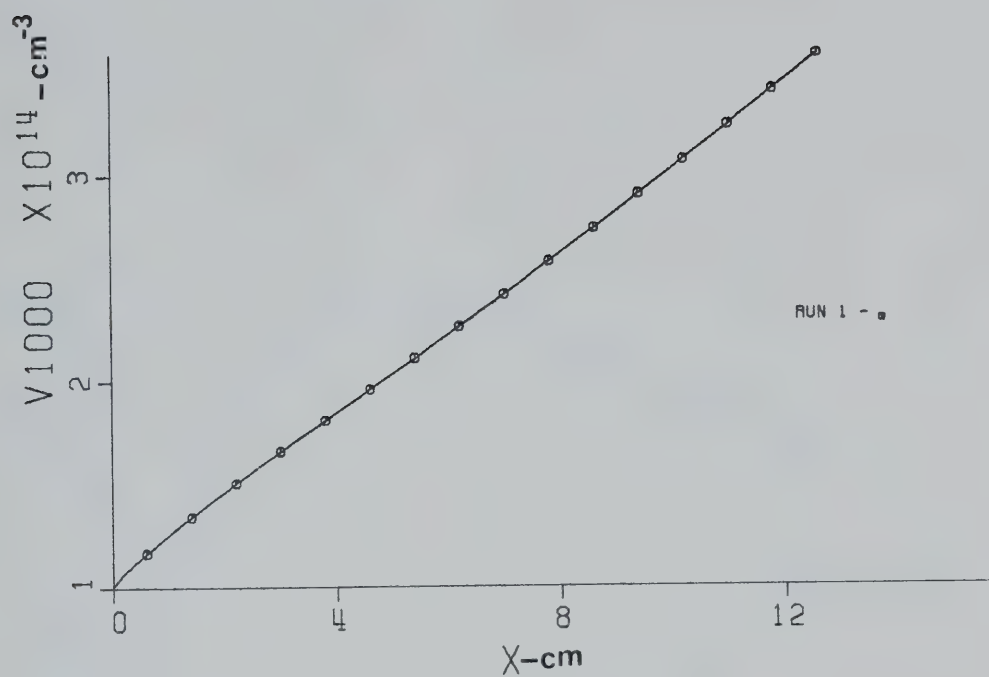


Figure APX3 Number Density - Computed (100^0)

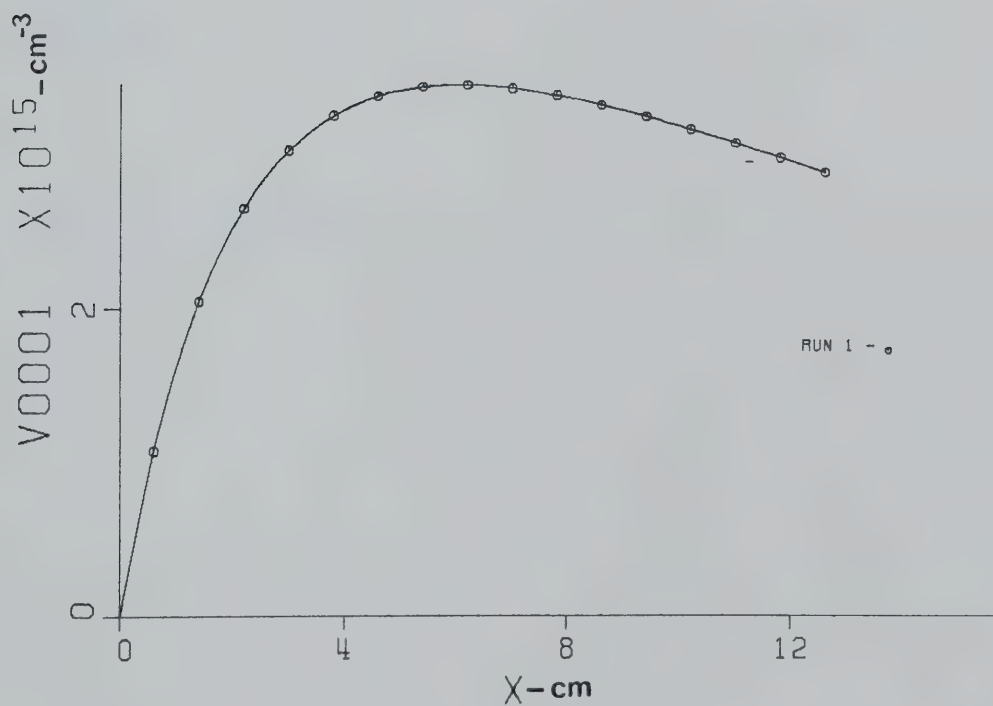


Figure APX4 Number Density - Computed (00^0_1)

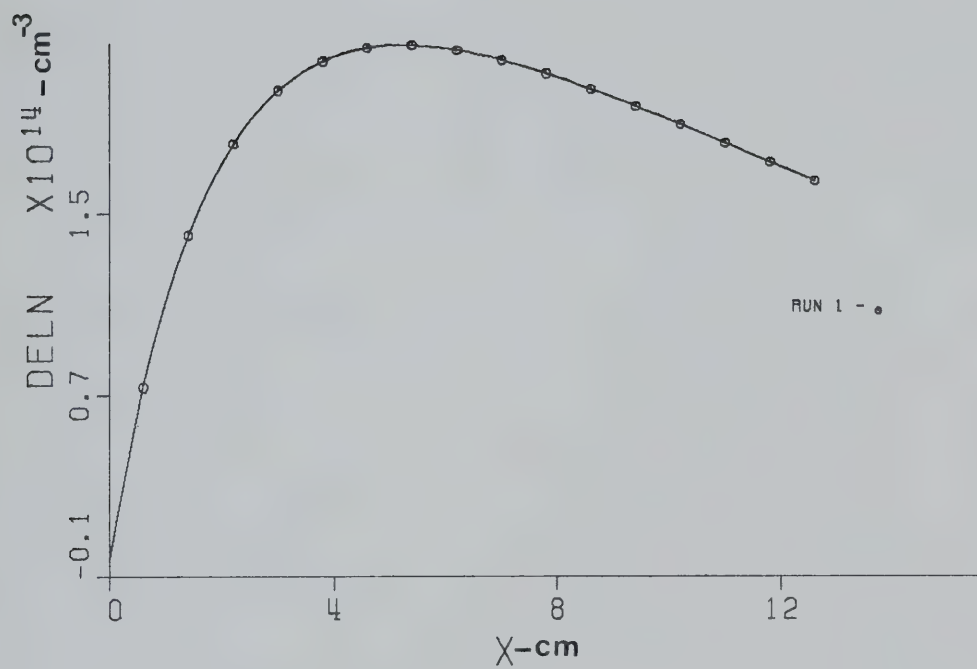


Figure APX5 Population Inversion - Computed

B30228